University of Alberta

Integrated Spectrometers for Lab-on-a-Chip Devices

by

Seyed Mohammad Azmayesh-Fard

A thesis submitted to the Faculty of Graduate Studies and Research
in partial fulfillment of the requirements for the degree of

Doctor of Philosophy
in
Photonics and Plasmas

Department of Electrical and Computer Engineering

Fall 2013
Edmonton, Alberta

In dedication to the loving memory of my supervisor, mentor, and friend

Professor James Neil McMullin

Abstract

Miniaturization of spectrometers for microfluidic applications is currently an intense area of research. This thesis is devoted to the design, fabrication, and testing of a planar optical microspectrometer. Optical microspectrometers are potentially important candidates for noninvasive detection and identification of cells and other biological material. The focus of this study was to improve the functionality of the present lab-on-a-chip devices, through monolithic integration of microfluidic channels, optical waveguides and diffraction gratings on a single disposable opto-bio-chip. One important device for spectral analysis of cells and other analytes is the diffraction grating and most fluorescence detection systems reported to date use off-chip bulk optical gratings. Here, an integrated approach based on a planar curved focusing transmission grating fabricated together with microfluidic channels, optical waveguides and a collimating lens in a single layer of polydimethylsiloxane (PDMS) is described. Layers of lower-index PDMS were bonded to this layer to provide optical and fluidic confinement. Because of the index contrast with the outer layers, light can be confined in the central "optofluidic" layer, so that propagation of light in the guiding (core) layer is governed by total internal reflection. The fabricated microspectrometer was tested using a variety of light sources including three different lasers and a broadband white light source. The optical performance of the fabricated microspectrometer closely matches the design specifications.

In summary I have made the following contributions: i) developed a new optofluidic integration process in PDMS (Chapter 5). ii) developed a set of numerical tools for analyzing individual elements of a spectrometer such as planar gratings and lenses or the device as a whole (Chapter 3). iii) fabricated and tested a novel, curved focusing transmission grating, and explored its use

for fluorescence spectroscopy (Chapter 6). iv) developed a novel dynamic strategy for sensing using the diffracted orders of the grating (Chapter 7).

Acknowledgements

My deepest gratitude goes to my late advisor Dr. James Niel McMullin, who provided me the opportunity, direction and resources to carry out this research project. Jim was a man with many great virtues and those who were fortunate to know him can easily attest to that. I wish he didn't leave so soon…

Deepest appreciations are also extended to Dr. Ray G. DeCorby who immediately took over the responsibility of my supervision and who has since diligently spent numerous hours of his time to guide me through every aspect of my work. I am grateful to him for all the academic achievements I have had in the past two years.

My sincere thanks to Dr. Robert Fedosejevs and Dr. Vien Van who graciously served in my advisory, candidacy and defense committees, reviewed my thesis, and provided me with their valuable suggestions and comments.

I would also like to thank the other members of my examination committee, Drs. Christopher Dennison of Mechanical Engineering, Sandipan Pramanik of Electrical and computer Engineering, Frank Hegmann of Physics, and Dr. Kevin P. Chen of University of Pittsburgh Swanson School of Engineering for taking the time to review my thesis, and for the many useful corrections and comments.

I am particularly grateful to Dr. Eric Flaim, Lawrence Lam, and Aaron Melnyk for their collaboration and contributions to this project. I am thankful to my colleagues and fellow graduate students, past and present, especially the members of the Photonic lab group, Dr. Trevor Allen, Minchang (Carson) Zhang, Brian Drobot, Mohammadhossein Bitarafan.

Many thanks to the staff at the University of Alberta's Nanofabrication facility, especially Scott Monro, whose expert advice on fabrication was always greatly appreciated.

Finally, I would like to thank my family, my brothers and sisters for their constant support and encouragement especially, my wife Nadia and my son Darius who had to make numerous sacrifices, without their love this work was impossible.

Table of Contents

List of Tables

List of Figures

List of Symbols, Abbreviations, and Nomenclature

Symbols

ρ	fluid density
v	fluid velocity
μ	fluid viscosity
D_h	hydraulic diameter
Re	Reynolds Number
A	absorbance
b	effective optical length
c	analyte concentration
ε	analyte's molar absorption
P_0	input optical power
P_t	transmitted optical power
ε	extinction coefficient
φ	quantum efficiency
λ	wavelength
ω_o	Gaussian beam radius (at 13.5% of maximum intensity)
ω	Gaussian beam radius
D_λ	angular dispersion

D_x	linear dispersion
k	wavenumber
H_0	zero-order Hankel function of the first kind
H_1	first-order Hankel function of the first kind

Nomenclature

i	angle of incidence
i’	angle of diffraction
m	diffraction order
d	grating period
u (r)	complex amplitude function
G	Green’s function
G_	a special Green’s function
$\vec{r}$	position vector
$\vec{n}$	unit normal (vector)
S	bounding surface
V	bounding volume
D	grating step
W	grating’s facet width
n	refractive index (medium 1)

n'	refractive index (medium 2)
n_1	refractive index (medium 1)
n_2	refractive index (medium 2)
$\delta\lambda$	small change in wavelength
$\delta\theta$	small change in angle of diffraction
α	angle of incidence
β	angle of diffraction
θ_1	angle of incidence
θ_2	angle of diffraction
β_B	blaze angle
(ξ,η)	aperture dimensions (Sec. 3.9)
K	propagation vector (Sec. 3.10)
ξ	propagation angle (Sec. 3.10)
f	lens focal length
R	lens radius

Abbreviations

LOC	Lab-on-Chip
TAS	Total (chemical) Analysis System
μ-TAS	Micro-Total Analysis System

PCR	polymerase chain reaction
CE	Capillary Electrophoresis
DNA	deoxyribonucleic acid
RNA	ribonucleic acid
MEMS	Micro-Electro-Mechanical System
UV	ultraviolet
EOP	Electroosmotic pumping
EOF	Electroosmotic flow
LIGA	X-ray lithography, Electroplating, Moulding (German acronym)
PDMS	Poly(dimethylsiloxane)
PMMA	Poly(methylmetacrylate)
PS	polystyrene
PC	polycarbonate
PVC	polyvinylchloride
PETG	polyethylenetetraphtalate glycol
C-O-C	cycloolefin copolymer
SU-8	a negative photoresist
NMR	nuclear magnetic resonance
MS	mass spectrometric
TIR	Total Internal Reflection

CCD	charge coupled device
LOD	limit of detection
SPR	surface plasmon resonance
IgG	Immunoglobulin G (biology assay)
LSPR	localized surface plasmon resonance
SERS	surface enhanced Raman spectroscopy
NA	numerical aperture
SWE	single-wavelength excitation
MWE	multi-wavelength excitation
PMT	photomultiplier tube
APD	avalanche photodiode
SPAD	single-photon avalanche diode
CMOS	complementary metal-oxide semiconductor
EM-CCD	electron multiplying charge-coupled device
DRIE	deep reactive ion etching
RP	resolving power
FSR	free spectral range
AWG	arrayed waveguide grating
SEM	scanning electron microscope
FWHM	full width half maximum

MM	multimode
DAQ	data acquisition (system)

CHAPTER 1

1. Introduction

1.1 Introduction

In the past two decades we have witnessed the increasingly stringent requirements for fast online measurements of chemicals and biological materials at low concentrations. This trend has fueled rapid advances in sensor technology and has driven the development of numerous sensing devices and miniaturized multifunctional systems known as Lab-on-a-Chip (LOC). These advancements are most noticeable in the fields of chemical production, analysis of DNA and RNA macromolecules, cytometry (cell detection, identification, separation and counting), high throughput screening of drugs for pharmaceutical purposes, medical diagnostics and environmental testing [1]. Most LOC devices rely on optical detection for sensing due its noninvasive nature; furthermore the most widely used optical method is fluorescence spectroscopy because of its sensitivity and specificity. The focus of this study is to design and build an integrated optical/fluidic LOC device that will function as a microspectrometer for the analysis of chemical and biological material.

In this introductory chapter, the necessary background information is provided to facilitate the understanding and the motivation behind this research, and provide context for the upcoming chapters.

1.1.1 Lab-on-a-Chip: A cursory review of early developments

In 1983 Widmer [2] (an analytical chemist) envisioned an integrated and fully automated analysis system, which he called Total (chemical) Analysis System (TAS). Such a system incorporates all of the stages of sampling, pre-treatment of the sample, driven chemical reactions, separation of products, detection, and isolation. Also, it was envisioned that the final analysis of data would be performed in a fully automated fashion.

The first step in realization of such systems came about in 1990 through the pioneering work of Manz et al. [3], who developed a miniaturized capillary electrophoresis device for separation of DNA molecules. Transformation of TAS to μ-TAS through miniaturization had a number of appealing advantages such as reduction of reagent and sample consumption, faster reaction times and improved analytical performance. The next milestones were the miniaturization of PCR[1] [4] and development of the first miniaturized system for mixing, injection and separation [5]. Another important development in the field was the integration of PCR and capillary electrophoresis (CE) [6]. Since these early developments, μ-TAS has found application to a variety of biological and medical problems. For μ-TASs that are used in biomedical applications, Lab-on-a-Chip, bio-chip and DNA chip are other commonly used terms. The motivation behind LOC is to make miniature systems capable of performing complete chemical and biomedical assays on a chip, and which would fit into a portable device as small as the palm of the hand or even smaller. LOC has a number of advantages over macro-scale laboratory operations, including:

1. The advantages gained by miniaturization, such as: lower consumption of samples and reagents, increased accuracy and speed of reactions, increased sensitivity, high throughput, low power consumption, reduced risk of cross-contamination, and potential for lower overall cost of the system.
2. The possibility for automation: Assays and routines are automatically performed on standard chips, reducing the cost of labor and possibility of human error.
3. Integration and parallelism: Multiple functions of sample preparation, mixing, injection, reaction, separation, detection, can be integrated into one process and many such processes can run in parallel.

Potential microfluidics LOC applications include detection of chemical and biological hazardous material, high-throughput screening for drug discovery, PCR

[1] PCR stands for Polymerase Chain Reaction, which is a molecular biology assay for rapid amplification of DNA and requires a machine, which is also called PCR.

techniques for DNA and RNA analysis, cytometry, cellular biosensing, cell culturing, cellular assay, enzyme assay, immunoassay, drug delivery, and environmental analysis, to name just a few.

LOC is a truly multidisciplinary subject and has developed rapidly in the last decade. This is easily observed by the number of publications that appear each year under headings that include terms such as "microfluidics", "lab-on-a-chip", "bio-chip", and "μ-TAS". For a detailed and up-to-date account of progress in the field of μ-TAS, please refer to the extensive review articles available in the literature [7-11].

1.1.2 Microfluidics

An integral element of a LOC device is the network of interconnected micro-chambers and micro-channels for the containment and flow of fluids. The technology that entails the generation of micro-devices capable of handling small (micro/nano/pico/femto-litre) volumes of fluid is called microfluidics. Microfluidic devices have dimensions that range from a micrometer to several millimeters and often at least one dimension of the device is in the micrometer range [12, 13]. In a microfluidic device, the fluid flow behaves significantly different from our day-to-day experiences. Specifically, the flow is almost always laminar due to small size of the channels [13]. In laminar flow, the velocity of a particle in the stream of fluid is not a random function of time. An interesting characteristic of laminar flow is that two or more streams can flow in contact with each other without mixing, except by diffusion. In fluid dynamics fluid flow is characterized by Reynolds number (Re), which describes the flow's regime (i.e. laminar or turbulent), and is defined by:

$$\mathrm{Re} = \frac{\rho v D_h}{\mu} \ , \qquad (1\text{-}1)$$

$\boldsymbol{\rho}$ is the fluid density, $\boldsymbol{v}$ is the velocity of the fluid, $\boldsymbol{D_h}$ is the hydraulic diameter, and $\boldsymbol{\mu}$ is the fluid viscosity.

$\boldsymbol{D_h}$ (hydraulic diameter) is a parameter that depends on the channel's cross-sectional geometry.

Laminar flow is indicated by small Reynolds number (Re < 2300). A flow with a Reynolds number greater than 2300 is considered turbulent [13].

The example below is given for a system which exhibits low Reynolds number. Let's assume a biomedical microfluidic device with square cross-sectional channels (100 μm x 100 μm), completely filled with water using the following parameters: $\mu = 10^{-3}$ kg/(s.m), $\rho = 10^{3}$ kg/m^3, $v = 1$ cm/s (10^{-2} m/s), and $D_h = 100$ μm (10^{-4}m).

(Please note that the hydraulic diameter of a channel with a square cross section when completely filled with fluid is simply equal to the width of the channel)

The obtained Reynolds number is: Re = 1, which signifies a laminar flow.

1.1.3 Microfluidic flow types and their mechanisms

Several mechanisms can be used to drive a microfluidic flow:

1. Classic Poiseuille flow results from an applied pressure difference. This type of flow is characterized by a parabolic flow velocity distribution across the channel. The flow velocity is maximum at the center of the channel and zero on the channel walls [12, 14].
2. Electroosmotic and electrophoretic flows are generated by the application of external electric fields. Electroosmotic flow occurs due to the formation of charged Debye double layers at the boundary regions between the fluid and the solid walls of the channels. In electroosmotic flow the velocity profile is uniform; electrophoretic flows arise from the dipole interactions with the external electric field. The response of the electrophoretic flow is proportional to the square of the externally applied electric field [12, 14].
3. Capillary action is due to capillary forces generated as a result of surface wetting. The flow has a parabolic front similar to Poiseuille flow described above, but strongly depends on the interface shape and its detail [12, 14].
4. Marangoni flow results from a differential surface tension that may exist between liquid layers in contact. The source of this surface tension can be temperature or a chemical concentration gradient [12, 14].

5. Spin associated flow is caused by the centrifugal forces that act on a spinning device, for example arrays of microchannels formed on a disk resembling a music compact disk (CD) [15].

1.1.4 Scaling effect: opportunities and challenges

Although the laws of physics are the same when we move from macro to micro scale, a number of effects which are relatively negligible at the macro-scale can become dominant at the micro-scale [13]. These effects include diffusion, fluidic resistance, surface area to volume ratio, surface charge and surface tension. For example, in microfluidics the flow is predominantly laminar (due mainly to viscosity), capillary action starts to appear due to surface forces, evaporation becomes significant due to the fluid's large surface to volume ratio and electrokinetic (electroosmosis + electrophoresis) flow becomes possible due to the presence of an electric double layer at the charged surface of the microfluidic channel. Therefore, it is not possible to simply scale down the macro-scale devices to build their micro-scale equivalents. At the same time, careful considerations given to the scaling effects can provide the grounds for unique opportunities and new paradigms for design.

1.2. Fabrication: Methods and choice of Material

Microfluidic fabrication techniques were originally adopted from microelectronic and Micro-Electro-Mechanical system (MEMS) technology. Silicon is widely used for the fabrication of microelectronic and MEMS devices. The first microfluidic devices were fabricated in silicon. However, it soon became evident that silicon is not an ideal material for microfluidic applications. Silicon is an expensive material and its processing cost is quite high. It is typically not economical to fabricate microfluidic LOC devices in silicon, especially when the device is for single use. In addition, optical opacity of silicon is a major disadvantage for applications involving optical detection in the UV-visible range. Nevertheless, some techniques still require silicon, e.g. silicon is used as supporting material in hot embossing or as a master in replication molding.

Some further disadvantages of silicon for LOC applications include:

1. Silicon fabrication is costly and requires skilled workers and highly specialized facilities such as clean rooms.
2. Silicon inhibits many biological reactions [16-20]. This effect becomes much more significant at micro scale fluidic volumes where the surface to volume ratio is dramatically increased.
3. The thermal conductivity in silicon is high. In some applications where heat is involved, insulation of the silicon is needed, which adds an additional layer of complexity to the fabrication.
4. Silicon is a semiconductor and thus is not compatible with electroosmotic pumping (EOP), which is presently a popular method for liquid transport in microfluidic devices.
5. Most importantly, as mentioned before silicon is not transparent and therefore it is not compatible with many important methods for optical sensing.

Glass is another substrate that has been used for LOC systems. Glass possesses a well defined surface chemistry, excellent thermal and mechanical properties, good optical transparency, low autoflourescence, and good electroosmotic flow (EOF) characteristics. It has also proven to be well suited for fluid handling, as it is inert to most organic and inorganic compounds. The disadvantages of glass as a microfluidic LOC substrate include: High cost of fabrication, difficulty associated with anisotropic etching, the need for high temperature bonding, and adsorption of DNA [13], [21-23] . Because of the disadvantages mentioned, polymers are gradually replacing silicon and glass in microfluidic applications.

1.2.1 Plastic as material of choice for fabrication of the optical biochip

Even though silicon and glass have been the most popular substrates for the fabrication of LOC devices in the past, a recent review of the literature reveals a very promising future for polymers, especially in the area of biomedical diagnostics. Polymers have the following advantages:

1. Polymers are cheap. They enable simpler, less expensive manufacturing processes (e.g., replica molding, casting, injection molding, and hot embossing) [24].

2. Polymer devices can easily be mass produced.
3. Single-use, disposable plastic devices eliminate the possibility of cross contamination between analytes.
4. Direct methods such as laser ablation, plasma etching, x-ray lithography, stereo-lithography, and LIGA[2] can be used for fabrication of single devices.
5. Polymers have a range of physical and chemical properties, which can be tailored to specific applications.
6. Many of the advances made in state-of-the-art Micro-Electro-Mechanical Systems (MEMS) apply directly to polymers, and new micromachining techniques associated with polymers are continuously being developed [25].

Polymers also have some disadvantages, such as: Poor thermal stability, high autofluorescence, Poor dimensional tolerance and complex surface chemistry [13], [21-23].

Polymers commonly used in LOC systems include poly(dimethylsiloxane) (PDMS), poly(methylmethacrylate) (PMMA), polystyrene (PS), poly-carbonate (PC), polyvinylchloride (PVC), polyimide, polyethylenetetraphthalate glycol (PETG), cycloolefin copolymer (COC), and UV-patternable negative photoresist SU-8 [26]. Among these, the most extensively used polymer is PDMS, which possesses many attractive properties for LOC systems [27].

1.3. Optical detection

Sensing or detection is a critical component of any LOC system and refers to mechanisms by which chemical or biological information is converted into meaningful electronic signals. The ultimate goal of a LOC is to incorporate all the processes necessary for a complete analysis into a microdevice. Thus, development of miniaturized detection modules for microfluidic systems is an important issue to be addressed. Detection systems currently under investigation can be broadly categorized into optical detectors, electrochemical detectors, mass

[2] German acronym: **Li**thographie, **G**alvanoformung, **A**bformung =X-ray lithography, Electroplating, Moulding

spectrometric (MS) detectors and nuclear magnetic resonance (NMR) detectors [28]. Optical detectors are especially appealing because no electrical interconnection is required between the detector unit and the microfluidic device. The optical interrogation involves photons only, so minimal disturbance is caused to the reaction system provided it is not susceptible to photochemical decomposition. Although optical detection is highly compatible with microfluidics, it can suffer from poor detection sensitivity due to the small amount of analyte present in the microchannels. As the analysis volume decreases and the number of molecules or ions present for detection diminishes, the need for sensing systems with higher sensitivity such as fluorescence detection arises. Many of the initial developments in microfluidics took advantage of fluorescence, and it is still a preferred mode of detection. The unique aspect of fluorescence detection is that its sensitivity improves as the volume of the sample under investigation becomes smaller. This is because Rayleigh and Raman scattered light are typically dominant noise sources in fluorescence experiment. As the volume of detection becomes smaller the ratio of fluorescent light to stray scattered light can be made larger. This is because fluorescence emission from a single molecule does not depend on the detection volume while scattered light noise scales directly with detection volume, leading to improvements in the signal to noise ratio [29]**.** Absorption, refractometric detection and fluorescence are the three most common modes of optical interrogation in microfluidics, and a brief overview of each is given in the following subsections.

1.3.1 Absorption

Absorption can be analyzed using Beer-Lambert law:

$$A = \log(P_0 / P_t) = \varepsilon \cdot b \cdot c \ , \qquad (1\text{-}2)$$

here A is the absorbance, P_0 is the input optical power, P_t is the transmitted optical power, ε is the analyte's molar absorption, b is the effective optical length, and c is the analyte concentration.

Thus, by measuring optical attenuation, analyte concentration can be calculated. In microfluidic systems, however, this method faces a major limitation because of

the small optical lengths (normally, width or depth of the microfluidic channels) involved. The sensitivity can be improved using a number of different strategies to increase optical path length, such as: using u-shaped channels, vertical channels through the thickness of the substrate, or multiple reflections on the channel walls. In reference [30], the authors incorporated small air cavities or "air mirrors" (Fig.1-1) adjacent to the bends of an illuminated bending flow cell. Because of the refractive index difference between PDMS and air, light was reflected back into the fluid at the bends causing an increase in the effective optical length.

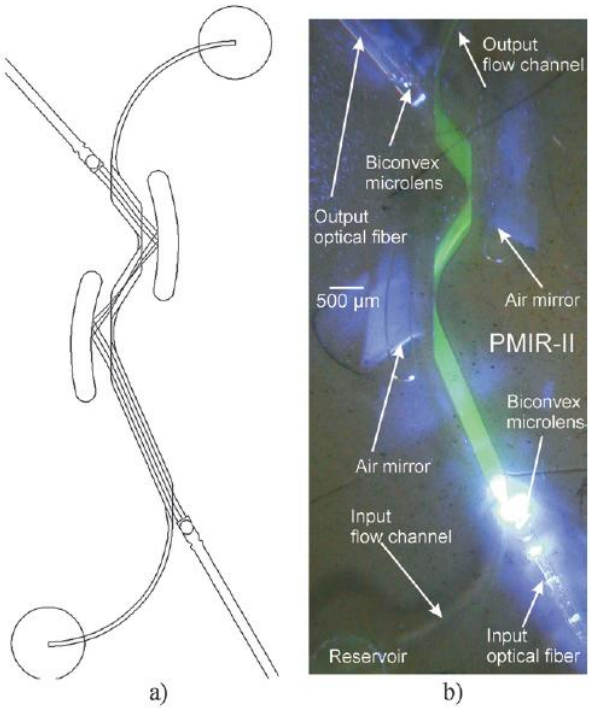

Fig. 1.1: (a) Schematic representation of a PDMS flow cell with air channels functioning as mirrors to reflect the light back into the flow cell. (b) Photograph of the flow cell showing fluorescein illumination which has an extended optical path length due to presence of air mirrors as well as biconvex microlenses [30].

1.3.2 Evanescent wave sensing

Another method of fluid analysis is by evanescent wave sensing [31]. In this method, the microfluidic channel is fabricated adjacent to an optical waveguide so that higher index core of the waveguide is one wall of the channel. Obviously, the fluid in the channel serves as a cladding for the waveguide. Any changes in the

fluid's refractive index, such as those introduced by chemical changes in the fluid or adsorption (i.e. DNA hybridization) and reaction of molecules on the channel wall, would affect the evanescent fields that penetrate into the fluidic cladding of the optical waveguide. However, the penetration depth of the evanescent field is typically around one half of the wavelength which sets a low limit on the sensitivity of these devices.

1.3.3 Leaky fluidic waveguide sensing

In reference [32], prism coupling was used and the fluid-containing microchannel itself was illuminated to act as a leaky waveguide. Here the lossy waveguiding in the channels containing aqueous solutions is based on Fresnel reflection rather than Total Internal Reflection. Since (TIR) is not the waveguiding mechanism, the restriction that the guiding layer must be of higher index is removed. In leaky waveguides, the reflections are less than 100% and light gradually escape the waveguide, e.g. some light is lost at each successive reflection through absorption and/or radiative loss. But since the required length scales for light guiding in a microfluidic device is a few millimeter to few centimeters at most, leaky waveguides are sufficient for guiding the light in the microfluidic device.

1.3.4 Interferometric detection

Label free and highly sensitive detection can potentially be accomplished by interferometric methods. Here, a single coherent light source is divided into two paths. Both paths either go through or are adjacent to the same sample media, but one path is chemically functionalized for sensitivity to the analyte under investigation. When an analyte differentially binds to the functionalized group/s in one optical path the refractive index for that optical path changes so that the two optical beams are no longer in phase. This phase shift between the two optical beams can have a dramatic effect on their projected interference pattern. Therefore, analyte binding events can be directly observed by imaging the interference patterns. The existence of a reference path is what makes interferometry so sensitive. Common mode interferences such as nonspecific molecular bindings and temperature and intensity fluctuations, do not alter the interference pattern. Ymeti et al. demonstrated an immunosensor interferometer

device based on Young's interferometer configuration and used it for the detection of herpes simplex virus [33]. Four waveguides were integrated into the microfluidic chip; three were functionalized using three different antibodies, while the fourth was not functionalized and thus served as reference. A change of refractive index resulting from antigen bonding modified the evanescent field at the surface of the functionalized waveguides. This resulted in a shift in the interference pattern as projected and observed on a CCD image sensor (Fig.1-2). The complete analysis took only a few minutes and the limit of detection (LOD) was in the femtomolar range. There is one potential drawback for interferometers of this kind: the waveguides must have identical geometries and must be precisely matched in terms of their material properties.

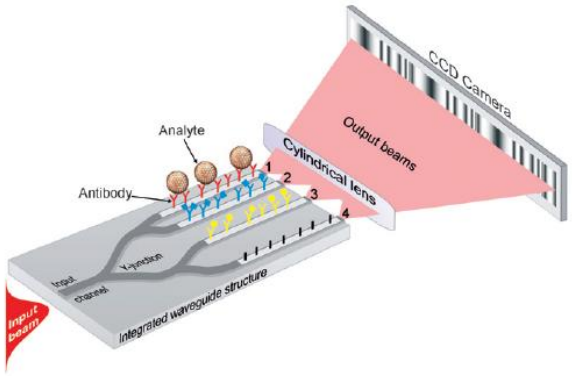

Fig. 1.2: A Young interferometer biosensor in which the interference pattern changes due to binding of analytes [34].

1.3.5 Surface plasmon resonance detection

Surface Plasmons are surface electromagnetic waves that are produced at the boundary between a metal (normally a thin film of gold or silver) and a dielectric medium (vacuum, air, water, etc…). Surface plasmons are extremely sensitive to small changes that take place at the boundary such as minute changes in refractive index due to adsorption of molecules on the metallic surface. This provides the underlying mechanism for Surface Plasmon Resonance (SPR) detection. In most implementations, a configuration known as the "Kretschmann" configuration, where a thin metal film is evaporated on the base of a prism, is used. The incident light is totally internally reflected inside the prism and at the same time an

exponentially decaying evanescent wave penetrates into the metallic film. If the light is monochromatic and p-polarized (a polarization that is parallel to the plane of incidence), there will be a specific incidence angle at which the intensity of the reflected light is sharply reduced and the surface Plasmon resonance (in the form of a sharp shadow) is excited. Since surface plasmon resonance is the result of a resonant energy transfer between the evanescent wave and surface plasmons, changes in the evanescent field (ex. when ligands are adsorbed on the surface of the metal and as a result change the refractive index of the media) alter the angle at which the reflectance is minimum. The SPR angle can be measured by monitoring the reflectance minimum as the incidence angle of a narrowly focused laser beam is varied, or by looking at the reflectance angle spectrum obtained by a slightly divergent laser beam upon its exit from the prism [35].

Several commercial laboratory scale systems for SPR detection exist. They are mostly used for immunosensing or DNA hybridization detection. Biacore from GE Healthcare is the most prominent one. The Sensata Spreeta SPR sensor (Fig.1-3) is a low cost commercially available miniaturized integrated microfluidic system that can be used for a variety of applications. The device performance as evaluated by Immunoglobulin G (IgG) tests was an impressive LOD of 80 pM. The sensor has been used for immunological detection of E. coli O157:H7 in ground beef extract, apple juice, and milk by Waswa *et al.*, who demonstrated reliable quantification of E. coli in 30 min, as compared to 1-3 days by conventional culturing methods [36].

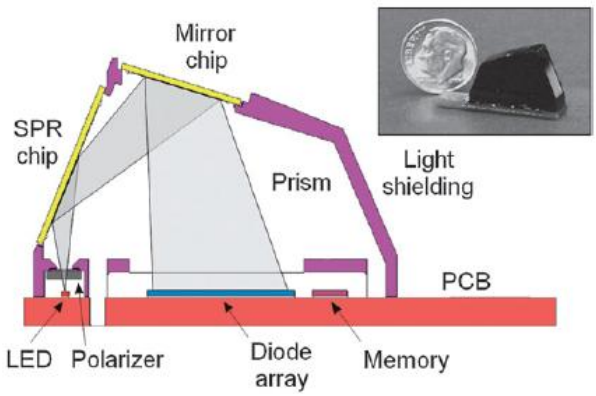

Fig. 1.3: Schematic representation showing cross-sectional view of the SPR sensor (Sensata Spreeta). The actual device is shown in the inset [37].

1.3.6 Localized surface plasmon resonance

Localized Surface Plasmon Resonance (LSPR) of metallic nanoparticles is a new and powerful sensing method that offers many of the same advantages that SPR has to offer plus several additional benefits [35]. Interaction between light and particles of metal which are smaller than the wavelength of the light causes the conduction electrons at the surface of the metal nanoparticle to go through a collective resonance oscillation. This creates plasmons that are confined to the surface of the metallic nanoparticle. The resonance frequency of a particle is highly dependent on its size, shape, and composition. Of particular importance for biosensing applications, the resonance also depends on the molecules that are in close proximity of the nanoparticle. The mechanism of sensing for LSPR is similar to that for SPR; changes in the local dielectric environment are monitored through LSPR wavelength-shift measurements. Like SPR, LSPR can provide real-time kinetic and thermodynamic data correlated with chemical and biological binding processes. In LSPR, a binding event directly translates to a corresponding shift in the wavelength, thus eliminating the need for additional labeling steps. Whereas in conventional SPR, the excitation light is normally coupled using a prism or a grating coupler, in LSPR sensing there is no need for such optics. Typically, only a white light source is needed for excitation. LSPR scattering is very intense. According to Anker *et al.* the scattering obtained from the cross section of a gold nanoparticle is a million times greater than the scattering produced by a molecule of fluorescein [38]. In addition, as will be discussed in the next section, LSPR causes a major increase in the intensity of surface-enhanced Raman scattering and has similar implications for other surface-enhanced spectroscopic processes.

1.3.7 Surface-enhanced Raman spectroscopy

Raman Spectroscopy is based on the Raman scattering effect, which is an extremely weak phenomenon. This effect occurs when a small fraction of photons (approximately 1 in 10^7) impinging on a molecule interact with the electron cloud surrounding the molecule and loose energy to or gain energy from the rotational and vibrational modes of the molecule. The scattering process is inelastic, and the

spectrum of the inelastically scattered light can be used to uniquely identify the molecule. Raman scattering can be dramatically increased using metal substrates with nanoscale features. This is the basis of a technique known as Surface Enhanced Raman Scattering (SERS) which was first demonstrated by Fleischmann *et al.* in 1974 using a roughened silver substrate [39]. Raman spectroscopy for chemical analysis typically involves powerful lasers and precision optics as well as large sample volumes. However nanoscale gaps or sharp features exhibited by certain LSPR substrates results in generation of extremely high electric field intensities in their neighboring volumes, which in turn causes a dramatic increase in the Raman scattering intensities of the molecules located in these volumes. Nano-structured LSPR substrates are currently a topic of active investigation by many research groups. For instance, Liu and Lee have developed a batch-fabrication process for the incorporation of patterned SERS substrates in microfluidic devices, and reported an enhancement of 10^7 in comparison with unpatterned (i.e. smooth metal) substrates [40].

1.4. Fluorescence

Fluorescence is the characteristic of some substances to absorb light of a particular wavelength and within a brief time interval, known as the fluorescence lifetime, to reemit light of a different wavelength. In most cases, the emitted light is at a longer wavelength than the light used for excitation [41]. Fluorescence detection is limited to compounds that either fluoresce themselves or have been chemically conjugated to a fluorescent material. Each fluorescent molecule has a specific absorption and emission spectra. The separation of the excitation and the fluorescence peaks is known as the "Stokes' shift"; in terms of wavelength, it ranges from approximately 7 nm to 238 nm [42]. This wavelength shift enables fluorescence detection of a target molecule; optical filters can be used to block the excitation signal, so that the typically weak fluorescent signal can be detected in spite of the stronger background excitation light. In addition, spectral filtering is normally combined with spatial separation in order to obtain higher sensitivities.

The brightness of a fluorescent material (or fluorochrome) is proportional to the product of the extinction coefficient ε and the quantum efficiency φ [43]:

$$Brightness \sim \varepsilon \cdot \phi \qquad (1\text{-}3)$$

The extinction cooeficient is the probability that the excitation photons are absorbed by fluorescent molecules. For useful fluorochromes the extinction coefficient ranges from 40,000 to 250,000 M^{-1} cm^{-1}. Quantum efficiency is the ratio of quanta emitted to quanta absorbed. In practice a quantum yield of greater than 0.1 is typically required.

Figure 1-4 shows the spectra for absorption and emission of cyanine fluorochrome ($Cy5_{TM}$) (Amersham Life Science Ltd., Bucks, England). In this case, the Stokes' shift is about 21 nm. This fluorescent marker is very bright and can be easily attached to proteins. In addition it has a longer excitation wavelength than many other fluorophores, which allows inexpensive red laser diode to be used.

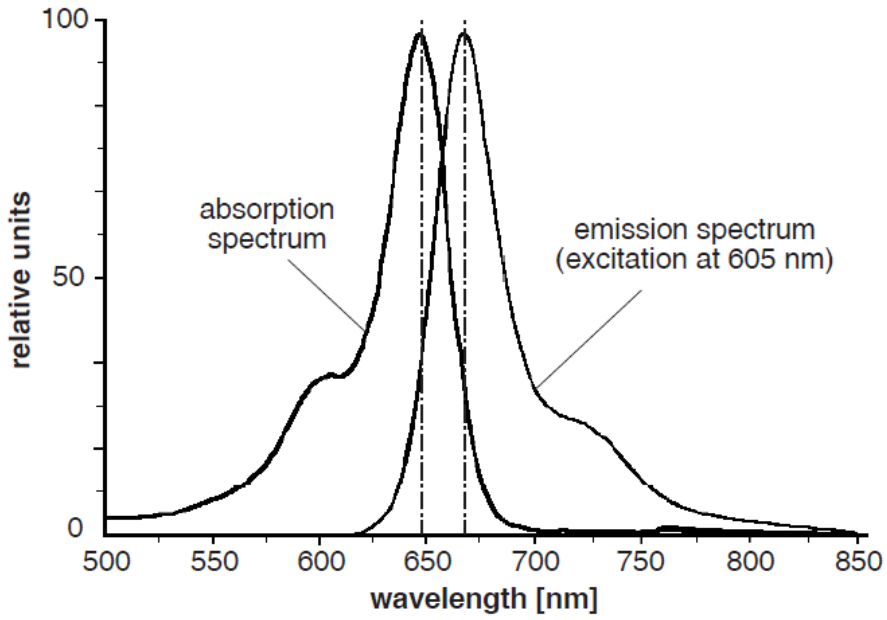

Fig. 1.4: Spectra for absorption and emission of $Cy5_{TM}$ fluorochrome in water. The position of the peaks for absorption and emission are at 649 nm and 670 nm respectively. $Cy5_{TM}$ has an extinction coefficient (ε) of 250,000 M^{-1} cm^{-1} and a quantum efficiency (φ) greater than 0.28 [43].

There are several practical challenges that should be mentioned. One is photobleaching, which is the photochemical destruction of a fluorophore as a

result of repeated excitation by high intensity illumination. All fluorophores, to varying degrees, are subject to photobleaching. In fluorescence techniques quenching and photobleaching are important sources of complication and need to be carefully avoided. Autofluorescence by polymers and non-specific biomolecules in the sample is another source of complication that can arise in practice; careful attention must be paid to the selection of the material and the purity of the samples. In fluorescence detection, the efficiency of fluorescence collection is often very low since fluorescence emission is isotropic, and it is typically possible to deliver only a fraction of fluorescence to the detector. This is because optical systems are limited in their light gathering ability (because of their limited numerical aperture (NA)) and have limited transmission and detection efficiencies. Collection efficiency is generally below a few percent, even for the most advanced fluorescence microscopes [44].

Fluorescence spectra can be altered by a variety of factors, which include interaction with other fluorophores, the solvent and ions in the solution, molecular association, and complex formation. For example, DNA hybridization can cause a dramatic shift in the spectrum as a result of a change in the solvent's PH and the change in fluorescence intensity (Reference). Thus one can make an assessment of the environment and chemical composition by observing fluorescence spectra.

Single Wavelength Excitation (SWE) and Multi-Wavelength Excitation (MWE) are the two distinct modes of fluorescence detection. SWE has the following advantages:

1. It is simple
2. Standard laser diodes can be used (high intensity).
3. Photomultiplier tube (PMT) can be used (highe sensitivity).
4. Many marker dyes are available.
5. Inexpensive bandpass filters can provide wavelength selectivity.

MWE detection is advantageous in that many different "species" can be simultaneously identified. For example, Fig. 1-5 exhibits a case where a 488 nm Argon source is used to excite four different dyes (Fluorescein, Phycoerythrin, Cy5-PE, and Cy7-PE) simultaneously.

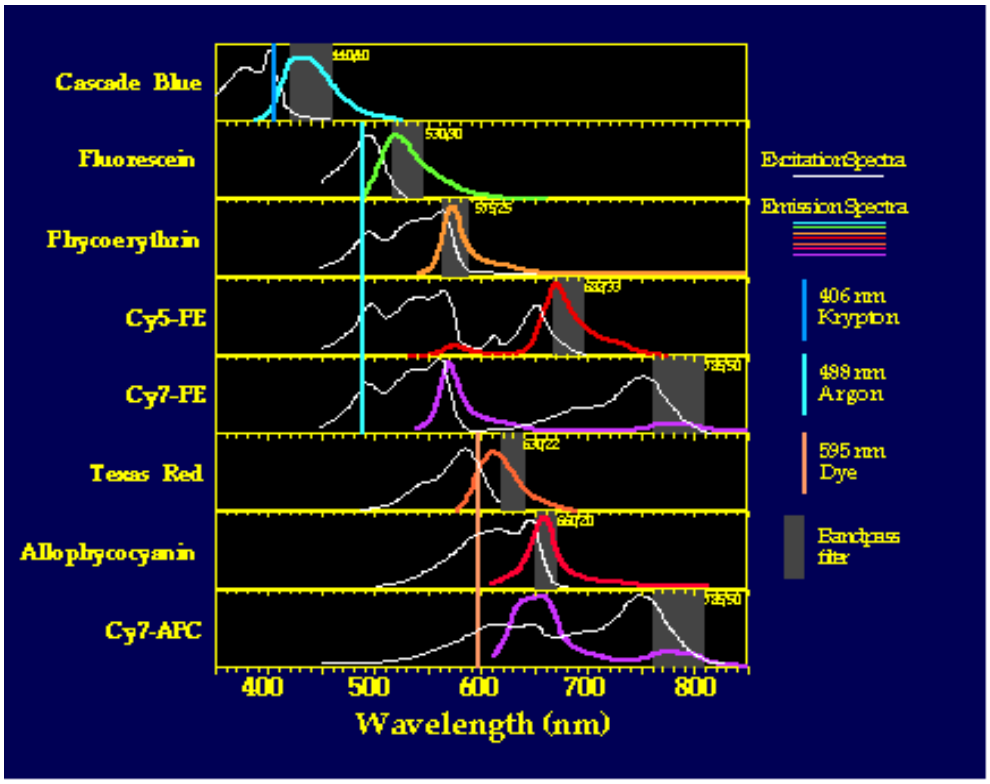

Fig. 1.5: Spectra (Excitation and emission) of 8 different dyes from a FACS immunofluorescence experiment. [Ref.: http://www.drmr.com/abcon/allspec.html].

1.5. Spectroscopy

Optical spectroscopy is a fundamental analytical tool that has applications in numerous fields of science. Simply speaking, spectroscopy is about breaking up an optical signal into its constituent wavelength components and measuring the intensity at each resulting wavelength. By spectroscopic measurements one can obtain valuable information about the sources of emission. In astronomy, for example, the spectral profile can reveal the composition and nature of gases that make up the atmosphere of stars. In chemistry and biology, as another example, one can identify a substance by analyzing the emitted or absorbed spectral profile.

1.5.1 Fluorescence spectroscopy

Fluorescence spectroscopy is the study of fluorescence emission and is accomplished by measuring the intensity of light emitted at different wavelengths. This work is accomplished by a spectrometer, which typically comprises a

dispersive element, a collimation element, and a detector [45]. The general layout of a spectroscopic device is shown in Fig. 1-6 [46].

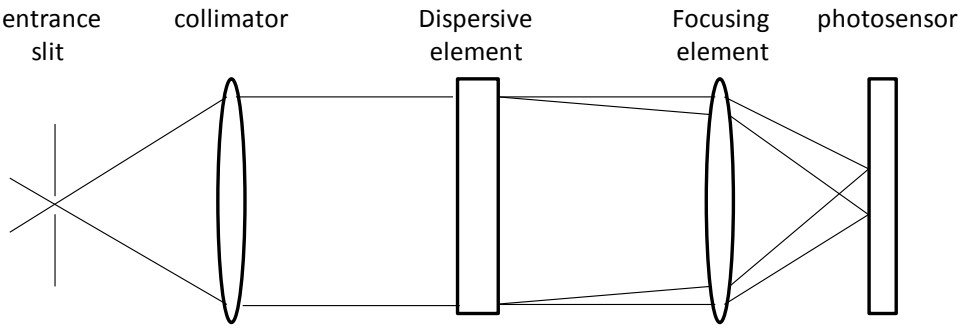

Fig. 1.6: General layout of a spectroscopic device [46].

The function of the dispersive element is to deflect wavelength components of an optical signal by varying amounts resulting in spatial separation among wavelengths, and thus allowing the intensity measurement of the spectral components. By passing the signal through an exit slit, a narrow bandwidth of the spectrum can be selected for measurement. Alternatively, large sections of the spectrum can be simultaneously detected by a charge-coupled device (CCD) camera or other types of detector array.

A major application of fluorescence spectroscopy is in cell biology, where multiple fluorescent markers in a given cellular sample are simultaneously detected. In many experiments, both the intensity and spectral profile of a fluorescent tag need to be measured. Since many fluorescent markers have unique emission spectra, it is possible to carry out multianalyte measurements by using a spectrometric detector. By using multiple fluorescent tags, each signifying a particular parameter in a sample, one can also study the interactions and responses of cellular parameters. There are a number of challenges associated with spectroscopic fluorescence measurements. The fluorescent signals are often very weak, and therefore highly sensitive detectors are required. Sensitive detectors such as PMT's and APD's are expensive, and more importantly they are not capable of wavelength discrimination. Typical spectrometers use a CCD camera as the detector and have trouble registering weak transient signals. The typical requirement is to detect an entire spectrum, with each wavelength read by a single

pixel (or a few pixels) on the CCD camera. A weak but constant signal can be integrated over time but this is not feasible for transient fluorescent signals. An alternative would be to use a photomultiplier-tube (PMT) or a single-photon avalanche diode (SPAD). These single point detectors are quite effective in amplifying weak signals, but their signal amplification physics does not allow them to be easily organized in an array format close enough for measuring tightly spaced wavelengths. Because these detectors lack spatial resolution they have to be combined with filters and/or slits in order to measure each wavelength component separately. Perfetto et al. [47] have organized eight PMT's in an octagon configuration with specific filters and reflectors in front of each PMT so that only a narrow band of electromagnetic spectrum is analyzed by each PMT. Figure 1-7 shows this octagon configuration. This setup is large, expensive, and requires careful calibration steps to account for the spectral overlap among PMT's.

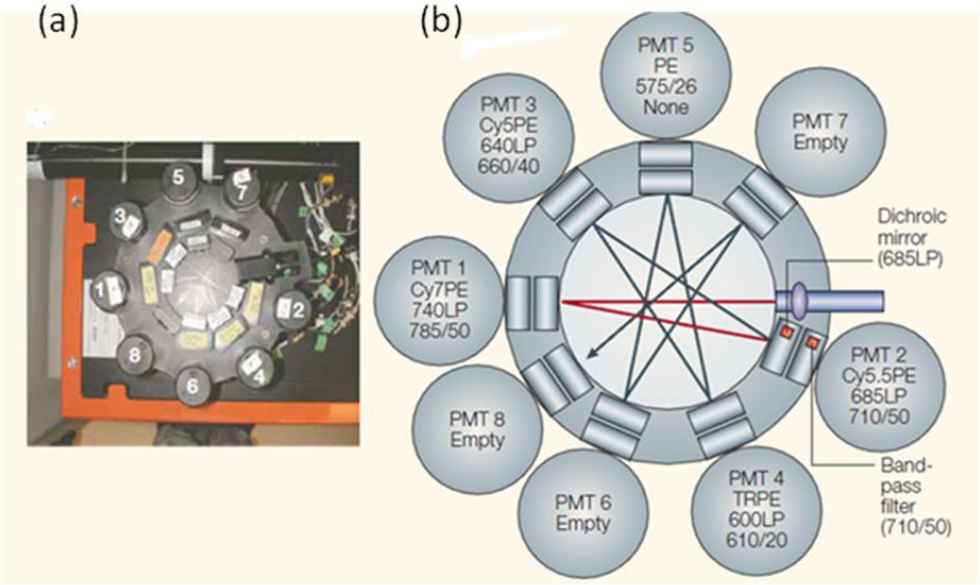

Fig. 1.7: A multi-parameter laser induced fluorescence-emission flow cytometer with an octagonal geometry. (a) Photograph of the actual assembly, (b) The schematic representation of the assembly, depicting a series of filters, reflectors, and PMTs in an octagonal arrangement [47].

1.5.2 Previously developed spectroscopy systems

In this section we review spectroscopy systems reported by other groups for the purpose of fluorescence detection.

Goldman et al. [48] reported a compact microspectrometer for chemical analysis, which consisted of polymeric and metal oxide planar waveguides in conjunction with buried grating couplers. Polymeric and metal oxide waveguides were deposited on a glass substrate with etched gratings. Light was coupled into the waveguide by one of the gratings and travelled through the waveguide and interacted with chemical samples. The resulting spectra were dispersed by the second grating and were analyzed by an array of photodiodes. The planar waveguide spectrometer demonstrated by Mohr et al. [49] was based on a reflection grating, which was fabricated by reactive ion etching. In this device, the detected light was introduced into the polymer waveguide using an optical fiber and was subsequently dispersed by the grating. Using a similar approach, Sander et al. [50] developed transmission gratings in SiON waveguides. A hybrid spectrometer system composed of silicon micromachined gratings and a CCD camera was demonstrated by Yee et al. [51]. More recently, a chip size spectrometer in a microfluidic platform was demonstrated by Schmidt et al. [52], who used a linear variable band-pass filter in combination with a CMOS camera.

An obstacle in microfabrication of spectrometers is the integration of lenses or mirrors for collimation and focusing. Microscale fabrication of these elements has proven difficult. Without a focusing element, the microspectrometer must have a large footprint or suffer from limited resolution. Some studies have used alternative designs to overcome this problem. For example, Traut et al. [53] developed a miniaturized spectrometer array by forming grating patterns on the top surface of an array of microlenses. In this design, each microlens in the array would function as a dispersive and focusing element. In the design by Grabarnik et al. a second grating was utilized as the focusing element [46]. Although, not integrated in a microfluidic platform, this miniaturized full system spectrometer is one of the smallest reported in the literature (Fig.1-8). A number of MEMS-based spectrometers were discussed by Wolfenbuttal [54, 55]. Smaller gratings were

typically utilized in these devices and the focusing element was omitted at the price of a reduction in resolution. In some of these devices, the diffracted signals were detected using custom-built photodiode arrays.

(a)

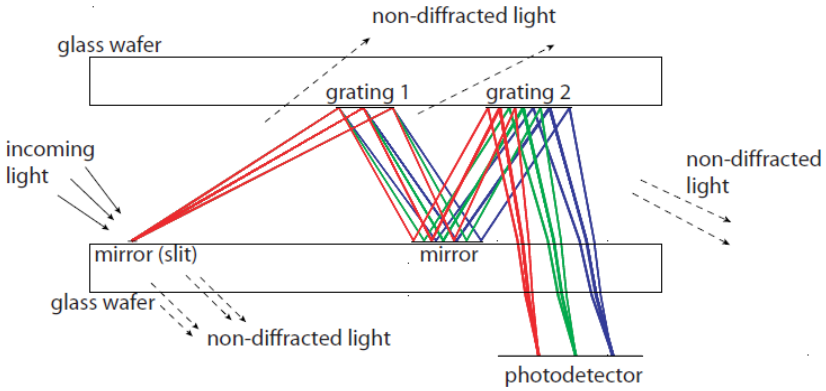

(b)

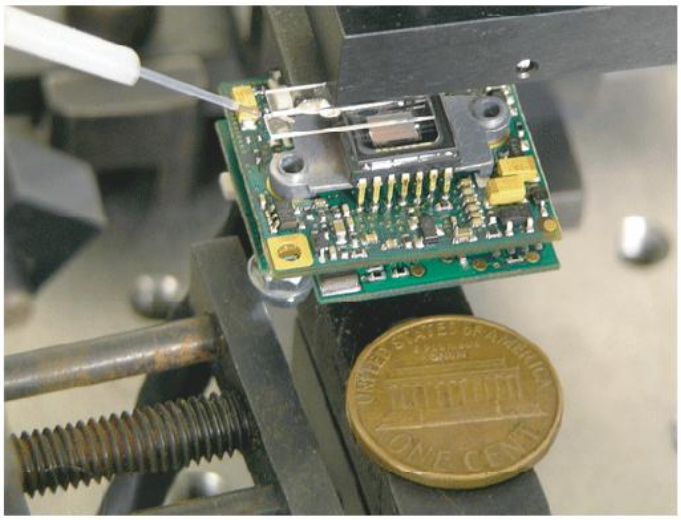

Fig. 1.8: The microspectrometer reported by Grabarnik et. al. [46]. (a) Illustration of a double grating setup. The first grating performs diffraction and the second grating is used for focusing (b) Image of the experimental setup.

Minas et al. [56, 57] designed an array of on-chip Fabry-Perot optical filters for simultaneous colorimetric measurements of biomolecules based on optical absorption. For each channel in the array only a specific wavelength band was allowed and the rest of the signal was filtered. For direct read out of the filtered

signals, photodetectors were placed underneath the channels. For the detection of fluorescence in a microfluidic channel, Damean et al. [58] used an array of custom-built microlenses and a commercially available transmission grating above a microfluidic channel. A benchtop microscope and a CCD camera were used to collect and read the optical signal after diffraction. In this way they were able to demonstrate resolving of a fluorescent signal in space and time in a microfluidic system. A somewhat similar method for biochemical analyses was reported by Yee et al. [51].

1.5.3 Single molecule spectroscopy

Single molecule spectroscopy is a relatively new field of research for the study of molecules [59, 60]. By studying one molecule at a time, detailed information about the molecule and its interactions can be obtained. Importantly, the method guarantee that the detected signal is the one emitted by the molecule under investigation not an ensemble-average of signals coming from different molecules. Detection of extremely weak emissions from a single molecule requires highly sensitive, single-point detectors or a spatial detector such as an Electron Multiplying Charge-Coupled Device (EM-CCD) camera. A multianode PMT is another possible option; this is an array of PMT's that allows spatial measurements to be made with PMT sensitivity [61]. Signal processing in a CCD camera is quite different from a multianode PMT. Unlike a CCD, a multianode PMT does not bin the detected signals and for each anode a separate readout connection is required. For a 32-anode PMT the required equipment and associated read out connections can become quite costly.

In this section, a variety of techniques for spectral measurement have been reviewed. It is clear that polychromatic measurements are becoming increasingly important tools for scientific analysis, particularly in LOC systems, because of the rich and detailed information they can potentially reveal about molecules and reactions.

1.5.4 Thesis outline

Chapter 2: Historical and theoretical background information on diffraction and diffraction gratings and the approximate models of diffraction.

Chapter 3: Development of numerical simulation tools for the study of gratings and grating-based microspectrometers.

Chapter 4: A comparative study of Gaussian beam propagation as a diffraction model used for the assessment of various scalar diffraction integral approximations.

Chapter 5: Development of a monolithic integration strategy for optical and fluidic devices using polymers for LOC applications.

Chapter 6: Design, fabrication, and characterization of a focusing transmission grating microspectrometer.

Chapter 7: Development of a novel method for wavelength sensing using spectral detection of moving emitters.

Chapter 8: Chapter summaries and suggested future work

CHAPTER 2

2. Background Theory

This chapter provides the supporting theory pertaining to the diffraction material presented in this thesis. First, the concept of diffraction is explained and the historical context for the early developments of wave diffraction theory is provided. The grating is introduced and the justification for spectral detection/spectroscopy is given. The key principles of diffraction gratings are discussed. The final part of this chapter is devoted to the scalar treatment of the theory of diffraction and the solution of diffraction integral using Green's theorem followed by Rayleigh-Sommerfeld, Fresnel and Fraunhoffer approximations.

2.1 Diffraction

"*Diffraction* *refers to various phenomena which occur when a wave encounters an obstacle. In classical physics, the diffraction phenomenon is described as the apparent bending of waves around small obstacles and the spreading out of waves past small openings*.**"** [Wikipedia].

Sommerfeld [62] conveniently defines diffraction as:

"*any deviation of light rays from rectilinear paths which cannot be interpreted as reflection or refraction.***"**

Diffraction is due to the lateral confinement of the propagating waves and diffraction effects are most prominent when the size of the diffractive object (i.e. the aperture) is comparable to the wavelength of the radiation that is being used.

Historically [63] Leonardo da Vinci is the first person to have given reference to this phenomenon in his work. But the first description of diffraction was provided by Grimaldi in a book which was published in 1665 shortly after his death. Later in 1678 Christian Huygens –the first proponent of the wave theory of light- who apparently did not know anything about Grimaldi's work proposed his theorem asserting that [63]:

"*each element of a wave-front may be regarded as the centre of a secondary disturbance which give rise to spherical wavelets*; moreover "*the*

position of the wave-front at any later time is the envelope of all such wavelets." Further development in the field occurred in 1804 when an English physician named Thomas Young introduced the concept of interference as a consequence of the wave property of light. The next major step in understanding diffraction is due to Augustine Jean Fresnel who brought the ideas of Huygens and Young together in his historical memoir in 1818. Using Huygens construction and principles of interference, he was able to give an accurate account of light distributions in the diffraction patterns for the first time. In 1882 Fresnel`s ideas were put in a sound mathematical form by Gustav Kirchhoff. In his formulation of the diffraction problem, Kirchhoff made some specific assumptions about the light`s boundary values on the screen and the aperture which later proved to be inconsistent. Despite these inconsistencies, the Kirchhoff formulation produces results that are well supported by the experiments done in the microwave region [62]. A modification to this theory was finally proposed by Sommerfeld (1894) which removed the aforementioned inconsistency. This theory is known as the Rayleigh-Sommerfeld theory of diffraction and will be discussed in detail later in this chapter.

2.2 Diffraction Grating

If an obstruction on the path of a travelling wave has dimensions comparable to the wave's wavelength some of the wave's energy will be scattered. In case of a periodic obstruction and in general whenever one of the parameters affecting wave propagation goes through a periodic variation, the scattered energy falls into a number of discrete directions, known as "diffracted orders", and the periodic structure which acts in this manner is referred to as a "diffraction grating". From the stand point of a travelling wave in a diffracted order, the grating action is to change the direction of propagation by an amount which depends on the wavelength of the wave and the period of the grating. It is in this way that a spectrum is formed from a continuum of wavelengths by the grating's dispersive action. Although a prism may perform a similar function, a grating is more convenient to use and it outperforms the prism in many respects. Gratings are important optical tools. Gratings produce spectra and the detailed analysis of

spectra forms the basis of spectroscopy- a science that has a wide range of applications. Spectroscopy is based on separation and ordering of the constituent wavelengths in an emerging wave bundle and the display of radiation distribution in the form of a spectrum. Every atom and molecule has a characteristic absorption spectrum or spectral signature by which it may be uniquely identified. By analysing a spectrum one can obtain valuable information about the source of radiation or the medium in which the radiation passed through. Spectroscopy is used in hospitals to analyse blood samples. It is used in industry for process and quality control. Spectroscopy allows the detection of trace elements and minute amounts of impurities in various chemicals and products. On the one hand, it is the science for the study of the innermost workings of atoms and molecules while on the other, it is our only means for knowing the composition of galactic particles and distant stars. Although, potentially any periodic structure may function as a diffraction grating, we shall only consider one dimensional array of parallel equispaced lines of arbitrary form which lie in the same plane. Diffraction equally applies to all wave motions (i.e. sound waves or water waves) when a suitable grating exist, but it is the optical region of electromagnetic radiation, and particularly the region between the infrared and X-rays that is most important and for which gratings of highest qualities have been developed [64] .

2.3 A Brief History of Grating Developments

It is widely believed that the American astronomer David Rittenhouse invented the diffraction grating in 1786. This grating consisted of parallel hairs which were laid across two fine screws. He was able to observe the spectral colours produced by the grating and noted that red light was bent more than blue and correctly attributed these effects to diffraction. Sir John Barton exploited the phenomenon of diffracted colours somewhat frivolously and in 1822 obtained a patent for the manufacture of various metallic ornaments. The claim entailed the fabrication of moulding dies formed by cutting crossed gratings on steel using a diamond. However, it was the work of Joseph von Fraunhofer which laid the foundation for the study of diffraction gratings. In 1821, unaware of the earlier reported work he made a grating with fine wire which resembled Rittenhouse's grating. He also

produced reflection gratings by making grooves on the surface of mirrors with a diamond. He was the first one to use a grating (12 mm wide, 9600 grooves) for measuring the wavelength of light. He discovered the grating's diffracted orders, derived the grating equation and verified it with experiments. He also made detailed analyses of the spectrum considering the effects dictated by the form of the grooves and such effects related to errors which occurred in the position of the grooves. Truly speaking, Fraunhofer set the grounds for studies which went on for over 150 years and still continue today. In 1826 Fraunhofer died and for almost 50 years from this date, the grating attracted little interest. Although the work of the Prussian instrument maker F. A. Nobert is quite notable. He began to supply the spectroscopists at the time (1850) with gratings which were superior to Fraunhofer's. The problem was no one knew how to make a grating with better or at least similar performance to a prism. In 1874 Lord Rayleigh theoretically proved that in resolving the spectral lines, the grating's ability is superior to that of a prism. In about 1870, L.M. Rutherfurd, a New-York lawyer who had a great interest in astronomy, became interested in gratings and in just a few years learned to rule reflection gratings which outperformed the most powerful prisms. A giant leap in the development of the grating was the construction of a sophisticated "ruling engine" in 1882 by H. A. Rowland, professor of physics at Johns Hopkins University. Another successful invention of Rowland is the concave grating in which the grating grooves are ruled on the surface of a spherical mirror. In addition to dispersion, the new concave grating had a focusing capability. Rowland's success in building the first ruling engine and his invention of the concave grating opened up a range of new possibilities in the field of spectroscopy. The work on gratings at Johns Hopkins University -the world's principle supplier of scientific grade diffraction gratings at the time- was followed with great success by J. A. Anderson, by R. W. Wood, and by J. Strong up until the Second World War. An important contribution of R. W. Wood was the introduction of a new technique known as "blazing", in which the distribution of light among different diffracted orders is controlled by the shape of the grating grooves. In this technique the grating grooves have a sawtooth profile and the

mirrored facets of the grating are designed to reflect the light preferentially into the direction of a chosen diffraction order, thereby concentrating a bigger proportion of the light energy in that order. Vacuum deposition of thin metal films such as aluminum on the surface of glass blanks was a new method introduced by Strong (1935). Before this date the grating grooves were ruled directly onto blanks formed by speculum metal. The new blanks were easier to make and easier to handle. In addition, the reflectance of aluminum was much higher than speculum and resulted in an increase in the grating's efficiency. The remarkable ideas of A. A. Michelson, who as early as 1915 had suggested an interferometric servo system for controlling the position of grooves, was finally put to practice in 1955 by Harrison and Stroke, and gratings of highest degrees of perfection were obtained. Next to the invention of the ruling engine itself, the most important development in the area of grating production is due to techniques introduced for high-quality replication of gratings by White and Fraser in the 1940s. Prior to replication, the gratings were never produced in any significant number and therefore the access to gratings was quite limited. It was in the 1950s that gratings started to replace prisms in commercial spectroscopic instruments due to increased availability of high quality gratings which had resulted from the advent of newly developed, fast and efficient replication techniques. The invention of the lasers in the 1960s greatly affected many branches of optics including spectroscopy. Soon, an entirely new technique for the fabrication of high-quality sinusoidal gratings based on the phenomenon of optical interference became available, which gave rise to a new category of gratings known as "Holographic Gratings". The essential feature of the interference technique is that the interference fringes generated by the intersection of two coherent laser beams, when recorded in an appropriate photoresistive material, could form the grooves of a grating. The fringe spacing is dictated by the wavelength of the light and the angle of intersection of the beams. As a result, the interference gratings are inherently free from periodic and random errors associated with the ruled gratings. The first interference gratings were made by Burch (1960), but gratings suitable for general spectroscopic applications were developed rather

simultaneously by Rudolph and Schmahl (1967) in Germany and by Labeyrie and Flamand (1967, 1969) in France after the high-powered lasers became available [64] . For a more detailed account of the grating developments, the reader should refer to references by Loewen [65] and Hutley [64].

2.4 Diffraction Grating Types

Diffraction gratings are differentiated based on various criteria, such as: method of manufacturing, geometry, material, usage, the efficiency behaviour, and the working spectral interval. The long list of categories such as phase – amplitude, phase – relief, transmission - reflection, concave – plane, dielectric – metallic, lamellar – triangular – sinusoidal – trapezoidal, ruled – holographic – lithographic, symmetrical - blazed, echelettes – echelles – echelons, flat-field spectrographic – based on Rowland circle – the ones used in Seya-Namioka monochromators, those for distributed feedback – those used in integrated optics, waveguide gratings - fiber gratings, Bragg type – Raman-Nath type, masters – replicas and so on, points to complexity and lack of clarity in diffraction grating classification [65]. The existence of these categories is either rooted in the historical development of the gratings or the differences in their properties and/or their applications. From the above mentioned categories, transmission-reflection, concave-plane, and lithographic gratings are directly related to the present studies and will be discussed briefly.

2.4.1 Transmission and Reflection Gratings

The distinction between transmission and reflection gratings is rather obvious; one works in transmission and the other in reflection. Transmission gratings with triangular, rectangular or trapezoidal groove shapes have been widely used as laser beam dividers and combiners. Another application of transmission gratings is in direct imaging spectrographs. In the most common configuration, a camera is simply converted to a spectrograph by placing a transmission grating directly in front of the objective lens of the camera. This system can be used to acquire the spectrum of a distant luminous object, for example a falling meteor. In general, transmission gratings exhibit higher efficiencies than reflection gratings although reflection gratings are in general far more common. We chose transmission

gratings for our devices, since they allow a convenient chip layout while the additional steps for making the reflective surfaces are conveniently omitted. In addition, transmission gratings can achieve dispersion that is similar to that of reflection gratings, while having facets which are significantly larger [50]. For example a bulk grating fabricated with a material with a refractive index of 1.5 when used in air or vacuum, can achieve similar dispersion as a reflection grating while having facets which are four times deeper. This is especially advantageous at the time of fabrication since large grating features are easier to fabricate.

2.4.2 Concave and Plane Gratings

The most commonly encountered gratings are formed on planar substrates and have straight, parallel, equidistant grooves. There are some instances (largely in integrated optics) where the grooves are bent slightly and the separation between the successive grooves is varied uniformly (chirped) to give the grating some focusing action in addition to dispersion. A more common practice is to form the curved and chirped grooves on a concave substrate to make a single element spectrograph or monochromator with the dual dispersion-focusing functionality. The first concave grating was made by H. A. Rowland in 1882. Rowland showed that by ruling the grating facets on a concave spherical substrate, both the dispersion and focusing of light can be simultaneously achieved. In this design a circle tangent to the spherical substrate at the pole of the grating has a radius that is one half the radius of curvature of the spherical blank substrate with the property that if a point source is located on this circle, the diffracted image would also be formed in another location on the same circle [64]. This circle is known as the Rowland circle. At the time of Rowland the reflective optical components were made using speculum metal with a maximum reflectance of R = 70%. For a device using plane gratings equipped with collimation and focusing optics, the total reflectance would be in the order of R^3 = 35% which is half of that for an instrument equipped with a single concave grating. For this reason, for many years, the concave reflection gratings dominated the field of spectroscopy. Moreover, for wavelengths below 110 nm where the reflectance at normal incidence is about 20%, the transmission through an instrument equipped with a

plane grating is a mere 0.8% while it is 20% for an instrument using a concave grating. For this reason the use of concave gratings in this region of the spectrum is absolutely essential. A shift towards monochromator-based instruments utilizing plane grating designs has been taking place in recent years as a result of the advances in photoelectronics. Although such designs require mirrors for focusing they still provide maximum resolution and efficiency due to the advantages obtained by near stigmatic imaging [65]. The design, fabrication, and characterization of a chirped, concave, focusing transmission grating is an important component of the present studies that appear later in Chapter 3.

2.4.3 Lithographic Gratings

Lithographic gratings are produced by transferring the geometrical pattern of a grating from a photo-mask into a photosensitive layer (photoresist), which is deposited on a suitable substrate (semiconductor, glass, or metal), followed by the subsequent etching of this layer and the underlying substrate material. The single-beam mask transfer method is limited by the diffraction phenomenon such that the lowest limit for the grating features that can be safely copied -in the best case- is in the range of ~1.5 – 2 μm. In the present study we use lithography by first transferring the device patterns on to a photoresist layer that is spin-coated on a silicon wafer and then use Deep Reactive Ion Etching (DRIE), to etch away the silicon to make a master stamp for the subsequent steps of moulding. The details for this method are given in Chapter 5.

2.5 Grating Equation

In the schematic shown in Fig. 2-1, a monochromatic light beam is incident on the surface of a reflection grating. Upon diffraction, light is distributed along several discrete directions known as diffracted orders. Diffraction is described by the general grating equation, normally written as:

$$m\lambda = d(\sin i + \sin i') \qquad m = 0,\ +/- 1,\ +/- 2, \ldots \qquad (2\text{-}1)$$

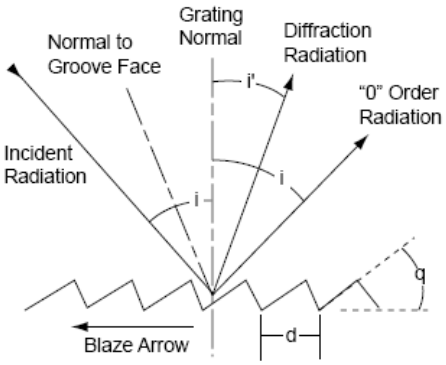

Fig. 2.1: GRATING ANGLE AND TERMS [66].

In this equation m is the diffraction order, λ is the wavelength, d is the period of the grating or the grating constant, which is the distance between successive grooves, i is the angle of incidence measured with respect to grating normal, and i' is the angle of diffraction also measured with respect to grating normal. If in this equation m is zero, i will be equal to i' in magnitude, which indicates that light is simply reflected. Let's consider the grating equation for a given set of angles of incidence and diffraction (i, i') and a set groove spacing (d). We notice that there are a number of wavelengths for which the grating equation is valid. In fact the condition for constructive interference is satisfied for successive values of the integer m (the diffraction order) at a number of different wavelengths. This implies that the constructive interference between the wave fronts emanating from successive grooves can only occur if the phase difference between the diffracted waves is an integral multiple of the wavelength. Since the maximum value which is possible for $|\sin i + \sin i'|$ is equal to 2, the only orders that are possible are those for which $|m\lambda/d|$ is less than 2. The zero order (m = 0), which signifies the specular reflection, is always possible and in most cases the existence of both negative and positive orders is possible according to the grating equation, as long as the inequality relation $-2d < m\lambda < 2d$ is maintained. A closer look at the grating equation reveals how a spectrum is actually made. A polychromatic radiation is incident on the grating surface. According to grating equation for a chosen diffracted order (m) and a specific angle of incidence (i), the angle of diffraction (i') would be different for different wavelengths such that each will appear at a

slightly different location. This is the mechanism by which a polychromatic light is resolved into its constituent wavelengths.

2.5.1 Dispersion

"Dispersion is a measure of the separation (either angular or spatial) between diffracted light of different wavelengths." [67]. The dispersion of a grating is a function of both the groove spacing and the angle of incidence. Imagine a spectrum in which two spectral lines in the vicinity of λ are separated by a small wavelength difference Δλ. There should be a minimum spatial distance between these two lines if we are to unambiguously tell them apart. What we really need to know is how the angle of diffraction is changing as the wavelength changes which can be simply answered by differentiating the grating equation with respect to the angle of diffraction i'. Assuming the angle of incidence i to be constant we have:

$$D_{\lambda} = \frac{\partial \mathrm{i}'}{\partial \lambda} = \frac{\mathrm{m}}{\mathrm{d} \cdot \cos(\mathrm{i}')} \tag{2-2}$$

The quantity D_{λ} is called the angular dispersion of the grating. In practice one often needs to know the linear dispersion D_x which is the product of the angular dispersion and the effective focal length ($\mathrm{f}_{\mathrm{eff}}$) of the instrument:

$$D_x = \frac{\partial \mathrm{x}}{\partial \lambda} = \mathrm{f}_{\mathrm{eff}} \cdot \frac{\partial \mathrm{i}'}{\partial \lambda} \tag{2-3}$$

It should be noted that for a waveguide-based grating the equations [Eq. (2-1), Eq. (2-2) and Eq.(2-3)] have to be modified to include the effective refractive indices.

2.5.2 Resolution

The minimum wavelength separation Δλ between two spectral lines of wavelength λ and λ + Δλ that can be unambiguously resolved is referred to as resolution. In determination of resolution the image effects of the system must be taken into consideration; these include the dimensions of the entrance and exit apertures, the image magnification and the aberrations involved. Thus for a spectroscopic system resolution is more relevant than the dimensionless theoretical resolving power.

2.5.3 Resolving Power

The product of the diffracted order and the number of grooves which are intercepted by incident radiation is the grating's theoretical resolving power (*RP*). The resolving power can also be given in terms of grating width, the incident and the diffracted angles. The formula to obtain the "theoretical resolving power" of a grating that has N grooves is:

$$RP = \frac{\lambda}{\Delta\lambda} = \mathrm{m}\cdot \mathrm{N} \qquad (2\text{-}4)$$

The accuracy of the ruling is the most important factor in determination of the actual resolving power of a grating. Usually 80-90% of the theoretical value for the resolving power can be achieved by using a high quality ruled grating. While resolution is dependent on the mechanical and optical characteristics of the instrument in which the grating is used, the resolving power is a property of the grating that is independent of these characteristics.

2.5.4 Free Spectral Range

The free spectral range (FSR) is the maximum spectral bandwidth which is possible in a given diffracted order in the absence of spectral interference (overlap) from neighbouring positive or negative orders. The free spectral range is inversely proportional to the period of the grating. The free spectral range is the separation between lower (λ_1) and upper (λ_2) limits for the band of interest and it can be represented by the following formula:

$$\mathrm{FSR} = \lambda_2 - \lambda_1 = \lambda_1/\mathrm{m} \qquad (2\text{-}5)$$

which indicates that at higher orders the free spectral range decreases. In fact at higher orders efficiency and free spectral range both decrease while dispersion increases.

2.6 The Scalar Theory of Diffraction

The electromagnetic properties of light are completely characterized by Maxwell's equations. However, light as a wave phenomenon was known long before Maxwell. Wave optics is capable of explaining the observed effects of

interference and diffraction with excellent accuracy as revealed by the results of measurements done in the microwave region [62].

In wave optics, one assumes that light may be represented with an (complex) amplitude function $u(\vec{r})$, satisfying the scalar wave equation:

$$(\nabla^2 + k^2)\, u(\vec{r}) = 0 \qquad (2\text{-}6)$$

where $k = \dfrac{2\pi}{\lambda}$ is the wavenumber.

the problem is to find a solution to this equation at an arbitrary point located on one side of a diffractive aperture in an otherwise opaque screen, while a light source $u(\vec{r}')$ of known distribution is illuminating the screen from the other side.

Kirchhoff approached this problem by invoking Green's theorem, which can be expressed as follows [62]:

$$\iiint_V (\psi\, \nabla^2\, \phi \,-\, \phi\, \nabla^2\, \psi)\, dv \;\equiv\; \iint_S \vec{n} \cdot (\psi\, \nabla\, \phi \,-\, \phi\, \nabla\, \psi)\, ds \qquad (2\text{-}7)$$

Here, $\vec{n}$ is the outward unit normal of the bounding surface S (see Fig.2-2)

Let $\phi(\vec{r}) = u(\vec{r})$, and let $\psi(\vec{r}, \vec{r}') = G(\vec{r}, \vec{r}')$,

where $$(\nabla^2 + k^2) G = \delta\,(\vec{r} - \vec{r}') \qquad (2\text{-}8)$$

A possible solution of this equation is:

$$G = -\frac{\exp(-jkR)}{4\pi R} \;;\; R = \left| \vec{r} - \vec{r}' \right| \qquad (2\text{-}9)$$

Since

$$\begin{aligned} G\, \nabla^2\, u \,-\, u\, \nabla^2 G \;&=\; G\, (-k^2 u) - u\, (-k^2 G \,+\, \delta\,(\vec{r} - \vec{r}')\,) \\ &= -u\,(\vec{r})\, \delta\,(\vec{r} - \vec{r}')\,. \end{aligned} \qquad (2\text{-}10)$$

Substitution into Green's function gives:

$$-u\,(\vec{r}') = \oiint_S \vec{n}\, \cdot (\, G\, \nabla\, u \,-\, u\, \nabla\, G\,)\, ds$$

$$\text{For } \vec{r}' \text{ in } V \qquad (2\text{-}11)$$

Multiplying thru by -1 and interchanging $\vec{r}'$ and $\vec{r}$

$$u\,(\vec{r}) = \oiint_S \left(u\,(\vec{r}')\, \vec{n}\, \cdot \nabla'\, G \,-\, G\, \vec{n}\, \cdot \nabla'\, u\right) ds' \qquad (2\text{-}12)$$

This relation is known as the Helmholtz-Kirchhoff Integral Theorem.

The theorem asserts the possibility of determining $u(\vec{r})$ which satisfies:

$$(\nabla^2 + k^2)\, u(\vec{r}) = 0\,, \tag{2-13}$$

at any point in the volume V provided $u(\vec{r}')$ and $\vec{n} \cdot \nabla' u(\vec{r}')$ can be specified in a constant fashion at all points on the surface bounding V.

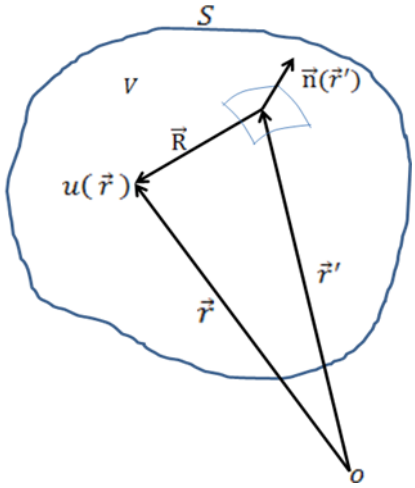

Fig. 2.2: Surface S bounding volume V with $R = \left| \vec{r} - \vec{r}' \right|$, and $\vec{n}(\vec{r}')$ the outward unit normal of S at point $\vec{r}'$ on S.

2.7 Rayleigh-Sommerfeld Diffraction Formula

In his formulation of diffraction, Kirchhoff made some simplifying assumptions regarding the field and its derivative at the boundary. Poincare, and later Sommerfeld, showed that these assumptions are inconsistent [62, 63]. Sommerfeld removed the inconsistency by choosing a special form of Green's function $(\psi = G_-)$ such that in addition to satisfying the Helmholtz-Kirchhoff integral theorem it was also zero at the boundary. There are two variations to the Rayleigh-Sommerfeld formula (I, II). In these formulas, the expression for $u(\vec{r})$ is considerably simplified. Rayleigh-Sommerfeld I and II formulations based on Hankel functions will be discussed in detail later in **3.10.** The derivation of Rayleigh-Sommerfeld diffraction formula is as follows:

First, we separate the surface S into two parts: S_1 a plain containing the aperture(s) and S_2 a sphere centered on the observation point $\vec{r}$ (see Fig.2-3).

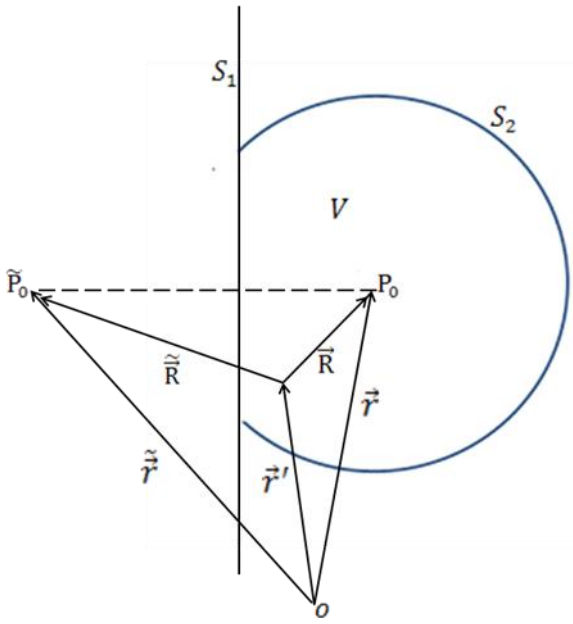

Fig. 2.3: Aperture containing surface S_1 nd the surface S_2.
S_2 is a portion of a sphere centered on the observation point P_0.

Let P_0 be the observation point $\vec{r}$ and $\tilde{P}_0$ be another point $\vec{\tilde{r}}$ outside the surface S.
With $R = \vec{r} - \vec{r}'$ and $\tilde{R} = \vec{\tilde{r}} - \vec{r}'$ we define:

$$G_- \equiv \frac{\exp(-jk\tilde{R})}{4\pi\tilde{R}} - \frac{\exp(-jkR)}{4\pi R}. \qquad (2\text{-}14)$$

Then:

$$(\nabla'^2 + k^2)\, G_- = \delta(\vec{r}' - \vec{r}) - \delta(\vec{r}' - \vec{\tilde{r}}) \qquad (2\text{-}15)$$

Substituting for $\nabla'^2 G_-$ into Green's theorem and noting that $\vec{\tilde{r}}$ is not a point of the volume V, we find as before:

$$u(\vec{r}) = \iint_S \vec{n} \cdot (u\, \nabla' G_- - G_- \nabla' u)\, ds' \qquad (2\text{-}16)$$

or,

$$u(\vec{r}) = \iint_{S_1} \vec{n} \cdot (u\, \nabla' G_- - G_- \nabla' u)\, ds' + \iint_{S_2} \vec{n} \cdot (u\, \nabla' G_- - G_- \nabla' u)\, ds'. \qquad (2\text{-}17)$$

With $\vec{r}'$ on S_2 so that $\vec{n} = -\vec{1}_R$, the condition under which $\iint_{S_2} \to 0$ as the radius R increases without bound can be shown to be:

$$\lim_{r \to \infty} r\,(jku + \vec{1}_r \cdot \nabla u) = 0.$$

(Here $\vec{r}'$ was ecchanged for $\vec{r}$ for simplicity). This is the Sommerfeld radiation condition.

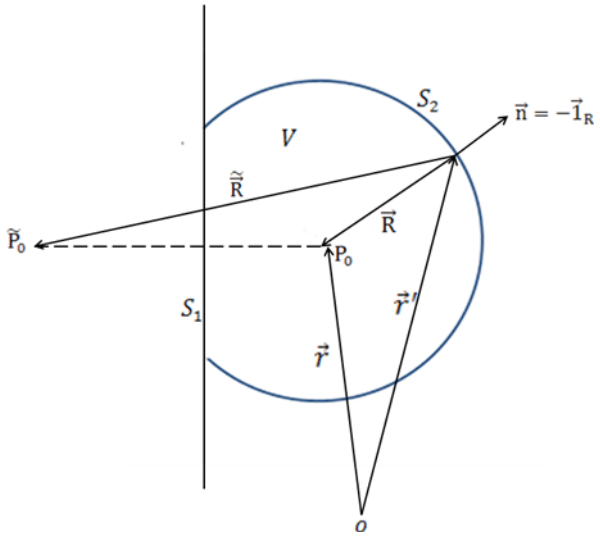

Fig. 2.4: Schematic representing Sommerfeld radiation condition.
Here $\vec{r}'$ is on S_2 so that $\vec{n} = -\vec{1}_R$.

$$G_- \equiv \frac{\exp(-jk\tilde{R})}{4\pi\tilde{R}} - \frac{\exp(-jkR)}{4\pi R} \tag{2-18}$$

$$\nabla' G_- = -\vec{1}_R \left(\frac{1}{R} + jk\right)\frac{\exp(-jkR)}{4\pi R} + \vec{1}_{\tilde{R}} \left(\frac{1}{\tilde{R}} + jk\right)\frac{\exp(-jk\tilde{R})}{4\pi\tilde{R}} \tag{2-19}$$

As $S_2 \to \infty$ (i.e. $\vec{r}' \to \infty$ and $R \to \infty$), so does $\tilde{R}$ and $\vec{1}_{\tilde{R}} \approx \vec{1}_R$ (see Fig.2-4). Since at optical wavelengths k is large in comparison to $\frac{1}{R}$ and $\frac{1}{\tilde{R}}$ (even for ordinary values of R and $\tilde{R}$), then:

$$\nabla' G_- \approx -\vec{1}_R\, jk \frac{\exp(-jkR)}{4\pi R} + \vec{1}_{\tilde{R}}\, jk \frac{\exp(-jk\tilde{R})}{4\pi\tilde{R}}$$

$$\sim j\, k\, \vec{1}_R\, G_- \tag{2-20}$$

As $S_2 \to \infty$, it follows that:

$$\vec{n} \cdot \nabla' G_- \sim -j\, k\, G_-$$

$$\iint_{S_2 \to \infty} = \lim_{R \to \infty} \iint_{S_2} (-j\, k\, u\, G_- + G_-\, \vec{1}_R \cdot \nabla' u)\, R^2\, d\Omega' \tag{2-22}$$

For this result to go to zero we must have:

$$\lim_{R\to\infty}\left(jk\,R\,u - \vec{R}\cdot\nabla' u\right) R\; G_- = 0 \tag{2-23}$$

Since $\lim_{R\to\infty} RG_-$ does not diverge therefore for

$$\iint_{S_2\to\infty} \to 0$$

we require

$$\lim_{r'\to\infty}\left(jk\,|\vec{r}-\vec{r}'|\,u-(\vec{r}-\vec{r}')\cdot\nabla' u\right)=0\,. \tag{2-24}$$

Neglecting finite $\vec{r}$ in comparison to $\vec{r}'\to\infty$ we have:

$$\lim_{r'\to\infty}\left(jk\,\vec{r}'\,u+\vec{r}'\cdot\nabla' u\right)=0\,. \tag{2-25}$$

Expressed in un-primed variables this is the **<u>Sommerfeld Radiation Condition</u>:**

$$\lim_{r\to\infty} r\left(jk\,u+\vec{1}_r\cdot\nabla u\right)=0\,. \tag{2-26}$$

Now with the double integral on S_2 going to zero we have:

$$u(\vec{r})=\iint_{S_1}\vec{n}\cdot(u\,\nabla' G_- - G_-\nabla' u)\,ds' \tag{2-27}$$

Where S_1 is of infinite extent and $\vec{r}$ is any point to the right of the plane S_1.
With $\vec{r}'$ on S_1, $\vec{n}=-\vec{1}_z$. For $\tilde{P}_0$ the mirror image of P_0 we have $\tilde{R}=R$.
Then $G_-=0$ and we obtain $\vec{n}\cdot\nabla' G_-$ as discussed below (Fig.2-5).

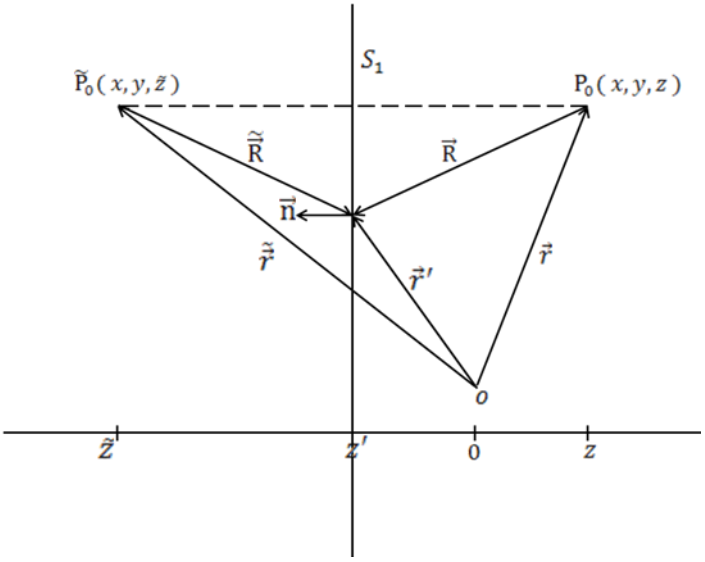

Fig. 2.5: Schematic showing the geometry of the problem with $\vec{r}'$ on S_1.

With $\vec{r}'$ on S_1, $\tilde{R}=R$.

$$\therefore\; G_- = \frac{\exp(-jk\tilde{R})}{4\pi\tilde{R}} - \frac{\exp(-jkR)}{4\pi R} = 0\,. \tag{2-28}$$

$$\nabla' G_- = -\vec{1}_R \left(\frac{1}{R} + jk\right)\frac{\exp(-jkR)}{4\pi R} + \vec{1}_{\tilde{R}} \left(\frac{1}{\tilde{R}} + jk\right)\frac{\exp(-jk\tilde{R})}{4\pi\tilde{R}} \tag{2-29}$$

$$= -(\vec{1}_R - \vec{1}_{\tilde{R}}) \left(\frac{1}{R} + jk\right) \frac{\exp(-jkR)}{4\pi R}, \text{ since } \tilde{R} = R. \tag{2-30}$$

$$\vec{1}_R - \vec{1}_{\tilde{R}} = \frac{\vec{R}}{R} - \frac{\tilde{\vec{R}}}{\tilde{R}} = \frac{\vec{R} - \tilde{\vec{R}}}{R} = \frac{\vec{r} - \vec{r}' - (\tilde{\vec{r}} - \vec{r}')}{R} = \frac{\vec{r} - \tilde{\vec{r}}}{R} = \vec{1}_z \frac{z - \tilde{z}}{R}$$

$$= \vec{1}_z \frac{2(z - z')}{R} \tag{2-31}$$

With $\vec{n} = -\vec{1}_z$, we have:

$$\nabla' G_-\big|_{\vec{r}' \text{ on } S_1} = \vec{n} \frac{2(z - z')}{R} \left(\frac{1}{R} + jk\right) \frac{\exp(-jkR)}{4\pi R}, \tag{2-32}$$

$$\vec{n} \cdot \nabla' G_-\big|_{\vec{r}' \text{ on } S_1} = \frac{1}{2\pi} \frac{z - z'}{R} \left(\frac{1}{R} + jk\right) \frac{\exp(-jkR)}{R}. \tag{2-33}$$

Finally:

$$u(\vec{r}) = \frac{1}{2\pi} \iint_{S_1} u(\vec{r}') \frac{z - z'}{R} \left(\frac{1}{R} + jk\right) \frac{\exp(-jkR)}{R} ds' \tag{2-34}$$

2.7.1 Approximations to the Rayleigh-Sommerfeld Formula

We can relegate the dependence on z to a subscript and introduce

$$u_z(x, y) \equiv u(x, y, z) \; ; \; u_{z'}(x', y') \equiv u(x', y', z')$$

$$h_{z-z'}(x - x', y - y') \equiv \frac{1}{2\pi} \frac{z - z'}{R} \left(\frac{1}{R} + jk\right) \frac{\exp(-jkR)}{R} \tag{2-35}$$

where $R = \sqrt{(x - x')^2 + (y - y')^2 + (z - z')^2}$.

With this notation we have:

$$u_z(x, y) = \int_{-\infty}^{\infty} \int_{-\infty}^{\infty} u_{z'}(x', y') \, h_{z-z'}(x - x', y - y') \, dx' dy'$$

$$\equiv u_{z'}(x, y) ** h_{z-z'}(x, y) \tag{2-36}$$

Where $**$ indicates convolution on the two variables *x* and *y*. In particular, with the origin in S_1, $z' = 0$. Then:

$$u_z(x,y) = \int_{-\infty}^{\infty}\int_{-\infty}^{\infty} u_0(x',y')\, h_z(x-x', y-y')\, ds' ,$$

$$u_z(x,y) = \int_{-\infty}^{\infty}\int_{-\infty}^{\infty} u_0(x',y')\, \frac{1}{2\pi}\, \frac{z}{\mathrm{R}_0} \left(\frac{1}{\mathrm{R}_0} + jk\right) \frac{\exp(-jk\,\mathrm{R}_0)}{\mathrm{R}_0}\, dx'dy' . \quad (2\text{-}37)$$

where $$\mathrm{R}_0 \equiv \mathrm{R}\big|_{z'=0} = \sqrt{(x-x')^2 + (y-y')^2 + z^2} ,$$

$$= |\vec{r} - \vec{\rho}'| , \quad (2\text{-}38)$$

while $\vec{\rho}' = \vec{1}_x x' + \vec{1}_y y' = \vec{1}_\rho(\phi')\rho'$ in cylindrical coordinates.

At optical wavelengths, generally $\lambda \ll \mathrm{R}_0$ even for small $\vec{r}$ and $\vec{\rho}'$, Thus $\frac{1}{\mathrm{R}_0} \ll k$

and we have:

$$h_z(x-x',\, y-y') \approx j\frac{k}{2\pi}\, \frac{z}{\mathrm{R}_0}\, \frac{\exp(-jk\,\mathrm{R}_0)}{\mathrm{R}_0} . \quad (2\text{-}39)$$

Hence:

$$u_z(x,y) \;=\; \iint_{S_1} u_0(x',y')\, \frac{j}{\lambda}\, \frac{z}{\mathrm{R}_0}\, \frac{\exp(-jk\,\mathrm{R}_0)}{\mathrm{R}_0}\, ds' \quad (2\text{-}40)$$

2.8 Fresnel Approximation

In the Fresnel approximation we have a configuration as shown in Fig. 2.6.

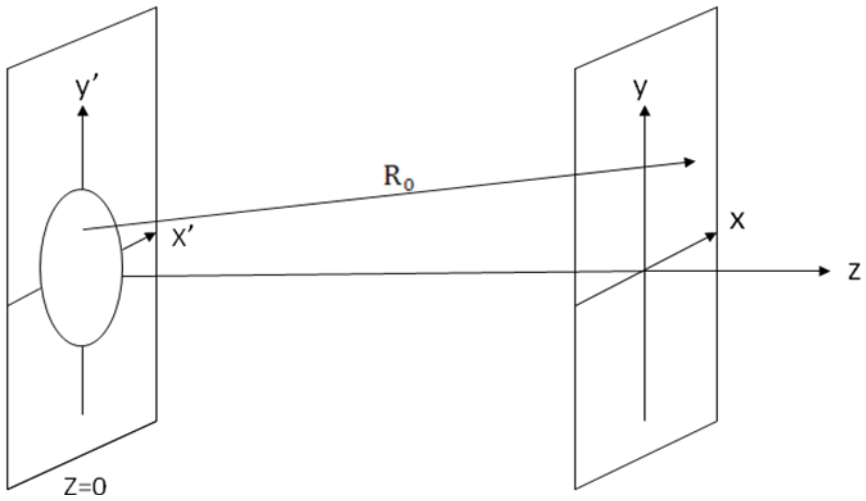

Fig. 2.6: Schematic showing the aperture and the observation screens in Fresnel approximation.

First note that we may write:

$$\mathrm{R_0}^2 = z^2\left[1+\left(\frac{x-x'}{z}\right)^2+\left(\frac{y-y'}{z}\right)^2\right]. \qquad (2\text{-}41)$$

In Fresnel approximation it is assumed that *z*, the distance between S_1 (input plane) and the observation (output) plane is such that

$$\left(\frac{x-x'}{z}\right)^2+\left(\frac{y-y'}{z}\right)^2 \ll 1. \qquad (2\text{-}42)$$

The Fresnel approximation consist of setting $\mathrm{R_0} \approx z$ in the denominator of h_z (this makes the obliquity factor $\frac{z}{\mathrm{R_0}}$ equal to unity) and using the binomial expansion:

$$(1+a)^{1/2} = 1+\frac{1}{2}a-\frac{1}{8}a^2+\cdots \qquad |a| < 1 \qquad (2\text{-}43)$$

in the phase term $\exp(-jk\,\mathrm{R_0})$.

(However it is inappropriate to replace $\mathrm{R_0}$ by the first order approximation

i.e. $\mathrm{R_0} \approx z$ in the phase term because it is multiplied by the large factor $k = \frac{2\pi}{\lambda}$)

$$\mathrm{R_0} = z\left\{1+\frac{1}{2}\frac{(x-x')^2+(y-y')^2}{z^2}-\frac{1}{8}\frac{\left[(x-x')^2+(y-y')^2\right]^2}{z^4}+\cdots\right\} \qquad (2\text{-}44)$$

$$\therefore\ \exp(-jk\,\mathrm{R_0}) \approx \exp(-jkz)\times\exp\left(-j\frac{k}{2z}\left[(x-x')^2+(y-y')^2\right]\right) \times\exp\left(+j\frac{k}{8z^3}\left[(x-x')^2+(y-y')^2\right]^2\right)\times\cdots \qquad (2\text{-}45)$$

In the Feresnel approximation

$$\exp\left(+j\frac{k}{8z^3}\left[(x-x')^2+(y-y')^2\right]^2\right)\approx 1 \qquad (2\text{-}46)$$

If this is true, higher order terms in the binomial expansion are even less significant.

The Fresnel approximation replaces,

$$h_z(x-x',\, y-y') \approx \frac{j}{\lambda}\,\frac{z}{\mathrm{R}_0}\,\frac{\exp(-jk\,\mathrm{R}_0)}{\mathrm{R}_0} \tag{2-47}$$

by the expression (which replaces the spherical Huygens' wavelets by quadratic surfaces):

$$h_z(x-x',\, y-y') \;\approx\; \frac{j}{\lambda}\,\frac{\exp(-jkz)}{z}\,\exp\left(-j\frac{k}{2z}\left[(x-x')^2+(y-y')^2\right]\right) \tag{2-48}$$

or

$$h_z(x,y) \;\approx\; \frac{j}{\lambda}\,\frac{\exp(-jkz)}{z}\,\exp\left(-j\frac{k}{2z}(x^2+y^2)\right) \tag{2-49}$$

thus:

$$u_z(\,x,\,y\,) \;\approx\; \frac{j}{\lambda}\,\frac{\exp(-jkz)}{z}\iint u_0(x',y')\,\exp\left(-j\frac{k}{2z}\left[(x-x')^2+(y-y')^2\right]\right)dx'dy' \tag{2-50}$$

2.9 Fraunhoffer Approximation

The Fresnel approximation defines a region in space in which

$$h_z(x,y) \;\approx\; \frac{j}{\lambda}\,\frac{\exp(-jkz)}{z}\,\exp\left(-j\frac{k}{2z}(x^2+y^2)\right) \tag{2-51}$$

$$u_z(x,\mathrm{y}) = u_0(\mathrm{x},\mathrm{y}) ** h_z(x,y) \tag{2-52}$$

$$u_z(x,y) = h_z(x,y)\int_{-\infty}^{\infty}\int_{-\infty}^{\infty} u_0(x',y')\exp\left(-j\frac{k}{2z}(x'^2+y'^2)\right)\exp\left(j\frac{k}{z}(xx'+yy')\right)dx'dy' \tag{2-53}$$

The Fraunhoffer approximation assumes further that for sufficiently large z

$$\exp\left(-j\frac{k}{2z}(x'^2+y'^2)\right)\approx 1 \tag{2-54}$$

over the part of S_1 for which $u_0(x',y') \neq 0$ (i.e. the aperture region).

In making this approximation we destroy the convolution relation between input and output.

We have:

$$u_z(x,y) \sim h_z(x,\mathrm{y})\int_{-\infty}^{\infty}\int_{-\infty}^{\infty} u_0(x',y')\exp\left(j2\pi\,(\frac{x}{\lambda z}\,x'+\,\frac{y}{\lambda z}\,y')\right)dx'dy'$$

$$\sim h_z(x,y)\,\mathrm{U}_0(\,\nu_x\,,\nu_y\,)$$

where

$$\nu_x = \frac{x}{\lambda z} \quad , \quad \nu_y = \frac{y}{\lambda z} \tag{2-55}$$

This important result shows that, apart from the quadratic phase factor of $h_z(x, y)$ which marks the result, the field distribution, $u_z(x, y)$ in any z plane in the Fraunhoffer region is related to the Fourier transform of the signal $u_0(x, y)$ in the input plane. The system behaves essentially as a **spectrum analyzer**. In fact:

$$u_z(x, y) \sim \frac{1}{\lambda z} |\, \mathrm{U}_0(\ \nu_x\ ,\ \nu_y\ )\,| \tag{2-56}$$

CHAPTER 3

3. Numerical Simulation Tools

This chapter provides a brief overview of the optofluidic Microsystems that were conceived and studied in this thesis research, followed by a detailed description of the numerical simulation tools developed to guide the design process.

3.1 Overview of the LOC spectrometer system

To facilitate the subsequent discussion of simulation tools, we start with a high-level description of the proposed system.

While the trend for incorporating more and more components on a single chip continues, cost and material incompatibilities remain as barriers to monolithic integration. The approach taken in this thesis research can best be described as a hybrid integration strategy, namely; to incorporate the optics and the fluidics on a single disposable chip while the excitation source and detection unit as well as the electronic parts, remain off the chip. LOC devices were designed and fabricated (Fig.3.1) in such a way that light confinement by total internal reflection is possible. The planar devices are composed of three layers of PDMS. The central layer contains both fluidic and optical components, which are formed in the same fabrication step. The outer layers are made of Sylgard-184®, which has a refractive index of 1.41. The central layer containing the optical and fluidic components is made from a formulation of PDMS that has higher refractive index of 1.43. Because of the index contrast with the outer layers, light can be confined in the central "optofluidic" layer, also referred to as the core layer.

The over-riding goal of the research project was to integrate a waveguide-based optical spectrometer into such a PDMS-based optofluidic chip. We chose to design diffraction-grating-based spectrometers. Along with the dispersive element (i.e. the diffraction grating), this implied the need to integrate lenses or mirrors for light collimation and focusing.

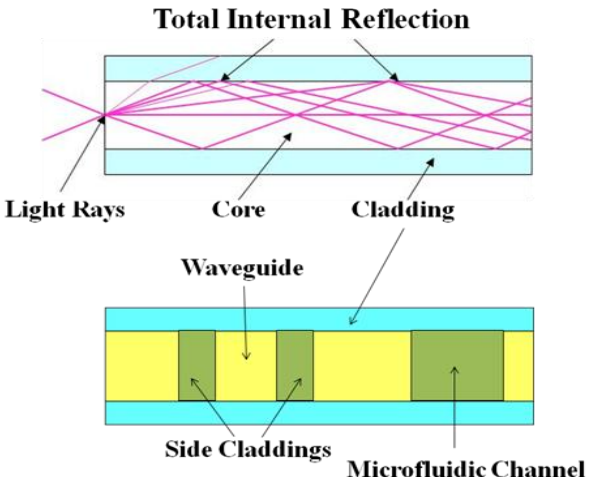

Fig. 3.1: Schematics representing total internal reflection (top) and the waveguide and microfluidic channel (bottom).

The first spectrometer we considered was based on a Grating Prism (Grism, also called carpenter prism), which is simply a right angle prism with periodic steps on its hypotenuse. A chip comprising the grating, optical waveguides, and microfluidic channels was designed, and the layout of the chip is shown in Fig. 3.2. The chip dimensions are (3.0 cm x 4.4 cm), and the steps of the grating are (3 μm x 6 μm). A section of the fluidic channel is in U shape, and two waveguides, one from the middle and one from the side, come to the vicinity of this section (lower right figure). This section is where optical interrogation of the fluidic sample takes place. In addition, there are two slab-waveguide bi-convex lenses (one for collimation and one for focusing) before and after the grating, respectively. The dark areas are voids or empty spaces formed in PDMS during processing. There is also a waveguide to pick up the diffracted signal at the edge of the chip (the triangular formations at the right end of the chip).

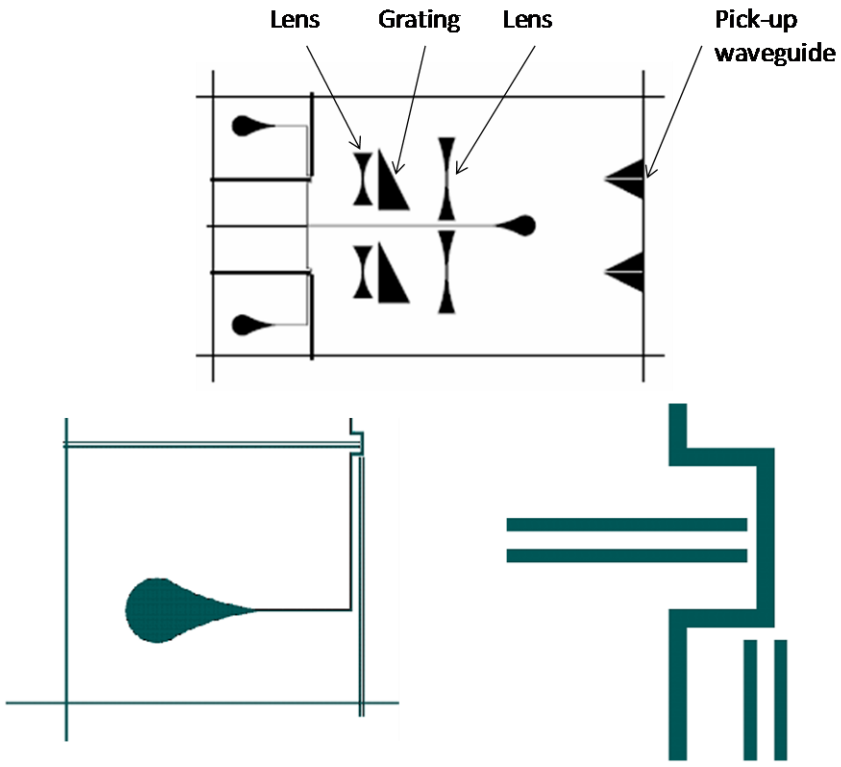

Fig. 3.2: Actual drawings of the grating prism microspectrometer chip (top figure).A reservoir and a portion of the microfluidic channel (bottom left figure). The U shaped section of the microfluidic channel and the horizontal and perpendicular waveguides coming to this section (bottom right figure).

Subsequently, we designed a chip in which the steps of the grating were placed on a curve, designed to both disperse and focus the light. This allows the chip to be smaller (1.7 cm x 2.1 cm), since the second lens can be eliminated. The grating was designed such that each facet is an arc or section of a circle, the radius of which is uniquely determined to obtain a common focal point among all facets. There are 600 facets on this grating and the facets gradually decrease from 6 μm (the first facet) to 4.93 μm (the last facet) each time reducing by 0.0018 μm. Gratings of this type where the facets are not equal and they vary slowly across the length of the grating are known as chirped gratings. A chirped grating further enhances the focusing action of the grating. As mentioned, in this geometry there is no need for a separate focusing lens. Thus, the number of interfaces that light has to go through is reduced. This is highly desirable, especially when we are

dealing with a weak source such as a fluorescent signal. Figure 3.3 shows the grating lens spectrometer and enlarged sections of this design. Details regarding the simulation of this chip follow, and experimental results are reported in Chapter 6.

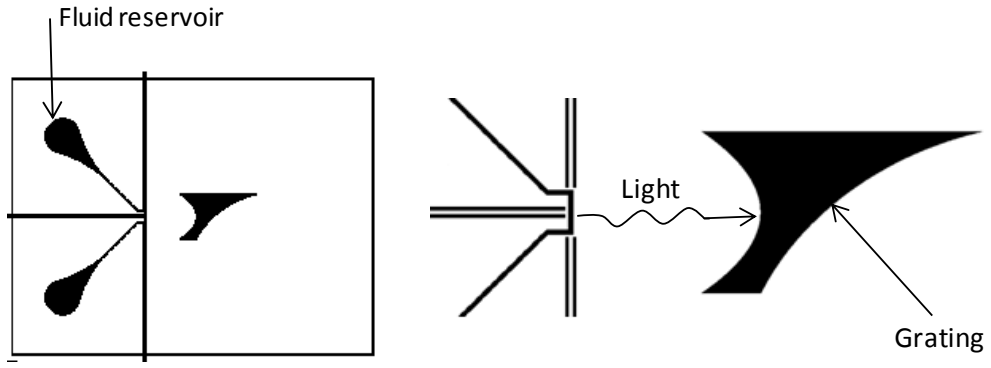

Fig. 3.3: Grating lens spectrometer design (left). Enlarged sections of the chip (middle and right).

3.2 Simulation details

3.2.1 Ray-tracing

In general, propagation of light can be treated using two fundamentally different theoretical approaches. One is the geometrical or ray optics approach and the other is the wave optics approach. Ray optics assumes that light consists of independent bundles of electromagnetic energy travelling along trajectories called rays. When the refractive index of the medium of propagation is constant, rays travel in straight lines and when they encounter a new refractive index at an interface they change direction according to Snell's law [68]. When the medium is a graded index medium, rays travel along curved trajectories but regardless of the index of the medium, at every point the ray trajectory is normal to the phase front of the propagating electromagnetic wave. The ray equation can be derived from an approximate solution to the wave equation and rays are solutions to this equation [68]. The concept of rays is easy to understand and visualize and ray-tracing softwares are easy to develop. Furthermore, since each ray is independent, parallel processing is possible. The ray picture is exact when the ratio of wavelength to feature sizes approaches zero. Ray theory has been used

extensively in fibre optics. In general, when a qualitative and fast analysis is intended, ray theory may be very helpful, However, in cases where the size of the guiding medium is comparable to a wavelength, interference and diffraction effects become important, the ray picture breaks down, and wave theory needs to be invoked.

Accordingly, a number of simple ray-tracing routines were written in Matlab to get a qualitative picture of the behaviour of light at spherical, parabolic, and simple aspheric interfaces. In addition, the extent and nature of aberrations in the focal regions of such lenses was determined. Fig. 3.4 below shows ray tracing in a double parabolic (a) and a single aspheric (b) lens. Note that these are two-dimensional simulations. For the cases shown in Fig. 3.4, each region has a refractive index, n = 1 (representing air), or n = 1.59 (representing SU-8).

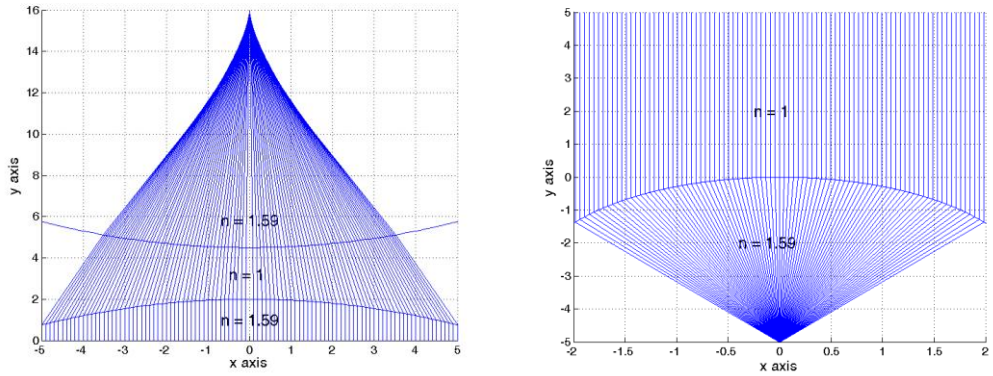

Fig. 3.4: Ray-tracing for a double parabolic lens (left). Ray-tracing for a single aspheric lens (right). The regions of the lens are demarcated by the solid lines. The assumed refractive index is indicated.

Ray-tracing Matlab codes for the double parabolic and single aspheric lens are listed in Appendix-I (App. I).

3.2.2 Wave optics simulations

As the name implies, in wave optics the wave nature of light is considered. Unlike ray optics, wave optics can provide a detailed account of interference and diffraction. We have utilized the two-dimensional Fresnel diffraction operator [69],

$$E(y,x) = \int \sqrt{\frac{i}{\lambda.\Delta x}} * e^{-i.k.\Delta x} * e^{-\frac{i.k.(\Delta y)^2}{2*\Delta x}} * E(y_0, x_0) * dy \qquad (3\text{-}1)$$

Using this operator, simulation routines were developed in Matlab that use an electric field,

$E(y_0, x_0)$, as input and calculate the resulting electromagnetic field intensity at an output plane (which could be a plane or any arbitrary surface) located at a distance Δx from the input. In case of multiple interfaces, the output obtained at the first interface in the cascade is treated as the input for the next interface and so on.

3.3 Free space propagation of a Gaussian beam

As the first test of the wave optics implementation, free pace propagation of a Gaussian beam was simulated. Fig. 3.5 shows the predicted profile for a beam with wavelength of 633 nm and input beam diameter of 200 μm, after travelling a distance of 10,000 μm. The results obtained using the Fresnel integral, were compared to the results obtained using an exact formulation of the two-dimensional Fresnel diffraction integral. The exact formulation was coded in a separate Matlab file.

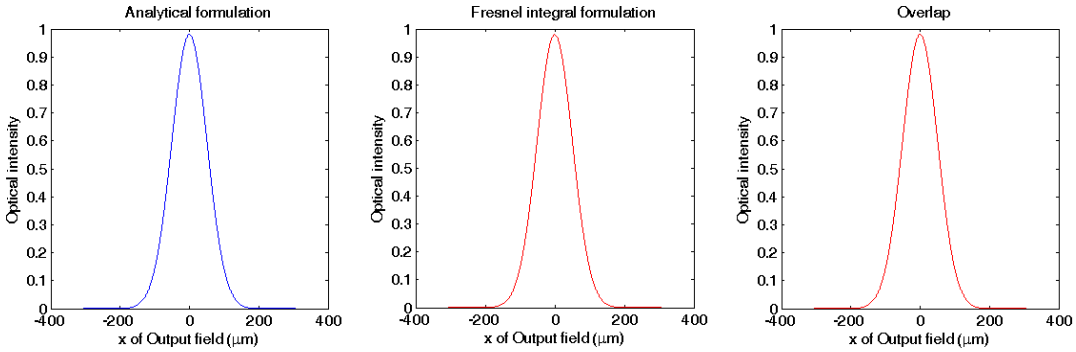

Fig. 3.5: Comparison of analytical (left window in blue) and integral (middle window in red) formulations of the Gaussian beam propagation. The right window shows their complete overlap.

3.4 Comparison of MathCAD and Matlab simulations of diffraction by slits

Next we tested the accuracy of the Fresnel diffraction operator approach for simulating structures involving interference and diffraction. To do this, far-field diffraction simulations of double and multiple slits were compared with MathCAD programs that used the well-known [70] exact formulae for the

calculation of intensity at the output. The parameters used for the next two simulations (Fig.3.6 and Fig. 3.7) are as follows: Propagation wavelength, λ = 0.0005 mm, slit width, d = 0.02 mm, centre to centre separation of slits, a = 0.02 mm, number of slits N = 2, propagation distance, X = 40,000 mm, and the output plane extends from Y = -2000 mm to Y = 2000 mm. Matlab code for this simulation is listed in App. I.

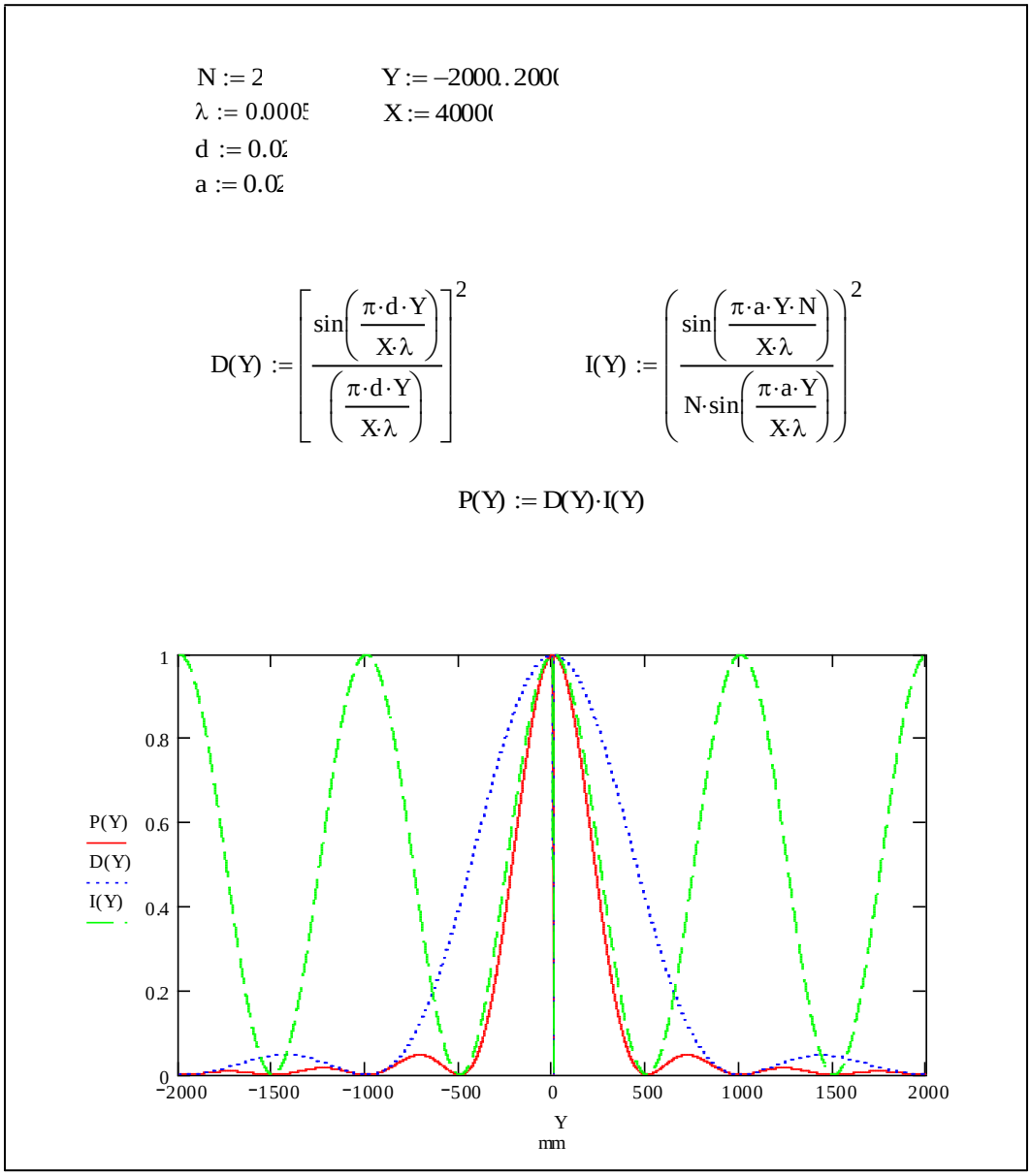

Fig. 3.6: MathCAD simulation of diffraction by two slits using closed form expressions for intensity. The resulting intensity profile is shown in red.

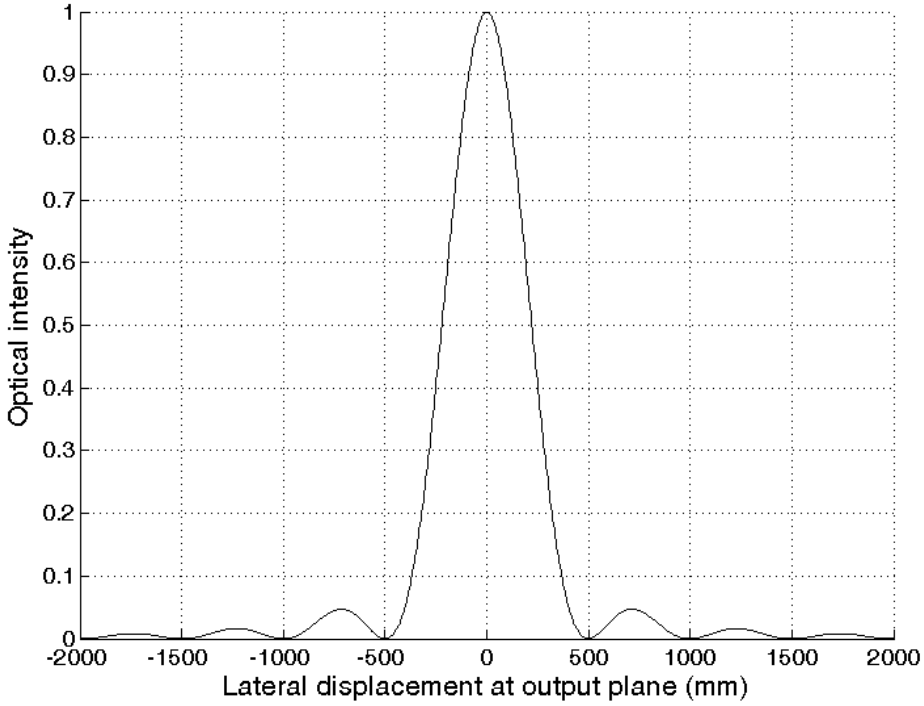

Fig. 3.7: Fresnel integral simulation (see App. I) of the far-field diffraction intensity by two slits. Note the location of minima and maxima is identical in Fig. 3.6 and Fig. 3.7.

The parameters of simulation for diffraction by four slits (Figs. 3.8 and 3.9) are as follows:

Propagation wavelength, λ = 0.5 μm, slit width, d = 4 μm, centre to center separation of slits,

a = 12 μm, number of slits N = 4, propagation distance, X = 4000 μm, and the output plane is extended from Y = -2000 μm to Y = 2000 μm. Matlab code for this simulation is listed in App. I.

$N := 4$ $\quad Y := -2000..2000$

$\lambda := 0.5$ $\quad X := 4000$

$d := 4$

$a := 12$

$$D(Y) := \left[\frac{\sin\left(\frac{\pi \cdot d \cdot Y}{X \cdot \lambda}\right)}{\left(\frac{\pi \cdot d \cdot Y}{X \cdot \lambda}\right)} \right]^2 \qquad I(Y) := \left(\frac{\sin\left(\frac{\pi \cdot a \cdot Y \cdot N}{X \cdot \lambda}\right)}{N \cdot \sin\left(\frac{\pi \cdot a \cdot Y}{X \cdot \lambda}\right)} \right)^2$$

$$P(Y) := D(Y) \cdot I(Y)$$

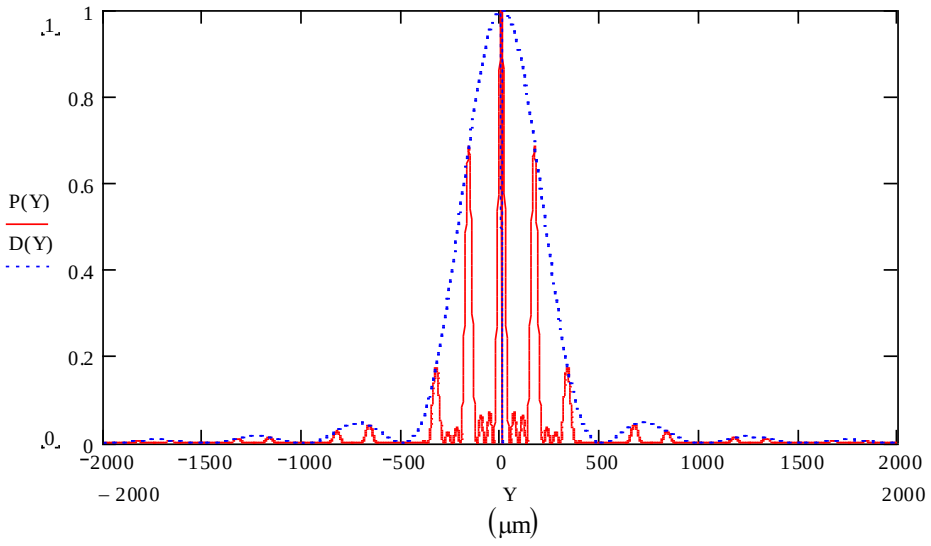

Fig. 3.8: MathCAD simulation of diffraction by four slits using closed form expressions for intensity. The resulting intensity profile is shown in red.

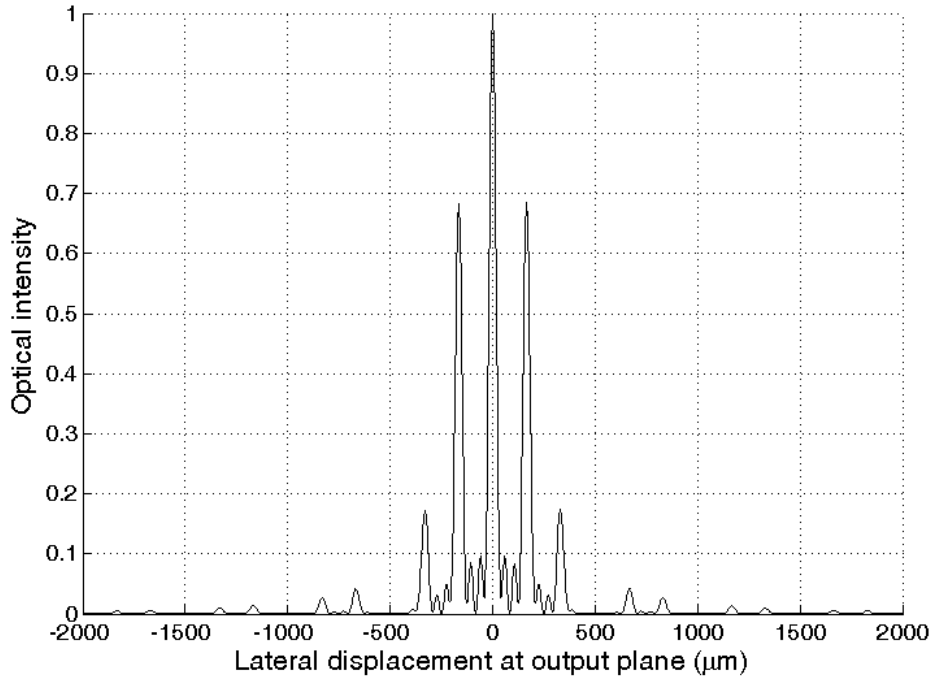

Fig. 3.9: Fresnel integral simulation (see App. I), of the far-field diffraction intensity by four slits. Note the location of minima and maxima is identical in Fig. 3.8 and Fig. 3.9.

3.5 Simulation of a grism

Another test of the Fresnel integral formulation was carried out for a grism in the paraxial regime, and the diffracted field was compared with that obtained analytically (Fig. 3.10 and Fig. 3.11). The calculation of the position of diffracted field for a grism based on geometrical optics is described in the following paragraphs.

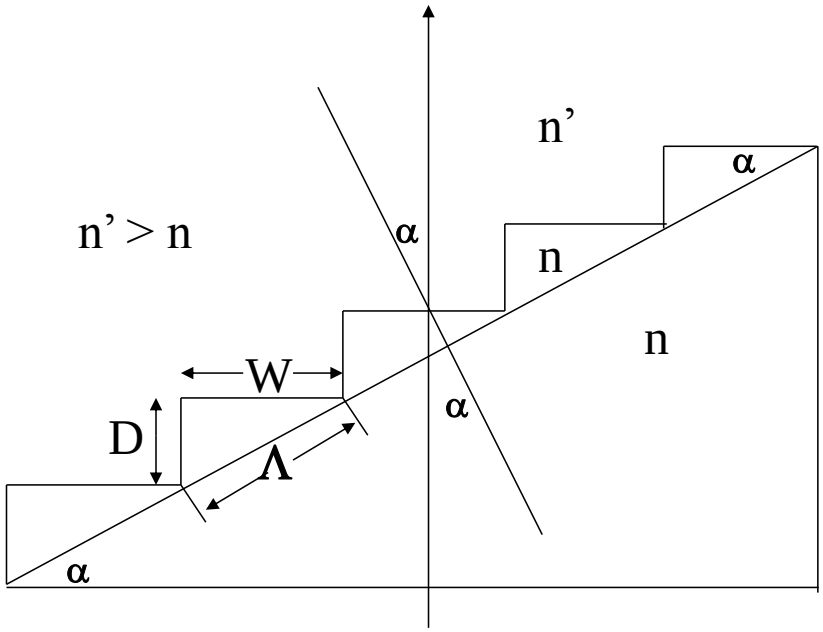

Fig. 3.10: Basic geometry of a grism.

Let W, D, and Λ denote the three sides of the right triangles which form, Echelle grating type steps on the hypotenuse face of a right-angle prism as illustrated in Fig. 3.10. Note that the following three trigonometric relations hold: $\Lambda^2 = W^2 + D^2$, $W = \Lambda \cos \alpha$, and $D = \Lambda \sin \alpha$.

For a straight-through wavelength λ (the design wavelength), the diffraction equation for the grism can be written as:

$$n' \sin \alpha = n \sin \alpha + \frac{m \lambda}{\Lambda} \quad , \qquad (3\text{-}2)$$

which can be rearranged as follows:

$$m = \frac{(n' - n)\, \Lambda \sin \alpha}{\lambda} \quad . \qquad (3\text{-}3)$$

Here, m is the diffraction order, α is the angle of incidence (and also the angle of diffraction for the design wavelength), Λ is the grating period, and n and n’ are the refractive indices before and after the grating, respectively. Note that the analysis and Fig. 3.10 use the convention that the angle of incidence and diffraction are both measured from the normal to the grating plane. It should also be noted that at the design wavelength (the wavelength that goes through the grating without

deflection) the angle of incidence and the angle of diffraction are equal in magnitude and of opposite signs.

Thus the constructive interference condition between adjacent facets is satisfied when:

$$D = \frac{m\,\lambda}{n' - n} \quad . \tag{3-4}$$

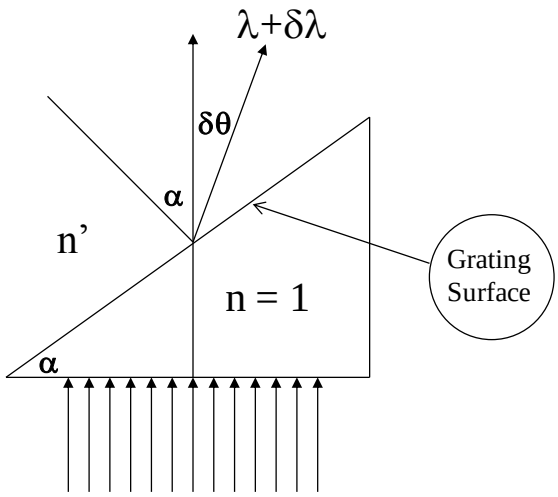

Fig. 3.11: Diffraction in a grism.

For a small change of wavelength, δλ there is a corresponding small change δθ in the angle of diffraction such that:

$$n' \sin(\alpha + \delta\theta) = \sin\alpha + \frac{m(\lambda + \delta\lambda)}{\Lambda} \quad . \tag{3-5}$$

A small angle approximation ($\sin\delta\theta = \delta\theta$ and $\cos\delta\theta = 1$) yields:

$$n' \sin\alpha + n'\,\delta\theta\cos\alpha = \sin\alpha + \frac{m(\lambda + \delta\lambda)}{\Lambda} \quad . \tag{3-6}$$

After some algebra, and using a paraxial approximation, the following equation can be derived.

$$\delta\theta = \frac{m\,\delta\lambda}{n'\,W} \quad . \tag{3-7}$$

This equation allows the wavelength-dependent position of diffracted light to be estimated analytically, and was used to assess the validity of the numerical simulations based on the Fresnel integral. A Fresnel integral simulation of a grating prism was carried out using the parameters shown in Table 3.1. For the simulation, the input field was assumed to have a Gaussian beam profile, with beam diameter of 40 μm. As can be seen in Fig. 3.12, the results perfectly match with those obtained using Eq. (3.7); $\delta\Theta = (2 \times 0.05) / (1.5 \times 3.7216)$, $\tan(\delta\Theta) \times 11163.6 = 200$ μm.

Figure 3.13 shows an enlarged section of the grating facets. The field intensity for different wavelengths on the grating facets is shown in Fig. 3.14. As can be seen in this figure, the shape of the beams on the grating facets is still Gaussian. Figure 3.15 shows the relative output efficiency for different wavelengths. Here the fields have been normalized to unity. Note that the central (design) wavelength has the maximal power. The Matlab file for this simulation is listed in App. I.

File name: mygrating_new_approximation_new_facets_6R_mod.m
Simulation Parameters
NF = 95 (number of facets)
m = 2 (diffraction order)
W = 3.7216 μm (facet width)
n = 1 (refractive index before grating)
n' = 1.5 (refractive index after grating)
beam diameter (1/e^2) = 40 μm
distance (input to grating centre) = 6500 μm
distance(output to grating centre) = 11163.6 μm
output plane span = 800 μm
simulation wavelengths = [0.5 , 0.55 , 0.6 , 0.65 , 0.7] μm

Table 3.1: Simulation parameters used for the grating prism

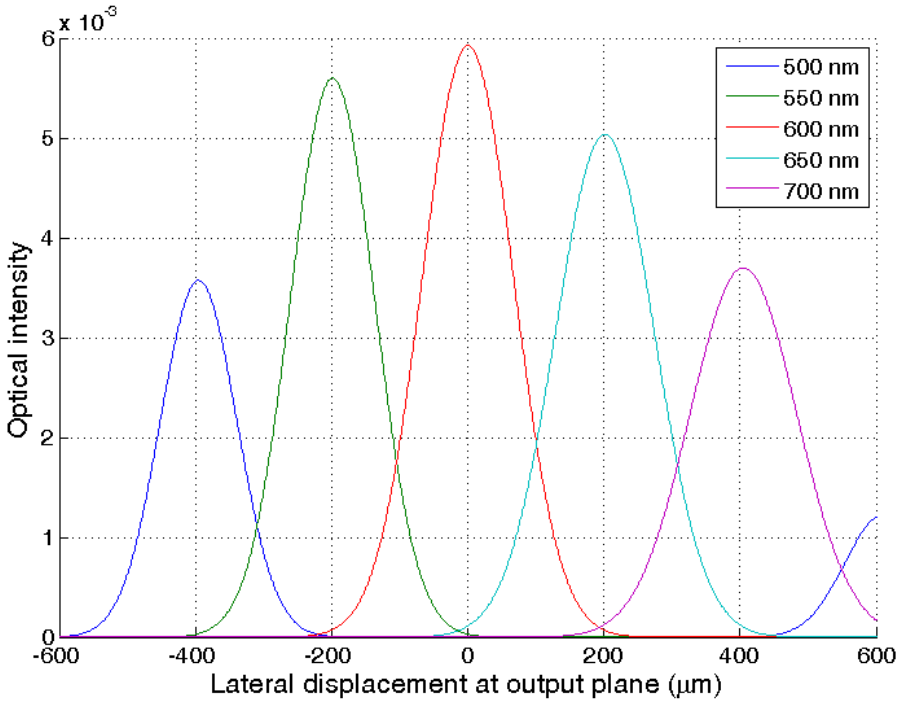

Fig. 3.12: Diffraction of a 40 μm Gaussian beam by the grating prism. The field intensity is plotted versus lateral displacement at the output plane.

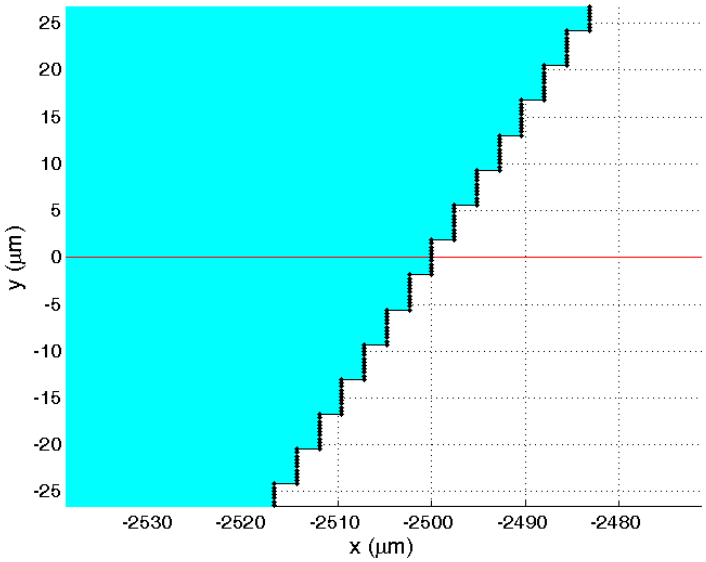

Fig. 3.13: A portion of the facets of the grism, as defined in the Matlab simulation.

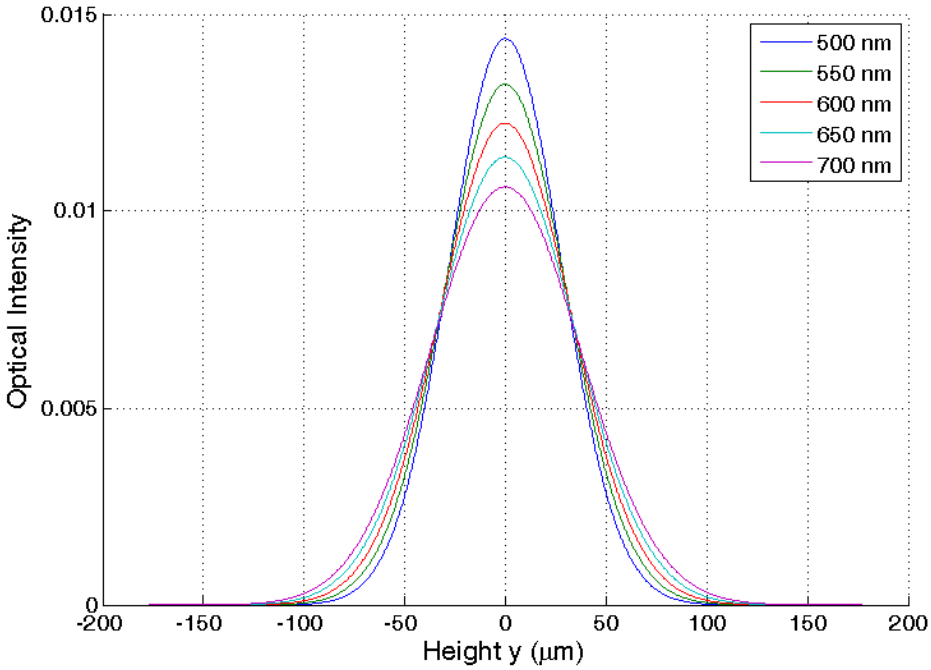

Fig. 3.14: Field intensity of different wavelengths on grating facets.

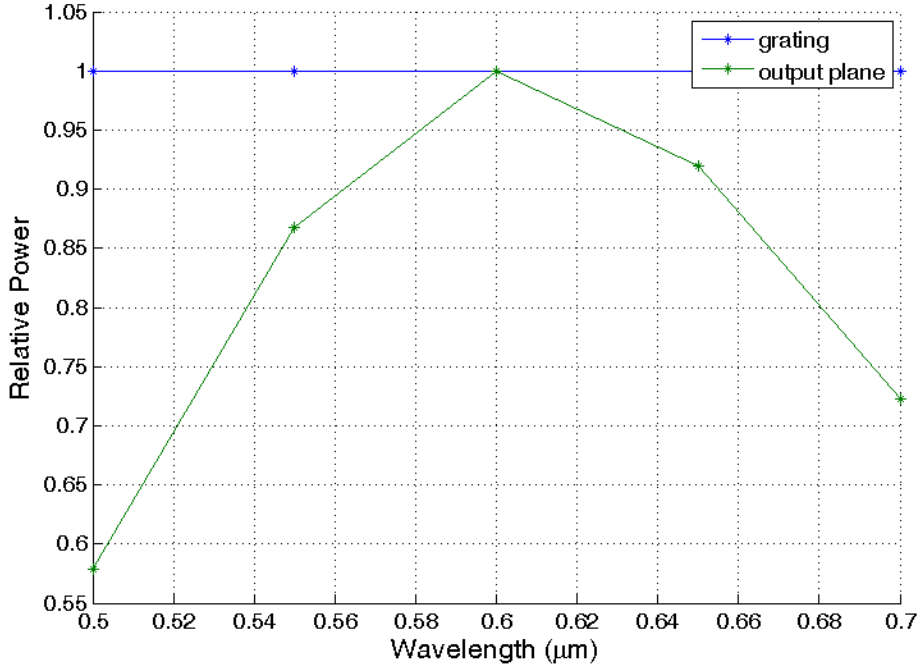

Fig. 3.15: Relative output efficiency for different wavelengths, for the grating prism, defined by the parameters in Table 3.1.

In the next simulation, we kept all the parameters as given in Table 3.1, except we doubled the number of facets, thus the widths of the facets are reduced by a factor of two i.e. from 3.7126 μm to 1.8608 μm. The simulation results are shown in Fig. 3.16, and verify that the resolution of the grating (i.e. the spatial dispersion) is doubled for the case of smaller grating facets.

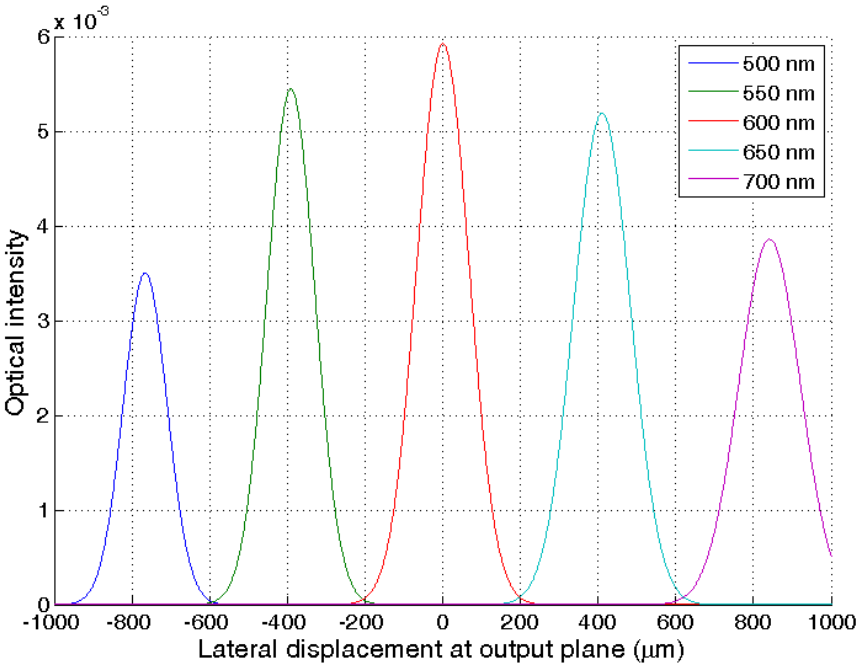

Fig. 3.16: Diffraction of a 40 μm Gaussian beam by a grating prism, where the facet size has been reduced by a factor of two compared to a grating defined in Table 3.1.

Next, consider the spectrometer system depicted in Fig. 3-17.

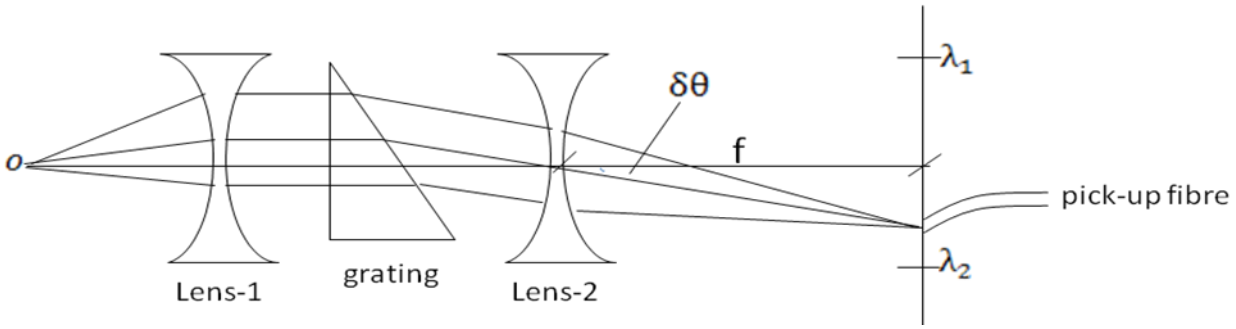

Fig. 3.17: Schematic representation of a general spectrometer system

Assume that λ_1 and λ_2 define the limits of the spectral range of interest. For example, if λ_1 = 600 nm and λ_2 = 800 nm, then $\delta\lambda$ = 200 nm is the spectral range considered. In this system the input signal gets collimated by lens-1, then the grating diffracts the signal, and finally lens-2 focuses the deflected signal at the output plane where a pick-up fiber directs the signal to a PMT. As an illustration, assume that the goal is to capture 10 nm wavelength channel in one pick-up fibre. Thus, for 200 nm total bandwidth there are 20 channels that must be dispersed over a distance that is equal to 20 times the fibre diameter. If the diameter of a fibre is 65 μm then 65 x 20 = 1300 μm or 1.3 mm is the spatial extent of the output. If we denote this length (1.3 mm) by L, the total angle of deflection by $\delta\theta$, and the focal length of the focusing lens by f, then we have:

$$L = f\ \delta\theta\ . \tag{3-8}$$

We also previously found

$$\delta\theta = \frac{m\,\delta\lambda}{n'\,W}\ , \tag{3-9}$$

so that

$$L = f\ \frac{m\,\delta\lambda}{n'\,W}\ , \tag{3-10}$$

or

$$W = \frac{f\ m\,\delta\lambda}{n'\,L}\ . \tag{3-11}$$

For a hypothetical spectrometer made in PDMS (refractive index of 1.43), a focusing lens with focal length equal to 10 mm, and operation in the 2nd diffraction order, the required facet width is

$$W = \frac{10\,\text{mm} \times 2 \times 0.2\,\mu\text{m}}{1.43 \times 1.3\,\text{mm}} = 2.15\,\mu\text{m}\ .$$

A spectrometer system with the above given parameters can achieve the intended spatial dispersion of approximately 10 nm / 65 μm.

3.5.1 Position of diffracted orders in grating prisms

Consider the basic geometry at the hypotenuse face of a grating prism (Fig. 3-18). Typically, the depth of the steps (D) is defined such that, for a specific diffraction

order (the design order) and design wavelength (λ_c), the incident beams which are perpendicular to grating facets continue along the same direction upon diffraction. This property provides in-line viewing for one wavelength and is useful in certain applications such as direct vision spectroscopy [67].

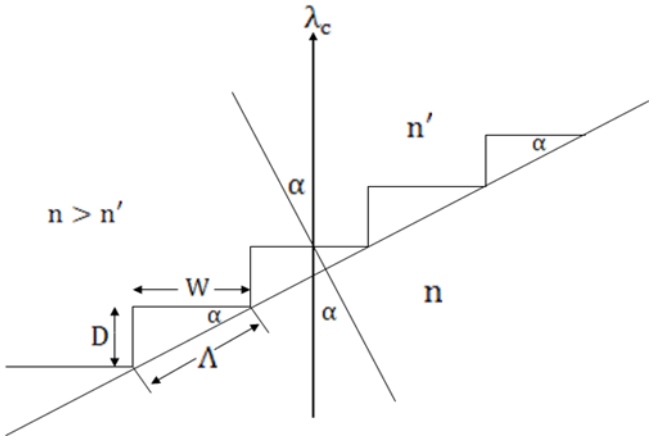

Fig. 3.18: The geometry at the hypotenuse face of a grism. The arrow shows the direction of the incident beam, and of the diffracted beam at the design wavelength.

Table 3.2 shows the parameters of simulation relevant to this discussion:

Simulation Parameters
NF = 95 (number of facets)
m = -2 (diffraction order)
W = 3.7216 μm (facet width)
n = 1.5 (refractive index before grating)
n' = 1 (refractive index after grating)
beam diameter (1/e^2) = 100 μm
distance (input to grating centre) = 5750 μm
distance(output to grating centre) = 1500 μm
output plane span = 2000 μm
simulation wavelength = [0.6] μm

Table 3.2: Simulation parameters used to determine the position of orders in a grating prism.

Note that for the grating simulated, a refractive index of 1.5 and 1 was assumed for the incident and exit sides of the grating, respectively. From Eq. (3-4) we calculate D = 2.4 μm and using right triangle trigonometric relations it follows that Λ = 4.428 μm and α = 32.817 degrees.

Now we write the grating equation [65]:

$$m\lambda = \Lambda\,(\mathrm{n}'\sin\beta - \mathrm{n}\sin\alpha)\,. \qquad (3\text{-}12)$$

With n' = 1, it follows that:

$$\frac{m\lambda}{\Lambda} + \mathrm{n}\sin\alpha = \sin\beta\,. \qquad (3\text{-}13)$$

Substituting the values from above into this equation and assuming the negative second order (m = -2), gives β = 32.817 degrees. This confirms that α and β at the design wavelength are equal in magnitude. The angle of deflection in the -2nd order is $\delta\theta_2 = \alpha - \beta = 0$, meaning that the -2nd order goes straight through the grating without deflection as expected.

For the -1st order, Eq. (3-13) gives β = 42.6 degrees and thus $\delta\theta_1 = \alpha - \beta = -9.8$ degrees. The position of the -1st order diffracted wave at the output plane is then given by x = tan(-9.8) .1500 (μm) = -259.8 (μm).

This result is very close to that obtained by simulation (-260.5 μm), as shown below in Fig. 3.20.

Next consider the position of the zero order, which can be calculated using Snell's law:

$$\mathrm{n}\sin\alpha = \sin\beta \quad , \qquad (3\text{-}14)$$

and results in β = 54.38 degrees and $\delta\theta_0 = \alpha - \beta = -21.567$ degrees. Thus the predicted position of the zero order diffracted wave at the output plane is given by x = tan(-21.587) .1500 = -592.89 (μm). This result also matches well with that obtained by simulation (-592 μm), as shown below in Fig. 3-20. As shown in Fig. 3-19, the numerical simulation predicts that almost all of the energy appears in the design order (m = -2). Figures 3-20 shows the output field intensities in logarithmic scale, to facilitate a better comparison. There are four other peaks to the right of zero that belong to -3, -4, -5 and -6 orders, but, because the intensities at these orders are weak, they don't show up in Fig. 3-19.

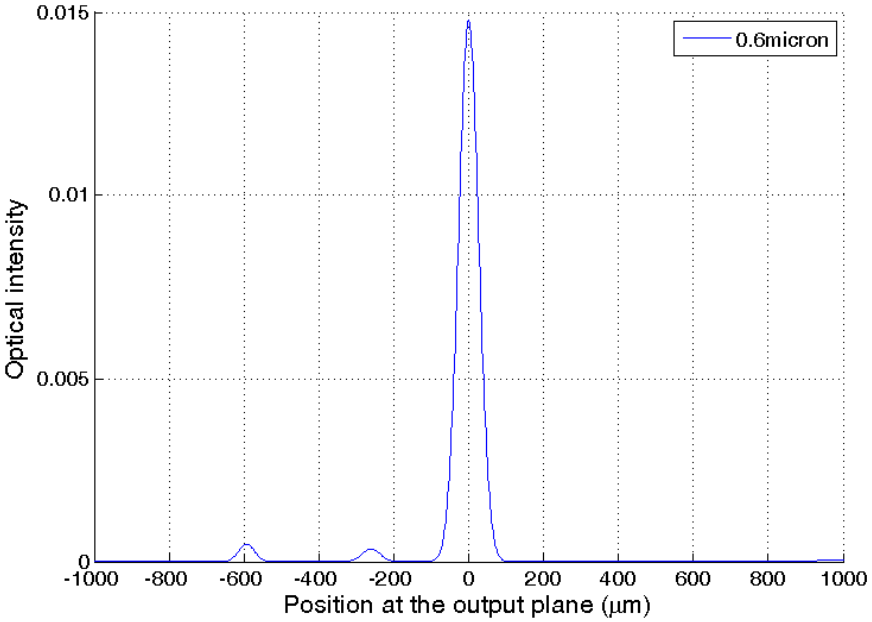

Fig. 3.19: Intensity versus position at the output plane, as predicted by numerical simulation of a grating prism. The peaks correspond to the zero, -1 and -2 diffracted orders as explained in the text.

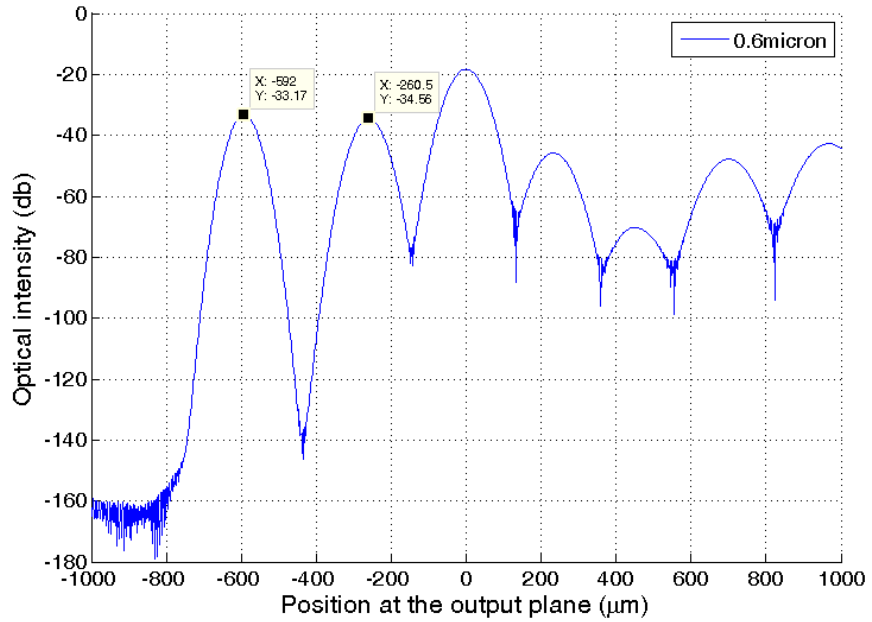

Fig. 3.20: As in Fig. 3.19, but with a logarithmic scale for clarity. The zero order is marked at -592 μm and -1st order is marked at -260.5 μm.

As demonstrated by this example, the numerical simulation based on the Fresnel diffraction integral produces results that are in good agreement with analytical

predictions for a simple grating. Further examples are provided in the following sections.

3.6 Simulation of a binary phase grating

A binary phase grating is perhaps the most basic form of grating. It is often used as a beamsplitter in laser systems. We developed a simulation program for a 1 x 2 beamsplitter to demonstrate this functionality. The beamsplitter system considered is composed of a parabolic lens for collimation and a binary phase grating for diffraction. The lens is located at a distance of 100 μm before the grating. The facets of the grating are approximately one wavelength (i.e. 0.6 μm) deep, as shown in Fig. 3-21. Other parameters of the simulation are listed in Table 3.3.

File name: binary_grating.m
Simulation Parameters
NF = 95 (number of facets)
Fw = 5.2632 μm (facet width)
n = 1 (refractive index before grating)
n' = 1.5 (refractive index after grating)
beam diameter (1/e^2) = 200 μm
distance (input to grating centre) = 2500 μm
distance(output to grating centre) = 10,000 μm
output plane span = 1600 μm
simulation wavelengths = [0.5 , 0.55 , 0.6 , 0.65 , 0.7] μm

Table 3.3: Parameters for simulation of a binary phase grating

Figure 3-22 shows the simulation results, confirming that the output energy gets divided equally between -1 and +1 orders while only a small portion of the total energy appears in the zero order (the peaks in the middle). It is worth mentioning that for the design wavelength (0.6 μm), the numerical simulation of the idealized

grating predicts that the energy is divided equally between -1 and +1 orders (Fig. 3-23).

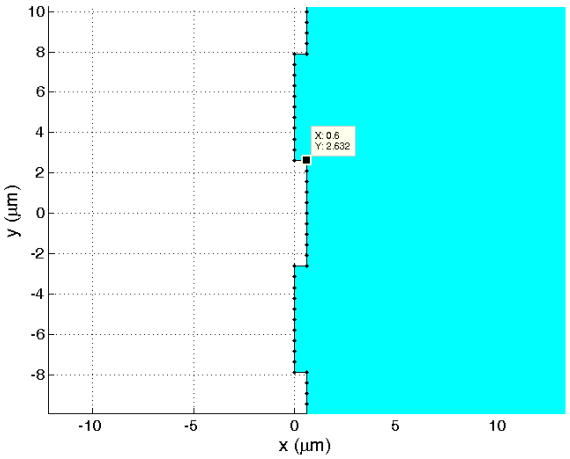

Fig. 3.21: A zoomed in section of the binary grating showing three facets

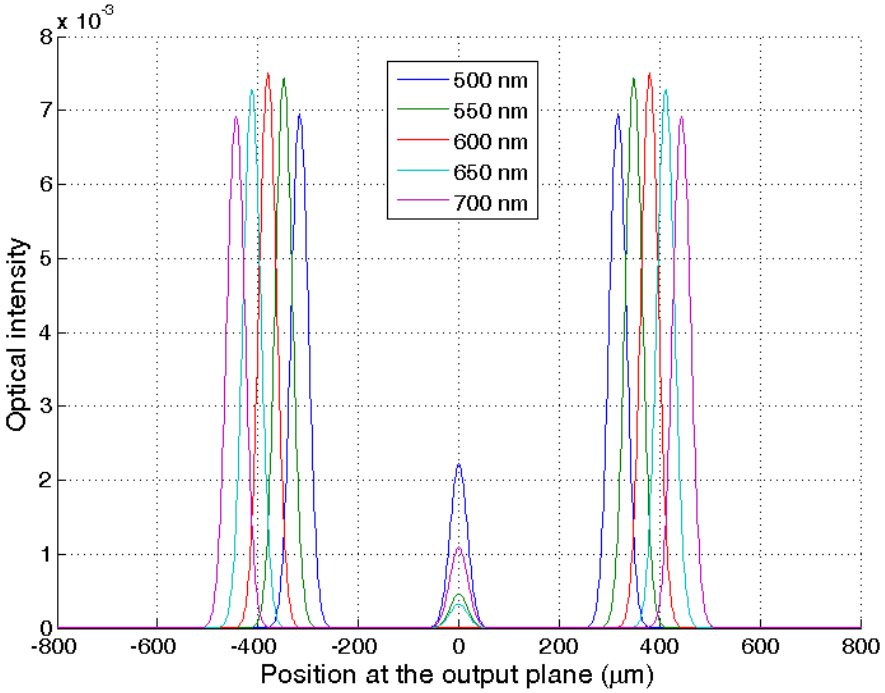

Fig. 3.22: Output of a binary phase grating showing -1, 0, and +1 diffracted orders.

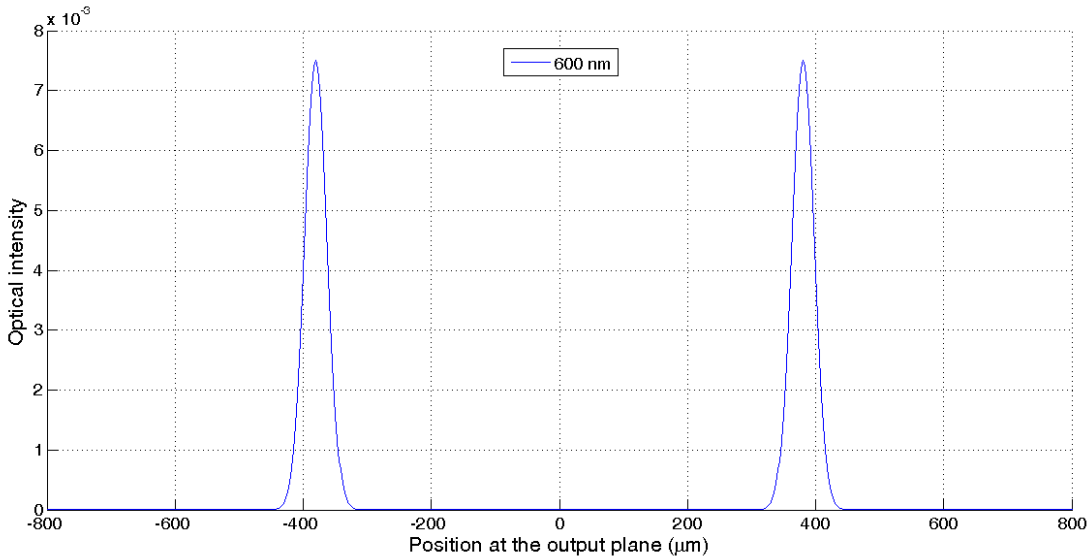

Fig. 3.23: Output field intensities of a binary phase grating functioning as a 1 x 2 beamsplitter.

We also made a variation of this code that allows tilting of the grating with respect to the input field, for situations where the incident beam is illuminating the grating facets at an angle (the incidence angle can be chosen). Figure 3-24 shows a section of a binary grating with a 10 degrees angular tilt in the positive direction.

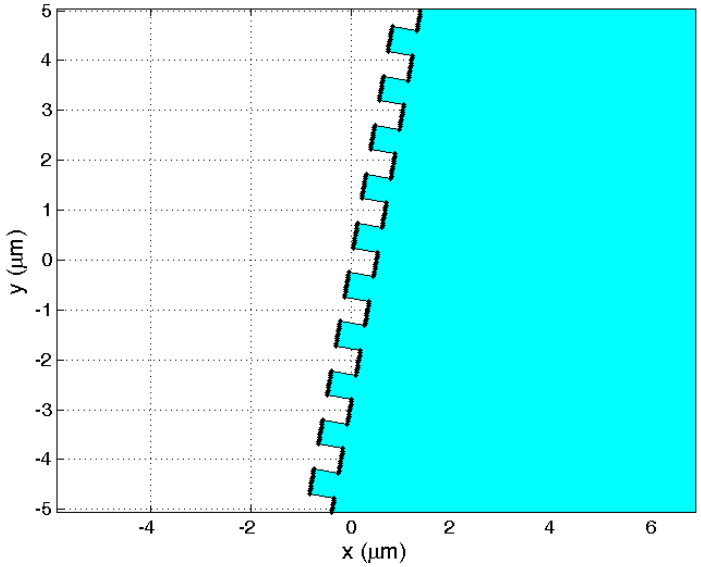

Fig. 3.24: Orientation of the facets in a tilted binary phase grating.

Matlab codes, binary_grating.m and binary_grating_10deg_tilt.m are listed in App. I.

3.7 Simulation of a blazed triangular-groove transmission grating

Triangular groove (saw-tooth) transmission gratings are frequently used in spectrometry.

Figure 3-25 shows the typical geometry of this type of grating. In this configuration the incident light is normal to the back surface of the grating (α = 0), so the grating equation reduces to:

$$m\lambda = \Lambda \sin\beta \tag{3-15}$$

Here m is the diffraction order (usually |m| = 2), λ is the wavelength, Λ is the groove spacing and β is the angle of diffraction.

Blazing for this type of grating occurs when the refraction of the incident beam at a mini prism that constitutes a grating groove coincides with the diffraction of the beam given by the grating equation. That is, in addition to the grating equation, the following Snell's law equation needs to be satisfied:

$$\mathrm{n}\sin x = \sin(x+\beta)\,. \tag{3-16}$$

Combining equations (3-15) and (3-16) sets the condition for blazing as:

$$\tan(x) = \frac{\sin\beta_{\mathrm{B}}}{\mathrm{n} - \cos\beta_{\mathrm{B}}}\ , \tag{3-17}$$

where β_{B} is the blaze angle.

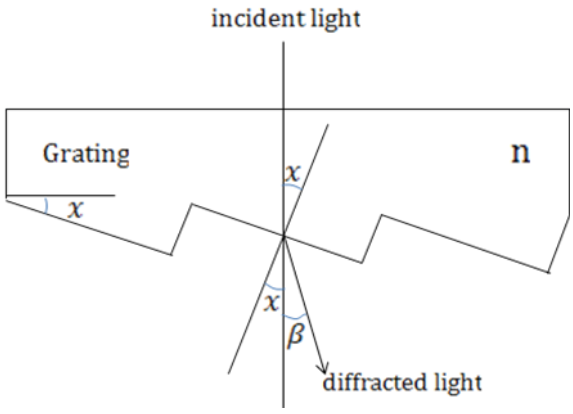

Fig. 3.25: Triangular-groove transmission grating.

Since our simulations are based on gratings formed in slab waveguides, we need to make some modifications to these equations. Consider the case shown in Fig. 3-26, where the incident light originates in air ($n_1 = 1$) and enters into a medium of higher refractive index n_2.

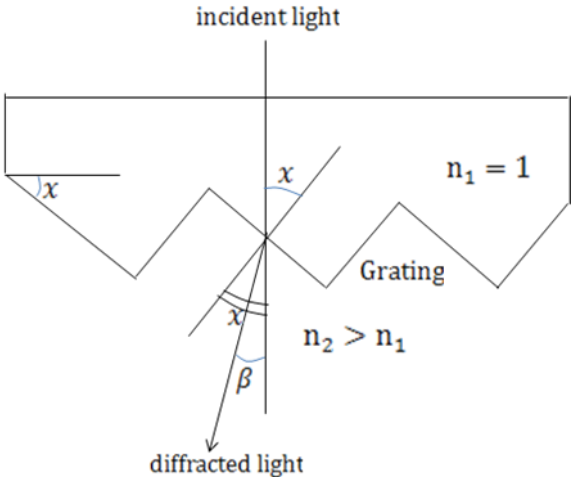

Fig. 3.26: Triangular-groove transmission grating with $n_2 > n_1$.

The grating equation for this configuration is:

$$m\lambda = \Lambda\, n_2 \sin\beta\,, \tag{3-18}$$

and the Snell's law equation is:

$$\sin x = n_2 \sin(x-\beta)\,. \tag{3-19}$$

Thus, the condition for blazing is as follows:

$$\tan(x) = \frac{-n_2 \sin\beta_B}{1 - n_2 \cos\beta_B}\,. \tag{3-20}$$

Using Eq. (3-18) and a small angle approximation, we can obtain an equation for the linear separation between diffracted wavelengths at the output plane of the spectrometer system.

If the design wavelength λ is increased by $\delta\lambda$, the angle of diffraction β will correspondingly increase by $\delta\theta$, so that:

$$m(\lambda+\delta\lambda) = \Lambda\, n_2 \sin(\beta+\delta\theta)\,. \tag{3-21}$$

In the small angle approximation, $\cos\delta\theta = 1$ and $\sin\delta\theta = \delta\theta$. Therefore:

$$m\lambda + m\,\delta\lambda = \Lambda\, n_2 \sin\beta + \Lambda\, n_2 \cos\beta\,\delta\theta\,, \tag{3-22}$$

$$m\,\delta\lambda = \Lambda\, n_2 \cos\beta\,\delta\theta\,, \tag{3-23}$$

and

$$\delta\theta = \frac{m\,\delta\lambda}{\Lambda\, n_2 \cos\beta}\ . \tag{3-24}$$

If we represent the linear separation between two wavelengths at the output plane by δL and the distance from grating to output plane by D, using the small angle approximation we have:

$$\tan(\delta\theta) = \delta\theta = \frac{\delta L}{D}\,, \tag{3-25}$$

$$\delta L = \frac{m\ \delta\lambda\ D}{\Lambda\, n_2 \cos\beta}\ . \tag{3-26}$$

Next consider an example simulation of a grating of this type. The simulation parameters are listed in Table 3.4.

File name: my_blazed_grating.m
Simulation Parameters
NF = 95 (number of facets)
Grating period (Λ) = 2 μm
m = 1 (diffraction order)
n = 1 (refractive index before grating)
n' = 1.5 (refractive index after grating)
Input Gaussian beam diameter (1/e^2) = 40 μm
distance (input to grating centre) = 1,250 μm
distance(output to grating centre) = 5,500 μm
output plane span = 3000 μm
simulation wavelengths = [0.306 , 0.356 , 0.406 , 0.456 , 0.506] μm

Table 3.4: Simulation parameters for a blazed triangular-groove grating in the first order

The output from this simulation is shown in Fig. 3.27 and Fig. 3.28. As can be seen in these figures, the output energy is primarily concentrated in the intended order (+1 order).

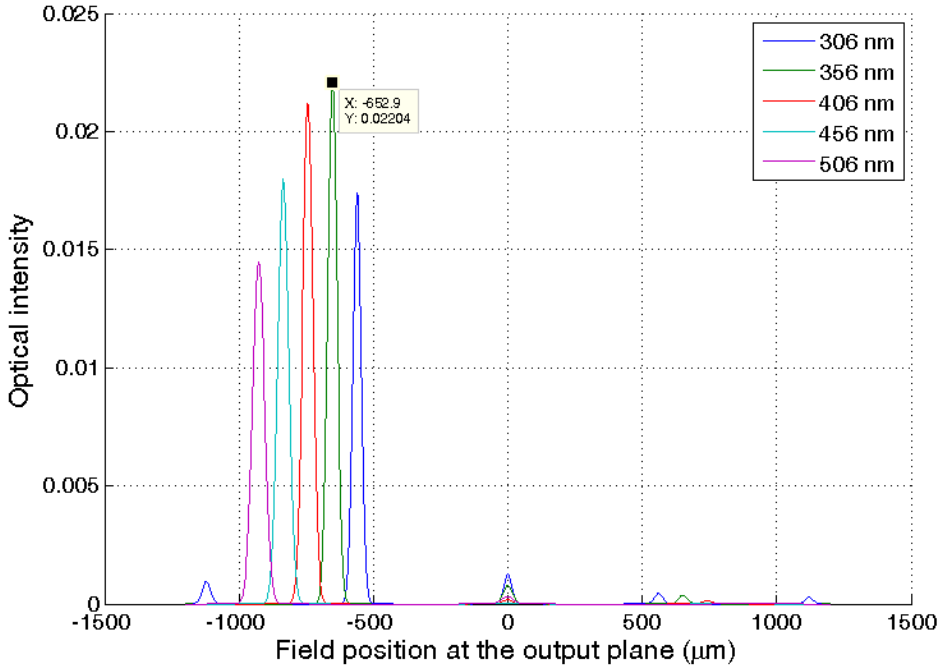

Fig. 3.27: Simulation output for a triangular-groove transmission grating. The position of two neighboring wavelengths is being marked for comparison with geometrical calculations.

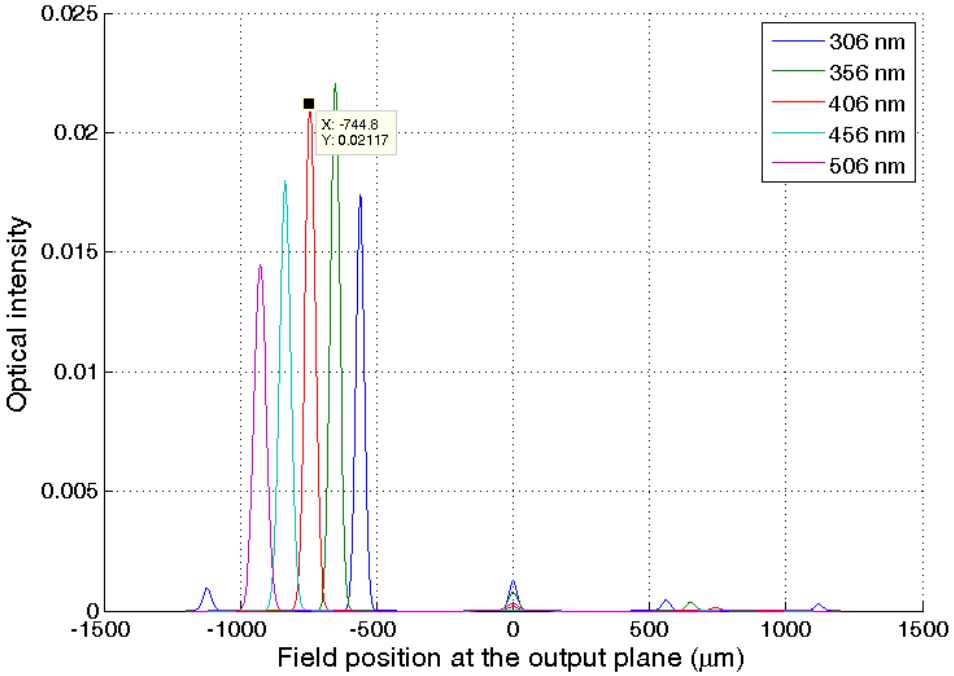

Fig. 3.28: Simulation output for a triangular-groove transmission grating. The position of two neighboring wavelengths is being marked for comparison with geometrical calculations.

From the grating equation:

$$m\lambda = \Lambda\, n_2 \sin\beta\,, \qquad (3\text{-}27)$$

The angle of diffraction β can be calculated and is given by $\beta = 7.778$ degrees. The two wavelengths marked in Figs. 3.27 and 3.28 are separated by 0.05 μm. We can calculate their linear separation δL at the output plane from Eq. (3-26), which results in $\delta L = 92.5$ μm.

According to the output of the simulation (Figs. 3.27 and 3.28), $\delta L = 91.9$ μm. The difference of 0.6 μm can be attributed to the fact that the geometrical calculations are based on small angle approximations.

3.7.1 Position of diffracted orders in triangular-groove gratings

We used the parameters listed in Table 3.5 to simulate the diffraction of a Gaussian beam at a specific wavelength by a triangular-groove transmission grating.

File name: my_blazed_grating_orders.m
Simulation Parameters
NF = 195 (number of facets)
Fw = 7.3923 μm (facet width)
m = 2 (diffraction order)
n = 1 (refractive index before grating)
n' = 1.43 (refractive index after grating)
Input Gaussian beam diameter (1/e^2) = 40 μm
distance (input to grating centre) = 1,250 μm
distance(output to grating centre) = 1,500 μm
output plane span = 800 μm
simulation wavelength = [0.533] μm

Table 3.5: Simulation parameters for determination of the position of orders in a sawtooth grating

The position of diffracted orders in a triangular-groove grating can also be obtained using the grating equation, Eq. (3-27). For the first order, m = 1 and

λ = 0.533 μm, the angle of diffraction is easily calculated as: β = 2.89 degrees. The lateral displacement at the output plane can be estimated as: $\delta L = \tan \beta \times D = \tan(2.89^{o}) .1500\ (\mu m) = 75.7\ (\mu m)$. Similarly, in the second order (m = 2), we have β = 5.79 degrees and δL = 152 μm. For the third order (m = 3) we have β = 8.7 degrees and δL = 229.5 μm.

From the graph of Fig. 3.29, the numerically predicted values of δL for the 1st, 2nd, and 3rd order diffractions are 75.86 μm , 151.7 μm, and 229.1 μm respectively, once again verifying the accuracy of the numerical simulations based on Fresnel diffraction integral. The simulation codes, my_blazed_grating.m and my_blazed_grating_orders.m are listed in App. I.

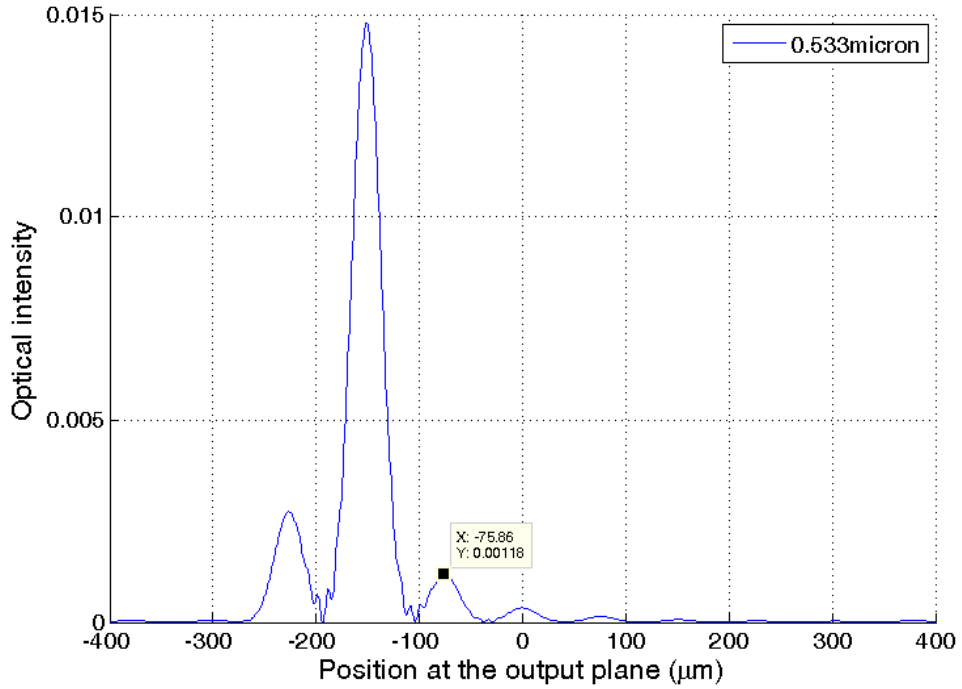

Fig. 3.29: Position of diffracted orders in a sawtooth transmission grating.

3.8 Simulation of a complete spectrometer system

Next, we describe results for the propagation of a Gaussian beam through a collimating lens, a diffraction grating and a focusing lens (i.e. a complete spectrometer system) using the Fresnel diffraction integral approximation. As shown in Fig. 3.30, the input field (located at the light blue rectangle) encounters a number of interfaces before it reaches the output plane (the dark blue rectangle).

From left to right, these interfaces are the collimating lens, the lens boundary, the grating boundary, the grating facets, and the focusing lens. Figure 3-31 shows the output of the system. Spectrometer.m is the Matlab routine for this system (see App. I). The Matlab program became very slow as the number of interfaces and the number of facets got larger so we found it necessary to rewrite this program in FORTRAN.

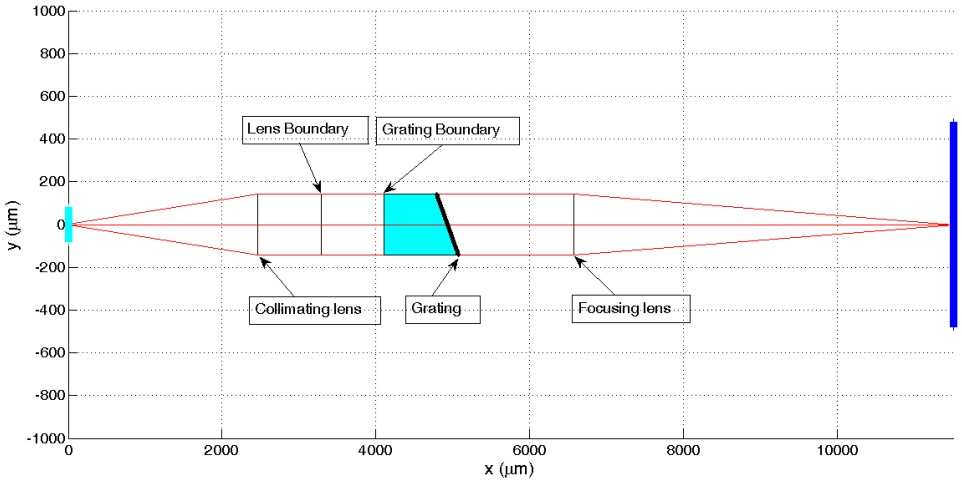

Fig. 3.30: Device layout of a complete spectrometer system

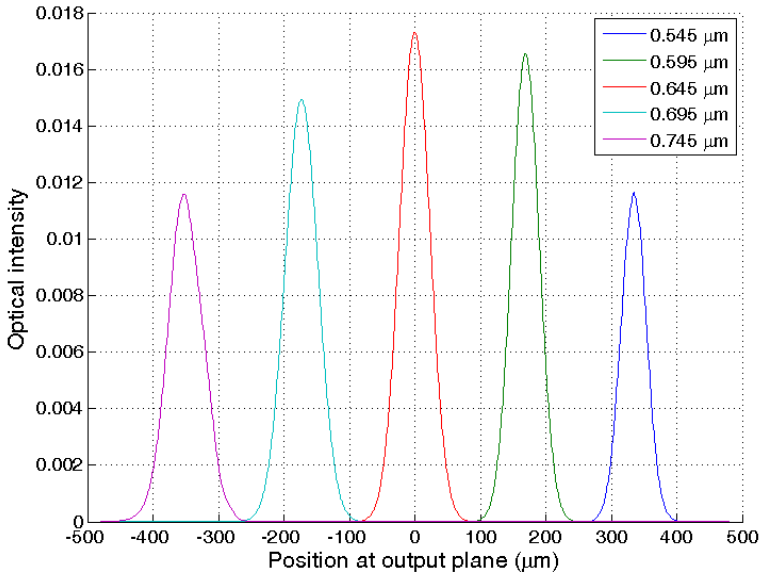

Fig. 3.31: Diffracted fields of the complete spectrometer system shown in Fig.3.30.

Based on the analysis above, we designed a microspectrometer system in which collimation and focusing elements are parabolic waveguide bi-convex lenses. In this design a parallel architecture is used to incorporate two microspectrometer systems side by side. In each system there are two waveguides, one along the spectrometer's optical axis and the other coming from the side of the chip. These waveguides provide alternative routes for the illumination of the microfluidic channel in the u-section intended for optical interrogation. As fluorescing particles pass through this section of the microfluidic channel (i.e. the interrogation region) they can get excited by the laser light carried by the waveguides coming to this section of the microfluidic channel. To prevent the excitation light from entering the detector, the orientation of the side waveguides is at 90 degree angle to that of the triangular shaped output waveguides located horizontally at the specified points along the output plane (right edge of the chip).

The schematic layout of this system is shown in Fig. 3.32. This layout was used to design a mask and to fabricate chips. However, the optical experiments with grating were not successful. This was attributed to fabrication imperfections, and to the fact that, in this design, the excitation light originating from the input waveguide must traverse five interfaces before landing on the grating wall. Based on a simple analysis, a slightly tilted side-wall would cause the light to miss the grating completely.

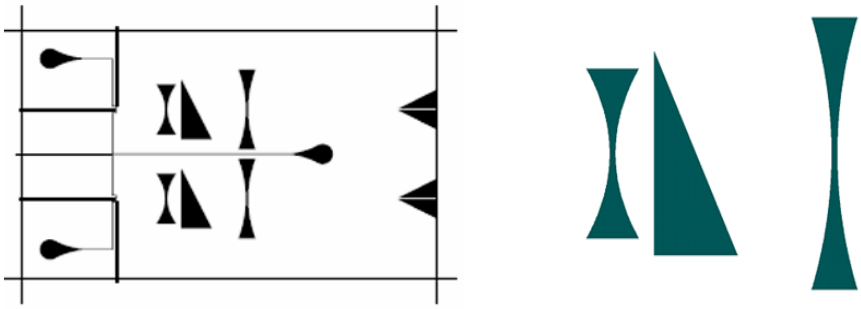

Fig. 3.32: Actual drawing of our first spectrometer chip (left). An enlarged section of the chip showing the two parabolic lenses and the grating in the middle (right).

We also discovered that we could not use our simulation program to analyze this design, because the two parabolic surfaces making up the lenses were in close

proximity of each other. This violated the condition for the validity of the Fresnel diffraction integral, as discussed further below. We specifically found that, with this configuration, for the Fresnel diffraction integral simulations to produce meaningful results, a minimum separation of ~ 1000 μm between two consecutive interfaces was needed. Our solution to this problem was to use other more rigorous diffraction models such as the scalar Kirchhoff or Rayleigh-Sommerfeld approximations [71], as discussed below.

3.9 Region of applicability of different diffraction models

The most rigorous treatment of the diffraction problem is to solve the vector wave equations derived directly from Maxwell's equations. However, this is truly a monumental task, especially when the geometry of the diffractive object is complex.

All other diffraction models belong to the scalar domain, where it is necessary to assume that the diffractive element is large in comparison to the wavelength, and the observation plane is not close to the diffractive element. In the category of scalar equations, there are four different approximations: Kirchhoff, Rayleigh-Sommerfeld, Fresnel (near-field), and Fraunhoffer (far-field). The range of applicability of Kirchhoff and Rayleigh-Sommerfeld approximations extends to all values of z (the distance from the aperture to observation plane), provided the basic assumptions of the scalar model stated above are met. Fresnel and Fraunhoffer approximations each have specific ranges of applicability, which we will discuss with the help of examples.

First, consider a 10 μm x 10 μm rectangular aperture, a 100 μm x 100 μm observation plane, and a monochromatic input field of $\lambda = 500$ nm. The Fresnel approximation is valid when the value of z is such that [62]:

$$z \gg \sqrt[3]{\frac{\pi}{4\lambda}\left[(x-\xi)^2+(y-\eta)^2\right]_{\max}^2}\,. \qquad (3\text{-}28)$$

Here z is the optical propagation distance, (ξ, η) represent the aperture size, and (x, y) represent the observation plane size. For the values mentioned above, the condition becomes

z >> 972.56 μm.

Next, consider a strictly paraxial case in which a 10 μm x 10 μm rectangular aperture is viewed at a 10 μm x 10 μm observation plane using monochromatic light with $\lambda = 500$ nm. Substituting these values into Eq. (3-28) yields z >> 100 μm.

The Fraunhoffer, or far-field approximation, is valid when:

$$z \gg \frac{k(\xi^2 + \eta^2)_{\max}}{2}. \qquad (3\text{-}29)$$

As above, z is the optical propagation distance, and (ξ, η) represent the aperture size, while $k = \frac{2\pi}{\lambda}$.

For the examples given above, the minimum distance between the aperture and the observation plane (i.e. the beginning of the Fraunhoffer range) would be z >> 1256.6 μm.

It is also worth mentioning that for an aperture that is 1 cm x 1 cm, z >> 1256 meters is the condition for validity of the Fraunhoffer approximation.

3.10 Kirchhoff and Rayleigh-Sommerfeld diffraction integrals

In solving a planar, scalar diffraction problem, there are three relatively accurate methods available: Kirchhoff, Rayleigh-Sommerfeld I and Rayleigh-Sommerfeld II. These methods are closely related and their differences result from different assumptions regarding the boundary conditions. As outlined by M. Totzeck, the two-dimensional Kirchhoff and Rayleigh-Sommerfeld I and II diffraction integrals can be written in terms of the Hankel function [71]. Consider the problem of finding simplified solutions for the two-dimensional diffraction of a monochromatic, cylindrical wave by a slit. The slit width is 2b and it is made in an opaque, completely absorbing and perfectly conducting screen (Fig. 3-33).

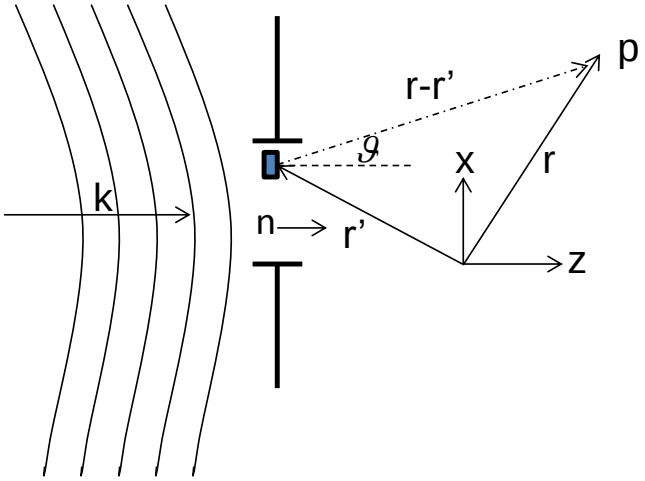

Fig. 3.33: Two dimensional diffraction of an incident cylindrical wave by a slit aperture [71]

According to the Kirchhoff and the Rayleigh-Sommerfeld theories, the field at any point beyond the aperture screen is due to the field and/or its derivative on the planar screen. In the Kirchhoff method, the assumption is that the field and its normal derivative are known everywhere on the screen. On the other hand, for the Rayleigh-Sommerfeld theory, the boundary condition is either on the field (Rayleigh-Sommerfeld I) or on the normal derivative of the field (Rayleigh-Sommerfeld II).

The following treatment is based on the expressions in reference [72].

The diffraction integral for the Rayleigh-Sommerfeld I, where U_0 is the boundary value, is given by:

$$U_{\mathrm{I}}(r) = \frac{1}{2\pi} \int_{-\infty}^{\infty} \int_{-b}^{b} U_0(r') \frac{\partial}{\partial \mathbf{n}} \left[\frac{\exp(ik|r-r'|)}{|r-r'|} \right] \mathrm{d}x' \, \mathrm{d}y' . \qquad (3\text{-}30)$$

The diffraction integral for the Rayleigh-Sommerfeld II, where $\frac{\partial U_0}{\partial \mathbf{n}}$ is the boundary value, is given by:

$$U_{\mathrm{II}}(r) = -\frac{1}{2\pi} \int_{-\infty}^{\infty} \int_{-b}^{b} \frac{\partial}{\partial \mathbf{n}} \left[U_0(r') \right] \frac{\exp(ik|r-r'|)}{|r-r'|} \mathrm{d}x' \, \mathrm{d}y' . \qquad (3\text{-}31)$$

For the Kirchhoff method, where both U_0 and $\frac{\partial U_0}{\partial \mathbf{n}}$ are boundary values, the diffraction integral is given by:

$$U_k(r) = 1/2\left[U_{\mathrm{I}}(r) + U_{\mathrm{II}}(r)\right]. \tag{3-32}$$

The three-dimensional diffraction integrals can be converted to two-dimensional diffraction integrals using the following transformation [71]:

$$\int_{-\infty}^{\infty} \frac{\exp(ik|r-r'|)}{|r-r'|}\,\mathrm{d}\,y' = i\pi H_0(k|\rho-\rho'|). \tag{3-33}$$

Here, ρ = (x, 0, z) and H_0 the zeroth-order Hankel function of the first kind. Substituting Eq. (3-33) into the diffraction integrals above, we find that for the Rayleigh-Sommerfeld I case:

$$U_{\mathrm{I}}(\rho) = \frac{i}{2}\int_{-b}^{b} U_0(\rho')\frac{\partial}{\partial \mathbf{n}} H_0(k|\rho-\rho'|)\,\mathrm{d}\,x', \tag{3-34}$$

whereas for the Rayleigh-Sommerfeld II case:

$$U_{\mathrm{II}}(\rho) = -\frac{i}{2}\int_{-b}^{b} H_0(k|\rho-\rho'|)\frac{\partial}{\partial \mathbf{n}} U_0(\rho')\,\mathrm{d}\,x'. \tag{3-35}$$

For the Kirchhoff integral, we take the mean value of U_{I} and U_{II}, as specified in Eq. (3-32).

In order to calculate the normal derivative of U_0, we can assume that U_0 is a plane wave with a constant magnitude A_0 and a propagation angle ξ, such that:

$$U_0(x,z) = A_0\exp(ik\cdot\rho) = A_0\exp\left[ik(x\sin\xi + z\cos\xi\right]. \tag{3-36}$$

Taking the normal derivative of Eq. (3-36), we have:

$$\frac{\partial U_0}{\partial \mathbf{n}} = \frac{\partial U_0}{\partial z} = ik\cdot U_0\cdot\cos(\xi). \tag{3-37}$$

The propagation angle ξ, between **n** and the plane wave's propagation vector K, can be found from:

$$\xi = \arcsin\left[\frac{\partial(\arg U_0)}{k\partial x}\right]. \tag{3-38}$$

The normal derivative of the Hankel function H_0 can be found as:

$$\begin{aligned}\frac{\partial}{\partial \mathbf{n}} H_0(k|\rho-\rho'|) &= -k\frac{\partial H_0(k|\rho-\rho'|)}{\partial k|\rho-\rho'|}\frac{(\rho-\rho')}{|\rho-\rho'|}\cdot\mathbf{n} \\ &= kH_1(k|\rho-\rho'|)\cos(\vartheta),\end{aligned} \tag{3-39}$$

where ϑ is the angle between **n** and (ρ- ρ') (refer to Fig. 3-33) and H_1 is the first-order Hankel function of the first kind.

Substitution of normal derivatives in the three scalar diffraction integrals yields:

$$U_{\mathrm{I}}(\rho) = \frac{ik}{2}\int_{-b}^{b} H_1(k\left|\rho-\rho'\right|)\cos(\vartheta)U_0(\rho')\,\mathrm{d}x' . \qquad \text{(Rayleigh-Sommerfeld I)} \tag{3-40}$$

$$U_{\mathrm{II}}(\rho) = \frac{k}{2}\int_{-b}^{b} H_0(k\left|\rho-\rho'\right|)\cos(\xi)U_0(\rho')\,\mathrm{d}x' . \qquad \text{(Rayleigh-Sommerfeld II)} \tag{3-41}$$

$$U_K(\rho) = \frac{ik}{4}\int_{-b}^{b}\left[H_1(k\left|\rho-\rho'\right|)\cos(\vartheta) - iH_0(k\left|\rho-\rho'\right|)\cos(\xi)\right]U_0(\rho')\,\mathrm{d}x' .$$

(Kirchhoff) (3-42)

We developed a Matlab program based on the Rayleigh-Sommerfeld-I theory of diffraction. Here, the two-dimensional diffraction integral is represented by an integral equation that incorporates the built-in Matlab function "besselh", which is the first-order Hankel function of the first kind. In order to prove the accuracy of this routine, we replaced the Fresnel diffraction operator of a number of previous simulation programs with the Rayleigh-Sommerfeld-I diffraction integral, and in all cases we obtained results that were similar to those obtained by Fresnel approximation. As stated above, this generation of software is capable of simulating near- field diffraction effects. In order to demonstrate this, we simulated the passage of a Gaussian beam (with a specific diameter) through a slab-waveguide bi-convex lens, as depicted in Fig. 3.34. Figure 3.35 shows that a 10 μm input Gaussian beam produces a 10 μm Gaussian output field. The output beam diameter was confirmed using ABCD matrix calculations [73]. It should be noted that the two lens interfaces are only twenty nanometers apart in this simulation, for Fresnel approximation this distance cannot be less than 100 μm.

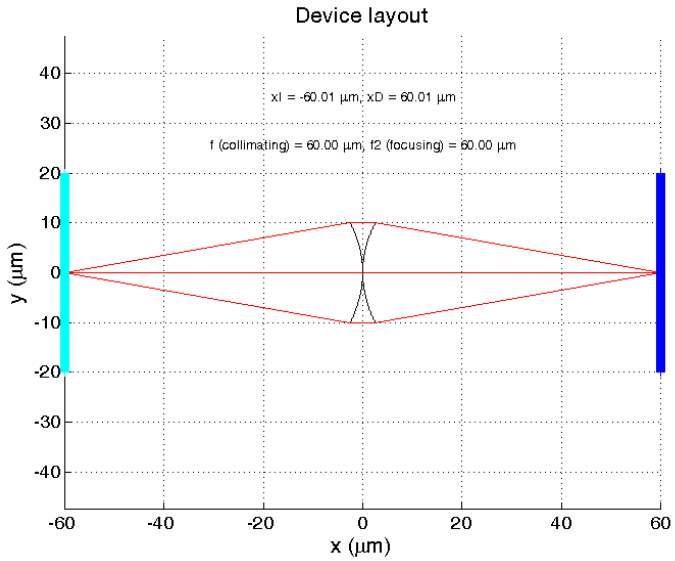

Fig. 3.34: Simulation set-up for a bi-convex slab-waveguide len

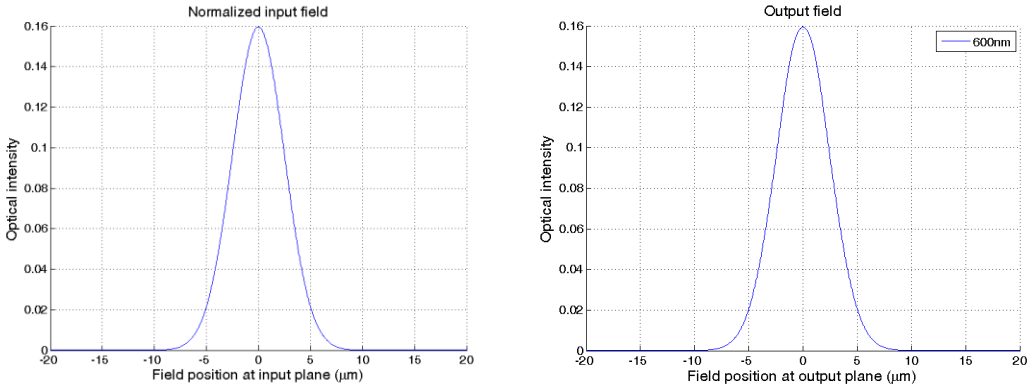

Fig. 3.35: Simulation results: 10 µm diameter Gaussian input beam (left). Gaussian output beam (right), which has a profile that is identical to the input beam.

The program for this simulation is my2lens_Hankel.m and is listed in App. I.

The accuracy of the Rayleigh-Sommerfeld I method was further investigated through simulations for the case of diffraction of a step input by a single slit. The results are shown in Figs. 3.36-3.39.

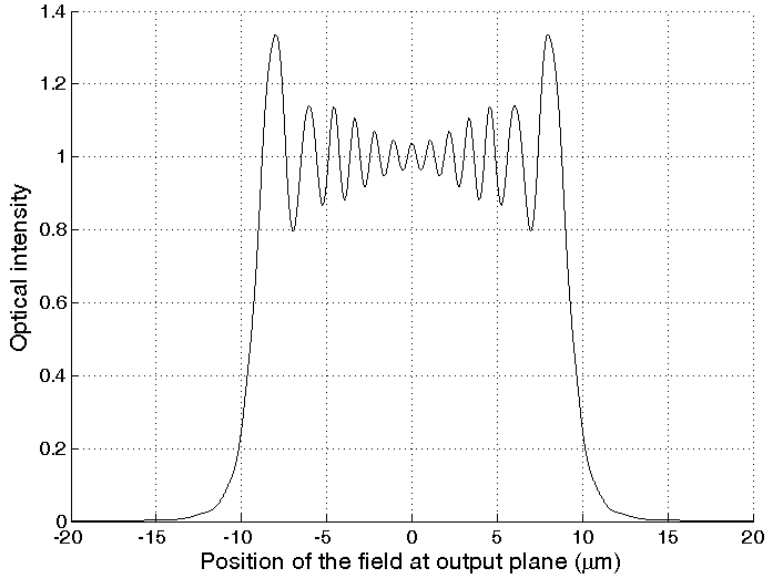

Fig. 3.36: Near-Field diffraction at a single slit (width 20 λ, Propagation distance 5 λ, λ = 1μm)

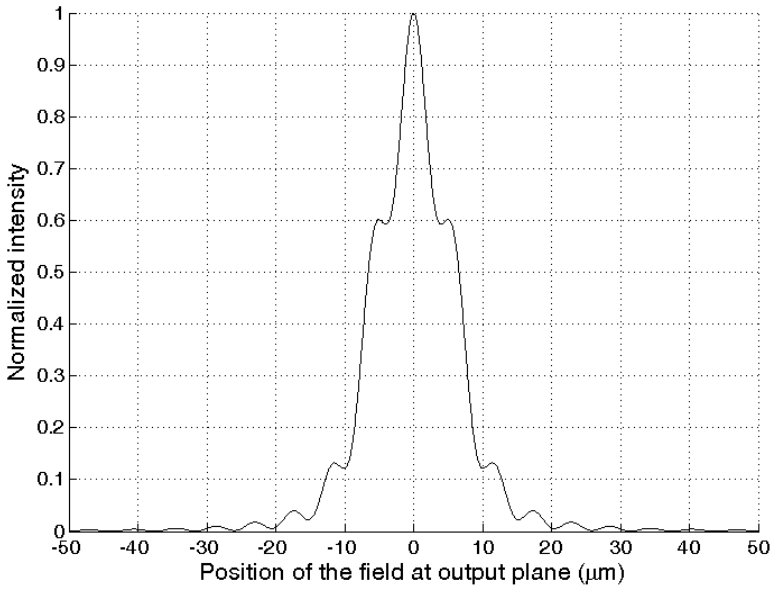

Fig. 3.37: Near-Field diffraction at a single slit(width 20 λ, Propagation distance 100 λ, λ = 1μm)

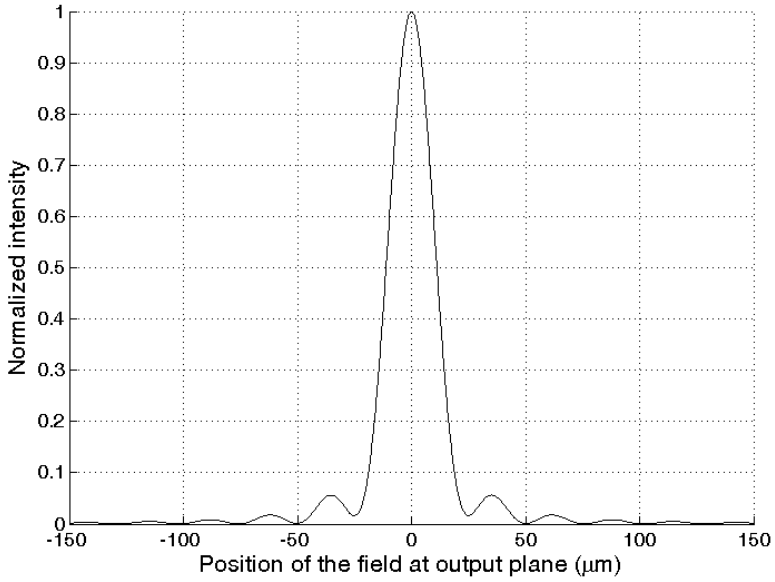

Fig. 3.38: Diffraction at a single slit (width 20 λ, Propagation distance 500 λ, λ = 1μm). At this distance, Fresnel diffraction is valid.

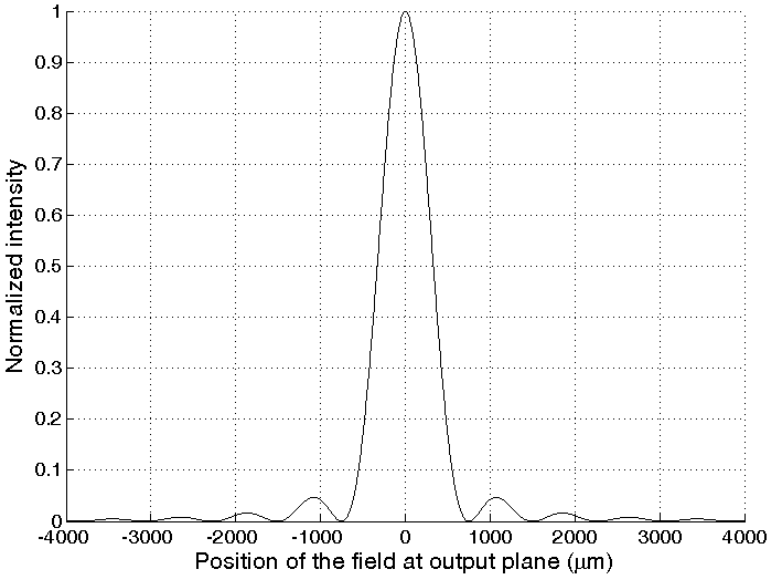

Fig. 3.39: Diffraction at a slit (width 20 λ, Propagation distance 15000 λ, λ = 1μm). At this distance, Fraunhoffer diffraction is valid.

Marathay et al. [74] utilized a full vectorial method in which the diffracted fields were calculated by the summation of the fields due to EM dipoles, and they reported results which are in good agreement with Figs. 3.36-3.39, verifying the accuracy of an integral formulation.

3.10.1 Asymptotic series for the Hankel function

According to the Handbook of Mathematical Functions by Abramowitz and Stegun (page 365) [75], it is possible to use asymptotic expansions for the Modulus and Phase of the Hankel function:

$$M_\nu^2 \sim \frac{2}{\pi x}\left\{1+\frac{1}{2}\frac{\mu-1}{(2x)^2}+\frac{1\cdot 3}{2\cdot 4}\frac{(\mu-1)(\mu-9)}{(2x)^4}+\frac{1\cdot 3\cdot 5}{2\cdot 4\cdot 6}\frac{(\mu-1)(\mu-9)(\mu-25)}{(2x)^6}+\cdots\right\}$$

$$\theta_\nu \sim x-\left(\frac{1}{2}\nu+\frac{1}{4}\right)\pi+\frac{\mu-1}{2(4x)}+\frac{(\mu-1)(\mu-25)}{6(4x)^3}+\frac{(\mu-1)(\mu^2-114\mu+1073)}{5(4x)^5}$$

$$+\frac{(\mu-1)(5\mu^3-1535\mu^2+54703\mu-375733)}{14(4x)^7}+\cdots$$

When ν is fixed, x is large and positive, and $\mu = 4\,\nu^2$.

Using the first two terms of the expansions, and for the Hankel function of the first order and first

kind, we have:

$$H_1^1(x) = \sqrt{2/\pi x}\exp\left(j(x-0.75\pi)\right). \qquad (3\text{-}43)$$

We tested this expression by writing a Matlab script (ahankel1.m), which compared the asymptotic values with the built in Matlab hankel function " besselh", for increasing values of x. The general conclusion was that for $x > 200$, that is for distances greater than approximately 20 μm, the error is < %1. Furthermore, this error decreases in proportion with the distance x. The Matlab script ahankel1.m is listed in App. I.

3.11 Focusing gratings

As discussed in Chapter 1, the primary motivation for the work on gratings was to develop a microspectrometer technology for LOC systems. Such a device would be especially useful for fluorescence spectroscopy applications.

Because of the weak nature of fluorescent signals, it is important to minimize the number of interfaces that the light has to go through before it reaches the output plane for detection. By using curved gratings, it is possible to incorporate the focusing action of the lens into the grating element. Another important advantage

of using a focusing grating is that a significant reduction in the size of the microspectrometer chip is possible.

An algorithm is required to define the curvature and the position of the grating facets. For reflection gratings, the well known Rowland Circle [64] as well as a number of other configurations are often employed. For example, our lab previously reported the design of circular and elliptical reflection gratings [76, 77], but these methods cannot be easily adapted to transmission gratings. Sander et al. [50] reported an analytical method to define the facets of a focusing transmission grating by solving a system of non-linear equations, for the geometry presented in Fig. 3.40.

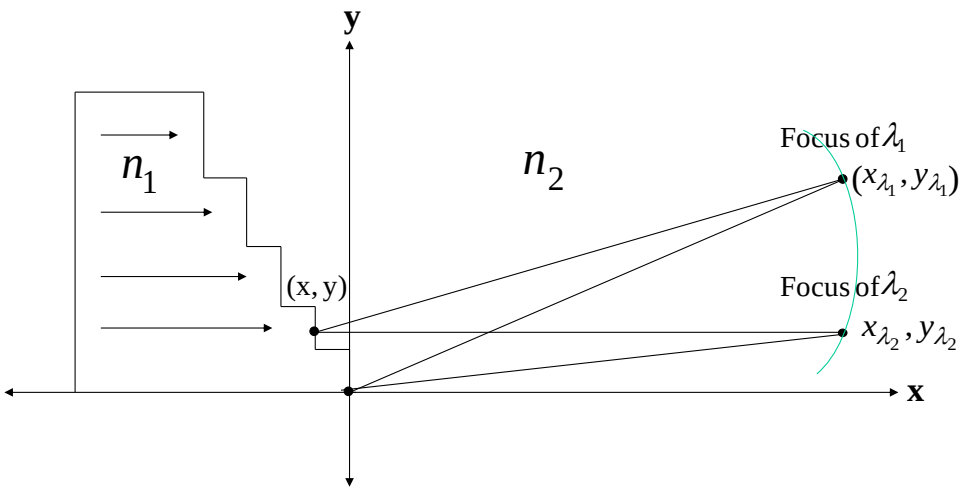

$$\sqrt{(x_{\lambda_1}-x_i)^2+(y_{\lambda_1}-y_i)^2}\cdot n_2-\sqrt{x_{\lambda_1}{}^2+y_{\lambda_1})^2}\cdot n_2+x_i\cdot n_1=i\cdot m\cdot\lambda_1$$

$$\sqrt{(x_{\lambda_2}-x_i)^2+(y_{\lambda_2}-y_i)^2}\cdot n_2-\sqrt{x_{\lambda_2}{}^2+y_{\lambda_2})^2}\cdot n_2+x_i\cdot n_1=i\cdot m\cdot\lambda_2$$

Fig. 3.40: Geometry and the geometrical relations for the focusing transmission grating proposed by Sander and Müller [50].

To verify this design, I used the Newton-Raphson method in order to solve the above system of over-determined nonlinear equations. Using parameters listed in Table 3.6 and by iteration of *m* from 1 to *m* (where *m* is the total number of facets), the positions x_i and y_i (unknowns of the equations) were determined. Setting these points as the centre of the facets, a non-periodic grating in planar

format can be produced, in which the width and depth of the facets are equal and they range from a = b = 0.5 μm to a = b = 1.5 μm. This type of grating, in which the facets are not equal but rather vary gradually and uniformly across the length of the grating, are known as chirped gratings. The self-focusing transmission grating obtained has a spectral dispersion equal to $D = (\lambda_2 - \lambda_1) / (y_{\lambda_2} - y_{\lambda_1}) = 60$ nm/mm.

$\lambda_1 = 400$ nm	$x_{\lambda 1} = 10000$ nm	$y_{\lambda 1} = 2500$ nm	$n_1 = 1.5$
$\lambda_2 = 550$ nm	$x_{\lambda 2} = 10000$ nm	$y_{\lambda 2} = 5000$ nm	$n_2 = 1$

Table 3.6: Parameters used in the Newton-Raphson iterations for defining the positions of the grating facets [50].

Although a grating defined in this way provides the focusing function (i.e. there is no need for additional focusing elements such as mirrors or lenses), it only focuses the two design wavelengths λ_1 and λ_2. The images of the other wavelengths, which fall in between and outside of the two design wavelengths will be blurred.

3.12 Design of a focusing grating/lens

Based on the insights gained from simulations described above, a compact LOC system for microspectrometry was conceived.

Here we present the preliminary details of the theory and simulation of this system. A more complete description, including fabrication details and experimental results, can be found in Chapter 6. As shown in Fig. 3.41, the optical system is composed of two principal components; a parabolic lens for collimation and a curved grating for dispersion and focusing.

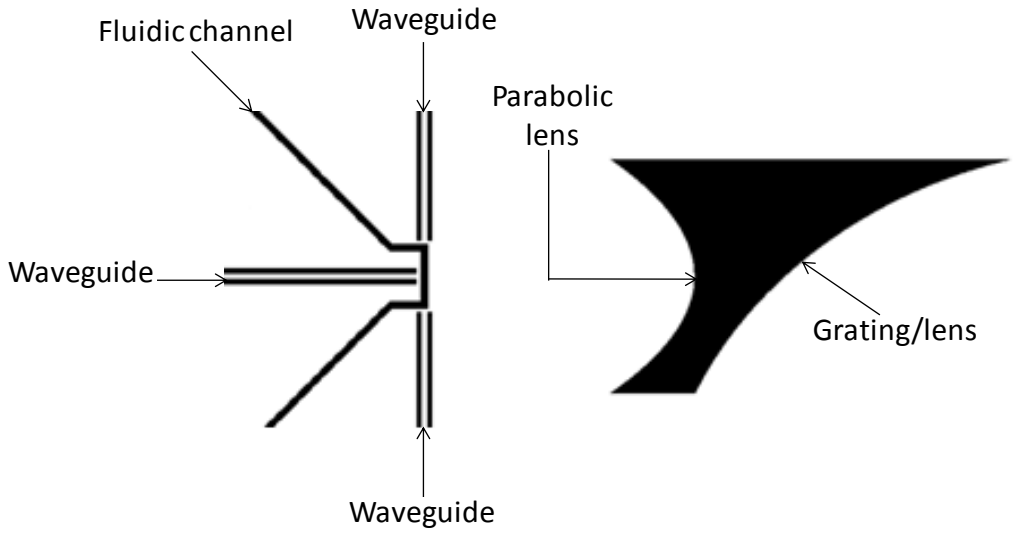

Fig. 3.41: Layout of the proposed microspectrometer. Fluidic channel and the three waveguides (left). Optical component comprising a parabolic collimating lens and a curved focusing grating (right). The black regions are air cavities embedded within the PDMS claddings (see sec. 3.1 and sec. 6.5)

Three waveguides (left), one along the optical axis and the other two coming from the top and bottom of the chip provide alternative ways to illuminate a section of the microfluidic channel used for optical interogation. As the fluorescing particles pass through this section of the channel they can get excited by the laser light carried by the waveguides coming to this region. To prevent the excitation light from entering the detector, the orientation of the waveguides coming from the top and bottom is in 90 degree angle to that of the detector which is to be positioned in a horizontal fashion at a specified point along the output plane (the right edge of the chip).

The dimensions of the lens-grating/lens (right figure shown above) is shown in Fig. 3.42,

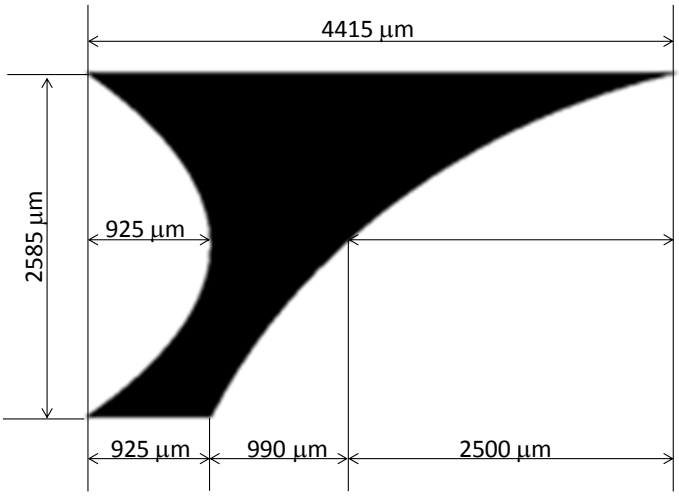

Fig. 3.42: Dimensions of the lens-grating/lens component.

3.12.1 Details of the collimating lens

The focal length of the collimating lens was chosen as 3 mm. The radius of the lens is obtained from the formula for spherical lenses given by:

$$R = \frac{n_2 - n_1}{n_2} f \,, \tag{3-44}$$

where f is the focal length of the lens, n_2 is the refractive index of the lens material (1.43), n_1 is the refractive index of vacuum (1.0) and R is the radius of the lens. The coordinates *x* and *y* for the collimating lens are obtained from the formula:

$$x = -\frac{y^2}{2R} \,, \tag{3-45}$$

which assumes a left opening parabola.

3.12.2 Design details for the curved grating/lens

We designed a grating where each facet is an arc or section of a circle, the radius of which is uniquely determined to obtain a common focal point among all facets (Fig. 3.43). This gives the grating a focusing property while making the spectrometer more compact. In this design, the number of interfaces is reduced, which is especially advantageous when faint signals such as fluorescent sources are involved.

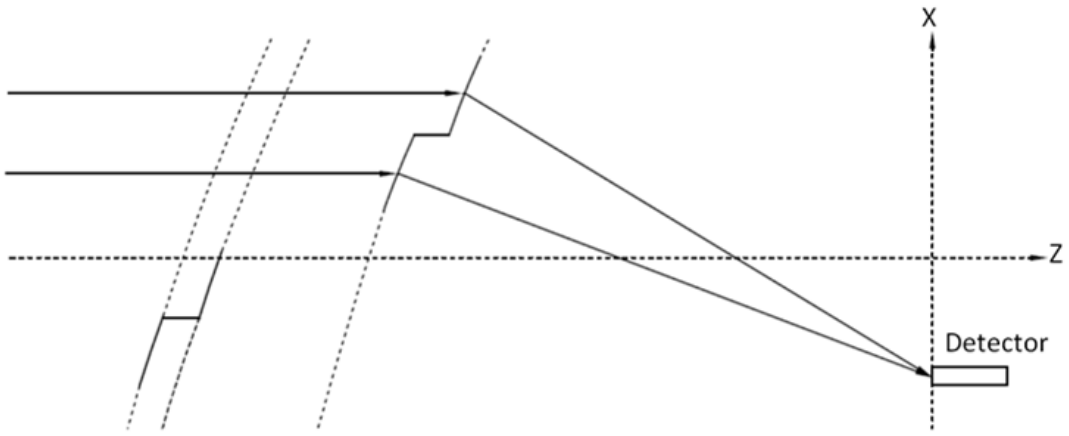

Fig. 3.43: Geometry of the focusing grating/lens. The facets of the grating are sections of circles that act like lenses with a common focal point. X and Z are coordinates within the horizontal plane of the slab-waveguide system.

For the design wavelength (λ = 0.645 μm), the constructive interference of light from adjacent facets will occur when the difference in focal length for the two facets, $\Delta f = f_j - f_{j+1}$ satisfies:

$$\Delta f = \frac{m\lambda}{n_2 - n_1}\ , \qquad (3\text{-}46)$$

where m is the diffraction order, n_2 = 1.43 is the refractive index of the grating material and n_1 = 1.0 is the refractive index of vacuum. using the parameters mentioned gives Δf = 3 μm.

In order to produce a compact spectrometer the focal length of the grating was chosen as 10 mm. The grating was designed to have 600 facets where each facet is a small section of a cylindrical lens. The facets gradually decrease from 6 μm (the first facet) to 4.93 μm (the last facet) each time reducing by 0.0018 μm. Gratings of this type, where the facets are not equal but vary slowly across the length of the grating, are known as chirped gratings. Chirping can further enhance the focusing function of the grating as discussed in sec. 3.11. Figure 3.44 shows the device layout. In this figure, the lower and upper boundary rays (the red lines) come together at the common focal point of the grating, which is actually the focal point of all the mini-lenses (i.e. the facets). The grating was furthermore designed to eliminate shadowing effects among facets. Figure 3.45, shows a

grating from an earlier design where facets partially shadow one another. As shown in Fig. 3.46, the facet layout was subsequently modified to eliminate shadowing effects.

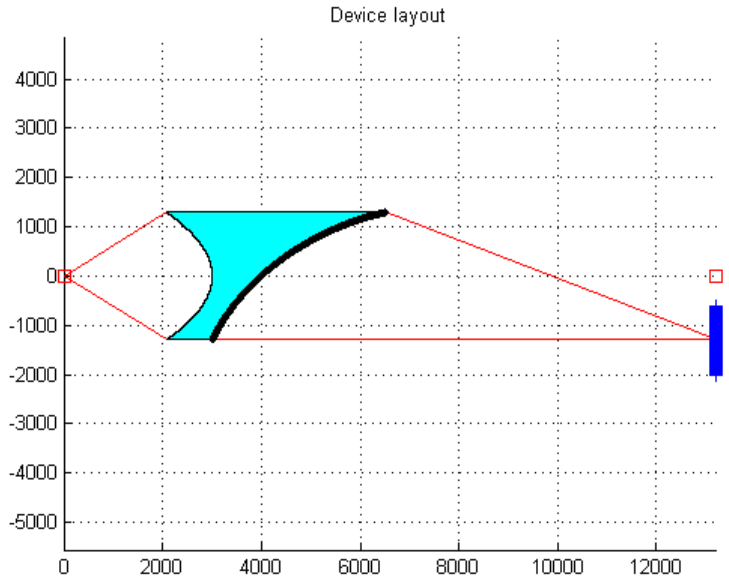

Fig. 3.44: The layout of the optical device (from Matlab simulation).

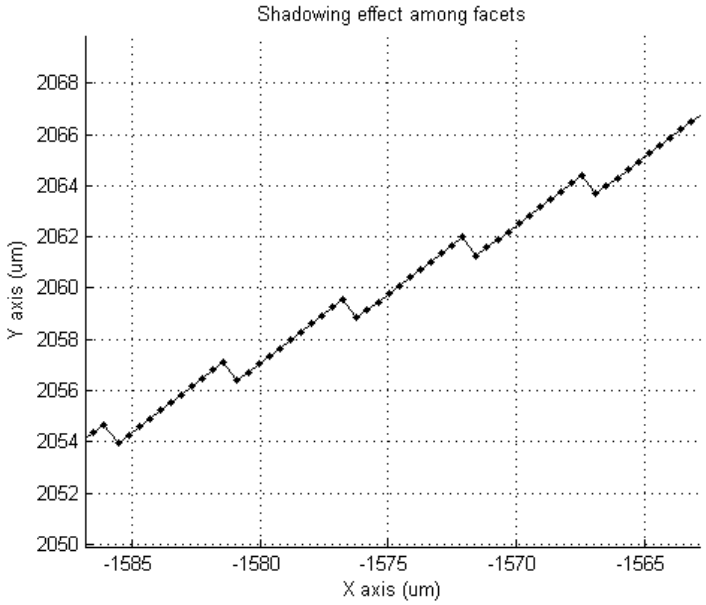

Fig. 3.45: Shadowing effect among grating facets
(i.e. consider a beam propagating along x from left).

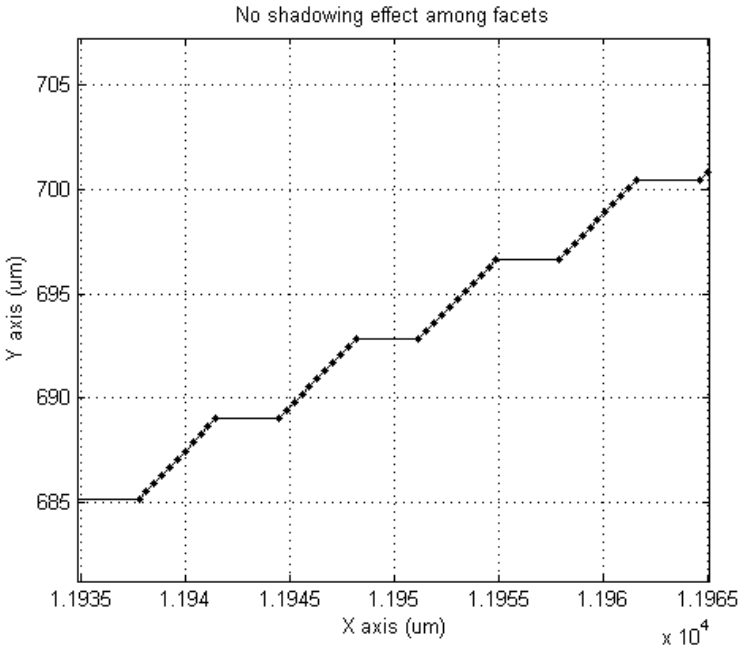

Fig. 3.46: No shadowing effect between the adjacent facets

This modification to the grating facets caused the focus of the grating to shift from 10000 μm to 10214 μm. Accordingly, we increased the length of the chip by 214 μm, in the actual drawings used for writing the mask.

We used the Rayleigh-Sommerfeld I method and simulated the diffraction of a 20 μm diameter Gaussian beam in the above mentioned lens-grating/lens optical system. Figure 3.47 shows the result of this simulation. As can be seen from this figure, the diffracted Gaussian beam for the design wavelength (0.645μm) appears at -1293 μm at the output plane. Figure 3.48 is an enlarged figure showing the first few grating facets. Note that the position of the first facet is also at -1293 μm on the vertical axis. Thus, at the design wavelength, the focusing grating brings the intended order into focus at the output plane, at a point directly in line with the first facet.

Although we were initially concerned about the rather large air-gap in the lensing region (the area between the parabolic lens and the curved grating in Fig. 3.44 and Fig. 3.42) which suggested a lower transmission efficiency, as some of the light trapped in the core layer would scape from this un-guided section, our laser experiments (please refer to Chapter 6) showed that the existence of this air-gap

does not pose major limitations on the performance of the spectrometer. In fact as observed by light transmission experiments with the "air-core waveguides" (discussed in sec. 6.2 and sec. 6.4) the air gap, is expected to work as an optical mode filter to enhance the resolution of the microspectrometer.

The Matlab code for this simulation is mygrating_lens_Gaussian_input.m which is listed in App. I.

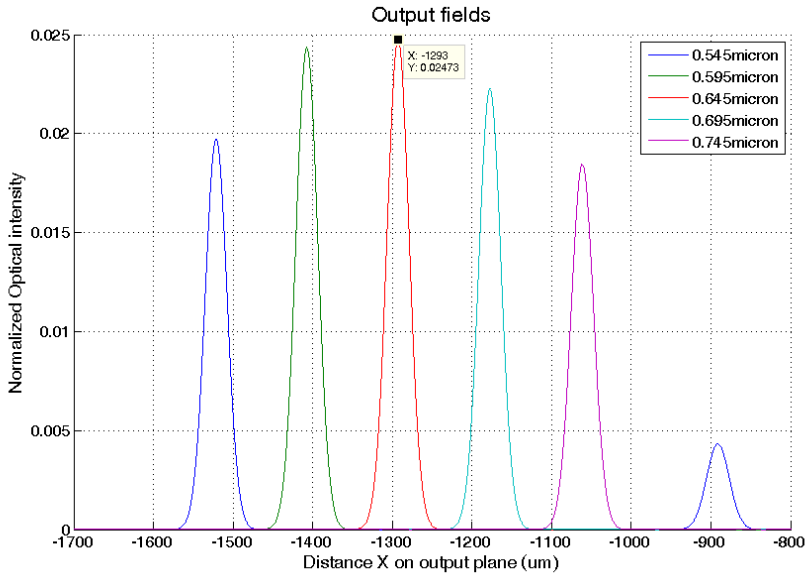

Fig. 3.47: 2nd order Gaussian beam diffraction of multiple wavelengths in the lens grating/lens optical system.

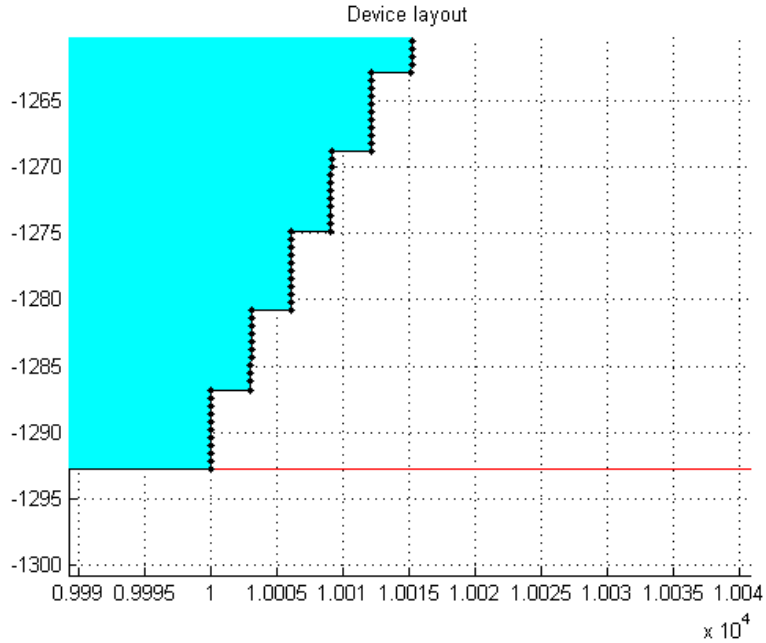

Fig. 3.48: Enlarged figure showing the first few facets of the grating/lens

Figure 3.49 shows the input Gaussian beam for a simulation which clearly illustrates the focusing function of the curved grating as a lens.

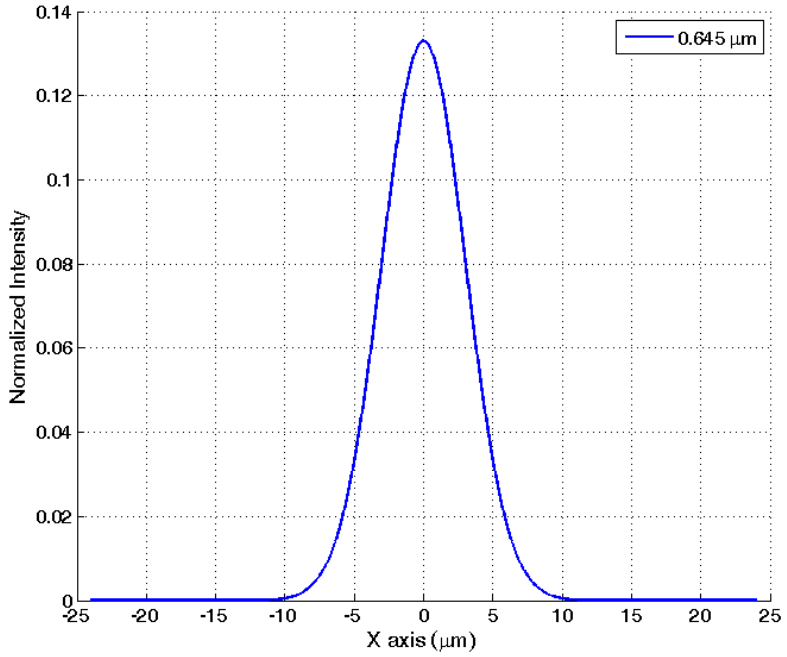

Fig. 3.49: Simulation input used for the demonstration of the grating's focusing action. The beam diameter is 12 μm and the propagation wavelength is $\lambda = 0.645$ μm.

Figures 3.50 and 3.51 correspond to the field distributions at the collimating lens and the focusing grating respectively.

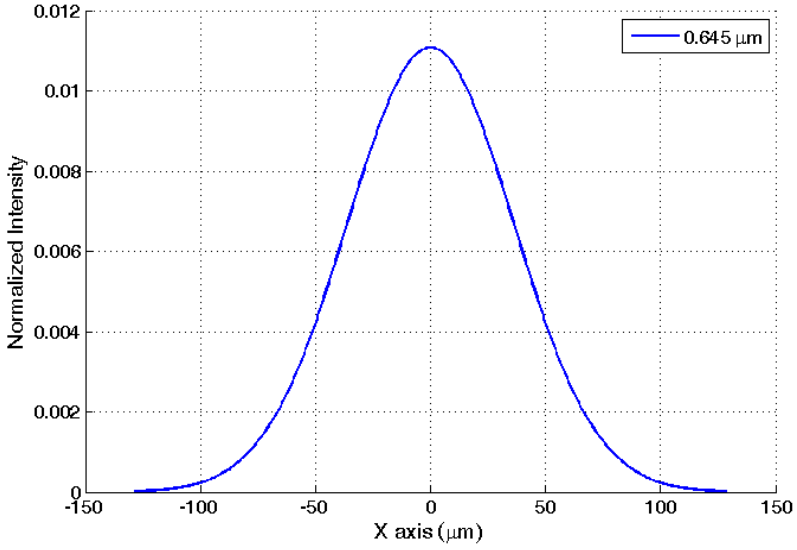

Fig. 3.50: Field distribution on the collimating lens.

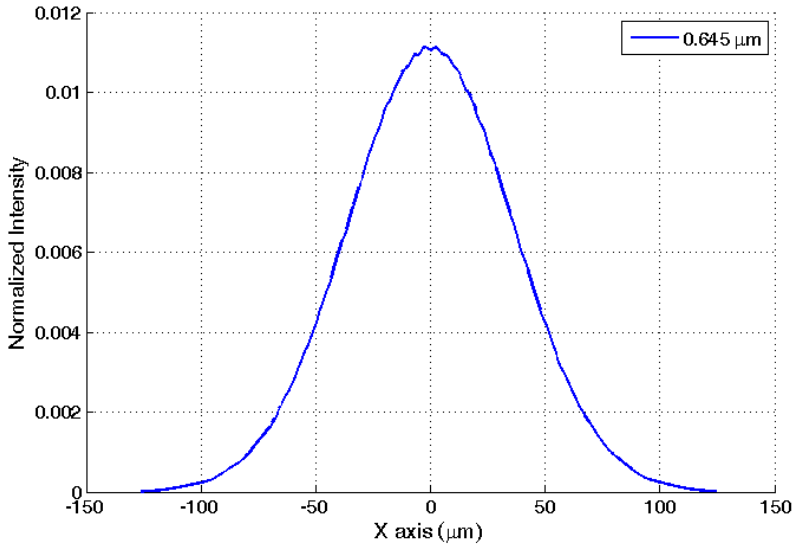

Fig. 3.51: Field distribution on the grating facets.

Figure 3.52 shows the Gaussian output field in which, the normalized intensity has peaked to ~ 0.04 at the focal region, as compared to ~ 0.01 at the position of the grating facets (Fig. 3.51). It should be noted that the beam diameter is considerably reduced as a result of the grating's focusing action.

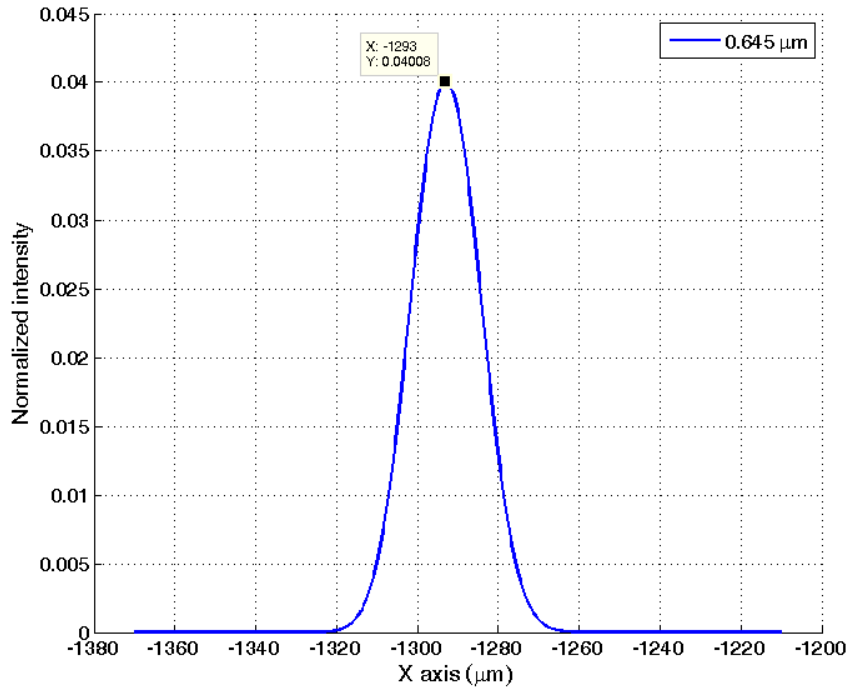

Fig. 3.52: Output Gaussian field at the gratin/lens focal region.

Figure 3.53 is a three-dimensional plot showing the field as it propagates through a region immediately after the grating and ending at the output plane (the exit end of the spectrometer). As can be seen in this plot the Gaussian beam intensity gradually increases and it reaches its peak near the focal point of the grating. This focusing property was experimentally verified by the observed narrowing of the laser beam fringes which started immediately after the grating and continued towards the spectrometer's focal point at the edge of the chip (data not shown).

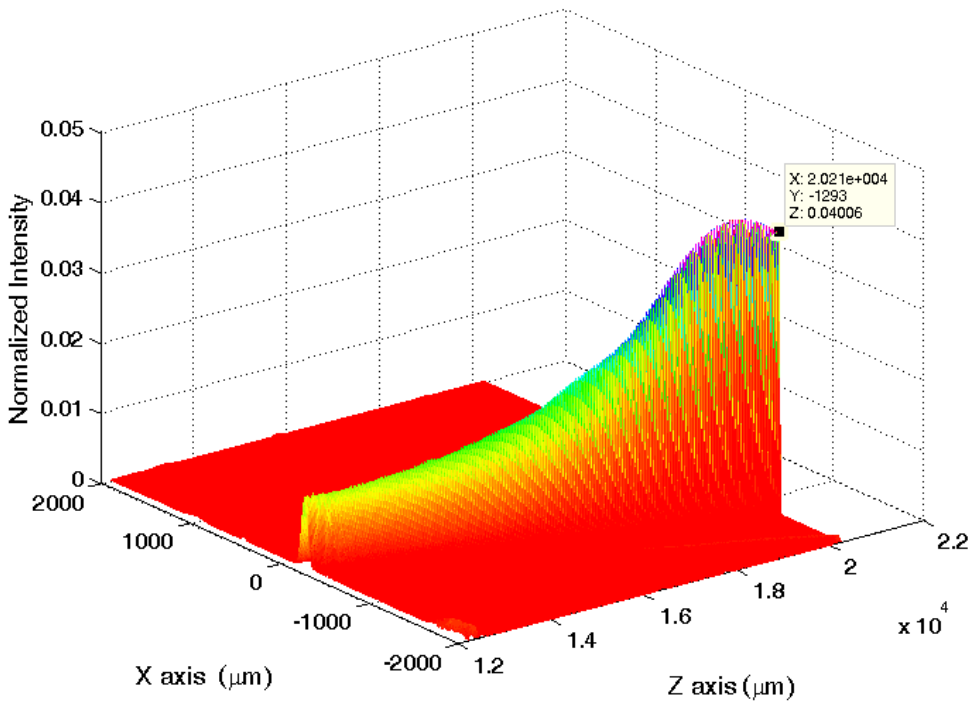

Fig. 3.53: Three dimensional plot of the scattered field in the region starting right after the grating and ending at the grating's focus (x = -1293 μm) at the spectrometer's exit.

A microspectrometer chip was fabricated based on this design. Experimental results are reported in Chapter 6, along with additional analytical and numerical results.

CHAPTER 4

4. Gaussian Beam Propagation: Comparison of the analytical closed-form Fresnel integral solution to the simulations of the Huygens, Fresnel, and Rayleigh-Sommerfeld I approximations[3]

4.1. Introduction

In physical optics, propagation of the field is normally posed as a diffraction problem. In order to solve this problem diffraction integrals need to be invoked. Because of mathematical difficulties rigorous solutions to diffraction integrals are rare [63]. As discussed in this paper Gaussian beam is an important special case for which an analytical solution exists. Otherwise in most cases of practical interest approximate methods are used [63]. We use the exact solution for the propagation of Gaussian beam as reference in order to determine the level of accuracy obtained from the Huygens, Fresnel and Rayleigh-Sommerfeld I approximations.

The propagation of waves can be effectively analyzed using the Huygens and Fresnel integral approaches. Anthony E. Siegman in his book "lasers" takes a brilliant approach and begins with the spherical waves as the general solution to the exact wave equation in order to facilitate the understanding of the Huygens' Principle and consequently the paraxial Fresnel approximation [73]. We adopt the same strategy and begin our discussion with the spherical waves.

4.2. Spherical Waves, Huygens' Principle and the Fresnel Approximation

A source point radiating a uniform diverging spherical wave from position $\mathbf{r}_0$ can be expressed as:

$$\tilde{E}(\mathbf{r};\mathbf{r}_0) = \frac{\exp[-jk\rho(\mathbf{r},\mathbf{r}_0)]}{\rho(\mathbf{r},\mathbf{r}_0)} \qquad (4\text{-}1)$$

[3] This chapter was published in J. Opt. Soc. Am. A **30**(4), 640-644 (2013)

where $\tilde{E}(\mathbf{r};\mathbf{r}_0)$ is the field at point $\mathbf{r}=(x,y,z)$ due to a source at point $\mathbf{r}_0=(x_0,y_0,z_0)$, and where the observation point $\mathbf{s},z$ is separated from the source point $\mathbf{s}_0,z_0$ by the distance $\rho(\mathbf{r},\mathbf{r}_0)$

given by:

$$\rho(\mathbf{r},\mathbf{r}_0)\equiv\sqrt{(x-x_0)^2+(y-y_0)^2+(z-z_0)^2} \qquad (4\text{-}2)$$

According to Huygens ' Principle: "every point on a propagating wavefront serves as the source of spherical secondary wavelets, such that the wavefront at some later time is the envelope of these wavelets" [78]. In other words, each of the Huygens' wavelets is a spherical wave of the form given by Equation (4-1) and sum of all these wavelets leads to Huygens' integral equation of the form [73]:

$$\tilde{E}(\mathbf{s},z)=\frac{j}{\lambda}\iint_{S_0}\tilde{E}_0(\mathbf{s}_0,z_0)\frac{\exp[-jk\rho(\mathbf{r},\mathbf{r}_0)]}{\rho(\mathbf{r},\mathbf{r}_0)}\cos\theta(\mathbf{r},\mathbf{r}_0)ds_0 \qquad (4\text{-}3)$$

Where $\tilde{E}_0(\mathbf{s}_0,z_0)$ is the incident field distribution, ds_0 is an incremental element of the surface S_0 at the point $\mathbf{s}_0,z_0$ and $\cos\theta(\mathbf{r},\mathbf{r}_0)$ is an "obliquity factor" defined by the angle $\theta(\mathbf{r},\mathbf{r}_0)$ between the line $\rho(\mathbf{r},\mathbf{r}_0)$ and the normal to the surface element ds_0 (Fig. 4.1).

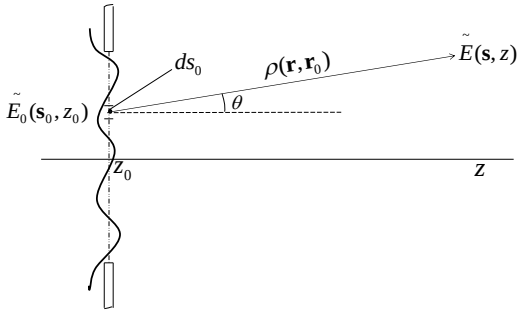

Fig. 4.1: Geometry for the evaluation of the Huygens' integral [73].

We are interested in Huygens' integral in one dimension since all our simulations are one dimensional. Considering only one transverse dimension: $\mathbf{r}=(x,z)$; $\mathbf{r}_0=(x_0,z_0)$ and for $z_0=0$, and replacing $\rho(\mathbf{r},\mathbf{r}_0)$ by L, the Equation (4-2) becomes

$$L\equiv\sqrt{(x-x_0)^2+z^2} \qquad (4\text{-}4)$$

For free space propagation and in the paraxial approximation where the point source x_0 is not too far off the z axis , L can be approximated as independent of x_0 and the one dimensional Huygens' integral [73] can be given by:

$$\tilde{E}(x,z) = \sqrt{\frac{j}{L\lambda}} \int \tilde{E}_0(x_0, z_0) \exp(-jkL) \cos\theta dx_0 \qquad (4\text{-}5)$$

To obtain the Fresnel integral in the paraxial approximation we expand Equation (4-2) as a power series

$$\rho(\mathbf{r}, \mathbf{r}_0) = z - z_0 + \frac{(x-x_0)^2 + (y-y_0)^2}{2(z-z_0)} + \cdots \qquad (4\text{-}6)$$

In rewriting the spherical wave of Equation (4-1) , we disregard all terms higher than quadratic terms in the power series expansion for the phase shift factor $\exp[-jk\rho(\mathbf{r}, \mathbf{r}_0)]$ and in the denominator we simply replace $\rho(\mathbf{r}, \mathbf{r}_0)$ by $z - z_0$, then we have what we may consider "paraxial-spherical wave" in the Fresnel approximation [73]:

$$\tilde{E}(x,y,z) \approx \frac{1}{z-z_0} \exp\left[-jk(z-z_0) - jk \frac{(x-x_0)^2 + (y-y_0)^2}{2(z-z_0)} \right] \qquad (4\text{-}7)$$

The two dimensional diffraction integral in the Fresnel approximation can be written as [73]:

$$\tilde{E}(x,y,z) \approx \frac{j}{(z-z_0)\lambda} \iint \tilde{E}_0(x_0, y_0, z_0) \exp\left[-jk(z-z_0) - jk \frac{(x-x_0)^2 + (y-y_0)^2}{2(z-z_0)} \right] \cdot \cos\theta dx_0 dy_0 \qquad (4\text{-}8)$$

With $z_0 = 0$, the one dimensional Fresnel integral has the form [73]:

$$\tilde{E}(x,z) \approx \sqrt{\frac{j}{z\lambda}} \int \tilde{E}_0(x_0, z_0) \exp\left[-jkz - jk \frac{(x-x_0)^2}{2z} \right] \cos\theta dx_0 \qquad (4\text{-}9)$$

4.3. Rayleigh-Sommerfeld I diffraction formula

For the case of the Rayleigh-Sommerfeld I formulation of diffraction [79] the two-dimensional diffraction integral can be written in terms of the Hankel

function as outlined by M. Totzeck in [71]. The example case chosen for the derivation of the Rayleigh-Sommerfeld I formula is the classical problem of two-dimensional diffraction of a monochromatic, cylindrical scalar wave by a slit, although we are going to use the obtained integral formula for propagation (diffraction) of a Gaussian beam. Figure 4.2 illustrates the geometry under consideration.

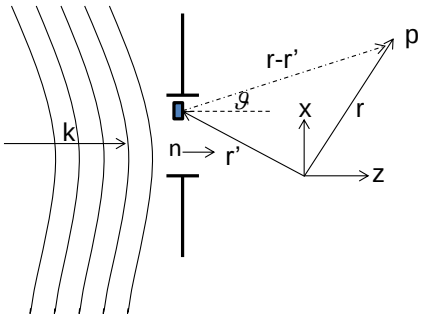

Fig. 4.2: Diffraction of an incident cylindrical wave by a slit aperture (after [71])

The slit width is 2b and the aperture screen is opaque, completely absorbing and perfectly conducting. According to the Rayleigh-Sommerfeld theory the field at any point beyond the aperture screen can be calculated from the field or its normal derivative on the planar screen. In the first Rayleigh-Sommerfeld integral the boundary condition is on the field while in the second Rayleigh-Sommerfeld formula the boundary condition is on the normal derivative of the field. For the Rayleigh-Sommerfeld I formulation the diffraction integral can be written as [72, 79]:

$$U_{\mathrm{I}}(r) = \frac{1}{2\pi} \int_{-\infty}^{\infty} \int_{-\mathrm{b}}^{\mathrm{b}} U_0(r') \frac{\partial}{\partial \mathrm{n}} \left[\frac{\exp(ik\,|\,r - r'\,|)}{|\,r - r'\,|} \right] dx' dy' \qquad (4\text{-}10)$$

With U_0 as the field at the aperture.

The following equation can be used to convert the three-dimensional diffraction integral into a two-dimensional diffraction integral [80]:

$$\int_{-\infty}^{\infty} \frac{\exp(ik\,|\,r - r'\,|)}{|\,r - r'\,|} dy' = i\pi H_0(k\,|\,\rho - \rho'\,|) \qquad (4\text{-}11)$$

Here H_0 is the zero-order Hankel function of the first kind, $\rho = (x, 0, z)$ and $\rho' = (x', 0, z')$.

By substituting Equation (4-11) in the integral of Equation (4-10) we obtain:

$$U_1(\rho) = \frac{i}{2}\int_{-b}^{b} U_0(\rho')\frac{\partial}{\partial \mathrm{n}} H_0(k\,|\,\rho-\rho'\,|)dx' \tag{4-12}$$

Taking the normal derivative of the Hankel function H_0 we have:

$$\begin{aligned}\frac{\partial}{\partial \mathrm{n}} H_0(k\,|\,\rho-\rho'\,|) &= -k\frac{\partial H_0(k\,|\,\rho-\rho'\,|)}{\partial k\,|\,\rho-\rho'\,|}\frac{(\rho-\rho')}{|\,\rho-\rho'\,|}\cdot \mathrm{n} \\ &= kH_1(k\,|\,\rho-\rho'\,|)\cos(\vartheta)\end{aligned} \tag{4-13}$$

Where H_1 is the first order Hankel function of the first kind and ϑ is the angle between n and $(\rho-\rho')$, (see Fig. 4.2).

By substituting Eq. (4-13) into Eq. (4-12) we obtain the first Rayleigh-Sommerfeld diffraction formula in terms of Hankel function [71]:

$$U_1(\rho) = \frac{ik}{2}\int_{-b}^{b} H_1(k\,|\,\rho-\rho'\,|)\cos(\vartheta)U_0(\rho')dx' \tag{4-14}$$

4.4. Propagation of a Gaussian beam

A Gaussian beam is an optical beam such that the amplitude of the wave function $u(x,y,z)$ associated with it has a Gaussian distribution at each cross-section. Laser beams emerging from cylindrically symmetric cavities have this character. For convenience we relegate the dependence on z to a subscript and introduce

$$u_z(x,y) \equiv u(x,y,z) \tag{4-15}$$

To study the propagation of a Gaussian beam we may consider a "signal" in an input plane $(z=0)$ with a Gaussian distribution

$$u_0(x,y) = c\exp\left(-\frac{(x^2+y^2)}{{\omega_0}^2}\right) \tag{4-16}$$

where c and ω_0 are constants. Its square amplitude, known as irradiance or intensity, is also Gaussian:

$$I(x,y) = |\,u_0(x,y)\,|^2 = c^2\exp\left(-\frac{2(x^2+y^2)}{{\omega_0}^2}\right) \tag{4-17}$$

Using the Fresnel diffraction formula we shall obtain an expression for $u_z(x,y)$, the complex optical signal at a plane z units distant from the input plane. It will be shown that the amplitude distribution remains Gaussian for all z and the radius of the beam increases with z.

In the Fresnel approximation we have

$$u_z(x,) = \frac{j}{\lambda}\frac{\exp(-jkz)}{z}\int_{-\infty}^{\infty}\int_{-\infty}^{\infty} c\exp\left(-\frac{(x'^2+y'^2)}{\omega_0{}^2}\right)\exp\left(-j\frac{k}{2z}\left[(x-x')^2+(y-y')^2\right]\right)dx'dy' \tag{4-18}$$

Separating the integral with respect to x'

$$\exp\left(-j\frac{k}{2z}x^2\right)\int_{-\infty}^{\infty}\exp\left(-(\frac{1}{\omega_0{}^2}+j\frac{k}{2z})x'^2\right)\exp\left(-j\frac{k}{z}xx'\right)dx' \tag{4-19}$$

We note that the integral is of the form of a Fourier transform of a Gaussian function

$$\int_{-\infty}^{\infty}\exp(-\alpha\,\xi^2)\exp(\pm j\beta\,\xi)\,d\xi = \sqrt{\frac{\pi}{\alpha}}\,\exp\left(-\frac{\beta^2}{4\alpha}\right) \tag{4-20}$$

Here
$$\alpha = (\frac{1}{\omega_0{}^2}+j\frac{k}{2z}) = \frac{2\,z+j\,k\,\omega_0{}^2}{2\,\omega_0{}^2\,z} \quad ; \quad \beta = \frac{k\,x}{z} \tag{4-21}$$

After some algebra we find for the x' part

$$\sqrt{\frac{2\,\pi\,\omega_0{}^2\,z}{2\,z+j\,k\,\omega_0{}^2}}\exp\left(-j\frac{2kz}{4z^2+k^2\omega_0{}^4}x^2\right)\exp\left(-\frac{k^2\omega_0{}^2}{4z^2+k^2\omega_0{}^4}x^2\right) \tag{4-22}$$

A similar result is found for the integral with respect to y' except that x is replaced by y.

Thus we obtain

$$u_z(x,y) = c\;\frac{j}{\lambda}\;\frac{\exp(-jkz)}{z}\;\frac{2\pi\omega_0{}^2 z}{2z+jk\omega_0{}^2}\;\exp\left(-j\frac{2kz}{4z^2+k^2\omega_0{}^4}(x^2+y^2)\right)\cdot$$
$$\cdot\exp\left(-\frac{k^2\omega_0{}^2}{4z^2+k^2\omega_0{}^4}(x^2+y^2)\right)$$

$$u_z(x,y) = c\ \frac{jk\omega_0^{\ 2}}{2z + jk\omega_0^{\ 2}}\ \exp(-jkz)\ \exp\left(-j\frac{2kz}{4z^2 + k^2\omega_0^{\ 4}}(x^2+y^2)\right)\cdot$$
$$\cdot\exp\left(-\frac{k^2\omega_0^{\ 2}}{4z^2 + k^2\omega_0^{\ 4}}(x^2+y^2)\right) \tag{4-23}$$

Note that at $z = 0$, this reduces to $c\exp\left(-\frac{(x^2+y^2)}{\omega_0^{\ 2}}\right)$ as it should.

If the real exponential is written

$$\exp\left(-\frac{k^2\omega_0^{\ 2}}{4z^2 + k^2\omega_0^{\ 4}}(x^2+y^2)\right) \equiv \exp\left(-\frac{(x^2+y^2)}{\omega^2(z)}\right) \tag{4-24}$$

Then for $(x^2+y^2) = \omega^2(z)$ the amplitude of $u_z(x,y)$ is down to e^{-1} (and its square is down to $e^{-2} = 13.5\%$) of its value at $x = 0$, $y = 0$. Thus $\omega(z)$ is a measure of the beam radius (half-width) at any plane z (Figure 4.3).

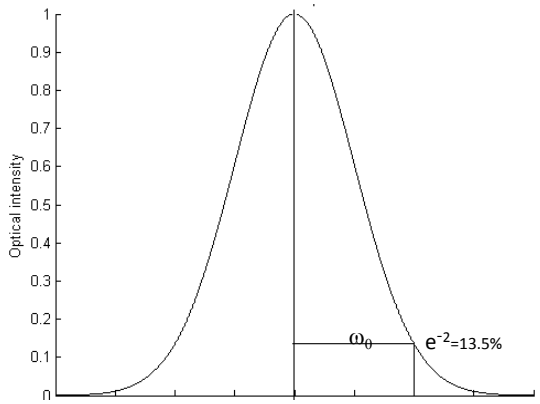

Fig. 4.3: Gaussian beam with radius of the beam (ω_0) at e^{-2} or 13.5% of its maximum intensity

From the above definition we have

$$\omega(z) \equiv \sqrt{\frac{4z^2 + k^2\omega_0^{\ 4}}{k^2\omega_0^{\ 2}}} = \omega_0\sqrt{1+\left(\frac{2z}{k\omega_0^{\ 2}}\right)^2} \tag{4-25}$$

Another parameter frequently used is the Rayleigh range: z_0

$$z_0 \equiv \frac{k\,\omega_0^{\ 2}}{2} = \frac{\pi\,\omega_0^{\ 2}}{\lambda} \tag{4-26}$$

In terms of z_0 we may write the beam radius and radius of curvature of the wavefront as

$$\omega(z) = \omega_0 \sqrt{1 + \left(\frac{z}{z_0} \right)^2} \tag{4-27};$$

$$R(z) = z \left[1 + \left(\frac{z_0}{z} \right)^2 \right] \tag{4-28}$$

Finally the closed form solution of the one dimensional Fresnel diffraction integral that can be used for the propagation of a Gaussian beam is given by

$$u_z(x) = \sqrt{c} \sqrt{\frac{j}{z\lambda}} \sqrt{\frac{2\pi\omega_0{}^2 z}{2z + jk\omega_0{}^2}} \exp(-jkz) \exp\left(-j \frac{2kz}{4z^2 + k^2\omega_0{}^4} x^2 \right) \cdot \cdot \exp\left(-\frac{k^2\omega_0{}^2}{4z^2 + k^2\omega_0{}^4} x^2 \right) \tag{4-29}$$

4.5. Results and Discussion

We have implemented the analytical closed form solution of the Fresnel diffraction integral for an input Gaussian field Eq. (4-29), together with Huygens, Fresnel and Rayleigh-Sommerfeld I approximations Eq. (4-5), Eq. (4-9), and Eq. (4-14) respectively, in a Matlab program for comparison. The parameters of the simulation are the beam radius ω_0 of the initial Gaussian field, the optical wavelength λ, and the propagation distance z. In all simulations the parameters ω_0 and λ were kept constant. We have increased z from $1\,\mu m$ to $1{,}000{,}000\,\mu m$ in increments that translate to half a unit in the logarithmic scale (i.e. $1, 3, 10, 32\ldots$). For each approximate method we recorded the values for the maximum intensity of the output Gaussian beam as the propagation distance z was incrementally increased. We then compared these values with maximum intensities obtained from the exact integration of the Fresnel diffraction integral. The results are compiled in the logarithmic graphs of Fig. 4-4. According to our simulations in the Fresnel approximation a Gaussian beam that has a radius of $\omega_0 = 20\,\mu m$ requires a minimum propagation distance of at least $10\,\lambda$ (Fresnel

near field criteria). We have implemented two versions of the Fresnel integral. In the first version (Fresnel 1) the obliquity factor is $\left(\frac{1+\cos\theta}{2}\right)$ while in the second version (Fresnel 2) the obliquity factor is $(\cos\theta)$. Based on our simulations, $\left(\frac{1+\cos\theta}{2}\right)$ provides more accurate results. See Fig. 4.4(a). As we expect the Rayleigh-Sommerfeld formula provides the most accurate approximation. For example at propagation distance of $1\,\mu m$ the relative error is less than 0.00000001%. Contrary to the other approximations used in this study in the Rayleigh-Sommerfeld approximation the level of accuracy falls off rapidly at the beginning as the propagation distance increases but even in the worst case the relative error is still around 0.001 %. See Fig. 4.4(b). To evaluate the Hankel function in the Rayleigh-Sommerfeld I integral we have used the built in Matlab function "besselh". In the program we have also included an integral simulation in which an asymptotic expansion for large arguments (4-30) is used in lieu of Hankel function (see the Handbook of Mathematical Functions by Abramowitz and Stegun page 364 section **9.2.3**) [75].

$$H_1^1(x) \sim \sqrt{2/(\pi x)}\exp\left(j(x-0.75\pi)\right) \qquad (4\text{-}30)$$

Looking at Fig. 4.4(c) we notice that using the above expansion instead of Hankel function we obtain results that are identical to the ones obtained by Huygens' approximation. As indicated by the logarithmic graphs of Fig. 4.4 the level of accuracy for each method fluctuates throughout the propagation region. While accuracies of the Fresnel method are generally increased as the propagation distance increases, the accuracy of the Rayleigh-Sommerfeld I approximation for propagation distances in the range of $1\,\mu m$ to $3162\,\mu m$ diminishes at first and later recovers as the propagation distance is further increased. The relative percent error for the ending point of all five simulations (at $z = 1$ meter) is in the 0.000003% range, which is an excellent approximation.

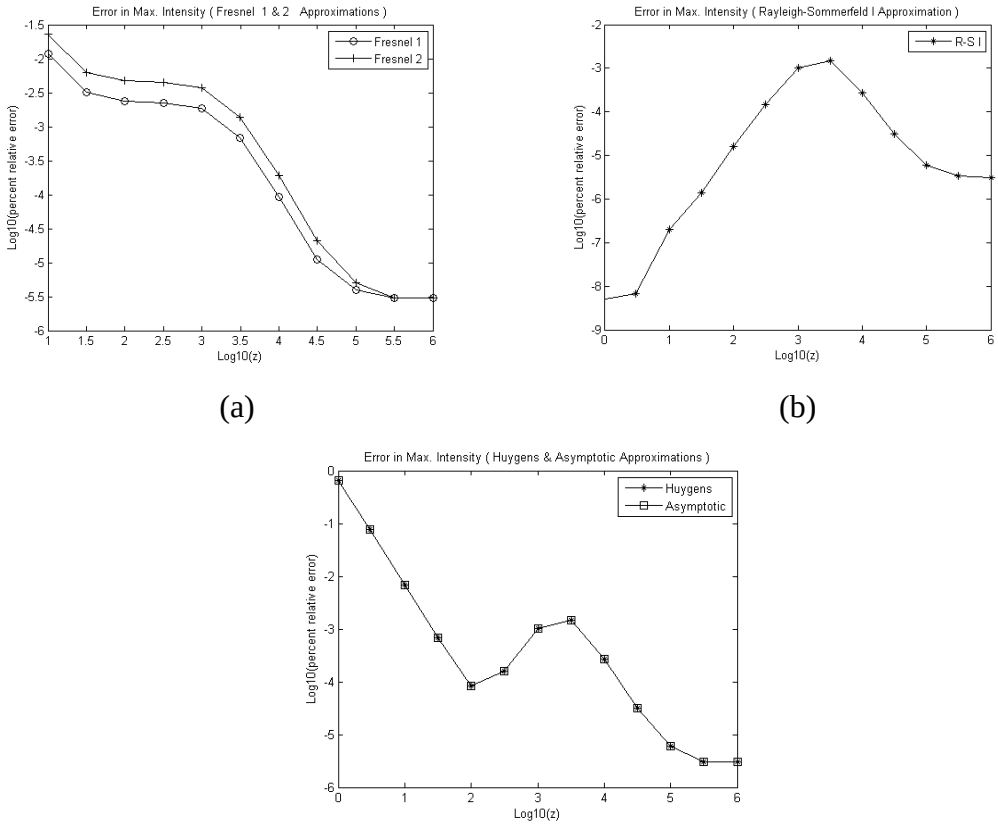

Fig. 4.4: Logarithmic graphs of percent relative error Vs. / propagation distance for maximum Gaussian beam intensity obtained from various approximations as compared to the values obtained from the exact integration. (a) Fresnel 1 & 2 approximations. (b) Rayleigh-Sommerfeld I approximation. (c) Huygens and asymptotic approximations.

CHAPTER 5

5. PDMS biochips with integrated waveguides[4]

5.1 Introduction

Optical waveguides in lab-on-a-chip devices (LOCs) can provide a number of important functionalities such as eliminating the need for the alignment of bulk optical instruments as the optical and fluidic elements can be precisely aligned at design level; increasing the optical path length in absorbance measurements; minimizing optical losses and reflections by reducing the number of interfaces and analysing multiple samples in parallel using arrays of elements such as waveguide splitters and combiners for multi-point excitation and detection [81].

Typically, a planar LOC with integrated optics consists of a central core layer that contains the microchannels and waveguides and outside layers of lower refractive index that act as the upper and lower waveguide claddings. Taking advantage of the advanced micromachining and processing techniques already developed for semiconductor technology, many lab-on-a-chip devices have been fabricated in silicon and glass [82-87]. However polymers such as optical adhesives, SU-8 and polydimethylsiloxane (PDMS) are favoured in many applications due to ease of fabrication and lower cost of production [88-97]. PDMS in particular is a cheap, easy-to-handle and safe material that possesses excellent physical and mechanical properties and has been widely used in microfluidic applications [27]. It is transparent in the UV-visible (230nm to 700nm) and selected bands of near-IR and hence is suitable for the fabrication of waveguides and other on-chip optical elements. A common method of making waveguides in PDMS LOCs is by the formation of dedicated channels that are subsequently filled by a higher index liquid or solid material. For liquid-core waveguides, higher-index PDMS pre-polymer and glycerine have been used [93, 94, 96]. For solid-core waveguides, a

[4] This chapter was published in Journal of Micromechanics and Microengineering **20**(8), 1-5 (2010)

UV-curable resin of higher refractive index has been injected into the waveguide channels and cured [98, 99].

Recently, other groups [100-102] have used a "doctor-blading" method to form a high-index PDMS waveguide/microfluidic core on a master of SU-8 that has the device features. In this method, a flexible blade is used to remove any excess material outside of the features on the master. After curing of the core, a lower-index PDMS cladding layer is bonded to the core and the two PDMS layers are removed from the master. A final PDMS layer is bonded to the exposed side of the core to complete the all-PDMS chip. The disadvantage of this method is that the excess material may not be completely removed [100, 103] thus leading to formation of a leaky layer by the remaining high index material. Also, there is the danger that doctor-blading may damage the fine micron-size features of the master even when soft PMMA blades are used. Furthermore, curvature in the surfaces of the waveguides due to surface tension cannot be easily avoided [102].

In this note, we demonstrate a practical alternative to the doctor-blading method for forming such all-PDMS optofluidic devices that is simple, inexpensive and does not require expensive equipments or special laboratory setups and uses commercially available PDMS materials. As in the doctor-blading method, the core is formed on a master (a silicon wafer in this case). However, the excess PDMS is removed by applying uniform pressure from an applied weight and when all the excess material has been squeezed out, the core is cured. The subsequent steps are similar. This method avoids the disadvantages of the doctor-blading method as well as the labour-intensive steps of filling the waveguide channels with high-index liquids (as is done for liquid-core waveguides) or high-index UV-curable resins (in case of solid-core waveguides).

In the next section, details of the fabrication are given. In the third section, the detection and identification of two fluorescent microparticle species is demonstrated in a LOC fabricated by this new method.

5.2 Fabrication and Properties

The optofluidic core layer contains channels that serve as fluidic pathways or hollow side claddings for the waveguides. The patterns for these channels are

transferred to the surface of a silicon wafer and the areas between these patterns are removed by a standard deep reactive ion etching (RIE) method to the desired channel depth, 50 um in our case. The silicon master is then silanized to enable easy removal of the PDMS core layer. The subsequent fabrication steps, shown schematically in Fig. 5.1(a), are as follows.

(A) A thin layer of low-temperature PDMS (Dow Corning 3-6121; grey in the figure) with refractive index 1.43 is cast on the silicon master (black). The uncured PDMS is then covered with two plastic sheets (textured), a thin Mylar™ sheet to which cured PDMS will not stick and a photocopier transparency sheet to provide a smooth cushion between the PDMS and the 12-15 kg weight that is next placed on top in Step B.

(B) The weight expels PDMS (indicated by the arrows) from all but the 50-um-deep etched regions over a 24-hour period. Since the unetched regions are a very small fraction of the total area, any remaining PDMS on these regions is expected to be very much smaller than a wavelength of light [103] and leakage of light to be negligible. If left, the PDMS layer will completely cure in 48 hours at room temperature. For more rapid processing, it can be cured in a vacuum oven in 20 min. at 100^{O} C.

(C) After curing of the core layer, the weight and plastic sheets are removed and a 1-mm layer of PDMS (dark grey), Sylgard® 184, refractive index 1.41, is cast and cured on the exposed core layer. The combined cladding /core layer is removed from the master and reservoirs and microchannel access holes are punched through the cladding and core layers as indicated by the white dashed lines. Figure 5.1(b) is a SEM image of the cross-section of a portion of the cladding/core showing a waveguide and its two side-channel air claddings. The boundary between the two types of PDMS, indicated by the white arrow, is faintly visible in the figure.

(D) To complete the fabrication, the cladding/core combination is bonded to a substrate (dark grey) of the low-index PDMS (dark grey), Sylgard 184®. Irreversible bonding is achieved by exposing the two parts to an oxygen plasma in a reactive ion etcher (O_2 flow: 25sccm; Pressure: 700 mTorr; RF Power: 40 W)

for 30 seconds. Figure 5.1(c) is an image of a waveguide and its two side-channel air claddings. This figure clearly shows how the rectangular shape of the channels is preserved in the fabrication process.

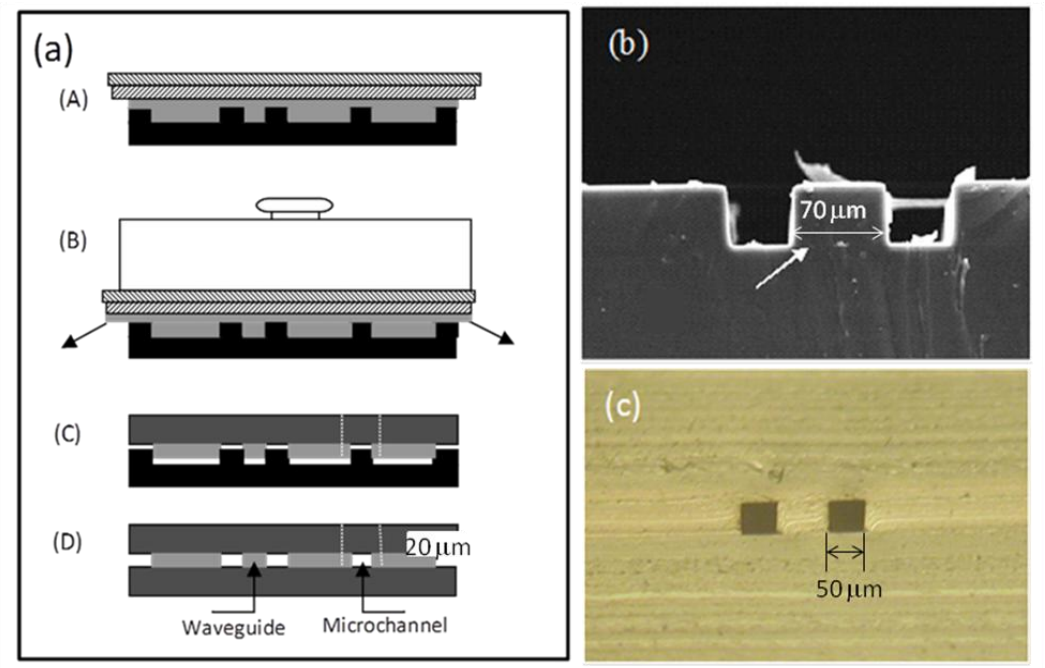

Fig. 5.1: Fabrication process for an all-PDMS LOC. (a) Steps (A-D) as described in the text. (b) SEM image of cross-section of a waveguide and air claddings before the final PDMS cladding layer is bonded; (c) cross-sectional image of a waveguide after the final cladding layer is attached.

The propagation loss in the PDMS waveguides was measured by a common technique that assumes that the side-scattered light power at any point along a waveguide is proportional to the propagation power at that point [94]. Laser light at 532-nm and 635-nm was launched into optical fibres that were butt-coupled to straight PDMS waveguides at the edge of a device. Side-scattered light was captured with a 1-mm plastic optical fibre at intervals of 1 mm and delivered to a photomultiplier tube (PMT) detection system under LabVIEW® control. The uncalibrated results in dB are plotted in Fig. 5.2 along with least square linear fits to the data from which the waveguide loss in dB/mm is obtained from the slopes of the straight lines. The measured losses of 0.31 db/mm at 532 nm and 0.29 db/mm at 633 nm are comparable with the waveguide losses in earlier PDMS LOC devices [94, 96, 97]. While these are not low losses by integrated optics

standards, they are adequate for LOC applications where light travels over short distances. The losses are most likely due to surface roughness that results from the deep RIE processing of the master since the inherent loss in PDMS has been reported to be much lower [104].

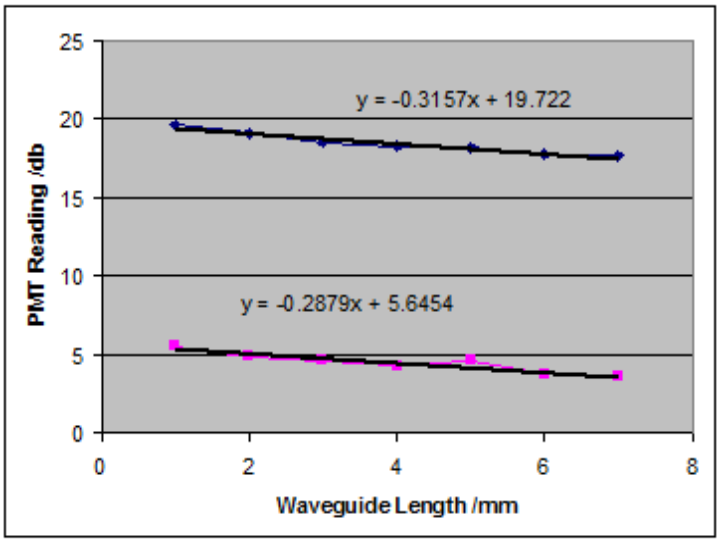

Fig. 5.2: Sidescattered power in dB along a PDMS waveguide at 532 nm and 633 nm. The average waveguide attenuation is determined from a linear fit to the raw data.

5.3 Demonstration of particle detection and identification†

The functionality of devices fabricated by this method is demonstrated by the detection and identification of 15-μm orange and scarlet fluorescent styrene beads [105] in a pressure-driven flow through a U-shaped section of a microfluidic channel as shown in Fig. 5.3 and in the video clip presented as electronic supplementary data. Red light is launched into the horizontal section of the channel from the left and illumiantes beads along the length of the horizontal channel. Green light from the top waveguide intersects the channel at its midpoint and illuminates beads only in a 50 um zone. The image also clearly shows stray light that propagates in the core layer outside the waveguides and scatters from the edges of the air claddings . This stray light aids in the observation of the beads before they enter the regions directly illuminated by the waveguides. Five beads are visible with one scarlet bead fluorescing brightly in the horizontal channel.

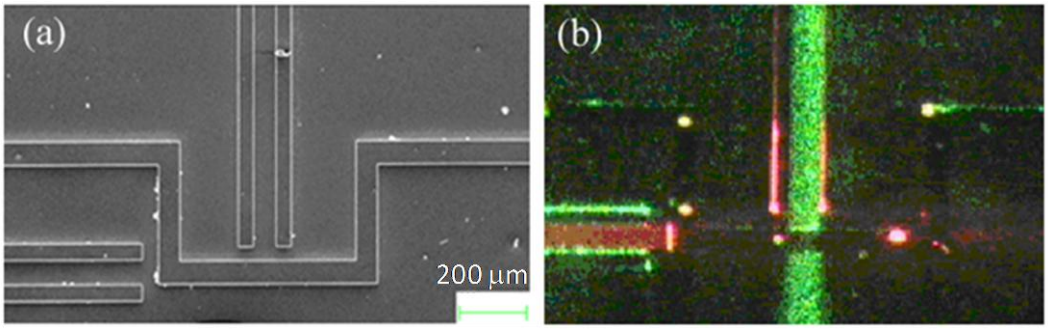

Fig. 5.3: (a) SEM image of the silicon master showing raised features that become channels in the core layer. The U-shaped feature forms a microchannel and the narrow straight lines form the air-claddings for two waveguides. (b) The U-shaped microchannel is illuminated along its length by 633-nm light from the waveguide on the left and intersected by 532-nm light from the waveguide at the top. Five fluorescent beads are visible in the channel.

The red (633 nm) and green (532 nm) excitation lasers are modulated with mechanical choppers at 250 Hz and 125 Hz respectively. The flourescent signals are picked up by a multimode plastic optical fiber placed underneath the chip at the intersection of the green and red lasers. The flourescent signals are directed to a Hamamatsu R2949 PMT equipped with high-pass (540 nm cut-off) and notch (627-637 nm) filters for suppression of scattered laser light. The electronic signal from the PMT is sampled by the DAQ system at 20000 Sample/s and 10 consecutive samples are averaged (to suppress PMT noise) providing an effective sampling frequency of 2000 Sample/s. The raw data are exported to a text file and a windowed Fourier transform algorithm is executed in Matlab™ to extract the components of the signal from each modulation frequency thus identifying the type of fluorescent bead (red or green) causing the signal at a specific time[99]. Figure 5.4 (a) shows 6.5 seconds raw data in which there are three pulses indicating the passage of three particles at 0.4 s, 3.9 s and 5.6 s. Figure 5.4 (b) shows the windowed Fourier transform component at 250 Hz indicating two scarlet particles at 3.9 s and 5.6 s. Figure 5.4 (c), the windowed Fourier transform component at 125 Hz, shows the third pulse at 0.4 s is a green particle. The small width of the third pulse (at 0.4 s) indicates that the green particle was moving faster compared to the two scarlet particles (at 3.9 s and 5.6 s).

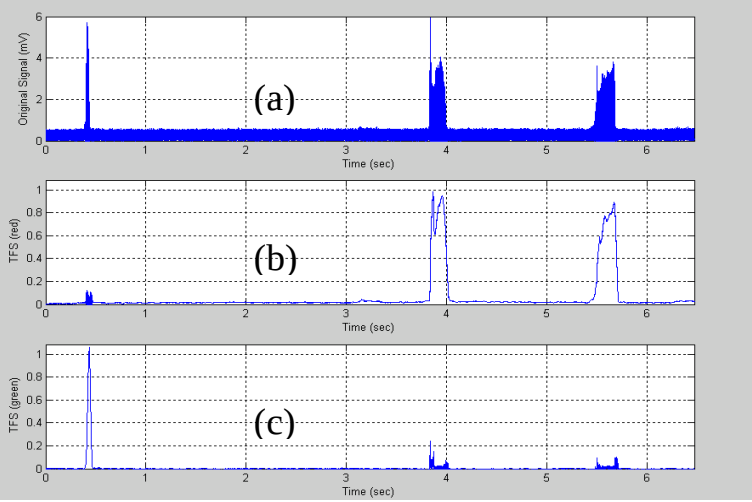

Fig. 5.4: (a) 6.5seconds of raw data from the PMT indicating the detection of three beads. (b) Processed data indicating the detection of two scarlet beads; (c) Processed data indicating the detection of one orange bead.

5.4 Summary

In summary, we have introduced an improved fabrication method for the integration of optical and fluidic components in all-PDMS lab-on-a-chip devices. The fabrication method is simple and overcomes the difficulties associated with previous methods for making all-polymer devices with liquid or solid core waveguides. In particular, there are no surface tension effects to distort the waveguide shape as in reference 21. After the fabrication of the master, no expensive equipment is required and many masters could be processed in parallel. The device functionality in a cytometry application was demonstrated by uniquely identifying fluorescent particles in a mixed population using lasers of different wavelengths modulated at distinct frequencies. Note that the propagation of light along a U-channel (red light in this case) could be utilized for absorbance measurements if a device were designed with a collection waveguide at the end of the channel to catch the throughput light.

Notes

†Please view "Video.wmv" (submitted supplementary media file). It is a video clip showing fluorescent microparticles flowing in the fluidic channels of the LOC device.

CHAPTER 6

6. Design and fabrication of a planar PDMS transmission grating microspectrometer[5]

6.1 Introduction

Optical spectroscopy, the precise determination of the wavelength composition of light, is arguably the most powerful analytical tool at the disposal of science. Optical spectrometers are required in the fields of chemical production, analysis of DNA and RNA macromolecules, high throughput screening of drugs for pharmaceutical purposes, medical diagnostics, and environmental testing [1]. Not surprisingly there has been great interest in microspectrometers [55] that can be integrated within lab-on-a-chip (LOC) and Micro-Total-Analysis-Systems (μTAS) [106]. One of the earliest works was by Goldman et al. [48], who reported spectral analysis based on waveguide grating couplers. Later, Yee et al. reported a hybrid spectrometer for chemical analysis [51], composed of silicon micromachined gratings and a CCD camera, in a system that was characterized by separate microfluidic and optical parts. For optimal performance, grating-based spectrometers require lenses or mirrors for collimation and focusing [55]. Micro-scale fabrication of these elements is often difficult, and this has prompted exploration of several alternative strategies. For example, Traut et al. [53] developed a miniaturized spectrometer by forming grating patterns on the top surface of an array of microlenses. In that design, each microlens in the array functioned as a dispersive and focusing element. In the design by Grabarnik et al. [46], a second grating was utilized as the focusing element. Adams et al. [107] proposed a non-grating approach based on monolithic integration of microfluidics and thin-film filters directly on top of image sensor arrays, but their experimental results were restricted to the filtering of excitation and fluorescence light. For many LOC applications, there remains a need for closer integration of the optical

[5] This chapter was published in Optics Express **21**(10), 11889-11900 (2013)

parts, including a diffraction-grating-based spectrometer, within the microfluidic platform.

Poly(dimethylsiloxane) (PDMS) is a low cost, biocompatible polymer increasingly used for the fabrication of microfluidic and LOC devices [27, 108]. It is transparent in the UV–visible range (230 nm to 700 nm) and within selected bands of the near-IR, and hence is suitable for the fabrication of waveguides and other on-chip optical components. Given the popularity of optical detection for LOC sensing systems, there is a natural impetus to develop optical componentry (including spectral dispersion devices) in PDMS. Previous research includes work on PDMS-based waveguides [109] and lenses [110]. Researchers have also considered both hybrid and monolithic integration of spectral discrimination devices with PDMS microfluidics. For example, Domachuk et al. [111] embedded a microfluidic channel adjacent to a PDMS-based planar grating and used external lenses for focusing and collimation, while Yang et al. [112] reported a PDMS-based diffractive optical element that combined both spectral dispersion and focusing functions.

Waveguide-based spectrometers (and waveguide-based optics, generally speaking) are attractive for optofluidics and LOC systems, since they enable built-in alignment of optics and fluidics. While hybrid approaches, such as wafer bonding of PDMS microfluidics to silicon-based arrayed waveguide gratings (AWG) [113], have been described recently, there are very few reports of PDMS-based waveguide gratings. For example, Kee et al. [114] described a PDMS-based arrayed waveguide grating (AWG) with ~1 nm resolution but only 4 output channels and a correspondingly limited operating range (~640 to 645 nm). Here, we describe a PDMS-microsystem that monolithically integrates microfluidic channels, multimode waveguides, a collimating lens, and a slab-waveguide-based, focusing transmission grating. In addition to enabling a convenient chip layout, the use of a transmission grating (rather than a reflection grating) is partly motivated by the possibility for high spectral dispersion with large facet dimensions [50]. The grating described operates in second order with feature sizes greater than 3 μm, and incorporates a novel self-focusing design based on the use

of cylindrical facets. Below, we provide a theoretical analysis and an experimental characterization of the spectrometer part of our chip. A wavelength resolution <10 nm over a free spectral range >200 nm in the visible band was predicted and verified by experimental results.

6.2 Design of the LOC spectrometer device

A typical spectrometer consists of a light source, a dispersive element (typically a diffraction grating), lenses or mirrors for light collimation and focusing, and a detector. In the present design, a parabolic lens is used to collimate the light while the necessary dispersion and focusing is accomplished by a curved transmission grating, as shown in Fig. 6.1.

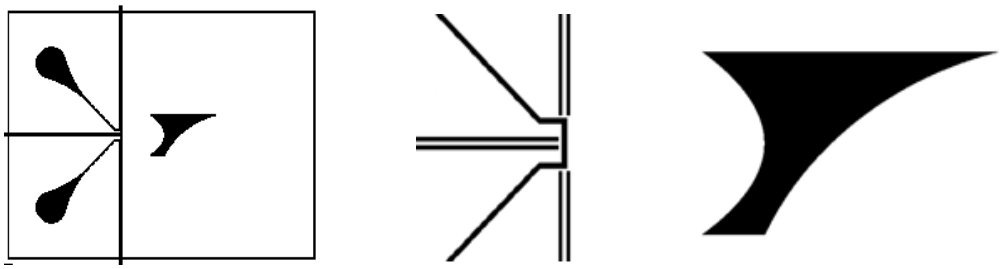

(a) **(b)** **(c)**

Fig. 6.1: (a) Mask design layout of the LOC spectrometer device. In the fabricated chip, the filled black regions become hollow (air-filled) cavities. The teardrop shaped features at upper and lower left are microfluidic reservoirs. (b) Magnified view of the intersection point between the microfluidic channel and three waveguides. (c) Magnified view of the parabolic collimating lens together with the curved focusing transmission grating.

The focal length of the collimating lens was set as 3 mm to match the lateral extent of the grating (2585μm). The radius of the lens is obtained from the well-known formula for spherical lenses:

$$R = \frac{n_2 - n_1}{n_2} \cdot f \quad , \qquad (6\text{-}1)$$

where f is the focal length of the lens, n_2 is the refractive index of the lens material (1.43), n_1 is the refractive index of air (1.0) and R ~ 902 μm is the value obtained for the radius of the lens.

As described previously [11], the optical waveguides are nominally configured to confine light by total internal reflection (TIR), between the high and low index PDMS layers in the vertical direction, and between the PDMS core and the adjacent air channels (side claddings, see Fig. 6.6 below) in the horizontal direction. Note, however, that the air channels themselves can act as 'leaky' waveguides, with propagation loss on the order of 1 dB/cm for the dimensions used here (~50 μm x ~50 μm) [115]. Such air-core waveguides can operate in a quasi-single-mode regime, since propagation loss scales quadratically with mode number [115]. Thus, a sufficient length of straight leaky waveguide preferentially suppresses high-order modes. For the optical characterization of the grating spectrometer (see below), laser light sources were coupled into the air-core leaky waveguides at the left edge of the chip (Fig. 6.1), whose inherent mode filtering resulted in an input field (at the start of the slab waveguide section prior to the lens) that better approximates the Gaussian input field assumed for numerical simulation purposes. This was motivated by a desire to simplify the comparison of experimental results with analytical and numerical predictions, and also allows us to assess the best-case resolution of the spectrometer. In practice, the existence of multiple waveguide modes will degrade the resolution of the instrument, as discussed in more detail below and elsewhere [76, 77, 116].

6.2.1. The curved focusing phase transmission grating

We designed a grating where each facet is an arc or section of a circle, the radius of which is uniquely determined to obtain a common focal point among all facets (Fig. 6.2). By using curved grating facets, the focusing action is obtained without a lens. Furthermore, by eliminating the focusing lens, the number of interfaces that light must traverse is reduced. This is advantageous in cases where the spectral measurement of a faint signal such as a fluorescent source is needed.

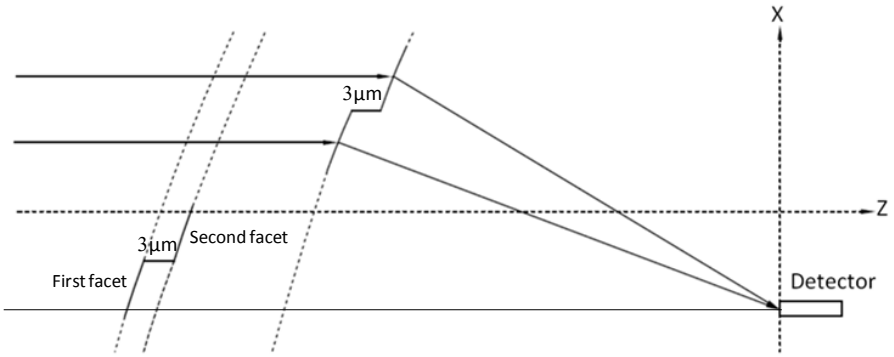

Fig. 6.2: Geometry of the focusing grating/lens. The facets of the grating are sections of circles that act like lenses with a common focal point. X and Z are coordinates within the horizontal plane of the slab-waveguide system.

The device shown in Fig. 6.2 is a slab waveguide phase transmission grating. The constructive interference of light from adjacent facets will occur when the difference in focal length for the two adjacent facets, $\Delta f = f_j - f_{j+1}$ satisfies [50]:

$$\Delta f = \frac{m\lambda}{n_2 - n_1} \quad , \qquad (6\text{-}2)$$

where m is the diffraction order, $n_2 = 1.43$ is the refractive index of the grating material (PDMS), and $n_1 = 1.0$ is the refractive index of the air region to the left of the facets. Here, a simple, single-stigmatic-wavelength criterion based on a design wavelength of $\lambda = 645$ nm was used to specify the facets. Furthermore, the grating was designed to operate in second order (m = 2) rather than the first order (m = 1), which allowed us to double the size of the grating steps. This greatly simplified the soft-lithography fabrication of the grating facets, while still ensuring a tolerable free spectral range for the grating. These parameters correspond to a nominal value of Δf (the size of the grating steps) equal to 3 µm. For the self-focusing grating described above, this means that the focal length of adjacent facets should differ by 3 µm. The grating was designed to have 600 facets, so that there are effectively 600 lens sections, each with a unique focal length. Fig. 6.3 shows the grating overlaid on the coordinate system we chose for design and discussion purposes. Note that the center of the grating lies on the z axis, and that we denote the lower-most facet as the 'first' facet of the grating, positioned at x = -1.293 mm and z = 1 cm. Furthermore, the grating is designed

to focus second-order diffracted light (of the design wavelength) at a position directly in line with the first facet and with a first-facet focal length of 1 cm. This focusing action is illustrated by the lower and upper boundary rays (the red lines) in Fig. 6.3, which come together at the common focal point of the grating. This focal point corresponds to the position denoted by x = -1.293 mm and z = 2 cm in our chosen coordinate system. In order for each of the 'lens' sections to share this common focal point, it is necessary to adjust the radius of curvature for each facet. Accordingly, we used the spherical lens equation, Eq. (6-1) to uniquely determine the necessary radius of each lens element in the grating. In order to avoid 'shadowing' between facets, the width of the facets was monotonically decreased from 6 μm (first facet) to 4.93 μm (last facet) by equal increments of 0.0018 μm across the length of the grating. The resultant spectrometer is reasonably compact, and is integrated within a microfluidic platform that has overall dimensions of (1.7 cm x 2.1 cm).

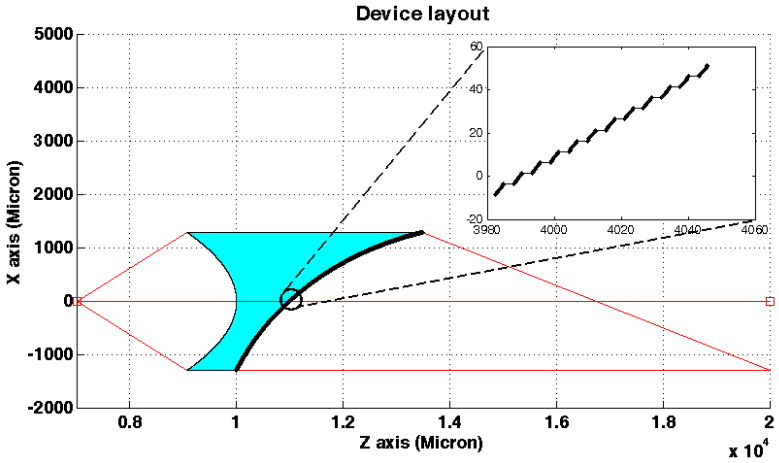

Fig. 6.3: The detailed layout of the grating/lens device is shown. The focal point is chosen to lie at the same height as the first grating facet (i.e. at x = -1293 μm). The inset shows a magnified view of the central part of the curved grating, which can be approximated as a linear grating with mean facet period ~7.4 μm.

6.3 Approximate analysis based on the grating equation

Analytical treatment of the curved, focusing phase grating is difficult [50]. However, as shown in the inset of Fig. 6.3, the central portion of the grating can be well-approximated as a straight grating with uniform facets. In practice

(including the experiments described below), most of the incident light interacts with the central portion of the grating. Thus, a first order approximation based on standard grating theory can be employed for insight.

Basic details of a grating's behavior can be readily obtained by using the grating equation from classical diffraction theory:

$$\Lambda \cdot \left(\mathrm{n}_2 \cdot \sin\theta_2 - \mathrm{n}_1 \cdot \sin\theta_1 \right) = m \cdot \lambda \quad , \tag{6-3}$$

where $n_1 = 1$ is the refractive index for the vacuum in the (air-core) cavity before the grating, $n_2 = 1.43$ is the refractive index of the PDMS material, θ_1 is the angle of incidence, θ_2 is the angle of diffraction, and Λ is the period of the grating.
Directly from the geometrical layout of the central portion of the grating and assuming incidence along the optical axis (x=0), we estimate $\theta_1 \sim 47.6$ degrees and a mean grating period $\Lambda \sim 7.4$ μm. From the grating equation, this results in an estimate for the second-order (m = 2) diffraction angle (at the design wavelength) of $\theta_2 \sim 39.6$ degrees. Note that this angle is relative to the effective grating normal at the central part of the grating; the predicted angle (of the second-order diffracted beam) relative to the optical axis is then simply $\theta_1 - \theta_2 \sim 8$ degrees, which is in very good agreement with the numerical simulations below.

For spectral analysis, another key parameter is the angular dispersion of the grating. From the grating equation with the angle of incidence θ_1 fixed, it follows that:

$$D_\lambda = \frac{\partial\theta_2}{\partial\lambda} = \frac{\mathrm{m}}{\mathrm{n}_2 \cdot \Lambda \cdot \cos(\theta_2)} \tag{6-4}$$

where D_λ is the angular dispersion of the grating. In practice one often needs to know the linear dispersion which is the product of the angular dispersion and the effective focal length ($\mathrm{f}_{\mathrm{eff}}$) of the instrument:

$$D_x = \frac{\partial \mathrm{x}}{\partial\lambda} = \mathrm{f}_{\mathrm{eff}} \cdot \frac{\partial\theta_2}{\partial\lambda} \tag{6-5}$$

The effective focal length in the present case is the geometrical distance from the grating center to the position of the focal point (for second-order diffraction at the design wavelength), which is ~ 9.3 mm. Given the diffraction angle and other geometrical parameters estimated above, this produces an estimate of the linear

dispersion (for m = 2) at the ouput plane D_X ~ 2.3 μm/nm. As discussed below, the numerical and experimental results are in good agreement with these first-order predictions.

6.4 Numerical simulation of the microspectrometer

The integrated planar microspectrometer, fabricated in PDMS as described below, is a multimode (MM) waveguide device. In a MM waveguide device, the polarization dependence can be neglected for simplified analyses [77]. Moreover, since the smallest features of the present device (i.e. the grating facets) are large in comparison to the operational wavelengths, a scalar electromagnetic simulation considering only the TE modes is expected to be sufficiently accurate. Consider a Cartesian coordinate system where x and z are the horizontal coordinates in the plane of the slab and y is the vertical (out-of-plane) coordinate. Strictly speaking, the field for each wavelength at a point (x, y, z) within the slab is a linear combination of vertical modes supported by the slab waveguide [77]. As discussed above and in Section 6 below, however, we used the air channels as leaky waveguides for launching the laser beams used to experimentally characterize the grating. This ensured that the field launched into the slab waveguide section prior to the collimating lens was quasi-single-moded in the vertical direction. Based on this assumption, only the fundamental slab waveguide mode was considered in the scalar simulation of the grating. Furthermore, a 'hard boundary' assumption [77] was used to obtain the relevant parameters of the fundamental mode, which is justified by the large thickness of the PDMS core. As mentioned above, excitation of higher-order modes is expected to degrade the resolution of the spectrometer. However, it should be noted that the use of air-core waveguides for delivery of excitation and emission light, and thus as a mode filter prior to the grating, is a realistic option in practice, and is a subject we hope to explore in greater detail in future work. To approximate the fundamental mode of the square hollow input waveguide, a 40μm diameter Gaussian field was assumed as the input field at the start of the slab waveguide section.

Grating-based microspectrometers typically operate in the Fresnel diffraction regime, and thus can be treated using the Fresnel diffraction integral [69]:

$$E(x,z) = \int \sqrt{\frac{i}{\lambda.\Delta z}} * e^{-i.k^{eff}.\Delta z} * e^{-\frac{i.k^{eff}.(\Delta x)^2}{2*\Delta z}} * E(x_0, z_0) * dx \qquad (6\text{-}6)$$

where $E(x_0, z_0)$ is the input field, $\Delta x = x - x_0$, $\Delta z = z - z_0$, $k^{eff} = n \cdot 2\pi / \lambda$ and n is the effective refractive index of the medium. As mentioned above, the Fresnel formalism is the usual approximation used for scalar electromagnetic field simulations. In the present design, however, the collimating lens and the curved grating are very close, such that the minimum distance required for the validity of Fresnel diffraction is violated. As described in the following, we used the diffraction formula known as the Rayleigh-Sommerfeld integral, which is valid for propagation distances as short as a few wavelengths.

6.4.1. Rayleigh-Sommerfeld I diffraction formula

The Rayleigh-Sommerfeld diffraction model was first proposed by A. Sommerfeld [79]. The so-called Rayleigh-Sommerfeld diffraction integrals I & II can be written in terms of Hankel functions, as outlined by M. Totzek [71]. A step-by-step derivation of the Rayleigh-Sommerfeld I diffraction integral in terms of the first-order Hankel function of the first kind can be found in our recent publication [117] . The Rayleigh-Sommerfeld I diffraction integral in terms of the Hankel function is given by:

$$U_1(\rho) = \frac{ik^{eff}}{2} \int_{-b}^{b} H_1(k^{eff} \mid \rho - \rho' \mid) \cos(\vartheta) U_0(\rho') dx' \qquad (6\text{-}7)$$

Here, $U_0(\rho')$ is the initial field at the position of the input field (ρ' = (x', 0, z')),$U_1(\rho)$ is the diffracted field at the point of observation or output (ρ = (x, 0, z)), H_1 is the first-order Hankel function of the first kind, $| \rho - \rho' |$ is the distance between the input and output points, ϑ is the angle between the normal and the line from ρ' to ρ , and , $k^{eff} = n \cdot 2\pi / \lambda$ is the effective wavenumber.

This integral expresses the fact that the field at every output point is due to the sum of fields at all input points. The simulation routine (encoded in Matlab) uses a Gaussian electric field as input and calculates the resulting electromagnetic field intensity at the output plane, which is located at a distance $| \rho - \rho' |$ from the input.

Since there are several interfaces (lens, curved grating and output plane), the output obtained at the first interface is treated as the input for the next interface and so on.

6.4.2. Simulation of multiple wavelengths in the 2nd diffraction order

Figure 6.4 shows the intensity profiles at the output plane of the spectrometer, for a 40 μm diameter input Gaussian beam and five different wavelengths ranging from 532 to 758 nm, centered around the design wavelength of 645 nm. For clarity, the zero, first and second diffraction orders are labeled.

Consistent with the discussion in Section 2, the second-order diffracted beam at the design wavelength (λ = 0.645 μm, which is shown in red) appears at x = -1293 μm, directly in line with the first grating facet (see Fig. 6.3). At the lower left corner of Fig. 6.4, the zero order beams for all wavelengths are shown overlapping at a single position. The explanation is that the position of the zero order beam (regardless of wavelength) is determined only by Snell's law of refraction ($n_1.\sin\theta_1 = n_2.\sin\theta_2$) applied to the air-PDMS interface along the line of the grating. Here $n_1 = 1$, $n_2 = 1.43$ (i.e. assumed wavelength-independent), θ_1 is the angle of incidence, and θ_2 is the angle of refraction. According to the simulation, the position of the zero order beams is at -2734μm. Since the horizontal distance (on the optical axis) from the grating centre to the output plane is 9224 μm, we can substitute $\theta_2 = [\theta_1 - \tan^{-1}(2734 / 9224)]$ into Snell's law to obtain an estimate for the effective incident angle, $\theta_1 = 47.6^o$, which is in agreement with the geometrical estimate from Section 6.3. This provides further evidence that good qualitative predictions are obtained by approximating the curved grating as a straight grating, in turn approximated by the central ~150 grating facets in the vicinity of the optical axis.

In keeping with the discussion in Section 6.3, we can thus use the diffraction equation Eq. (6-3) to obtain an analytical estimate of the position of any wavelength in any given order. For example, consider the second-order (m = +2) diffraction of λ = 0.532 μm light. Using $n_1 = 1$, $n_2 = 1.43$, $\theta_1 = 47.6^o$, m = 2, λ = 0.532 μm and Λ = 7.4 μm for the mean value of the grating period near the

optical axis, we obtain $\theta_2 = 38.1^o$ as the angle of diffraction. As above, the angle with respect to the optical axis follows as $\theta_2 - \theta_1 = -9.54^o$. The position on the output plane is then obtained as tan $(-9.54^o) \times$ 9224 μm = -1551 μm. As shown in Fig. 6.4, the simulated results are in nearly exact agreement with this analytical prediction.

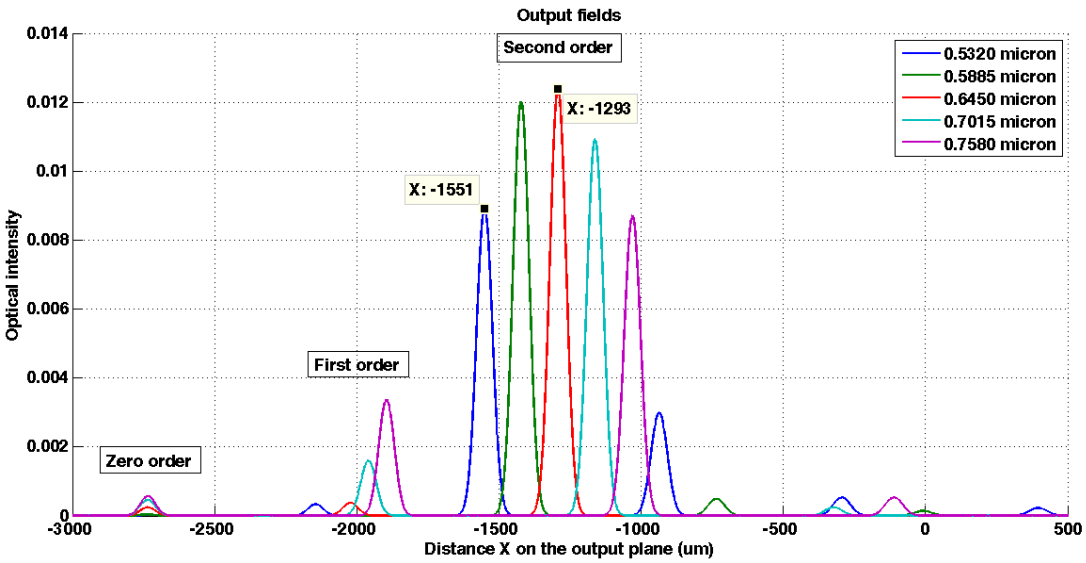

Fig. 6.4: The intensity profile at the output plane is shown, for a 40 μm input Gaussian beam and wavelengths ranging from 532 to 758 nm. The zero, first and second diffracted orders are labeled accordingly.

6.4.3. Simulation of multiple orders at a single wavelength

Figure 6.5 shows the predicted intensity profile at the output plane, for the same Gaussian input beam mentioned above, and for λ = 0.532 μm. Note that the horizontal axis encompasses 10 diffracted orders and that the intensity is plotted on a logarithmic scale. The position of each order at the output plane (X_m) is indicated on the plot. As expected from the design criteria above, the 2nd diffracted order (i.e. the design order) is located at X_2 = -1551 μm and has the highest intensity. Given the distance from the grating centre to the output plane mentioned above (Z = 9224 μm) , the angle (θ_m) between a given order and the optical axis is obtained from tan(θ_m) = X_m/Z. The relative angles between successive orders were extracted from the simulation in this way, and are compared to the experimental results in Section 6.6 below.

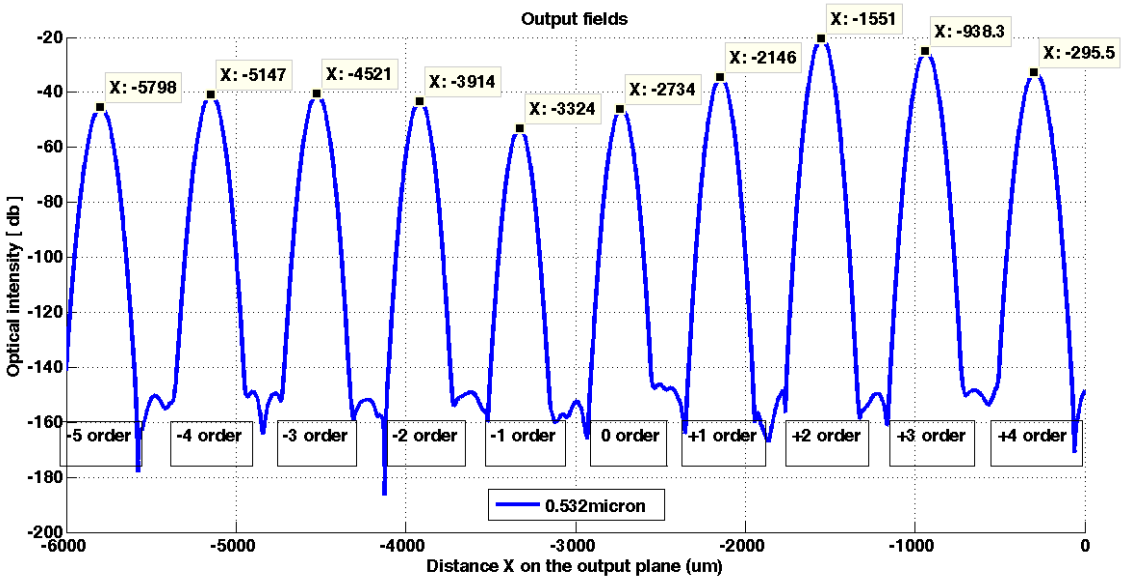

Fig. 6.5: The intensity profile at the output plane is plotted, for an input Gaussian beam and $\lambda = 0.532\mu m$. The horizontal axis was scaled to encompass 10 diffracted orders as indicated by the labels, including the m=+2 design order centered at – 1551μm.

6.5 Method of Fabrication

The main details of our fabrication process, which enables the integration of optical and fluidic components in a monolithic LOC platform, have been described elsewhere [109]. Briefly, the planar system (Fig. 6.6.a) comprises three layers of PDMS. The upper and lower layers are Sylgard-184®, which has a refractive index of 1.41, while the central layer is a higher index (n ~ 1.43) formulation of PDMS. The higher index PDMS is patterned using a soft-lithography molding technique, to simultaneously define both fluidic channels and optical waveguide channels (i.e. waveguide cores) within the same layer. Because of the index contrast with the upper and lower cladding layers, light can be confined within the central "optofluidic" layer, also referred to as the core layer. Furthermore, channel waveguides are enabled by the in-plane refractive index offset between the PDMS core and the adjacent air channels (i.e. 'side claddings', see Fig. 6.6 and Fig. 6.1 above). As briefly discussed in Section 6.2, the side claddings themselves were found to function as excellent air-core, leaky waveguides while providing a desirable suppression of high-order modes. For the

experimental characterization of the grating described below, these air-core waveguides were used for the in-coupling of laser light

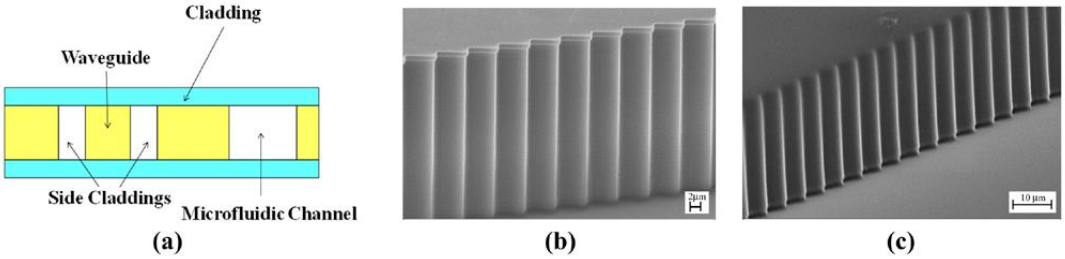

Fig. 6.6: (a) A schematic illustration of the integration strategy is shown. The diagram represents the cross-sectional view of the 3-layer PDMS system with waveguides and microfluidic channels patterned in the higher-index, central PDMS layer. (b) SEM image of the grating facets on the silicon master. (c) SEM image of the grating facets transferred to PDMS using a soft-lithography process.

A single silicon master (see Fig. 6.1) was used to pattern the entire optofluidic chip, including microchannels, waveguides, the lens, and the curved focusing transmission grating. From a fabrication tolerance perspective, the curved grating represents the most critical aspect of the fabrication process. In particular, it is important that the grating facets on the silicon master are smooth and vertical. As shown in Fig. 6.6(b), this was accomplished using the well-known "Bosch®" deep reactive ion etching (DRIE) process. Furthermore, proper operation of the grating relies on an accurate transfer of these facets into the PDMS waveguide core layer. As shown in Fig. 6.6(c), excellent replication of the grating features was achieved using an optimized soft-lithography process [11].

6.6 Experimental results

In order to verify the functionality of the grating/lens combination, we first launched a green laser into one of the air-core leaky waveguides aligned with the optical axis. This ensured that the light field was nearly single-moded at the start of the slab waveguide section prior to the lens, and was approximately aligned with the centre of the grating. Diffraction effects were studied by imaging the light scattered from the waveguide core layer onto a color camera mounted on top of a standard zoom microscope. This circumvented the problem of preparing a

high-quality facet at the output plane of the chip, although end-facet light collection was also verified (not shown) and would likely be the most desirable configuration in practice. As expected and shown in Fig. 6.7(a), the input light was dispersed into a number of diffraction orders. As described in Section 6.2, the grating is designed to diffract light preferentially into the second diffraction order. Consistent with this 'blaze' condition, the second-order beam was observed to be significantly brighter than those of adjacent orders. As an initial assessment of the grating, we measured the angles between consecutive diffracted orders, and compared the results to the predictions of the numerical simulations from Section 6.4. The comparison is summarized in Table 6.1, and reveals excellent agreement between experimental and numerical results.

Table 1 - Relative angles between adjacent orders

Orders	3, 2	2, 1	1, 0	0, -1	-1, -2	-2, -3	-3, -4	-4, -5
Simulation (degrees)	3.76^o	3.56^o	3.41^o	3.31^o	3.17^o	3.12^o	3.05^o	2.99^o
Experiment (degrees)	3.76^o	3.54^o	3.42^o	3.24^o	3.15^o	3.08^o	3.09^o	2.95^o

We performed similar experiments using other laser sources, including a red laser with wavelength $\lambda = 632$ nm (Fig. 6.7(b)) and an amber laser with wavelength $\lambda = 594$ nm (Fig. 6.7.(c)). Data from these experiments was used to quantify the dispersion and resolution of the grating. A key figure of merit for a spectrometer is the resolving power (RP), commonly expressed as $RP \equiv \lambda / d\lambda$, where $d\lambda$ is the resolution, in turn defined by the full width half maximum (FWHM) or -3db power bandwidth for the fringe of interest. Most microspectrometers reported in the literature have a RP in the range of ~10 -100 [55].

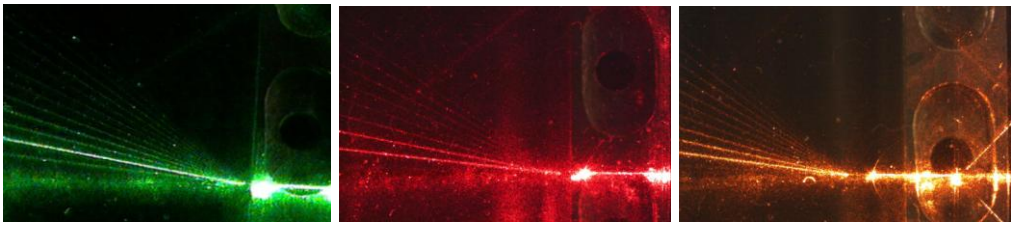

(a) **(b)** **(c)**

Fig. 6.7: Scattered light images captured by a color camera are shown. The images correspond to diffraction of a green laser, $\lambda = 532$ nm (a), a red laser, $\lambda = 632$ nm (b), and an amber laser, $\lambda = 594$ nm (c). The light path, including the input waveguide, spherical lens interface, and diffraction grating interface, are most clearly visible in part (c).

In order to experimentally assess the optical resolution of the grating, we observed the second-order diffraction fringes produced by two laser sources. Figure 6-8 plots the average pixel intensity versus distance along the output plane for the second order diffracted modes associated with 594 and 532 nm laser light. These lasers were coupled into the same air–core leaky waveguide, and scattered light images were captured near the output end of the device. Column-wise averaging of the pixel intensity was used to reduce noise. Device features of known size were used to scale the images and to enable a mapping between pixel number and spatial coordinates. Based on this mapping, the resolution was estimated from $d\lambda \sim dx/(\Delta x/\Delta\lambda)$, where $\Delta\lambda$ is the known wavelength spacing between the two lasers. Resolution as good as ~6nm was extracted from such measurements (i.e. RP ~ 100) ; a typical example is shown in Fig. 6.8. For a grating, RP ~ mN , where N is the number of grating facets contributing to the interference fringes. From the experimental estimate of the second-order RP above, this suggests ~ 50 facets are effectively illuminated by the input laser beam, which is reasonably well supported by close inspection of the images in Fig. 6.7. However, it is also likely that fabrication defects contributed to the lowering of the measured RP. Optimization for these details is left for future work.

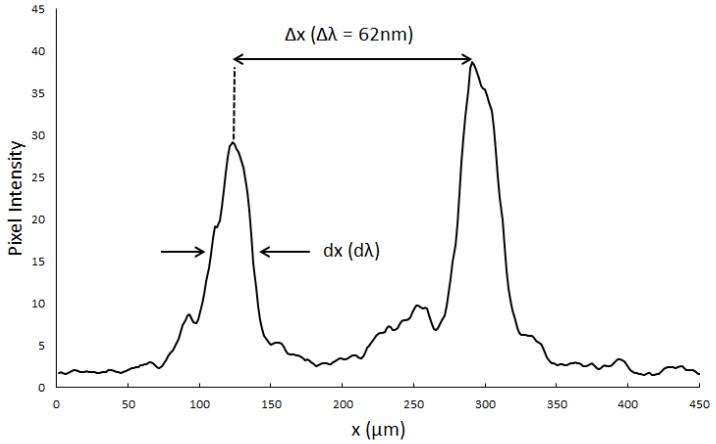

Fig. 6.8: Average pixel intensity plotted versus vertical distance x along the output plane for the 2nd order diffracted modes of 594 nm (left peak) and 532 nm laser light (right peak).

6.7 Concluding remarks

To our knowledge, this is the first report of a slab-waveguide-based transmission grating fabricated directly in PDMS. The parameters of the microspectrometer (RP~100 and a free spectral range >200 nm in the visible region) compare favorably to most other microspectrometers reported in the literature. Moreover, these performance specifications should be adequate to address many applications of current interest in LOC analysis systems, including visible-band fluorescence and absorptance spectroscopy. Furthermore, since the device is fabricated directly in PDMS, it offers good potential for monolithic integration within LOC and optofluidic microsystems.

We expect that the RP of the grating could be improved by optimization of the light collection and collimation prior to the grating, to increase the number of illuminated facets. Furthermore, it should be possible to fabricate significantly smaller grating facets in PDMS using an optimized soft-lithography process, thereby increasing the spectral dispersion and RP of the spectrometer. These refinements are left for future work.

CHAPTER 7

7. Spectral detection of moving emitters

In this chapter we disclose a novel strategy for wavelength sensing in grating-based spectroscopic devices using a single sensitive point detector such as a PMT.

7.1 Development of a Robust Detection Scheme

The most common approach for spectral detection in LOC spectrometer devices is to use a CCD camera or an array of photodetectors placed at the edge of the chip. Another option is to use custom built integrated photodiode arrays. For example, a number of MEMS-based spectrometers using custom built photodiode arrays were discussed by Wolfenbuttal [54, 55]. For cheap, portable, handheld systems, avalanche photodiodes may be used in place of the bulkier and more expensive CCD camera. In the following, we propose alternative strategies based on a single fixed detector (i.e. a PMT) for dynamic detection of spectral information from moving fluorescent particles.

7.1.1 Dynamic Strategies for Optical Spectral Sensing

First, consider the dynamic detection strategy for obtaining spectra from moving fluorescent particles depicted in Fig. 7-1[6]. In the approach depicted, a single fixed detector is placed in the output plane, and used to capture the spectrum of a moving, fluorescing particle as it passes in front of the grating (thus causing the diffraction pattern to sweep spatially across the output plane, so that the spectrum can be de-convolved from the time dependence of the detected power).

[6] The late professor J. N. McMullin is gratefully acknowledged for suggesting some of the underlying ideas for the work described in this chapter.

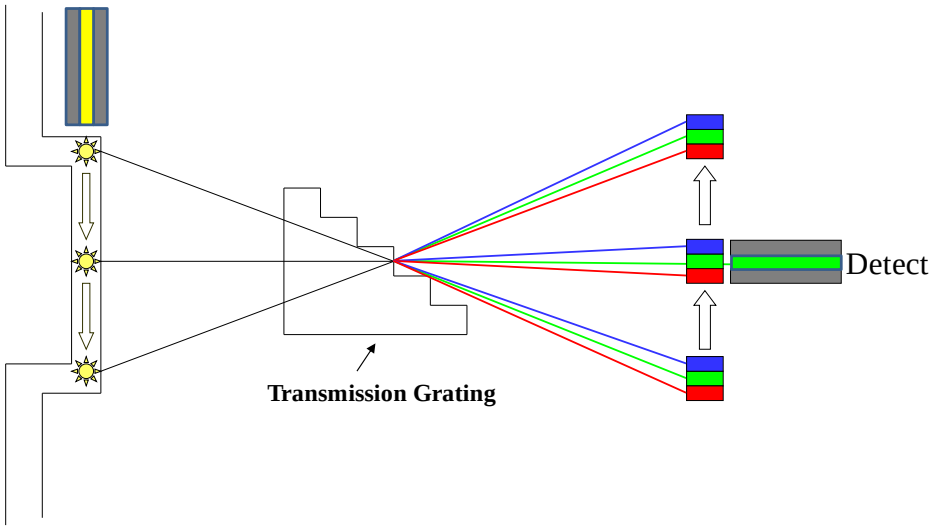

Fig. 7.1: Schematic description: A dynamic strategy for spectroscopic detection of moving fluorescent microparticles. As a microparticle moves down the microchannel, its spectrum moves in the opposite direction. A waveguide positioned at an appropriate position (on the right edge of the microspectrometer) can sequentially detect the entire spectrum.

A preliminary theoretical analysis of this strategy was reported previously [118]. An important feature and motivation for that work was that, using an Echelle transmission grating of modest feature sizes (grating step = 3.56 μm and grating facet width = 5.7 μm), a 200-nm spectrum with 10-nm resolution might be obtained using a single sensitive PMT.

7.1.2 A Novel Method for Wavelength Sensing

In line with these ideas, we explored another novel detection strategy based on using multiple diffracted orders of the grating. The idea is quite simple, and relies on the fact that the separation between the diffracted orders is a wavelength dependent quantity. Thus the separation of two neighboring orders can be used as a wavelength sensing mechanism. To illustrate the idea we first performed simulations using the curved focusing transmission grating described in Chapter 6 [119]. In the first set of simulations, we placed an input Gaussian beam at the focal point of the collimating lens (Fig. 6.7) on the optical axis (x = 0) and looked at the position of diffracted orders at the output plane for a number of

wavelengths. From these simulations we obtained the distance between two neighboring orders (i.e. between 2nd and 3rd order or 1st and 2nd order, etc.). Table 7.1 shows the distance between first and second diffracted orders in μm for wavelengths between 500 to 800 nm, according to simulation.

Wavelength (nm)	500	525	550	575	600	625	650	675	700	725	750	775	800
Spacing (μm) 1st & 2nd	556	586	614	642	672	702	733	763	791	821	851	882	912.2

Table 7.1: Spacing (μm) between first and second diffracted orders for different wavelengths

Figure 7.2 shows the Excel plot of the spacing between first and second grating orders versus wavelength.

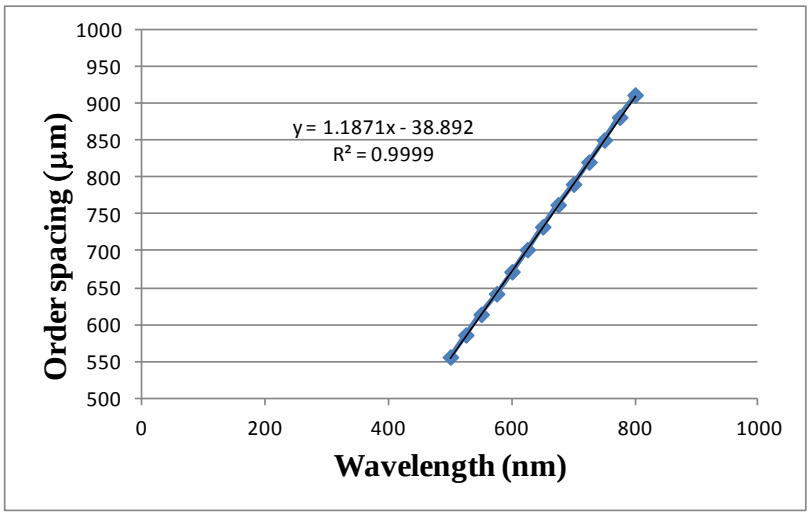

Fig. 7.2: Spacing between first and second diffracted orders versus wavelength.

Thus, from the linear relationship between wavelength and order spacing, it should be possible to extract the wavelength of a source from the measured order spacing. For example the output intensity profile for an input signal of 560 nm is

shown in Fig. 7.3. This wavelength is representative of orange fluorescent beads that are available from Invitrogen (orange Fluospheres).

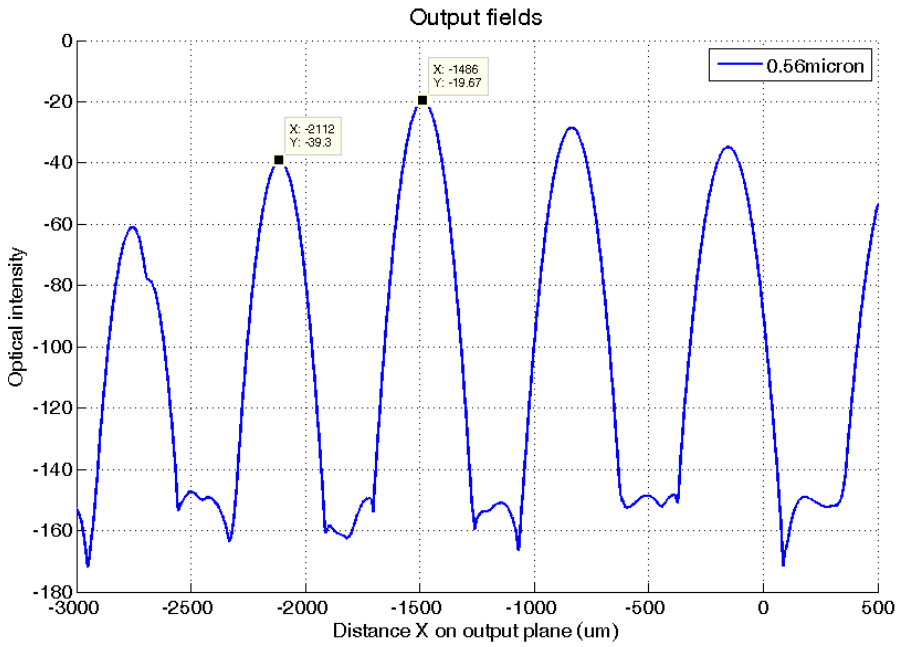

Fig. 7.3: Position of diffracted orders in the focusing grating microspectrometer for $\lambda = 560$ nm.

As can be seen, the separation between first and second orders according to simulation is: 2112 μm - 1486 μm = 626 μm, which is in agreement with the graphical result in Fig. 7.2.

This result is interesting, since it suggests we can identify the wavelength of a source from the distance between orders, without knowing the spectral composition of diffracted light within the individual orders. However, we would still need an array of detectors at the output plane to find the separation between orders.

In the next set of simulations, we placed a 70 μm detector at a fixed point (ex. 0 or -1293 μm) at the output plane and started a sequential shift of the input field at the input plane that resembled a moving fluorescing particle. The power was integrated over a 70 μm distance (the span of detection region) at the output plane. These simulations allowed us to determine the input position that would cause a given order at a given wavelength to appear at the position of the detector.

Figure 7.4 is the result of a simulation showing second and third diffracted orders appearing at the output for λ = 532 nm.

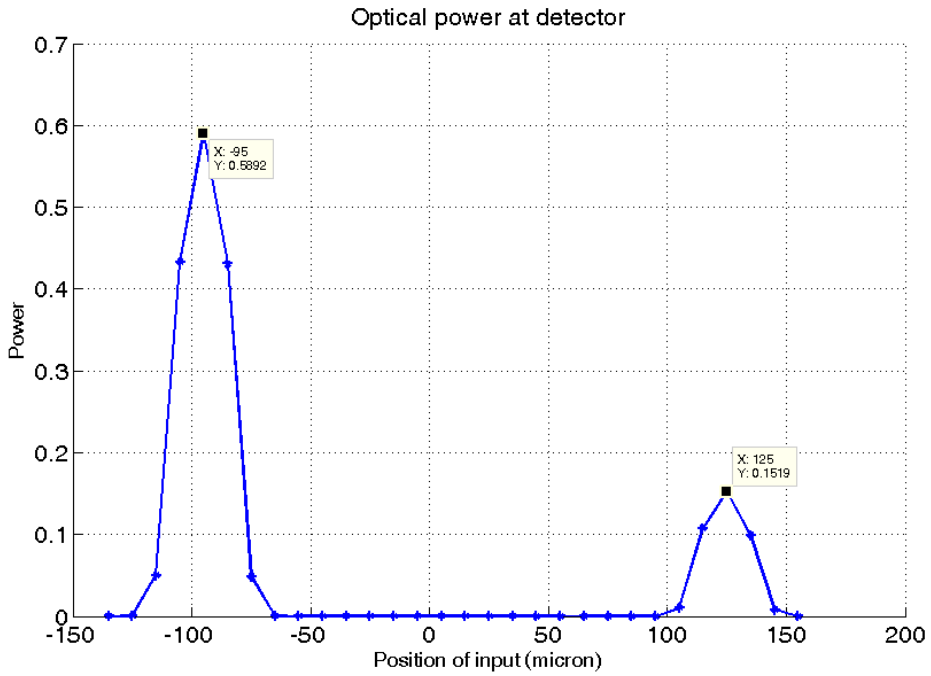

Fig. 7-4. Detected power versus particle position for the second (left peak) and the third (right peak) diffracted orders at a 70 μm wide detector positioned at -1293 μm at the output plane (λ = 532 nm).

Based on this simulation, when a moving particle (with peak fluorescent intensity at λ = 532 nm) is at -95 μm from the optical axis, the second order appears at the position of the detector (-1293 μm), and when the moving particle is at +125 μm from the optical axis, the third order appears at the detector. We performed simulations for a range of wavelengths, to position the 1st & 2nd orders at the detector (-1293 μm) or to position the 2nd & 3rd orders at the detector. The simulation results for the latter case are shown in Table 7.2 and Table 7.3.

Wavelength (nm)	500	525	532	550	560	575	594	600
Particle Position (μm)	-122.4	-101	-95	-80	-71.4	-58.7	-43	-37.7

Table 7.2: The position of moving particles (wavelengths 500 to 600 nm) in order to have the second diffracted order to appear at the position of the fixed detector (-1293 μm)

Wavelength (nm)	500	525	532	550	560	575	594	600
Particle Position (μm)	86.5	117	125	146.5	157.9	175.5	197.3	204

Table 7.3: The position of moving particles (wavelengths 500 to 600 nm) in order to have the third diffracted order to appear at the position of the fixed detector (-1293 μm)

Next, we calculated the spacing between input particle positions using the data provided in Table 7.2 and Table 7.3 and the results are shown in Table 7.4 and plotted in Fig. 7.5.

Wavelength (nm)	500	525	532	550	560	575	594	600
Spacing (μm)	208.9	218	220	226.5	229.3	234.2	240.3	241.7

Table 7.4: The spacing between input particle positions for wavelengths from 500 to 600 nm

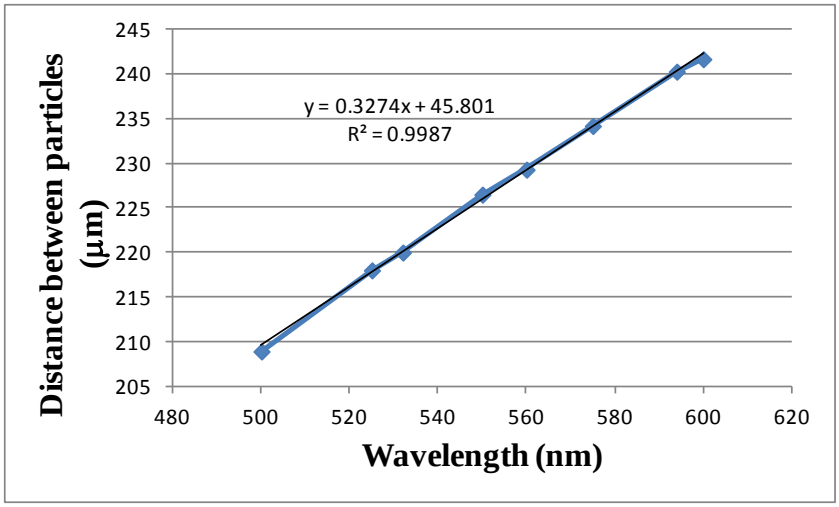

Fig. 7-5. Distance between input particle positions corresponding to the two peaks (2nd and 3rd diffracted orders) at the detector versus wavelength.

Thus, If we know the velocity of the moving particle, we can calculate the spacing between input particle positions corresponding to the two peaks from the time dependent signal recorded by a detector (for example a PMT). Using the value obtained for the spacing, the wavelength of the fluorescing particle can be extracted from the linear relationship in Fig. 7.5.

We believe that this idea represents a fundamentally new strategy for the spectral detection of fluorescent particles. For example, it would allow the counting and sorting of two or more types of particles that are uniquely labeled to fluoresce at different wavelengths. Compared to using a conventional spectrometer approach, the system described requires only a single sensitive detector, rather than a detector array. Moreover, PMT's are widely used for fluorescence studies in LOC systems.

Supporting experiments and corroboration of the results with first order diffraction theory are the subjects of ongoing work, and we hope to report the results elsewhere.

CHAPTER 8

8. Chapter summaries and suggested future work

8.1 Chapter summaries

8.1.1 Chapter 2 summary

Chapter 2 is intended to serve as an introductory chapter for the diffraction material presented in later chapters. Although brief, a historical overview on the development of diffraction theory, similarly, diffraction gratings is provided. Grating equation is presented and key diffraction grating principles are discussed. The final part of this chapter is devoted to the scalar treatment of the theory of diffraction and the solution of diffraction integral using Green's theorem followed by Rayleigh-Sommerfeld, Fresnel and Fraunhoffer approximations.

8.1.2 Chapter 3 summary

An overview of the optofluidic microsystems studied in this research, and their high level design details are provided. Simulation tools, based on Fresnel diffraction integral were developed, and their accuracy was verified analytically in a number of different grating structures and optical systems. In order to accommodate diffraction effects in the near field region, simulations based on Rayleigh-Sommerfeld I diffraction model, were implemented.

8.1.3 Chapter 4 summary

Simulations of the Huygens, Fresnel, and Rayleigh–Sommerfeld I approximations in the case of free-space propagation of a Gaussian beam were compared with analytical solutions. The most accurate results were obtained by the Rayleigh–Sommerfeld I approximation. This study reveals that the approximations are not uniform throughout the propagation region. While the accuracies of the Huygens and Fresnel methods generally increase as the propagation distance increases, the

accuracy of the Rayleigh–Sommerfeld I approximation at first starts to diminish and later recovers as the propagation distance is further increased.

8.1.4 Chapter 5 summary

Development of a new LOC integration strategy, and its use for fluorescence detection is the subject of this chapter. A general method is described for the fabrication of polydimethylsiloxane (PDMS) lab-on-a-chip (LOC) devices with integrated optic and fluidic elements. The PDMS core layer containing the optic and fluidic components is cast and cured under pressure on a silicon master. Subsequently, outer layers of lower-index PDMS are bonded to the core layer to provide optical and fluidic confinement. The functionality of the waveguides and microchannels is demonstrated by the detection and identification of two different types of fluorescent polystyrene beads in a pressure-driven flow inside a microfluidic channel in a device fabricated by this process.

8.1.5 Chapter 6 summary

Development of a novel focusing grating-based microspectrometer and its integration into a PDMS optofluidic system is presented. Using methods described in Chapter 5 (see above), a monolithic integration of microfluidic channels, optical waveguides, a collimating lens and a curved focusing transmission grating in a single PDMS-based microsystem is demonstrated. Here, we focus on the design and characterization of the microspectrometer part, which employs a novel self-focusing strategy based on cylindrical facets, and exhibits resolution <10 nm in the visible wavelength range. The dispersive behavior of the grating was analyzed both experimentally and using numerical simulations, and the results are in good agreement with simplified analytical predictions.

8.1.6 Chapter 7 summary

A novel strategy is proposed to identify the color of a fluorescent particle, using a fixed grating and a single detector. Based on the simulation results obtained using the focusing grating microspectrometer, the spacing between two adjacent grating orders is a wavelength-dependent quantity, which suggests that we can identify the wavelength of a source, simply from the distance between orders, without

knowing the full spectral composition in that order. But more interesting results were obtained through simulations of moving emitters (of particular wavelength) in front of the grating, using a single detector fixed at an arbitrary location at the microspectrometer exit. As a fluorescing particle is moving in a microfluidic channel directly across the grating, the diffracted orders sequentially sweep across the detector. For every intensity peak (i.e. diffracted order) at the detector, there is a corresponding position for the particle in the channel. We performed these simulations for two adjacent orders (i.e. 2^{nd} and 3^{rd}), and for a range of wavelengths and obtained the corresponding particle positions for the two peaks. Interestingly, particle spacing was also linearly related to wavelength. Thus, if we know the velocity of the moving particle, we can calculate the spacing between input particle positions, corresponding to adjacent peaks from the time dependent signal recorded by a detector (for example a PMT). Using the value obtained for the spacing, the wavelength of the fluorescing particle can be extracted from the linear relation between particle spacing and wavelength.

8.2 Suggested future work

While proof-of-principle experimental results were described, there is significant scope for future work. For example, functionality of the fabricated devices should be experimentally tested using fluorescent dyes and fluorescent microparticles. Ultimately, similar experiments could be performed using fluorescently tagged living cells. It should also be possible to improve the quality of devices, as follows.

The fabrication process of the silicon master might be further optimized, to reduce the surface roughness in order to minimize waveguide propagation losses as well as optical scattering losses at the facets and the surfaces of the lens.

Using an optimized soft-lithography process, it should furthermore be possible to fabricate significantly smaller grating facets. For example, by reducing the size of the facets from 6 μm to 3 μm, the acquired dispersion and, in turn, resolution might be doubled.

It might also be possible to automate the fabrication of the chips by using a hot embossing process. A process plan for this method of fabrication might use Cyclic-Olefin-Copolymer (C-O-C) elastomer (i.e. Topas 8007) which is a glass-like transparent material with refractive index slightly higher (1.53-1.54 in the visible range) than glass (~1.52).

The steps of the proposed fabrication process are as follows:

- Spin-coat a thin layer (~50 μm) of C-O-C on a glass wafer and cure;
- Use a silicon master as the stamp in hot-embossing equipment to make the optofluidic components in the thin layer of C-O-C produced in the first step;
- Bond a second glass wafer in order to seal the device and provide an upper cladding;
- Dice the wafer in to individual microspectrometer chips.

This process could potentially be used for mass-production.

Bibliography

[1] C. P. Bacon, Y. Mattley, and R. DeFrece, "Miniature spectroscopic instrumentation: applications to biology and chemistry," *Rev. Sci. Instrum.* , vol. 75, pp. 1-16, 2004.

[2] H. M. Widmer, "Trends in industrial analytical chemistry," *TrAC Trends in Analytical Chemistry*, vol. 2, pp. VIII-X, 1983.

[3] A. Manz, N. Graber, and H. M. Widmer, "Miniaturized total chemical analysis systems: A novel concept for chemical sensing," *Sensors and Actuators B: Chemical*, vol. 1, pp. 244-248, 1990.

[4] M. A. Northrup, M. T. Ching, R. M. White, and R. T. Watson, "DNA amplification in a microfabricated reaction chamber," presented at seventh international conference on solid-state sensors and actuators, 1993.

[5] D. J. Harrison, K. Fluri, K. Seiler, Z. Fan, C. S. Effenhauser, and A. Manz, "Micromachining a Miniaturized Capillary Electrophoresis-Based Chemical Analysis System on a Chip," *Science*, vol. 261, pp. 895-897, 1993.

[6] A. T. Woolley, D. Hadley, P. Landre, A. J. deMello, R. A. Mathies, and M. A. Northrup, "Functional Integration of PCR Amplification and Capillary Electrophoresis in a Microfabricated DNA Analysis Device," *Analytical Chemistry*, vol. 68, pp. 4081-4086, 1996.

[7] J. West, M. Becker, S. Tombrink, and A. Manz, "Micro Total Analysis Systems: Latest Achievements," *Analytical Chemistry*, vol. 80, pp. 4403-4419, 2008.

[8] T. Vilkner, D. Janasek, and A. Manz, "Micro Total Analysis Systems. Recent Developments," *Analytical Chemistry*, vol. 76, pp. 3373-3386, 2004.

[9] P. S. Dittrich, K. Tachikawa, and A. Manz, "Micro Total Analysis Systems. Latest Advancements and Trends," *Analytical Chemistry*, vol. 78, pp. 3887-3908, 2006.

[10] P.-A. Auroux, D. Iossifidis, D. R. Reyes, and A. Manz, "Micro Total Analysis Systems. 2. Analytical Standard Operations and Applications," *Analytical Chemistry*, vol. 74, pp. 2637-2652, 2002.

[11] D. R. Reyes, D. Iossifidis, P.-A. Auroux, and A. Manz, "Micro Total Analysis Systems. 1. Introduction, Theory, and Technology," *Analytical Chemistry*, vol. 74, pp. 2623-2636, 2002.

[12] H. A. Stone and S. Kim, "Microfluidics: Basic issues, applications, and challenges," *AIChE Journal*, vol. 47, pp. 1250-1254, 2001.

[13] D. J. Beebe, G. A. Mensing, and G. M. Walker, "PHYSICS AND APPLICATIONS OF MICROFLUIDICS IN BIOLOGY," *Annual Review of Biomedical Engineering*, vol. 4, pp. 261, 2002.

[14] G. M. Whitesides and A. D. Stroock, "Flexible Methods for Microfluidics," *Physics Today*, vol. 54, pp. 42-48, 2001.

[15] M. J. Madou and G. J. Kellogg, "LabCD: a centrifuge-based microfluidic platform for diagnostics," presented at Systems and Technologies for Clinical Diagnostics and Drug Discovery, San Jose, CA, USA, 1998.

[16] S. C. Bayliss, L. D. Buckberry, P. J. Harris, and M. Tobin, "Nature of the silicon animal cell interface," *Journal of Porous Materials*, vol. 7, pp. 191-195, 2000.
[17] J. D. Birchall and J. S. Chappel, "The chemistry of aluminum and silicon in relation to Alzheimer's disease," *Clin. Chem*, vol. 34, pp. 265 - 267, 1988.
[18] J. D. Birchall and A. W. Espie, "Biological implications of the interaction (via
silanol groups) of silicon with metal ions," presented at Ciba Foundation Symposium, Chichester, UK, 1986.
[19] L. L. Hench and J. Wilson, "Biocompatibility of silicates for medical use," presented at Ciba Foundation Symposium, Chichester, UK, 1986.
[20] C. O'Neil, P. Jordan, T. Bhatt, and R. Newman, "Silica and oesophageal cancer " presented at Ciba Foundation Symposium Chichester, UK, 1986.
[21] A. Hierlemann, O. Brand, C. Hagleitner, and H. Baltes, "Microfabrication Techniques for Chemical/Biosensor," *Proceedings of the IEEE*, vol. 91, pp. 839 - 863, 2003.
[22] E. Verpoorte and N. F. D. Rooij, "Microfluidics Meets MEMS," *Proceedings of the IEEE*, vol. 91, pp. 930-953, 2003.
[23] J. Voldman, M. L. Gray, and M. A. Schmidt, "Microfabrication in Biology and Medicine," *Annual Review of Biomedical Engineering*, vol. 1, pp. 401-425, 1999.
[24] M. K. N. Jessamine, G. Irina, D. S. Abraham, and M. W. George, "Components for integrated poly(dimethylsiloxane) microfluidic systems," *ELECTROPHORESIS*, vol. 23, pp. 3461-3473, 2002.
[25] A. S. Holmes, "Laser fabrication and assembly processes for MEMS," presented at Proc. SPIE, San Jose, CA 2001.
[26] H. Lorenz, M. Despont, N. Fahrni, N. LaBianca, P. Renaud, and P. Vettiger, "SU-8: a low-cost negative resist for MEMS," *Journal of Micromechanics and Microengineering*, vol. 7, pp. 121-124, 1997.
[27] C. M. Klapperich, "Microfluidic diagnostics: time for industry standards," *Expert Review of Medical Devices*, vol. 6, pp. 211-213, 2009.
[28] Y. Changqing, Z. Qi, L. Cheuk-Wing, Y. Jun, Z. Jianlong, and Y. Mengsu, "Optical and electrochemical detection techniques for cell-based microfluidic systems," in *Analytical & Bioanalytical Chemistry*, vol. 384: Springer Science & Business Media B.V., 2006, pp. 1259-1268.
[29] P. S. Dittrich and A. Manz, "Single-molecule fluorescence detection in microfluidic channels-the Holy Grail in μTAS?," *Analytical & Bioanalytical Chemistry*, vol. 382, pp. 1771-1782, 2005.
[30] A. Llobera, S. Demming, R. Wilke, and S. Buttgenbach, "Multiple internal reflection poly(dimethylsiloxane) systems for optical sensing," *Lab on a Chip*, vol. 7, pp. 1560-1566, 2007.
[31] S. Blair and Y. Chen, "Resonant-Enhanced Evanescent-Wave Fluorescence Biosensing with Cylindrical Optical Cavities," *Appl. Opt.*, vol. 40, pp. 570-582, 2001.

[32] N. J. Goddard, S. Mohr, K. Singh, J. Hulme, R. J. Holmes, K. Joyce, F. Bounaira, and P. R. Fielden, "Leaky Waveguide Devices as Simple Sensitive Optical Detectors for Use in μTAS Applications," presented at MicroTec 2000, Hannover, Germany, 2000.

[33] A. Ymeti, J. Greve, P. V. Lambeck, T. Wink, H. van, Beumer, R. R. Wijn, R. G. Heideman, V. Subramaniam, and J. S. Kanger, "Fast, Ultrasensitive Virus Detection Using a Young Interferometer Sensor," *Nano Letters*, vol. 7, pp. 394-397, 2007.

[34] A. Ymeti, J. Greve, P. V. Lambeck, T. Wink, S. W. F. M. v. Hövell, T. A. M. Beumer, R. R. Wijn, R. G. Heideman, V. Subramaniam, and J. S. Kanger, "Fast, Ultrasensitive Virus Detection Using a Young Interferometer Sensor," *Nano Letters* vol. 7, pp. 394–397, 2007.

[35] F. B. Myers and L. P. Lee, "Innovations in optical microfluidic technologies for point-of-care diagnostics," *Lab on a Chip*, vol. 8, pp. 2015-2031, 2008.

[36] T. M. Chinowsky, J. G. Quinn, D. U. Bartholomew, R. Kaiser, and J. L. Elkind, "Performance of the Spreeta 2000 integrated surface plasmon resonance affinity sensor," *Sensors and Actuators B: Chemical*, vol. 91, pp. 266-274, 2003.

[37] F. B. Myers and L. P. Lee, "Innovations in optical microfluidic technologies for point-of-care diagnostics," *Lab Chip, 2008, 8, 2015–2031*, vol. 8, pp. 2015–2031 2008.

[38] J. N. Anker, W. P. Hall, O. Lyandres, N. C. Shah, Z. Jing, and R. P. Van Duyne, "Biosensing with plasmonic nanosensors," *Nature Materials*, vol. 7, pp. 442-453, 2008.

[39] M. Fleischmann, P. J. Hendra, and A. J. McQuillan, "Raman spectra of pyridine adsorbed at a silver electrode," *Chemical Physics Letters*, vol. 26, pp. 163-166, 1974.

[40] G. L. Liu and L. P. Lee, "Nanowell surface enhanced Raman scattering arrays fabricated by soft-lithography for label-free biomolecular detections in integrated microfluidics," *Applied Physics Letters*, vol. 87, pp. 074101-3, 2005.

[41] B. Herman, *Fluorescence Microscopy*. Berlin, Heidelberg, NewYork: Springer-Verlag, 1998.

[42] F. H. Kasten, "Introduction to fluorescent probes: Properties, history and applications," in *Fluorescent and Luminescent Probes for Biological Activity*, W. T. Mason, Ed. London: Academic Press, 1993, pp. 12-33.

[43] J.-C. Roulet, "Microoptical systems for fluorescence detection in chemical Microsystems (Ph.D Thesis)," Universite de Neuchatel-Institut de microtechnique, 2001.

[44] A. Periasamy, *Methods in Cellular Imaging, Part I*: Oxford University Press, 2001.

[45] J. F. James and R. S. Sternberg, *The Design of Optical Spectrometers*. London: Chapman and Hall LTD, 1969.

[46] S. Grabarnik, R. Wolffenbuttel, A. Emadi, M. Loktev, E. Sokolova, and G. Vdovin, "Planar double-grating microspectrometer," *Opt. Express*, vol. 15, pp. 3581-3588, 2007.

[47] S. P. Perfetto, P. K. Chattopadhyay, and M. Roederer, "Innovation: Seventeen-colour flow cytometry: unravelling the immune system," *Nature Reviews Immunology*, vol. 4, pp. 648-655, 2004.

[48] D. S. Goldman, P. L. White, and N. C. Anheier, "Miniaturized spectrometer employing planar waveguides and grating couplers for chemical analysis," *Appl. Opt.*, vol. 29, pp. 4583-4589, 1990.

[49] J. Mohr, B. Anderer, and W. Ehrfeld, "Fabrication of a planar grating spectrograph by deep-etch lithography with synchrotron radiation," *Sensors and Actuators A: Physical*, vol. 27, pp. 571-575, 1991.

[50] D. Sander and J. Müller, "Selffocussing phase transmission grating for an integrated optical microspectrometer," *Sensors and Actuators A: Physical*, vol. 88, pp. 1-9, 2001.

[51] G. M. Yee, N. I. Maluf, P. A. Hing, M. Albin, and G. T. A. Kovacs, "Miniature spectrometers for biochemical analysis," *Sensors and Actuators A: Physical*, vol. 58, pp. 61-66, 1997.

[52] O. Schmidt, M. Bassler, P. Kiesel, C. Knollenberg, and N. Johnson, "Fluorescence spectrometer-on-a-fluidic-chip," *Lab on a Chip*, vol. 7, pp. 626-629, 2007.

[53] S. Traut and H. P. Herzig, "Holographically recorded gratings on microlenses for a miniaturized spectrometer array," *Optical Engineering*, vol. 39, pp. 290-298, 2000.

[54] R. F. Wolffenbuttel, "MEMS-based optical mini- and microspectrometers for the visible and infrared spectral range," *Journal of Micromechanics and Microengineering*, vol. 15, pp. S145-S152, 2005.

[55] R. F. Wolffenbuttel, "State-of-the-art in integrated optical microspectrometers," *Instrumentation and Measurement, IEEE Transactions on*, vol. 53, pp. 197-202, 2004.

[56] G. Minas, R. F. Wolffenbuttel, and J. H. Correia, "An array of highly selective Fabry–Perot optical channels for biological fluid analysis by optical absorption using a white light source for illumination," *Journal of Optics A: Pure and Applied Optics*, vol. 8, pp. 272-278, 2006.

[57] G. Minas, J. C. Ribeiro, R. F. Wolffenbuttel, and J. H. Correia, "On-chip integrated CMOS optical detection microsystem for spectrophotometric analyses in biological microfluidic systems," presented at Industrial Electronics, 2005. ISIE 2005. Proceedings of the IEEE International Symposium on, 2005.

[58] N. Damean, S. K. Sia, V. Linder, M. Narovlyansky, and G. M. Whitesides, "Space- and time-resolved spectrophotometry in microsystems," *Proc Natl Acad Sci U S A*, vol. 102, pp. 10035-9, 2005.

[59] X. Michalet, O. H. W. Siegmund, J. V. Vallerga, P. Jelinsky, J. E. Millaud, and S. Weiss, "Detectors for single-molecule fluorescence imaging and spectroscopy," *Journal of Modern Optics*, vol. 54, pp. 239-281, 2007.

[60] W. E. Moerner and D. P. Fromm, "Methods of single-molecule fluorescence spectroscopy and microscopy," *Review of Scientific Instruments*, vol. 74, pp. 3597-3619, 2003.
[61] A. K. Luong, G. C. Gradinaru, D. W. Chandler, and C. C. Hayden, "Simultaneous time- and wavelength-resolved fluorescence microscopy of single molecules," *Journal of Physical Chemistry B*, vol. 109, pp. 15691-15698, 2005.
[62] J. W. Goodman, *Introduction to Fourier Optics* McGraw-Hill Inc., 1968
[63] M. Born and E. Wolf, *Principles of Optics*, 5th ed. ed: Pergamon Press, 1975.
[64] M. C. Hutley, *Diffraction Gratings*. New York: Academic Press, 1982.
[65] E. G. Loewen and E. Popov, *Diffraction gratings and applications*. New York: Marcel Dekker, Inc., 1997.
[66] "Diffraction Gratings: Background and Technology," Optometrics Corporation
[67] C. Palmer, *Diffraction Grating Handbook*, Fifth ed. New York: Thermo RGL Richardson Grating Laboratory, 2002.
[68] T. Tamir, *Integrated Optics*, vol. 7. Berlin: Springer-Verlag, 1979.
[69] H. A. Haus, *Waves and Fields in Optoelectronics*. Englewood Cliffs, N. J.: Prentice Hall, 1984.
[70] K. D. Möller, *Optics: Learning by Computing, with Examples Using MathCad*. New York: Springer-Verlag 2003.
[71] M. Totzeck, "Validity of the scalar Kirchhoff and Rayleigh-Sommerfeld diffraction theories in the near field of small phase objects," *J. Opt. Soc. Am. A*, vol. 8, pp. 27-32, 1991.
[72] C. J. Bouwkamp, "Diffraction theory," *Phys. Soc. Rep. Prog. Phys.*, vol. 17, pp. 35-100, 1954.
[73] A. E. Siegman, *Lasers*
Mill Valley, Calif.: University Science Books, 1986.
[74] A. S. Marathay and J. F. McCalmont, "Vector diffraction theory for electromagnetic waves," *J. Opt. Soc. Am. A* vol. 18, pp. 2585-2592, 2001.
[75] M. Abramowitz and I. A. Stegun, *Handbook of Mathematical Functions With Formulas, Graphs, and Mathematical Tables, 7th Printing*: National Bureau of Standards, 1986.
[76] X. Chen, J. N. McMullin, C. J. Haugen, and R. G. DeCorby, "Planar concave grating demultiplexer for coarse WDM based on confocal ellipses," *Opt. Commun.*, vol. 237, pp. 71-77, 2004.
[77] J. N. McMullin, R. G. DeCorby, and C. J. Haugen, "Theory and simulation of a concave diffraction grating demultiplexer for coarse WDM systems," *J. Lightwave Technol.* , vol. 20, pp. 758-765, 2002.
[78] C. Huygens, *Treatise on Light* New York: Dover Publications, Inc, 1962.
[79] A. Sommerfeld, *Optics*
vol. III of Lectures on Theoretical Physics, translated from German: (Academic Press), 1964.
[80] L. Eyges, *The Classical Electromagnetic Field*. Reading, Mass.: Addison-Wesley, 1972.

[81] K. B. Mogensen, H. Klank, and J. P. Kutter, "Recent developments in detection for microfluidic systems " *Electrophoresis* vol. 25 pp. 3498–512 2004

[82] O. Leistiko and P. F. Jensen, "Integrated bio/chemical microsystems employing optical detection: the clip-on " *Journal of Micromechanics and Microengineering*, vol. 8, pp. 148-150, 1998.

[83] P. Friis, K. Hoppe, O. Leistiko, K. B. Mogensen, J. Hubner, and J. P. Kutter, "Monolithic integration of microfluidic channels and optical waveguides in silica on silicon," *Applied Optics*, vol. 40, pp. 6246-6251, 2001.

[84] K. B. Mogensen, N. J. Petersen, J. Hübner, and J. P. Kutter, "Monolithic integration of optical waveguides for absorbance detection in microfabricated electrophoresis devices," *Electrophoresis*, vol. 22, pp. 3930–3938, 2001.

[85] H. Qiao, S. Goel, A. Grundmann, and J. N. McMullin, "Fabrication of micro-optical/microfluidic biochips," *Proceedings of SPIE*, vol. 4833, pp. 54-59, 2001.

[86] R. Mazurczyk, J. Vieillard, A. Bouchard, B. Hannes, and S. Krawczyk, "A novel concept of the integrated fluorescence detection system and its application in a lab-on-a-chip microdevice," *Sensors and actuators. B, Chemical* vol. 118, pp. 11-19, 2006.

[87] D. Spicer, J. N. McMullin, and H. Rourke, "A multi-layer biochip with integrated hollow waveguides," *Journal of Micromechanics and Microengineering* vol. 16, pp. 1674-1680, 2006.

[88] J. N. McMullin, "Laser fabrication of integrated microfluidic/micro-optic systems," *Proceedings of SPIE*, vol. 4087, pp. 1050-1055, 2000.

[89] K. B. Mogensen, J. El-Ali, A. Wolff, and J. P. Kutter, "Integration of Polymer Waveguides for Optical Detection in Microfabricated Chemical Analysis Systems " *Applied Optics*, vol. 42, pp. 4072-4079, 2003.

[90] M. Fleger, D. Siepe, and A. Neyer, "Microfabricated polymer analysis chip for optical detection," *IEEE Proceedings- Nanobiotechnology* vol. 151, pp. 159-161, 2004.

[91] S.-H. Huang and F.-G. Tseng, "Development of a monolithic total internal reflection-based biochip utilizing a microprism array for fluorescence sensing," *Journal of micromechanics and microengineering* vol. 15, pp. 2235-2242, 2005.

[92] S. Balslev, A. M. Jorgensen, B. Bilenberg, K. B. Mogensen, D. Snakenborg, O. Geschke, J. P. Kutter, and A. Kristensen, "Lab-on-a-chip with integrated optical transducers," *Lab on a Chip*, vol. 6, pp. 213-217, 2006.

[93] C. L. Bliss, C. J. Backhouse, and J. N. McMullin, "Two-Colour Microparticle Detection in PDMS Biochips with Integrated Optics," *Proceedings of SPIE*, vol. 6796, pp. 67960A1-67960A6, 2007.

[94] C. L. Bliss, J. N. McMullin, and C. J. Backhouse, "Rapid fabrication of a microfluidic device with integrated optical waveguides for DNA fragment analysis," *Lab on a Chip*, vol. 7, pp. 1280-1287, 2007.

[95] H. Hosseinkhannazer, L. Kostiuk, and J. N. McMullin, "Multilayer Biochips with Integrated Optics Replicated in PMMA and PDMS," *Proceedings of SPIE*, vol. 6796, pp. 76960B1-76960B7, 2007.

[96] C. L. Bliss, J. N. McMullin, and C. J. Backhouse, "Integrated wavelength-selective optical waveguides for microfluidic-based laser-induced fluorescence detection," *Lab on a Chip*, vol. 8, pp. 143-151, 2008.

[97] H. Hosseinkhannazer, L. W. Kostiuka, and J. N. McMullin, "Two-Species Microparticle Detection in Optofluidic Biochips with Polymeric Waveguides," *Proceedings of SPIE*, vol. 7099, pp. 70990H1-70990H6, 2008.

[98] H. Hosseinkhannazer, L. Kostiuk, and J. N. McMullin, "Multilayer Biochips with Integrated Optics Replicated in PMMA and PDMS," *Photonics North, Proceedings of SPIE*, vol. 6796, pp. 67960B1-67960B7, 2007.

[99] H. Hosseinkhannazer, L. W. Kostiuk, and J. N. McMullin, "Two-Species Microparticle Detection in Optofluidic Biochips with Polymeric Waveguides," *Proceedings of SPIE*, vol. 7099, pp. 70990H1-70990H6, 2008.

[100] D. A. Chang-Yen, R. K. Eich, and B. K. Gale, "A Monolithic PDMS Waveguide System Fabricated Using Soft-Lithography Techniques," *Journal of Lightwave Technology*, vol. 23, pp. 2088-2093, 2005.

[101] M. Fleger and A. Neyer, "PDMS microfluidic chip with integrated waveguides for optical detection," *Microelectronic Engineering*, vol. 83, pp. 1291-1293, 2006.

[102] A. Neyer, S. Kopetz, E. Rabe, and D. Cai, "Polymer Waveguide Technologies for Optical Interconnects," *European Conference on Integrated Optics (ECIO)-Copenhagen, Denmark* 2007 http://www.ecio-conference.org/2007/paper/2007_ThD0.pdf.

[103] U. Kloter, H. Schmid, H. Wolf, B. Michel, and D. Juncker, "High-Resolution Patterning and Transfer of Thin PDMS Films: Fabrication of Hybrid Self-Sealing 3D Microfluidic Systems," *Proceedings of the 17th IEEE International Conference on Micro Electro Mechanical Systems (MEMS): Maastricht, Netherlands*, pp. 745-748, 2004.

[104] J. Jon V. DeGroot, A. W. Norris, S. O. Glover, and T. V. Clapp, "Highly Transparent Silicone Materials," *Linear and Nonlinear Optics of Organic Materials IV, Proceedings of SPIE* vol. 5517, pp. 116-123, 2004.

[105] "Fluospheres," *Molecular Probes: http://probes.invitrogen.com/handbook/sections/0605.html*, 2009.

[106] S. C. Jakeway, A. J. d. Mello, and E. L. Russell, "Miniaturized total analysis systems for biological analysis " *Fresenius J. Anal. Chem.*, vol. 366, pp. 525-539, 2000.

[107] M. L. Adams, M. Enzelberger, S. Quake, and -. A. Scherer104(1), "Microfluidic integration on detector arrays, for absorption and fluorescence micro-spectrometers," *Sensors and Actuators A: Physical* vol. 104, pp. 25-31.

[108] S. K. Sia and G. M. Whitesides, "Microfluidic devices fabricated in poly(dimethylsiloxane) for biological studies," *Electrophoresis*, vol. 24, pp. 3563–3576, 2003.
[109] S. M. Azmayesh-Fard, E. Flaim, and J. N. M. . "PDMS biochips with integrated waveguides," *Journal of Micromechanics and Microengineering* vol. 20
pp. 1-5, 2010.
[110] S. Camou, H. Fujita, and T. Fujii, "PDMS 2D optical lens integrated with microfluidic channels: principle and characterization," *Lab Chip* vol. 3 2003
[111] P. Domachuk, H. Perry, M. Cronin-Golomb, and F. G. Omenetto, "Towards an integrated optofluidic diffractive spectrometer," *IEEE Photon. Technol. Lett.* , vol. 19, pp. 1976-1978, 2007.
[112] C. Yang, K. Shi, P. Edwards, and Z. L. O. Express, "Demonstration of a PDMS based hybrid grating and Fresnel lens (G-Fresnel) device," *Opt. Express*, vol. 18, pp. 23529-23534, 2010.
[113] Z. Hu, A. Glidle, C. N. Ironside, M. Sorel, M. J. Strain, J. Cooper, and H. Yin, "Integrated microspectrometer for fluorescence based analysis in a microfluidic format," *Lab Chip*, vol. 12, pp. 2850-2857 2012.
[114] J. S. Kee, D. P. Poenar, P. Neuzil, L. Yobas, and Y. Chen, "Design and fabrication of poly(dimethylsiloxane) arrayed waveguide grating," *Opt. Express*, vol. 18, pp. 21732-21742, 2010.
[115] F. E. Lytle and B. G. Splawn, "Performance of submillimeter square hollow waveguides," *Appl. Opt.*, vol. 41, pp. 6660-6665, 2002.
[116] X. Chen, J. N. McMullin, C. J. Haugen, and R. G. DeCorby, "Integrated diffraction grating for lab-on-a-chip microspectrometers," *Proc. SPIE*, vol. 5699, pp. 511-516, 2005.
[117] S. M. Azmayesh-Fard, "Gaussian beam propagation: comparison of the analytical closed-form Fresnel integral solution to the simulations of the Huygens, Fresnel, and Rayleigh–Sommerfeld I approximations," *Journal of Optical Society of America A*, vol. 30, pp. 640-644, 2013.
[118] H. Hosseinkhannazer and J. N. McMullin, "Scanning Integrated Microspectrometer for Lab-on-a-Chip Applications," *Proceedings of SPIE*, vol. 6796, pp. 679609-1 - 679609-7, 2007.
[119] S. M. Azmayesh-Fard, L. Lam, A. Meknyk, and R. G. DeCorby, "Design and fabrication of a planar PDMS transmission grating microspectrometer," *Optics Express*, vol. 21, pp. 11891-11900, 2013.

APPENDIX-I: Simulations

%full_parabolic2.m is a program to simulate collimated rays hitting a double
% parabolic lens in a slab waveguide with refractive index of 1.59
% (i.e. in photoresist material SU-8)

```
clear all
x1=zeros(51);
x2=zeros(51);
x3=zeros(51);
y1=zeros(51);
y2=zeros(51);
y3=zeros(51);
n = 1.59;
figure(1)
hold on
grid on
x1 = 0:0.1:5;
y1 = -x1.^2/20+2;
plot(x1,y1)
plot(-x1,y1)
x2 = 0:0.1:5;
y2 = x2.^2/20+4.5;
plot(x2,y2)
plot(-x2,y2)

m = -x1/10;
alpha = abs(atan(m));
alpha_1 = asin(n*sin(alpha));
m2 = tan(alpha_1+(pi./2-alpha));
x3 = 10.*m2 + sqrt(100*m2.*m2-20*m2.*x1+20.*y1-90);
y3 = x3.*x3./20 + 4.5;
for i=2:length(x1)
%rays hit the first lens
yray(1)=0;
xray(1)=x1(i);
xray(2)=x1(i);
yray(2)=y1(i);
plot(xray,yray);
plot(-xray,yray)
end
for j=2:length(x1)
%rays hit the second lens
yray2(1)=y1(j);
xray2(1)=x1(j);
xray2(2)=x3(j);
yray2(2)=y3(j);
plot(xray2,yray2)
plot(-xray2,yray2)
end
m3=x2/10;
beta = atan(m3);
beta_1=beta-(alpha_1-alpha);
beta_2=asin(sin(beta_1)./n);
m4=tan(pi./2+(beta-beta_2));
y_focal=-m4.*x3+y3;
```

```
for k=2:length(x1)
%rays hit the y axis (the focal points)
yray3(1)=y3(k);
xray3(1)=x3(k);
xray3(2)=0;
yray3(2)=y_focal(k);
plot(xray3,yray3)
plot(-xray3,yray3)
end
```

The following three programs need to be executed sequentially for the description and the ray-tracing of a specially designed aspheric lens.
These programs are: 1) runge_katta4.m 2) aspheric_runge_katta4.m and 3) aspheric_point_source_test.m

The following function needs to be saved as runge_katta4.m and placed in the matlab folder where the other two programs for the aspheric lens are being executed.

```
function [x, w] = runge_kutta4(a, b, N, alpha)

b=2;
a=0;
alpha=0;
N=800;

h = (b-a)/N;         %the step size
x(1) = a;
w(1) = alpha;        %the initial value

for i = 1:N
   k1 = h*f(x(i), w(i));
   k2 = h*f(x(i)+h/2, w(i)+(k1)/2);
   k3 = h*f(x(i)+h/2, w(i)+(k2)/2);
   k4 = h*f(x(i)+h, w(i)+k3);
   w(i+1) = w(i) + (k1 + 2*k2 + 2*k3 + k4)/6;
   x(i+1) = a + i*h;
end

plot(x, w)

function dy = f(x, y)

dy=(1.59*sqrt(x.^2/(x.^2+(5-y).^2)))/...
(1.59*sqrt((5-y).^2/(x.^2+(5-y).^2))-1);
```

```
% aspheric_runge_katta4.m is a program that obtains the values of
% x and w from a function called runge_katta4.m and produces a data file
% named lens_coordinates_runge_katta4.dat  which contains the coordinates
```

% of a specially designed aspheric lens.

```
clear all
n=1.59;
[x, w] = runge_kutta4(0, 2, 800, 0);

c = x';
d = w';
e = [c d]';
fid = fopen('lens_coordinates_runge_katta4.dat','w');
fprintf(fid,'%1.12f %1.12f\n', e);
fclose(fid);

g = [x(1:500)' w(1:500)']';
fid = fopen('my_lens_coordinates_runge_katta4.dat','w');
fprintf(fid,'%1.12f %1.12f\n', g);
fclose(fid);

x_coord = c;
y_coord = d;

x2 = 5-y_coord;
y2 = x_coord;
m = y2./x2;

for i = 1:length(x)
    theta(i) = atan(m(i));
end
%theta = (theta./pi)*180;
for i = 1:length(x)
    tan_theta2(i) = (n*sin(theta(i))/(n*cos(theta(i))-1));
end
theta2 = atan(tan_theta2);
%theta2 = (theta2./pi)*180;
theta1=theta2-theta;

for i = 1:length(x)
    sin_theta2(i) = sin(theta2(i));
end
 sin_theta2 = sin_theta2';

 for i = 1:length(x)
    n_times_sin_theta1(i) = n*sin(theta1(i));
end
 n_times_sin_theta1 = n_times_sin_theta1';

 final_proof = [sin_theta2(1:200,1) n_times_sin_theta1(1:200,1)]


figure(1)
hold on
grid on
plot(x,w,'k')
title('Solution of differential Equation');
```

```
xlabel('x');
ylabel('g(x)');
b=0:0.01:3;
g=b.^2/4;
plot(b,g)
```

% aspheric_point_source_test.m is the third and final program needed to simulate %ray-tracing
% from a point source through an especially designed aspheric lens

```
clear all
n = 1.59;
fid = fopen('lens_coordinates_runge_katta4.dat','r');
pts = fscanf(fid,'%g %g');
[m p]=size(pts);
pts=[reshape(pts,2,m/2)];
pts=pts';
x=pts(:,1);
y=-pts(:,2);
fclose(fid);
[x y];

for i = 2:length(x)-1
    vx_t(i) = x(i+1) - x(i-1);
    vy_t(i) = y(i+1) - y(i-1);
    norm_factor(i) = sqrt((x(i+1)-x(i-1))^2 + (y(i+1)-y(i-1))^2);
    vx_tan(i) = vx_t(i)/norm_factor(i);
    vy_tan(i) = vy_t(i)/norm_factor(i);

    vx_s(i) = x(i);
    vy_s(i) = y(i) +5 ;
    norm_factor_s(i) = sqrt((x(i)^2 + (y(i)+5)^2));
    vx_source(i) = vx_s(i)/norm_factor_s(i);
    vy_source(i) = vy_s(i)/norm_factor_s(i);

end

vz_tan = zeros(1,length(vx_t));
vx_horiz = ones(1,length(vx_t));
a = [vx_tan' vy_tan' vz_tan'];
b = [-vy_tan' vx_tan' vz_tan']; % b is the normal (n)
c = [vx_horiz' vz_tan' vz_tan'];
s = [vx_source' vy_source' vz_tan']; % s is the rays incident
%upon the aspheric lens from source ( source at x=0, y=-5 )
for k = 2:length(x)-1
theta(k,1:3) =
atan2(norm(cross(s(k,1:3),b(k,1:3))),dot(s(k,1:3),b(k,1:3)));
alpha(k,1:3) =
atan2(norm(cross(b(k,1:3),c(k,1:3))),dot(b(k,1:3),c(k,1:3)));

theta_1(k,3) = asin(n*sin(theta(k,3)));

m(k,3) = tan(theta_1(k,3)+alpha(k,3));
```

```
x_wall(k) = (m(k,3)*x(k) - y(k)+5)/m(k,3);
end
x_wall'

figure(1)
hold on
grid on
plot(x,y,'--')
plot(-x,y,'--')
for i=2:18:length(x)-1
%rays hit the lens
yray(1)=-5;
xray(1)=0;
xray(2)=x(i);
yray(2)=y(i);
plot(xray,yray);
plot(-xray,yray)
end
for k=2:18:length(x)-1
%rays hit the wall at y=5 (producing parallel rays)
yray3(1)=y(k);
xray3(1)=x(k);
xray3(2)=x_wall(k);
yray3(2)=5;
plot(xray3,yray3)
plot(-xray3,yray3)
end
```

```
%two_slits.m is a Fresnel integral approximation for
%diffraction of a plane input field due to a double_slit
clear all
clc
close all

lambda0 = 0.0005;
n1 = 1;   %index of slab for simulation

W=0.02;
h=0.02;
N=2;

n1 = 1;
k1 = (2*pi/lambda0)*n1;
y=40000;

dxin=lambda0/5;
xtot=(N-1)*h+W;
Npts=1001;
xin=linspace(-xtot/2,xtot/2,Npts);

for j=1:N
    C(j)=(N-1)*(-h/2)+(j-1)*h;

end;
```

```
x_output = linspace(-2000,2000,Npts);

j=1;
n=1;
while   n<=Npts;
        if abs(xin(n)-C(j))<=W/2
            E(n)=1;
        end

        n=n+1;
        if n==Npts+1
            break;
        end;

        if (abs(xin(n)-C(j))) >= W/2 & (n~=Npts)
            j=j+1;
            n=n+((h-W)/dxin);
        end;
end

for n=1:Npts;
    L = sqrt((x_output(n)).^2+y^2);
     obliq=y/L;
     E_out(n) = sum(sqrt(i*k1/(2*pi.*y)).*exp(-i*k1*y).*...
exp((-i*k1*((x_output(n)-xin).^2))/(2*y)).*...
((1+obliq)/2).*E.*dxin);
 end;
figure(1)
hold on
grid on;
plot(x_output,(abs(E_out).^2)/max(abs(E_out).^2),'k');   %filed
%on grating boundary
title('Plane wave diffraction (double-slit)');
xlabel('x of Output field (mm)');
ylabel('Optical intensity');
```

%four_slits.m is a Fresnel integral simulation that shows
%diffraction of a plane input field due to four slits

```
clear all
clc
close all

lambda0 = .5;
n1 = 1;   %index of slab for simulation

W=4;
h=12;
N=4;

n1 = 1;
```

```
k1 = (2*pi/lambda0)*n1;
y=4000;

dxin=lambda0/20;
xtot=(N-1)*h+W;
Npts=(xtot/dxin)+1;
xin=linspace(-xtot/2,xtot/2,Npts);

for i=1:N
    C(i)=(N-1)*(-h/2)+(i-1)*h;

end;

x_output = linspace(-2000,2000,Npts);

i=1;
n=1;
while   n<=Npts;
        if abs(xin(n)-C(i))<=W/2
            E(n)=1;
        end

        n=n+1;
        if n==Npts+1
            break;
        end;

        if (abs(xin(n)-C(i))) >= W/2 & (n~=Npts)
            i=i+1;
            n=n+((h-W)/dxin);
        end;
end

for n=1:Npts;
    L = sqrt((x_output(n)).^2+y^2);
     obliq=y/L;
            A=sqrt(j*k1/(2*pi.*y)).*exp(-j*k1*y);
            B=((x_output(n)-xin).^2);
            C=((1+obliq)/2)*dxin;
            E_out(n) = sum(A*C*exp((-j*k1*B)./(2*y)).*E);
 end;
figure(1)
grid on;
hold on;
plot(x_output,(abs(E_out).^2)/max(abs(E_out).^2),'k');   %field
%on grating %boundary
title('Plane wave diffraction (Multi slit)');
xlabel('x of Output field (um)');
ylabel('Optical intensity');
```

```
%From here on all routines listed require to accompany a function
%file named
%make_gaussian1.m to run. This function is listed below:
```

```
% make_gaussian1.m is the function that produces Gaussian beams
%---output---
%y: y-coordinate of field points, vector
%E: complex field amplitude, vector
%dy: distance between field points

function [y,E,dy] = make_Gaussian1(ms,nms,NP,y0)

%make sure NP is odd
% if mod(NP,2)==0
%     NP = NP+1;
% end

dy = nms*ms/(NP-1);
y = [-nms*ms/2:dy:nms*ms/2];
E = exp(-(y-y0).^2/(ms/2)^2);
% normalize power
pow = (sum(E.^2)*dy);
E = E./sqrt((pow));
```

```
% mygrating_new_approximation_new_facets_6R_mod_T.m is a program
%for %simulation
% of a gaussian beam diffraction due to an echelle grating. a
%function named
% make_gaussian1.m must be placed in the same directory in order
%to run this %routine.

clear all;
f = 250;
d = 7500;
R = 250;
R2 = 12000;
a = -2500;
n1 = 1.0;
n2 = 1.5;
lambda0 = 0.6;    %design wavelength
lambda1 = 0.5;    %lowest wavelength
S = 100;
m = 2;  %grating diffraction order
NF = 95;
NFP = 11;     %number of points per facet, odd
TFP = NF*NFP;
xI = -d-3*500;    %input point
yI = 0.0;
yD = yI;

yup = sqrt(R.^2/2.);
ylow = -yup;%-sqrt(R.^2/2.);
xup = -d-(R-sqrt(R.^2/2.));
xlow = xup;

w= (yup-ylow)/NF;
f2= f;
```

```
xD = 11163.60574-2500;   %output center

%parabolic collimating lens
yL = [ylow:(yup-ylow)/(TFP-1):yup]; %y for collimating lens
xL = -d-yL.^2/(4*f); %x for collimating lens

xLB = -12*R;
yLB = yL;
xFL = -d-yL.^2/(4*f2)+d+R;
yFL = yL;
xGB=-3000;

figure(1);
title('Device layout');
hold on;
grid on;
axis equal;
plot(xI,yI,'rs');   %input point
plot(xD,yD,'rs');   %output center
%plot(xL,yL,'k-');  %collimating lens
%plot(xLB,yLB,'k-'); %boundary of space behind lens
%plot(xFL,yL,'k-');  %focusing lens
plot([xI,-d,d,xD],[yI,0,0,yD],'r-');  %central ray
plot([xI,xGB,xFL(TFP),xD],[yI,yL(TFP),yL(TFP),yD],'r-');  %upper
%boundary ray
plot([xI,xGB,xFL(1),xD],[yI,yL(1),yL(1),yD],'r-'); %lower
%boundary ray


%----------------------------
%construct grating
dx = m*lambda0/(n1-n2); %dx displacement from facet to facet

Fw = (yup-ylow)/NF;
dyLin = Fw/(NFP-1);
NF2=(NF+1)/2;
for n=1:NF

    dFP(n)=(NF2-n)*dx+a;

end
for j=1:NF
    k=1:NFP;
        xFP(j,k)=dFP(j);
    end
    xFP=xFP';
xFP=reshape(xFP,1,TFP);
h=ylow
for n=1:NF
    for m=1:NFP
    yFP(n,m)=h+(m-1)*dyLin;
end
h=yFP(n,NFP)
end
yFP=yFP'
```

```
yFP=reshape(yFP,1,TFP);

TFP=TFP;
FPw=Fw/NFP;
xGB = -3000  %x of left boundary of grating area
fill([xFP(1),xFP,xGB,xGB],[yFP(1),yFP,yup,ylow],'c');   %plot
%grating area and facets;
plot(xFP,yFP,'k.');    %plot grating facet points
gtext(['dx = ',num2str(abs(dx),'%2.2f'),...
' um    dy = ',num2str(min(Fw),'%2.4f'),' um']); %facet feature
%size
clear yend;



%--------------------------------------
lambda0 = 0.6;
lambda1 = 0.5;
n1 = 1.0;   %index of slab for simulation
n2 = 1.5;   %index of grating groove for simulation

NINP = TFP; %number of input points, odd
in_ms = 40;  %input Gaussian field mode size
in_range = 4;   %input field calculation range, in number of mode
%size
NOP = NINP;  %number of output field points, odd
out_range = 12;   %output field calculation range, in number of S
dlambda = 0.05;    %simulation wavelength step
lambda = [lambda1:dlambda:2*lambda0-lambda1];   %wavelengths to
%be simulated

%get input field
[Sin,Ein,dyin] = make_Gaussian1(in_ms,in_range,NINP,0);  %assume
%Gaussian
xin = xI;
yin = Sin;
plot(xin,yin,'c+'); %input plane
figure(2);
hold on;
grid on;
plot(Sin,abs(Ein).^2);  %input field
title('Normalized input field');
xlabel('Distance (um)');
ylabel('Optical intensity');

% %boundary of vertical flat surface behind collimating lens,
%take same %number of points as on grating
yLB = yL;
yGB = yLB;
figure(1);
plot(xGB,yGB,'k-')
%output plane
dout = out_range*S/(NOP-1); %output point width
Sout = [-out_range/2*S:dout:out_range/2*S];
xout = xD;
```

```
yout = Sout;
plot(xout,yout,'b+');   %flat output plane

%loop thru wavelength
for nWL=1:length(lambda)
    k1 = 2*pi/lambda(nWL)*n1;
    k2 = 2*pi/lambda(nWL)*n2;
    powGG = 0.0;

    %calculate field on grating
    for n=1:TFP

        EG(nWL,n) = sum(sqrt(i*k1/2/pi./(xFP(n)-xin)).*...
exp(-i*k1*(xFP(n)-xin)).*...
exp(-i*k1*((yFP(n)-yin).^2)./(2*(xFP(n)-xin))).*Ein.*dyin);
        powGG = powGG+abs(EG(nWL,n))^2*FPw;   %power on grating
%boundary %before calibration

    end

    EG(nWL,:) = EG(nWL,:)/sqrt(powGG); %calibrate field on
%grating
    powG(nWL) = powGG;  %grating power

    for n=1:NOP
        Eout(nWL,n) = sum(sqrt(i*k2/2/pi./(xout-xFP)).*...
exp(-i*k2*(xout-xFP)).*...
exp(-i*k2*((yout(n)-yFP).^2)./(2*(xout-xFP))).*EG(nWL,:).*FPw);
    end
    powOUT(nWL) = sum(abs(Eout(nWL,:)).^2*dout); %total output
%power
end

leg_txt = [];
for nWL=1:length(lambda)
    leg_txt = strvcat(leg_txt,[num2str(lambda(nWL)),'micron']);
end


figure(6);
hold on;
grid on;
plot(yFP,abs(EG).^2);   %field intensity on grating facets
title('Optical field on grating facets');
xlabel('Height y (um)');
ylabel('Optical Intensity');
legend(leg_txt);

figure(8);
hold on;
grid on;
plot(Sout,abs(Eout).^2);    %field on output plane
title('Output fields');
xlabel('Distance (um)');
ylabel('Optical intensity');
```

```
legend(leg_txt);

figure(9);
hold on;
grid on;
plot(lambda,[powG;powOUT],'-*');    %field on output plane
title('Optical power');
xlabel('Wavelength (micron)');
ylabel('Power');
legend('grating','output plane');
```

```
% binary_grating.m simulates the diffraction of a gaussian beam
% by a binary phase grating
% this simulation shows the function of binary grating as 1x2
%beam splitter
clear all
clc
n1 = 1.0;   %index between the lens and the grating
n2 = 1.5;   %index of the slab waveguide
lambda0 = 0.6;
x_grating=0.0;
depth_grating=lambda0;
f = 20; %focal length of the first parabolic lens interface (1)
R = 2*f; %Radius of the first parabolic lens interface
yup=250;
ylow=-250;
NFP = 11;
NF = 95;
NF2plus= floor(NF/2)+1;
TFP=NF*NFP;
Fw=(yup-ylow)/NF;
FPW=Fw/(NFP-1);
dy=FPW;
FPw=Fw/NFP;
for n=1:NFP

    d1(n)=x_grating

end
for n=1:NFP

    d2(n)=x_grating+depth_grating

end
d=[d1 d2];
d=d';
d=repmat(d,NF2plus,1);
d=d(1:end-NFP);
xFP=d'

for n=1:NF
    for m=1:NFP
    y(n,m)=ylow+(m-1)*dy;
end
ylow=y(n,NFP)
```

```
end
y=y';
yFP=reshape(y,1,TFP);

xI=-2500;
yI=0.0;
xD=10000;
yD=0.0;
xout = xD;

yup = yFP(end);
ylow = -yup;
dyLin=(yup-ylow)/(TFP-1);
%parabolic collimating lens
yL = [ylow:(yup-ylow)/(TFP-1):yup]; %y for collimating lens
xL = -100-yL.^2/(10000); %x for collimating lens

figure(1);
title('Device layout');
hold on;
grid on;
axis equal;
plot(xI,yI,'rs');  %input point
plot(xD,yD,'rs');  %output center
plot(xL,yL,'k-');  %collimating lens
xGB = 100;         %x of left boundary of grating area
fill([xFP(1),xFP,xGB,xGB],[yFP(1),yFP,ylow,yup],'c');   %plot
%grating facets;
plot(xFP,yFP,'k.');    %plot grating facet points

TFP=TFP;
lambda0 = 0.6;   %design wavelength
lambda1 = 0.5;   %second stigmatic wavelength
dlambda = 0.05;    %simulation wavelength step
lambda = [lambda1:dlambda:2*lambda0-lambda1];   %wavelengths to
%be simulated
% lambda = [0.6];

S = 50;
in_ms = 200;  %input Gaussian field mode size
in_range = 4;   %input field calculation range, in number of mode
%size

%get input field
[Sin,Ein,dyin] = make_Gaussian1(in_ms,in_range,TFP,0);  %assume
%Gaussian

pow=(sum(abs(Ein).^2*dyin)^2);

xin = xI;
yin = Sin;
plot(xin,yin,'c+'); %input plane
figure(2);
hold on;
grid on;
```

```
plot(Sin,abs(Ein).^2);  %input field
title('Normalized input field');
xlabel('Distance (um)');
ylabel('Optical intensity');


%output plane
Sout = linspace(-800,800,TFP);
dout = Sout(2)-Sout(1);

xout = xD;
yout = Sout;
figure(1);
plot(xout,yout,'b+');   %flat output plane
plot(xin,yin,'c+'); %input plane

%loop thru wavelength
for nWL=1:length(lambda)
    k1 = 2*pi/lambda(nWL)*n1;
    k2 = 2*pi/lambda(nWL)*n2;

%calculate field on the first lens
    for n=1:TFP
        theta_d_in = atan((yL(n)-yin)./(xL(n)-xin));
        l = sqrt((xL(n)-xin).^2+(yL(n)-yin).^2);
         EL(nWL,n) = sum((i*k2/2).*besselh(1,k2*l).*...
cos(theta_d_in).*Ein.*dyin);
    end
%calculate field on grating
      powGG = 0.0;
        for n=1:TFP
        theta_d_in = atan((yFP(n)-yL)./(xFP(n)-xL));
        l = sqrt((xFP(n)-xL).^2+(yFP(n)-yL).^2);
        EG(nWL,n) = sum((i*k1/2).*besselh(1,k1*l).*...
cos(theta_d_in).*EL(nWL,:).*dyLin);
         powGG = powGG+abs(EG(nWL,n))^2*FPw;   %power on grating

    end

    EG(nWL,:) = EG(nWL,:)/sqrt(powGG); %calibrate field on
%grating
    powG(nWL) = powGG;  %grating power

    for n=1:TFP
        theta_d_out = atan((yout(n)-yFP)./(xout-xFP));
        l = sqrt((xout-xFP).^2+(yout(n)-yFP).^2);
        Eout(nWL,n) = sum((i*k2/2).*besselh(1,k2*l).*...
cos(theta_d_out).*EG(nWL,:).*FPw);
    end
    powOUT(nWL) = sum(abs(Eout(nWL,:)).^2*dout); %total output
%power
end

leg_txt = [];
for nWL=1:length(lambda)
```

```
    leg_txt = strvcat(leg_txt,[num2str(lambda(nWL)),'micron']);
end

figure(3);
hold on;
grid on;
plot(yFP,abs(EG).^2);   %field intensity on grating facets
title('Optical field on grating facets');
xlabel('Height y (um)');
ylabel('Optical Intensity');
legend(leg_txt);

figure(4);
hold on;
grid on;
plot(Sout,abs(Eout).^2);    %field on output plane
title('Output fields');
xlabel('Position of the fields across the output plane (um)');
ylabel('Optical intensity');
legend(leg_txt);

figure(5);
hold on;
grid on;
plot([lambda],[powG;powOUT],'-*');
title('Optical power');
xlabel('Wavelength (micron)');
ylabel('Power');
legend('grating','output plane');
```

```
% binary_grating_10deg_tilt.m is a program that simulates
%diffraction of a
% gaussian beam due to a binary phase grating that is tilted by
%10 degrees
clear all
clc
n1 = 1.0;   %index after the grating
n2 = 1.6;   %index before the grating
lambda0 = 0.6328;   %design wavelength
lambda1 = 0.5328;   %second stigmatic wavelength
dlambda = 0.05;    %simulation wavelength step
lambda = [0.5328:0.05:0.6328];   %wavelengths to be simulated
incidence_angle = pi/18
x_grating=0.0;
depth_grating=0.5;
yup=23.75;
ylow=-23.75;
NFP = 11;
NF = 95;
NF2plus= floor(NF/2)+1;
TFP=NF*NFP;
Fw=(yup-ylow)/NF;
FPW=Fw/(NFP-1);
dy=FPW;
FPw=Fw/NFP;
```

```
for n=1:NFP

    d1(n)=x_grating

end
for n=1:NFP

    d2(n)=x_grating+depth_grating

end
d=[d1 d2];
d=d';
d=repmat(d,NF2plus,1);
d=d(1:end-NFP);
xFP=d'

for n=1:NF
    for m=1:NFP
    y(n,m)=ylow+(m-1)*dy;
end
ylow=y(n,NFP)
end
y=y'
yFP=reshape(y,1,TFP);


xFP_r=xFP*cos(incidence_angle)+yFP*sin(incidence_angle);
yFP_r=yFP*cos(incidence_angle)-xFP*sin(incidence_angle);
plot(xFP_r,yFP_r)


xI=-1000;
yI=0.0;
xD=10000;
yD=0.0;
xout = xD;

yup = yFP(end);
ylow = -yup;
dyLin=(yup-ylow)/(TFP-1);

figure(1);
title('Device layout');
hold on;
grid on;
axis equal;
plot(xI,yI,'rs');   %input point
plot(xD,yD,'rs');   %output center
xGB = 100;  %x of left boundary of grating area
fill([xFP_r(1),xFP_r,xGB,xGB],[yFP_r(1),yFP_r,ylow,yup],'c');
%plot grating facets;
plot(xFP_r,yFP_r,'k.');    %plot grating facet points

S = 50;
```

```
in_ms = 20;  %input Gaussian field mode size
in_range = 4;   %input field calculation range, in number of mode
%size

%get input field
[Sin,Ein,dyin] = make_Gaussian1(in_ms,in_range,TFP,0);  %assume
%Gaussian
xin = xI;
yin = Sin;
plot(xin,yin,'r'); %input plane
figure(2);
hold on;
grid on;
plot(Sin,abs(Ein).^2);  %input field
title('Normalized input field');
xlabel('Distance (um)');
ylabel('Optical intensity');

%output plane
Sout = linspace(-10000,10000,TFP);
dout = (Sout(2)-Sout(1))*cos(incidence_angle);


xout = xD;
yout = Sout;
figure(1);
plot(xout,yout,'b+');   %flat output plane
plot(xin,yin,'c+'); %input plane

%loop thru wavelength
for nWL=1:length(lambda)
    k1 = 2*pi/lambda(nWL)*n1;
    k2 = 2*pi/lambda(nWL)*n2;


%calculate field on grating
      powGG = 0.0;
        for n=1:TFP
        theta_d_in = atan((yFP_r(n)-yin)./(xFP_r(n)-xin));
        l = sqrt((xFP_r(n)-xin).^2+(yFP_r(n)-yin).^2);
        EG(nWL,n) = sum((i*k2/2).*besselh(1,k2*l).*...
cos(theta_d_in).*Ein.*dyin);
         powGG = powGG+abs(EG(nWL,n))^2*FPw;
        end

    EG(nWL,:) = EG(nWL,:)/sqrt(powGG); %calibrate field on
%grating
    powG(nWL) = sum(abs(EG(nWL,:)).^2*FPw);  %grating power


    for n=1:TFP
        theta_d_out = atan((yout(n)-yFP_r)./(xout-xFP_r));
        l = sqrt((xout-xFP_r).^2+(yout(n)-yFP_r).^2);
        Eout(nWL,n) = sum((i*k1/2).*besselh(1,k1*l).*...
cos(theta_d_out).*EG(nWL,:).*FPw);
```

```
    end
    powOUT(nWL) = sum(abs(Eout(nWL,:)).^2*dout); %total output
%power
end

leg_txt = [];
for nWL=1:length(lambda)
    leg_txt = strvcat(leg_txt,[num2str(lambda(nWL)),'micron']);
end

figure(3);
hold on;
grid on;
plot(yFP,abs(EG).^2);   %field intensity on grating facets
title('Optical field on grating facets');
xlabel('Height y (um)');
ylabel('Optical Intensity');
legend(leg_txt);

figure(4);
hold on;
grid on;
plot(Sout,abs(Eout).^2);    %field on output plane
title('Output fields');
xlabel('Distance (um)');
ylabel('Optical intensity');
legend(leg_txt);

figure(5);
hold on;
grid on;
plot(lambda,[powG;powOUT],'-*');    %field on output plane
title('Optical power');
xlabel('Wavelength (micron)');
ylabel('Power');
legend('grating','output plane');

figure(6);
hold on;
grid on;
plot(lambda,[powOUT./sum(powOUT)],'-*');    %field on output
plane
title('Optical power at output');
xlabel('Wavelength (micron)');
ylabel('Power');
legend('output plane');
```

```
% my_blazed_grating.m is a program to simulate diffraction
% of a gaussian beam by a sawtooth grating, the grating
% is blazed for +1 order
clear all;
clc;
f = 500;
d = 3000;
```

```
R = 250;
R2 = 12000;
a = -2500; %distance from device center to grating center
n1 = 1.0;   %index before grating
n2 = 1.5;   %index after grating
lambda0 = 0.406;   %design wavelength
lambda1 = 0.306;   %second stigmatic wavelength
S = 100;
m = 1;  %grating diffraction order
NF = 95;     %number of facets
NFP = 11;    %number of points per facet, odd
TFP = NF*NFP;

xI = -d-3*R;   %input point
yI = 0.0;
yD = yI;


%---------------------------------------
yup = sqrt(R.^2/2.);
ylow = -sqrt(R.^2/2.);
xup = -d-(R-sqrt(R.^2/2.));
xlow = xup;

w= (yup-ylow)/NF;
f2= f;
xD = 6*R*2;   %output center
xGB=-3000;

%----------------------------
%construct grating
dx = m*lambda0/(n2-n1); %dx displacement from facet to facet
NF2 = (NF-1)/2;
NFP2 = (NFP-1)/2;
blaze_angle = pi/8.149;
theta = pi/2 - blaze_angle;
x = dx*sin(theta);
dd = dx/sin(blaze_angle);
y = dx/tan(blaze_angle);
dy = (dx/tan(blaze_angle))/(NFP-1);
h=-(dy*NF2*(NFP-1) + NFP2*dy);
for n=1:NF
    for m=1:NFP
    yFP(n,m)=h+(m-1)*dy;
end
h=yFP(n,NFP);
end
yFP=-yFP';
yFP=reshape(yFP,1,TFP);

yup = (dy*NF2*(NFP-1)+ NFP2*dy);
ylow = -(dy*NF2*(NFP-1) + NFP2*dy);
Fw = x/sin(blaze_angle);
dyLin_grating = Fw/(NFP-1);
```

```
xdiff = dy*tan(blaze_angle);
for n=1:NFP
    xFP(n)= x-(n-1)*xdiff+a;
end
xFP = repmat(xFP,1,NF);


figure(1);
title('Device layout');
hold on;
grid on;
axis equal;
plot(xI,yI,'rs');   %input point
plot(xD,yD,'rs');   %output center
plot([xI,-d,d,xD],[yI,0,0,yD],'r-');  %central ray
plot([xI,xGB,xFP(TFP),xD],[yI,yFP(TFP),yFP(TFP),yD],'r-');%upper
%boundary ray
plot([xI,xGB,xFP(1),xD],[yI,yFP(1),yFP(1),yD],'r-'); %lower
%boundary ray

FPw=Fw/(NFP);
xGB = -3000;   %x of left boundary of grating area
fill([xFP(1),xFP,xGB,xGB],[yFP(1),yFP,ylow,yup],'c');   %plot
%grating facets;
plot(xFP,yFP,'k.');    %plot grating facet points
gtext(['dx = ',num2str(abs(dx),'%2.3f'),...
' um, dy min = ',num2str(min(Fw),'%2.5f'),' um']); %facet feature
%size
clear yend;
%-------------------------------------
NINP = TFP; %number of input points, odd
in_ms = 40;  %input Gaussian field mode size
in_range = 4;   %input field calculation range, in number of mode
%size
out_range = 24;   %output field calculation range, in number of S
dlambda = 0.05;    %simulation wavelength step
lambda = [lambda1:dlambda:2*lambda0-lambda1];   %wavelengths to
%be simulated

%get input field
[Sin,Ein,dyin] = make_Gaussian1(in_ms,in_range,NINP,0);  %assume
%Gaussian
xin = xI;
yin = Sin;
plot(xin,yin,'c+'); %input plane
figure(2);
hold on;
grid on;
plot(Sin,abs(Ein).^2);  %input field
title('Normalized input field');
xlabel('y (vertical axis) (um)');
ylabel('Optical intensity');

%output plane
dout = out_range*S/(TFP-1); %output point width
Sout = [-out_range/2*S:dout:out_range/2*S];
```

```
xout = xD;
yout = Sout;
figure(1);
plot(xout,yout,'b+');   %flat output plane

%loop thru wavelength
for nWL=1:length(lambda)
    k1 = 2*pi/lambda(nWL)*n1;
    k2 = 2*pi/lambda(nWL)*n2;

     powGG = 0.0;
    %calculate field on grating
    for n=1:TFP
        EG(nWL,n) = sum(sqrt(i*k1/2/pi./(xFP(n)-xin)).*...
exp(-i*k1*(xFP(n)-xin)).*...
exp(-i*k1*((yFP(n)-yin).^2)./(2*(xFP(n)-xin))).*Ein.*dyin);
        powGG = powGG+abs(EG(nWL,n))^2*FPw;   %power on grating
    end

    EG(nWL,:) = EG(nWL,:)/sqrt(powGG); %calibrate field on
%grating
    powG(nWL) = powGG;  %grating power

%     %calculate field on output plane
    for n=1:TFP
        Eout(nWL,n) = sum(sqrt(i*k2/2/pi./(xout-xFP)).*...
exp(-i*k2*(xout-xFP)).*...
exp(-i*k2*((yout(n)-yFP).^2)./(2*(xout-xFP))).*EG(nWL,:).*FPw);
    end
    powOUT(nWL) = sum(abs(Eout(nWL,:)).^2*dout); %total output
%power
end

leg_txt = [];
for nWL=1:length(lambda)
    leg_txt = strvcat(leg_txt,[num2str(lambda(nWL)),'micron']);
end


figure(3);
hold on;
grid on;
plot(yFP,abs(EG).^2);   %field intensity on grating facets
title('Optical field on grating facets');
xlabel(' y (vertical axis) (um)');
ylabel('Optical Intensity');
legend(leg_txt);
%

figure(4);
hold on;
grid on;
plot(Sout,abs(Eout).^2);    %field on output plane
title('Output fields');
xlabel('Field position at the output plane (um)');
```

```
ylabel('Optical intensity');
legend(leg_txt);

figure(5);
hold on;
grid on;
plot(lambda,[powG;powOUT],'-*');    %field on output plane
title('Optical power');
xlabel('Wavelength (micron)');
ylabel('Power');
legend('grating','output plane');
```

```
% my_blazed_grating_orders.m is a program that predicts
% the position of different diffracted orders in a sawtooth
% transmission grating
clear all;
clc;
f = 500;
d = 3000;
R = 250;
R2 = 12000;
a = -2500; %distance from device center to grating center
n1 = 1.0;   %index before grating
n2 = 1.43;   %index after grating
lambda0 = 0.645;   %design wavelength
lambda1 = 0.533;   %wavelength of the orders
S = 100;
m = 2;  %grating diffraction order
NF = 195;
NFP = 11;    %number of points per facet, odd
TFP = NF*NFP;

xI = -d-3*R;   %input point
yI = 0.0;
yD = yI;
%---------------------------------------
yup = sqrt(R.^2/2.);
ylow = -sqrt(R.^2/2.);
xup = -d-(R-sqrt(R.^2/2.));
xlow = xup;

w= (yup-ylow)/NF;
f2= f;
xD =-1000;% 6*R*2;   %output center
xGB=-3000;          %grating boundary
%-----------------------------
%construct grating
dx = m*lambda0/(n2-n1); %dx displacement from facet to facet
NF2 = (NF-1)/2;
NFP2 = (NFP-1)/2;
blaze_angle = pi/8.149;
theta = pi/2 - blaze_angle;
x = dx*sin(theta);
dd = dx/sin(blaze_angle);
y = dx/tan(blaze_angle);
```

```
dy = (dx/tan(blaze_angle))/(NFP-1);
h=-(dy*NF2*(NFP-1) + NFP2*dy);
for n=1:NF
    for m=1:NFP
    yFP(n,m)=h+(m-1)*dy;
end
h=yFP(n,NFP);
end
yFP=-yFP';
yFP=reshape(yFP,1,TFP);

yup = (dy*NF2*(NFP-1)+ NFP2*dy);
ylow = -(dy*NF2*(NFP-1) + NFP2*dy);
Fw = x/sin(blaze_angle);
dyLin_grating = Fw/(NFP-1);

xdiff = dy*tan(blaze_angle);
for n=1:NFP
    xFP(n)= x-(n-1)*xdiff+a;
end
xFP = repmat(xFP,1,NF);

figure(1);
title('Device layout');
hold on;
grid on;
axis equal;
plot(xI,yI,'rs');   %input point
plot(xD,yD,'rs');   %output center
plot([xI,-d,d,xD],[yI,0,0,yD],'r-');  %central ray
plot([xI,xGB,xFP(TFP),xD],[yI,yFP(TFP),yFP(TFP),yD],'r-');%upper
%boundary ray
plot([xI,xGB,xFP(1),xD],[yI,yFP(1),yFP(1),yD],'r-'); %lower
%boundary ray



FPw=Fw/(NFP);
xGB = -3000;   %x of left boundary of grating area
fill([xFP(1),xFP,xGB,xGB],[yFP(1),yFP,ylow,yup],'c');   %plot
%grating facets;
plot(xFP,yFP,'k.');    %plot grating facet points
gtext(['dx = ',num2str(abs(dx),'%2.3f'),...
' um, dy min = ',num2str(min(Fw),'%2.5f'),' um']); %facet feature
%size
clear yend;
%-----------------------------------
NINP = 1045; %number of input points, odd
in_ms = 40;  %input Gaussian field mode size
in_range = 4;   %input field calculation range, in number of mode
%size
NOP = 1045;  %number of output field points, odd
out_range = 8;   %output field calculation range, in number of S
dlambda = 0.05;    %simulation wavelength step
% lambda = [lambda1:dlambda:2*lambda0-lambda1];   %wavelengths to
%be simulated
lambda=[lambda1];
```

```
%get input field
[Sin,Ein,dyin] = make_Gaussian1(in_ms,in_range,NINP,0);  %assume
%Gaussian
xin = xI;
yin = Sin;
plot(xin,yin,'c+'); %input plane
figure(2);
hold on;
grid on;
plot(Sin,abs(Ein).^2);  %input field
title('Normalized input field');
xlabel('y (vertical) axis (um)');
ylabel('Optical intensity');

%output plane
dout = out_range*S/(NOP-1); %output point width
Sout = [-out_range/2*S:dout:out_range/2*S];
xout = xD;
yout = Sout;
figure(1);
plot(xout,yout,'b+');   %flat output plane

%loop thru wavelength
for nWL=1:length(lambda)
    k1 = 2*pi/lambda(nWL)*n1;
    k2 = 2*pi/lambda(nWL)*n2;
     powGG = 0.0;
    %calculate field on grating
    for n=1:TFP
        EG(nWL,n) = sum(sqrt(1i*k1/2/pi./(xFP(n)-xin)).*...
exp(-1i*k1*(xFP(n)-xin)).*...
exp(-1i*k1*((yFP(n)-yin).^2)./(2*(xFP(n)-xin))).*Ein.*dyin);
        powGG = powGG+abs(EG(nWL,n))^2*FPw;   %power on grating
    end

    EG(nWL,:) = EG(nWL,:)/sqrt(powGG); %calibrate field on
%grating
    powG(nWL) = powGG;  %grating power

%     %calculate field on output plane
    for n=1:NOP
        Eout(nWL,n) = sum(sqrt(1i*k2/2/pi./(xout-xFP)).*...
exp(-1i*k2*(xout-xFP)).*...
exp(-1i*k2*((yout(n)-yFP).^2)./(2*(xout-xFP))).*...
EG(nWL,:).*FPw/1.027);
    end
    powOUT(nWL) = sum(abs(Eout(nWL,:)).^2*dout); %total output
%power
end

leg_txt = [];
for nWL=1:length(lambda)
    leg_txt = strvcat(leg_txt,[num2str(lambda(nWL)),'micron']);
end
```

```
figure(3);
hold on;
grid on;
plot(yFP,abs(EG).^2);   %field intensity on grating facets
title('Optical field on grating facets');
xlabel(' Position on grating plane (um)');
ylabel('Optical Intensity');
legend(leg_txt);
%
figure(4);
hold on;
grid on;
plot(Sout,(abs(Eout).^2));    %field on output plane
title('Output fields');
xlabel('Position at the output plane (um)');
ylabel('Optical intensity');
legend(leg_txt);

figure(5);
hold on;
grid on;
plot(lambda,[powG;powOUT],'-*');
title('Optical power');
xlabel('Wavelength (micron)');
ylabel('Power');
legend('grating','output plane');
```

```
%spectrometer.m is a Program to construct and simulate an
% integrated microspectrometer based on two parabolic lenss
% and a single transmission grating in between them.
% Seyed Azmayesh-Fard Dec-2008

clear all;
clc;
f = 3000; %focal length of the collimating lens
R = 822; %Radius of the collimating lens
n1 = 1.43;   %index of slab for grating construction
n2 = 1.0;   %index inside grating compartment
n3 = 1.0;   %index behind lenses
lambda0 = 0.645;   %design wavelength
lambda1 = 0.545;   %second stigmatic wavelength
S = 40;
m = 2;  %grating diffraction order
NF = 95;
NFP = 11;    %number of points per facet, odd
TFP = NF*NFP;%number of points on lens
NLP = TFP;

xI = 0;   %input point
yI = 0.0;
yD = yI;
```

```
%---------------------------------------
%construct lenses
%search lens boundary
yup = R*sin(pi/18);
ylow = -yup;
xup = 3*R-(R-R*cos(pi/18));
xlow = xup;

w= (yup-ylow)/NF;
xD = 14*R;   %output center

%parabolic collimating lens
yL = [ylow:(yup-ylow)/(NLP-1):yup]; %y for collimating lens
xL = 3*R-yL.^2/((4*f)*(n1/n3-1)); %x for collimating lens

xLB = 4*R;
yLB = yL;
xGB = 5*R; %x of left boundary of grating area
xFL = 8*R-yL.^2/((4*f)*(n1/n3-1));
yFL = yL;

figure(1);
title('Device layout');
hold on;
grid on;
axis([0 11508 -1000 1000]);
plot(xI,yI,'rs');   %input point
plot(xD,yD,'rs');   %output center
%plot(xS,yS,'gs');   %second stigmatic point
plot(xL,yL,'k-');  %collimating lens
plot(xLB,yLB,'k-'); %boundary of space behind lens
plot(xFL,yL,'k-');  %focusing lens
plot([xI,xD],[yI,yD],'r-');  %central ray
plot([xI,xL(NLP),xFL(NLP),xD],[yI,yL(NLP),yL(NLP),yD],...
'r-');%upper boundary ray
plot([xI,xL(1),xFL(1),xD],[yI,yL(1),yL(1),yD],'r-');%lower
%boundary ray
%----------------------------
%construct grating
dx = m*lambda0/(n1-n2); %dx displacement from facet to facet
Fw = (yup-ylow)/NF;
dyLin = Fw/(NFP-1);
NF2=(NF+1)/2;
for n=1:NF

    dFP(n)=(NF2-n)*dx+6*R;

end
for j=1:NF
    k=1:NFP;
        xFP(j,k)=dFP(j);
    end
    xFP=xFP';
xFP=reshape(xFP,1,TFP);
h=ylow;
for j=1:NF
```

```
    for k=1:NFP
    yFP(j,k)=h+(k-1)*dyLin;
end
h=yFP(j,NFP);
end
yFP=yFP';
yFP=reshape(yFP,1,TFP);

FPw=Fw/(NFP);
fill([xFP,xGB,xGB,xFP(1)],[yFP,yup,ylow,yFP(1)],'c');   %plot
%grating facets;
plot(xFP,yFP,'k.');    %plot grating facet points
gtext(['dx = ',num2str(abs(dx),'%2.2f'),...
' um, dy min = ',num2str(min(Fw),'%2.4f'),' um']); %facet feature
%size
%-------------------------------------
NINP = TFP; %number of input points, odd
in_ms = 40;  %input Gaussian field mode size
in_range = 4;   %input field calculation range, in number of mode
%size
NOP = TFP;  %number of output field points, odd
out_range = 24;   %output field calculation range, in number of S
dlambda = 0.05;    %simulation wavelength step
lambda = [lambda1:dlambda:2*lambda0-lambda1];   %wavelengths to
%be simulated

%get input field
[Sin,Ein,dyin] = make_Gaussian1(in_ms,in_range,NINP,0);  %assume
%Gaussian
xin = xI;
yin = Sin;
plot(xin,yin,'c+'); %input plane
figure(2);
hold on;
grid on;
plot(Sin,abs(Ein).^2);  %input field
title('Normalized input field');
xlabel('Distance (um)');
ylabel('Optical intensity');

% %boundary of vertical flat surface behind collimating lens
yLB = yL;
yGB = yLB;
figure(1);
plot(xGB,yGB,'k-')
%output plane
dout = out_range*S/(NOP-1); %output point width
Sout = [-out_range/2*S:dout:out_range/2*S];
xout = xD;
yout = Sout;
plot(xout,yout,'b+');   %flat output plane

%loop thru wavelength
for nWL=1:length(lambda)
    k1 = 2*pi/lambda(nWL)*n1;
    k2 = 2*pi/lambda(nWL)*n2;
```

```
    k3 = 2*pi/lambda(nWL)*n3;

    %calculate field on the first lens
    for n=1:TFP
        %theta_d_in = atan((yL(n)-yin)./(xL(n)-xin));
        %l = sqrt((xL(n)-xin).^2+(yL(n)-yin).^2);
        EL(nWL,n) = sum(sqrt(1i*k1/2/pi./(xL(n)-xin)).*...
exp(-1i*k1*(xL(n)-xin)).*...
exp(-1i*k1*((yL(n)-yin).^2)./(2*(xL(n)-xin))).*Ein.*dyin);
    end

    %calculate field on boundary of flat surface behind first
%lens
    dyLin = (yup-ylow)/(NLP-1);
    for n=1:TFP
        ELB(nWL,n) = sum(sqrt(1i*k3/2/pi./(xLB-xL)).*...
exp(-1i*k3*(xLB-xL)).*...
exp(-i*k3*((yLB(n)-yL).^2)./(2*(xLB-xL))).*EL(nWL,:).*dyLin);
    end

    %calculate field on grating boundary
    powGG = 0.0;
    for n=1:TFP
        EGB(nWL,n) = sum(sqrt(1i*k1/2/pi./(xGB-xLB)).*...
exp(-1i*k1*(xGB-xLB)).*...
exp(-1i*k1*((yGB(n)-yLB).^2)./(2*(xGB-xLB))).*ELB(nWL,:).*dyLin);
    end

    %calculate field on grating
    for n=1:TFP
        EG(nWL,n) = sum(sqrt(1i*k2/2/pi./(xFP(n)-xGB)).*...
exp(-1i*k2*(xFP(n)-xGB)).*...
exp(-1i*k2*((yFP(n)-yGB).^2)./(2*(xFP(n)-xGB))).*...
EGB(nWL,:).*dyLin);
        powGG = powGG+abs(EG(nWL,n))^2*FPw;   %power on grating
    end

    EG(nWL,:) = EG(nWL,:)/sqrt(powGG); %calibrate field on
%grating
    powG(nWL) = powGG;  %grating power
    %calculate field on focusing lens
    for n=1:NLP
        EFL(nWL,n) = sum(sqrt(1i*k1/2/pi./(xFL(n)-xFP)).*...
exp(-1i*k1*(xFL(n)-xFP)).*...
exp(-1i*k1*((yFL(n)-yFP).^2)./(2*(xFL(n)-xFP))).*EG(nWL,:).*FPw);
    end
    powFL(nWL) = sum(abs(EFL(nWL,:)).^2*(yup-ylow)/(NLP-1));

    %calculate field on output plane
    for n=1:NOP
        Eout(nWL,n) = sum(sqrt(1i*k3/2/pi./(xout-xFL)).*...
exp(-1i*k3*(xout-xFL)).*...
exp(-1i*k3*((yout(n)-yFL).^2)./(2*(xout-xFL))).*...
EFL(nWL,:).*dyLin);
    end
```

```
    powOUT(nWL) = sum(abs(Eout(nWL,:)).^2*dout); %total output
%power
end

leg_txt = [];
for nWL=1:length(lambda)
    leg_txt = strvcat(leg_txt,[num2str(lambda(nWL)),'micron']);
end

figure(3);
hold on;
grid on;
plot(yL,abs(EL).^2);   %filed on first lens
title('Optical field on first lens');
xlabel('Height y (um)');
ylabel('Optical intensity');
legend(leg_txt);

figure(4);
hold on;
grid on;
plot(yL,abs(ELB).^2);   %filed on plane surface after first lens
title('Optical field on plane surface after first lens');
xlabel('Height y (um)');
ylabel('Optical intensity');
legend(leg_txt);


figure(5);
hold on;
grid on;
plot(yGB,abs(EGB).^2);   %filed on grating boundary
title('Optical field on grating boundary');
xlabel('Height y (um)');
ylabel('Optical intensity');
legend(leg_txt);

figure(6);
hold on;
grid on;
plot(yFP,abs(EG).^2);   %field intensity on grating facets
title('Optical field on grating facets');
xlabel('Height y (um)');
ylabel('Optical Intensity');
legend(leg_txt);

figure(7);
hold on;
grid on;
plot(yFL,abs(EFL).^2);   %filed on focusing lens
title('Optical field on focusing lens');
xlabel('Height y (um)');
ylabel('Optical intensity');
legend(leg_txt);
```

```
figure(8);
hold on;
grid on;
plot(Sout,abs(Eout).^2);    %field on output plane
title('Output fields');
xlabel('Position at output plane (um)');
ylabel('Optical intensity');
legend(leg_txt);

figure(9);
hold on;
grid on;
plot(lambda,[powG;powFL;powOUT],'-*');    %field on output plane
title('Optical power');
xlabel('Wavelength (micron)');
ylabel('Power');
legend('grating','focusing lens','output plane');
```

```
%my2lens_Hankel.m is a Program to construct and simulate
%the results obtained from a given Gaussian input field
%after passing through a collimating and a focusing lens.
%Field calculations are based on Rayleigh-Sommerfeld-I
% diffraction integral that uses Hankel function
clear all;
f = 10; %focal length of the collimating lens
f2 = 10; %focal length of the focusing lens
d = .02; %distance from first lens vertex to device center
R = 2*f; %Radius of the collimating lens
R2 = 2*f2; %Radius of the focusing lens
n1 = 1.5;   %index of slab for lens construction
n2 = 1.0;   %index between two lens interfaces
lambda0 = 0.6;   %design wavelength
lambda1 = 0.5;   %second stigmatic wavelength
S = 10;
NF = 95;
NFP = 11;   %number of points per facet, odd
NLP = NF*NFP;  %number of points on lens
TFP = NLP;
xI = -d/2-3*R;   %input point
xD = 3*R+d/2;   %output center

yI = 0.0;
yD = yI;

%---------------------------------------
%construct lenses
%search lens boundary
alpha = pi/18; % alpha is the positive ray angle with optic axis
yup = (-2*R + sqrt(R.^2*(4+24*(tan(alpha))^2)))/(2*tan(alpha));
ylow = -yup;

%parabolic collimating lens
yL = [ylow:(yup-ylow)/(NLP-1):yup]; %y for collimating lens
xL = -d-yL.^2/(4*f);    %x for collimating lens
```

```
yup2 = (-2*R2 +
sqrt(R2.^2*(4+24*(tan(alpha))^2)))/(2*tan(alpha));
ylow2 = -yup2;


%parabolic focusing lens
yFL = [ylow2:(yup2-ylow2)/(NLP-1):yup2]; %y for focusing lens
xFL = yFL.^2/(4*f2);    %x for focusing lens


figure(1);
title('Device layout');
hold on;
grid on;
axis equal;
plot(xI,yI,'rs');   %input point
plot(xD,yD,'rs');   %output center
plot(xL,yL,'k-');  %collimating lens
%plot(xLB,yLB,'k-'); %boundary of space behind lens
plot(xFL,yFL,'k-');  %focusing lens
plot([xI,-d,d,xD],[yI,0,0,yD],'r-');  %central ray
plot([xI,xL(NLP),xFL(NLP),xD],[yI,yL(NLP),yFL(NLP),yD],'r-');
%upper boundary ray
plot([xI,xL(1),xFL(1),xD],[yI,yL(1),yL(1),yD],'r-'); %lower
%boundary ray


%-----------------------------
gtext(['xI = ',num2str((xI),'%2.2f'),...
' um, xD = ',num2str((xD),'%2.2f'),...' um']); %input and optput
%points
gtext(['f (collimating) = ',num2str((f),'%2.2f'),...
' um, f2 (focusing) = ',num2str((f2),'%2.2f'),' um']);



%-------------------------------------

NINP = 1045; %number of input points, odd
in_ms = 10;  %input Gaussian field mode size
in_range = 4;   %input field calculation range, in number of mode
%size
out_range = 4;   %output field calculation range, in number of S
dlambda = 0.05;    %simulation wavelength step
lambda = [lambda1:dlambda:2*lambda0-lambda1];   %wavelengths to
%be simulated

%get input field
[Sin,Ein,dyin] = make_Gaussian1(in_ms,in_range,NINP,0);  %assume
%Gaussian
xin = xI;
yin = Sin;
plot(xin,yin,'c+'); %input plane
```

```
figure(2);
hold on;
grid on;
plot(Sin,abs(Ein).^2);  %input field
title('Normalized input field');
xlabel('Field position at input plane (um)');
ylabel('Optical intensity');


figure(1);

dout = out_range*S/(NLP-1); %output point width
yout = [-out_range/2*S:dout:out_range/2*S];
xout = xD;

plot(xout,yout,'b+');   %flat output plane

    k1 = 2*pi/lambda0*n1;
    k2 = 2*pi/lambda0*n2;

    %calculate field on the first lens
    for n=1:TFP
        theta_d_in = atan((yL(n)-yin)./(xL(n)-xin));
        l = sqrt((xL(n)-xin).^2+(yL(n)-yin).^2);
        %EL(n) = sum(sqrt(i*k1/2/pi./(xL(n)-xin)).*exp(-
%i*k1*(xL(n)-xin)).*exp(-i*k1*((yL(n)-yin).^2)./(2*(xL(n)-
%xin))).*(1+cos(theta_d_in))./2.*Ein.*dyin);
        EL(n) = sum((i*k1/2).*besselh(1,k1*l).*...
cos(theta_d_in).*Ein.*dyin);
    end
    powL(n) = sum(abs(EL(1,:)).^2*(yup-ylow)/(NLP-1));

%     %calculate field on second lens
    dyLin = (yup-ylow)/(NLP-1);

    for n=1:TFP
        theta_d_F = atan((yFL(n)-yL)./(xFL(n)-xL));
        l = sqrt((xFL(n)-xL).^2+(yFL(n)-yL).^2);
        %EFL(n) = sum(sqrt(i*k3/2/pi./(xFL(n)-xL)).*exp(-
%i*k3*(xFL(n)-xL)).*exp(-i*k3*((yFL(n)-yL).^2)./(2*(xFL(n)-
%xL))).*(1+cos(theta_d_F))./2.*EL(1,:).*dyLin);
        EFL(n) = sum((i*k2/2).*besselh(1,k2*l).*...
cos(theta_d_F).*EL.*dyLin);
    end
    powFL(n) = sum(abs(EFL(1,:)).^2*(yup-ylow)/(NLP-1));

    %calculate field on output plane

    for n=1:NLP
        theta_d_out = atan((yout(n)-yFL)./(xout-xFL));
        l = sqrt((xout-xFL).^2+(yout(n)-yFL).^2);
        %Eout(1,n) = sum(sqrt(i*k1/2/pi./(xout-xFL)).*exp(-
%i*k1*(xout-xFL)).*exp(-i*k1*((yout(n)-yFL).^2)./(2*(xout-
%xFL))).*(1+cos(theta_d_out))./2.*EFL(1,:).*dyLin);
        Eout(n) = sum((i*k1/2).*besselh(1,k1*l).*...
```

```
cos(theta_d_out).*EFL.*dyLin);
    end
    powOUT(n) = sum(abs(Eout(1,:)).^2*dout); %total output power
    %end

leg_txt = [];
for nWL=1:length(lambda)
    leg_txt = strvcat(leg_txt,[num2str(lambda(nWL)*1E3),'nm']);
end



figure(3);
hold on;
grid on;
plot(yL,abs(EL).^2);   %field intensity on collimating lens
title('Optical field on first lens');
xlabel('Height y (um)');
ylabel('Optical Intensity');
legend(leg_txt);


figure(4);
hold on;
grid on;
plot(yFL,abs(EFL).^2);   %filed on focusing lens
title('Optical field on focusing lens');
xlabel('Height y (um)');
ylabel('Optical intensity');
legend(leg_txt);

figure(5);
hold on;
grid on;
plot(yout,abs(Eout).^2);    %field on output plane
title('Output field');
xlabel('Field position at output plane (um)');
ylabel('Optical intensity');
legend(leg_txt);
```

```
%ahankel1.m FOR THE
%TEST OF THE ASYMPTOTIC EXPANSION OF THE HANKEL-1 FUNCTION
%USING THE MAGNITUDE AND PHASE SERIES FROM Abramowitz&Stegun,
%PAGE 365,
%AND COMPARING TO THE MATLAB FUNCTION
%
clear all;
clc;
%Expansion coefficients
  A1 = 3/8; A2 = -45/128;
  B1 = -21/128; B2 = 1899/5120;
%Loop thru values of x of argument (1, 10, 100, ..., 100000)
  fprintf('\n            x        percent err    x*(p.c.er)');
for ix=1:11
```

```
  xix = (10^6)/(10^(0.5*(12-ix)));
  x(ix) = xix;
  %Matlab hankel.................
  h1 = besselh(1,xix);  magnh1 = abs(h1);  anglh1 = angle(h1);
  %Asymptotic hankel.............
  rtpx = sqrt(2/(pi*xix));  xmtp4 = xix - 3*pi/4;
  Mah1 = rtpx*(1+A1/xix^2+ A2/xix^4);
  Thah1 = xmtp4 + B1/xix;
  ah1(1) = Mah1*exp(i*Thah1);
%Find error and print
  pcrelerr= (100*abs((ah1-h1)/h1));
  xpcerr= xix*pcrelerr;
  fprintf('\n %12.0f        %8.5f      %8.5f',xix, pcrelerr,...
xpcerr);
  logx(ix) = log10(xix);  pcerr(ix) = pcrelerr;
  logpcerr(ix) = log10(pcrelerr); xpce(ix) = xix*pcerr(ix);
end; %of x-value loop
;
  plot(logx,logpcerr);
  xlabel('Log10(x)');
  ylabel('Log10(percent error)')
  title('Error in Asymptotic Approx. of H1(x)');
```

```
%system_of_nonlinear_equations_it_is_order_2.m is a program for
%constructing a self focusing transmission grating which
%simulates
%the diffraction of a gaussian beam for different wavelengths
clear all
clc
NF=395;
NFP=11;
TFP=NF*NFP;
n1=1.5;
n2=1.0;

x=0.55;
y=0.55;
delta=zeros(2,1);
epsilon=1e-3;
err=1;

for j=1:NF

    while err >= epsilon

        f1=(sqrt((5000-y)^2+(10000-x)^2))*...
n2-(sqrt((5000)^2+(10000)^2))*n2+x*n1+j*0.4;
        f2=(sqrt((2500-y)^2+(10000-x)^2))*...
n2-(sqrt((2500)^2+(10000)^2))*n2+x*n1+j*0.7;

        r_f1_x=-n2*(10000-x)/(sqrt((5000-y)^2+(10000-x)^2))+n1;
        r_f1_y=-n2*(5000-y)/(sqrt((5000-y)^2+(10000-x)^2));

        r_f2_x=-n2*(10000-x)/(sqrt((2500-y)^2+(10000-x)^2))+n1;
```

```
        r_f2_y=-n2*(2500-y)/(sqrt((2500-y)^2+(10000-x)^2));

        A=[r_f1_x r_f1_y; r_f2_x r_f2_y];
        B=[-f1;-f2];

        delta=A\B;
        x=x+delta(1);
        y=y+delta(2);

        err=max(delta);
    end
    err=1;
    delta=zeros(2,1);
    xx(j)=x;
    yy(j)=abs(y);
    x=0.55;
    y=0.55;
end

for j=1:NF
    k=1:NFP;
        xFP(j,k)=xx(j);
end
xFP=xFP';
xFP=reshape(xFP,1,TFP);

h=0.0;
yy(NF+1)= yy(NF)+(yy(NF)-yy(NF-1));

for n=1:NF
    dyLin(n)= (yy(n+1)-yy(n))/(NFP-1);
end
for n=1:NF

    for m=1:NFP

        yFP(n,m)=h+(m-1)*dyLin(n);
    end
h=yFP(n,NFP);
end
yFP=yFP';
yFP=reshape(yFP,1,TFP);


yFP= yFP-(yFP(end)-yFP(1))/2;
xFP= xFP-(((xFP(end)-xFP(1))/2)+xFP(1));



Fw=[abs((yFP(1:NFP:end)-yFP(NFP:NFP:end)))']
Fd=[abs(xFP(1:NFP:end-NFP) - xFP(1+NFP:NFP:end))']

dyLin = (yFP(end)*2)/TFP;
FPw=mean(dyLin);
```

```
xI=-1000;
yI=0.0;
xD=10000;
yD=0.0;
xout = xD;

figure(1);
title('Device layout');
hold on;
grid on;
axis equal;
plot([xI,xD],[yI,yD],'-k.');  %central ray
plot(xI,yI,'rs');   %input point
plot(xD,yD,'rs');   %output center
fill([xI,xFP(1),xD,xFP(end)],[0,yFP(1),0,yFP(end)],'c');%plot
%grating facets;
plot(xFP,yFP,'-k.');    %plot grating facet points

TFP=TFP;
lambda0 = 0.6;   %design wavelength
lambda1 = 0.5;   %second stigmatic wavelength
dlambda = 0.05;    %simulation wavelength step
lambda = [lambda1:dlambda:2*lambda0-lambda1];   %wavelengths to
%be simulated


S = 50;
TFP = TFP; %number of input points, odd
in_ms = 100;  %input Gaussian field mode size
in_range = 4;   %input field calculation range, in number of mode
%size
out_range = 40;   %output field calculation range, in number of S

%get input field
[Sin,Ein,dyin] = make_Gaussian1(in_ms,in_range,TFP,0);  %assume
%Gaussian
xin = xI;
yin = Sin;
figure(2);
hold on;
grid on;
plot(Sin,abs(Ein).^2);  %input field
title('Normalized input field');
xlabel('Distance (um)');
ylabel('Optical intensity');
figure(1);
%output plane
dout = out_range*S/(TFP-1); %output point width
Sout = [-out_range/2*S:dout:out_range/2*S];
xout = xD;
yout = Sout;

%calculation of linear shift of principal maxima(for when there
%is no
```

```
%dispersion of the wavelengths)
Sin_gama_b=(sum(Fd(1:end))/length(Fd))/...
(sum(Fw(1:end))/length(Fw));
Linear_shift_maxima=asin((n2-n1)*Sin_gama_b)*xout



plot([0,0],[Sout(1),Sout(end)],'k-');  %central ray
plot(xout,yout,'b+');   %flat output plane
plot(xin,yin,'c+'); %input plane

%loop thru wavelength
for nWL=1:length(lambda)
    k1 = 2*pi/lambda(nWL)*n1;
    k2 = 2*pi/lambda(nWL)*n2;
       powGG = 0.0;
        for n=1:TFP
        EG(nWL,n) = sum(sqrt(i*k1/2/pi./(xFP(n)-xin)).*...
            exp(-i*k1*(xFP(n)-xin)).*...
            exp(-i*k1*((yFP(n)-yin).^2)./(2*(xFP(n)-xin))).*...
            Ein.*dyin);
        powGG = powGG+abs(EG(nWL,n))^2*FPw;   %power on grating

    end

    EG(nWL,:) = EG(nWL,:)/sqrt(powGG); %calibrate field on
%grating
    powG(nWL) = powGG;  %grating power

    for n=1:TFP
        Eout(nWL,n) = sum(sqrt(i*k2/2/pi./(xout-xFP)).*...
            exp(-i*k2*(xout-xFP)).*...
            exp(-i*k2*((yout(n)-yFP).^2)./(2*(xout-xFP))).*...
            EG(nWL,:).*FPw);
    end
    powOUT(nWL) = sum(abs(Eout(nWL,:)).^2*dout); %total output
%power
end

leg_txt = [];
for nWL=1:length(lambda)
    leg_txt = strvcat(leg_txt,[num2str(lambda(nWL)),'micron']);
end



figure(3);
hold on;
grid on;
plot(yFP,abs(EG).^2);   %field intensity on grating facets
title('Optical field on grating facets');
xlabel(' y axis (um)');
ylabel('Optical Intensity');
legend(leg_txt);

figure(4);
```

```
hold on;
grid on;
plot(Sout,abs(Eout).^2);    %field on output plane
title('Output fields');
xlabel(' Position at output plane (um)');
ylabel('Optical intensity');
legend(leg_txt);

figure(5);
hold on;
grid on;
plot(lambda,[powG;powOUT],'-*');    %field on output plane
title('Optical power');
xlabel('Wavelength (micron)');
ylabel('Power');
legend('grating','output plane');
```

```
% A function named make_gaussian1.m listed previously must be
%placed in the
% same directory in order to run the following routine.
```

```
% The following two programs have to be executed in sequence.
% First program to run is mygrating_lens_facet_definition.m which
%defines the % facets of the lens-grating/lens optical system.
% Second program is mygrating_lens_Gaussian_input.m which
%simulates the
% diffraction of a Gaussian beam in the lens-grating/lens optical
%system at
% different wavelengths. "Processing time for this program is >10
%minutes"
```

```
% mygrating_lens_facet_definition.m is a program which defines
%the
% facets of the lens-grating/lens optical system.
clear all
clc
NF=600;
NFP=11;
TFP=NF*NFP;
Fw=6;
n1=1.43;
n2=1.0;
f=10000;
R1=f/(n1/(n1-n2));
lambda0 = 0.645;   %design wavelength
lambda1 = 0.545;   %second stigmatic wavelength
m = 2;  %grating diffraction order
xI = 0.0;   %x of input point
yI = 0.0;   %y of input point
% xD = 456*2;   %x of output center
yD = yI;  %y of output center
%construct lens and grating
dx = m*lambda0/(n1-n2); %dx displacement from facet to facet
F(1) = f;
for i = 1:NF
    F(i) = F(1)-(i-1)*dx;
```

```
    R(i) = ((n1-n2)/n1)*F(i);
end
theta=linspace(pi,1.944383494,NF)%2.842290364
polar(theta,R,'r');
[x,y]=pol2cart(theta,R);
plot(x,y)
for i=1:NF-1
theta2(i,:)=linspace(theta(i),theta(i+1),NFP);
end
theta2=theta2';
theta3=theta(end):(theta(2)-theta(1))/...
(NFP-1):(theta(end)+(NFP-1)*((theta(2)-theta(1))/(NFP-1)));
theta2=reshape(theta2,[1,(NF-1)*NFP]);
theta2=[theta2 theta3];
theta=theta';
theta2=reshape(theta2,[NFP,NF]);
for i=1:NF
    r(i,:) = ones(1,NFP) * R(i);
end
[x2,y2]=pol2cart(theta2,r');
figure(1)
hold on
grid on
axis equal
% axis([-1600 0, 0 1200])
plot(x2,y2,'r-')
x2 = x2 +10000+3007;
y2 = y2 -1.2928e+003;
x2=reshape(x2,[1,(NF*NFP)]);
d1=x2(:,1:NFP);
for i=1:(length(x2)-1),
    j=NFP:NFP:(length(x2)-1);
    c1=x2(j+1)-x2(j);
end
c1
x2=x2(NFP+1:end);
x2=reshape(x2,[NFP,NF-1]);
x2=x2';
x2=x2(:,:)-c1(1);
a1=x2(1,:);
for i=1:(NF-2)
x2=x2(2:end,:)-c1(i+1);
e1(i,:)=x2(1,:)
end
e1;
g1=(NF-2)*NFP;
e1=reshape(e1',[1,g1]);
x2=[d1 a1 e1];
x2=reshape(x2,[NFP,NF]);
   t=x2(:,1);
   x2=x2(:,2:end);

for i=1:NFP,
for j=1:(NF-1),
b(i,j)=j*3;
end
end
```

```
x2=x2+b;
   x2=[t x2];
   x2=reshape(x2,[1,TFP]);

y2=reshape(y2,[1,(NF*NFP)]);
d=y2(:,1:NFP)
 for i=1:(length(y2)-1),
    j=NFP:NFP:(length(y2)-1);
    c=y2(j+1)-y2(j);
end
c
y2=y2(NFP+1:end);
y2=reshape(y2,[NFP,NF-1]);
y2=y2';
y2=y2(:,:)-c(1);
a=y2(1,:);
for i=1:(NF-2)
y2=y2(2:end,:)-c(i+1);
e(i,:)=y2(1,:);
end
e;
g=(NF-2)*NFP;
e=reshape(e',[1,g]);
y2=[d a e];
xFP=x2;
yFP=y2;
xFP'
    fid = fopen('xFP1.out','w');
    fprintf(fid,'%f\n', xFP);
    fclose(fid);
yFP'
    fid = fopen('yFP1.out','w');
    fprintf(fid,'%f\n', yFP);
    fclose(fid);

% xFP_t=xFP(1926:3575)
% yFP_t=yFP(1926:3575)
%
% xFP_t'
%     fid = fopen('xFP_t.out','w');
%     fprintf(fid,'%f\n', xFP_t);
%     fclose(fid);
% yFP_t'
%     fid = fopen('yFP_t.out','w');
%     fprintf(fid,'%f\n', yFP_t);
%     fclose(fid);

    xFP_t=xFP(1596:3575)
    yFP_t=yFP(1596:3575)

    xFP_t2=xFP(1035:4400)
    yFP_t2=yFP(1035:4400)

xFP_t'
    fid = fopen('xFP_t.out','w');
    fprintf(fid,'%f\n', xFP_t);
```

```
    fclose(fid);
yFP_t'
    fid = fopen('yFP_t.out','w');
    fprintf(fid,'%f\n', yFP_t);
    fclose(fid);

xFP_t2'
    fid = fopen('xFP_t2.out','w');
    fprintf(fid,'%f\n', xFP_t2);
    fclose(fid);
yFP_t2'
    fid = fopen('yFP_t2.out','w');
    fprintf(fid,'%f\n', yFP_t2);
    fclose(fid);
```

```
% mygrating_lens_Gaussian_input.m is a program which simulates
%the
% diffraction of a Gaussian beam in the lens-grating/lens optical
%system at
% different wavelengths.
clear all
clc
NF=600;
NFP=11;
TFP=NF*NFP;
n1=1.43;
n2=1.0;
f=3000;
R1=f/(n1/(n1-n2));
lambda0 = 0.645;   %design wavelength
lambda1 = 0.545;   %second stigmatic wavelength
m = 2;  %grating diffraction order
xI = 7000.0;   %x of input point
yI = 0.0;   %y of input point
xD = 20214%2*642.88;   %x of output center
yD = yI;  %y of output center
%construct lens and grating
dx = m*lambda0/(n1-n2); %dx displacement from facet to facet
%--------------------------------------
%construct collimating lens
%search lens boundary
alpha1 = pi/5; % alpha is the positive ray angle with optic axis
yup1 = (-2*R1 +
sqrt(R1.^2*(4+24*(tan(alpha1))^2)))/(2*tan(alpha1));
ylow1 = -yup1;
%--------------------------------------
%parabolic collimating lens
yL1 = [ylow1:(yup1-ylow1)/(TFP-1):yup1]; %y for collimating lens
xL1 = 7000+(n1/(n1-n2))*R1-yL1.^2/(2*R1);    %x for collimating
%lens
dyLin = (yup1-ylow1)/(TFP-1);

xL1'
    fid = fopen('xL1.out','w');
    fprintf(fid,'%f\n', xL1);
    fclose(fid);
```

```
yL1'
    fid = fopen('yL1.out','w');
    fprintf(fid,'%f\n', yL1);
    fclose(fid);

[xFP]=textread('xFP1.out', '%f')
[yFP]=textread('yFP1.out', '%f')
xFP=xFP'
yFP=yFP'

x11=xFP(11:11:end-11);
y11=yFP(11:11:end-11);

x12=xFP(12:11:end);
y12=yFP(12:11:end);

     fid = fopen('x11.out','w');
    fprintf(fid,'%f\n', x11);
    fclose(fid);

    fid = fopen('y11.out','w');
    fprintf(fid,'%f\n', y11);
    fclose(fid);

    fid = fopen('x12.out','w');
    fprintf(fid,'%f\n', x12);
    fclose(fid);

    fid = fopen('y12.out','w');
    fprintf(fid,'%f\n', y12);
    fclose(fid);


figure(1);
title('Device layout');
hold on;
grid on;
axis equal;
% axis([1000 1400 -200 200]);;
plot(xI,yI,'rs');   %input point
plot(xD,yD,'rs');   %output center
plot(xL1,yL1,'k-');  %first parabolic lens
% plot(xL2,yL2,'k-');  %second parabolic lens
% plot(xL3,yL3,'k-');  %third parabolic lens
% plot(xL4,yL4,'k-');  %fourth parabolic lens
plot([xI,xD],[yI,yD],'r-');  %central ray
plot([xI,xL1(TFP),xFP(end),xD],[yI,yL1(TFP),yFP(end),yD],'r-');
%upper boundary ray
plot([xI,xL1(1),xFP(1),xD],[yI,yL1(1),yFP(1),yD],'r-'); %lower
%boundary ray
fill([xFP(1),xFP,xL1(end),...
xL1(end-1:-1:1)],[yFP(1),yFP,yL1(end),...
yL1(end-1:-1:1)],'c');
```

```
%
%fill([xFP(1),xL1,xFP(end),wrev(xFP)],[yFP(1),yL1,yFP(end),wrev(y
%FP)],'c');
%plot grating area and facets;
plot(xFP,yFP,'-k.');    %plot grating facet points


%-----------------------------
gtext(['xI = ',num2str((xI),'%2.2f'),...
' um, xD = ',num2str((xD),'%2.2f'),' um']); %input and optput
%points
t=yFP(2:end)-yFP(1:(end-1));
FPw=[0.6010 t];

dlambda = 0.05;    %simulation wavelength step
lambda = [0.545 0.595 0.645 0.695 0.745]; %wavelengths to be
%simulated
S = 40;
in_ms = 20;  %input Gaussian field mode size
in_range = 4;   %input field calculation range, in number of mode
%size
out_range = 60;   %output field calculation range, in number of S
%-------------------------------------

NINP = 1045; %number of input points, odd
%get input field

[Sin,Ein,dyin] = make_Gaussian1(in_ms,in_range,NINP,0);  %assume
%Gaussian
xin = xI;
yin = Sin;
%plot(xin,yin,'c+'); %input plane
figure(10);
hold on;
grid on;
plot(Sin,abs(Ein).^2);  %input field
title('Normalized input field');
xlabel('Distance (um)');
ylabel('Optical intensity');
figure(1);
%output plane
Sout=linspace(-1700,-800,TFP);
dout=Sout(2)-Sout(1);
xout = xD;
yout = Sout;
plot(xout,yout,'b+');   %flat output plane
plot(xin,yin,'c+'); %input plane

%loop thru wavelength
for nWL=1: length(lambda)
    k1 = 2*pi/lambda(nWL)*n1;
    k2 = 2*pi/lambda(nWL)*n2;

    for n=1:TFP
    theta_d_in = atan((yL1(n)-yin)./(xL1(n)-xin));
```

```
    l = sqrt((xL1(n)-xin).^2+(yL1(n)-yin).^2);

    EL1(nWL,n) = sum((i*k1/2).*besselh(1,k1*l).*...
cos(theta_d_in).*Ein.*dyin);
    end
    powL1(nWL) = sum(abs(EL1(nWL,:)).^2*dyLin); %power on lens
%calculate field on grating
      powGG = 0.0;
    for n=1:TFP
    theta_d_in = atan((yFP(n)-yL1)./(xFP(n)-xL1));
    l = sqrt((xFP(n)-xL1).^2+(yFP(n)-yL1).^2);
    EG(nWL,n) = sum((i*k2/2).*besselh(1,k2*l).*...
cos(theta_d_in).*EL1(nWL,:).*dyLin);
      powGG = powGG+abs(EG(nWL,n))^2*FPw;   %power on grating
%boundary
     end
      powG(nWL) = sum(abs(EG(nWL,:)).^2*FPw');

    for n=1:TFP
        theta_d_out = atan((yout(n)-yFP)./(xout-xFP));
        l = sqrt((xout-xFP).^2+(yout(n)-yFP).^2);
        Eout(nWL,n) = sum((i*k1/2).*besselh(1,k1*l).*...
cos(theta_d_out).*EG(nWL,:).*FPw);
    end
    powOUT(nWL) = sum(abs(Eout(nWL,:)).^2*dout); %total output
%power
end

leg_txt = [];
for nWL=1:length(lambda)
    leg_txt = strvcat(leg_txt,[num2str(lambda(nWL)),'micron']);
end

figure(5);
hold on;
grid on;
plot(yL1,abs(EL1).^2);   %field intensity on collimating lens
title('Optical field on first lens');
xlabel('Height y (um)');
ylabel('Optical Intensity');
legend(leg_txt);

figure(6);
hold on;
grid on;
plot(yFP,abs(EG).^2);   %field intensity on grating facets
title('Optical field on grating facets');
xlabel('Height y (um)');
ylabel('Optical Intensity');
legend(leg_txt);

figure(8);
hold on;
grid on;
plot(Sout,(abs(Eout).^2));    %field on output plane
title('Output fields');
```

```
xlabel('Distance X on output plane (um)');
ylabel('Optical intensity');
legend(leg_txt);

figure(9);
hold on;
grid on;
plot(lambda,[powL1;powG;powOUT],'-*');    %field on output plane
title('Optical power');
xlabel('Wavelength (micron)');
ylabel('Power');
legend('lens','grating','output plane');
```
